Electro-active boundary control for noise mitigation : local and advective strategie

Emanuele de Bono

N° d'ordre NNT : 2021LYSEC24

THÈSE DE DOCTORAT DE L'UNIVERSITÉ DE LYON

opérée au sein de **l'École Centrale de Lyon**

École Doctorale ED162

Mécanique - Énergétique - Génie Civil - Acoustique

Spécialité : Génie Mécanique

Soutenue publiquement le 29/06/2021, par :

Emanuele DE BONO

Electro-active boundary control for noise mitigation: Local and Advective strategies

---

Devant le jury composé de :

Yves AUREGAN, Directeur de Recherches CNRS, Université du Maine,	**Rapporteur**
Alain BERRY, Professeur, Unversité de Sherbrooke,	**Rapporteur**
Marie-Annick GALLAND, Professeur, École Centrale de Lyon,	**Présidente du jury**
Emeline SADOULET, Maître de Conférences, Université de Franche-Comté,	**Examinatrice**
Romain FLEURY, Professeur, École polytechnique fédérale de Lausanne,	**Examinateur**
Gerard SCORLETTI, Professeur, École Centrale de Lyon,	**Examinateur**
Emmanuel GOURDON, Professeur, École Nationale des Travaux Publics de l'État,	**Examinateur**
Manuel COLLET, Directeur de recherche CNRS, École Centrale de Lyon,	**Directeur de thèse**

Acknowledgments

The author acknowledges the support of the European Commission's Framework Program "Horizon 2020" through the Marie Sklodowska-Curie Innovative Training Networks (ITN) "SmartAnswer - Smart mitigation of flow-induced acoustic radiation and transmission" grant agreement No. 722401 to the present research project.

In the SmartAnswer consortium, I have found an incredible environment, with inspiring professors, researchers, and extremely nice colleagues. I hope the bond created during this experience will produce future collaborations.

Mes premiers remerciements sont pour mon directeur de thèse, Manuel Collet, pour avoir cru en moi, pour m'avoir motivé et poussé à donner tout ce que je pouvais dans mon travail de recherche. Je suis très reconnaisant à lui aussi pour avoir eu la possibilité d'apprendre plusieurs disciplines dans cette thèse.
Un remerciement particulaire va aussi à Sami Karkar, qui m'a coencadré en debut de doctorat, et m'a très bien introduit au sujet et à les utiles nécessaires. J'ai eu la chance à avoir un coencadrant comment lui, même si c'était pour un bref periode.

Un enorme remerciement à Stéphane Lamahieu, Lionel Charles et Sebastien Leone, pour leur constant soutien technique dans les manips. Leur aide était très precieux.
Un très grand remerciement à tous mes collegues, en particulaires à Adrien Pyskir, pour avoir rendu notre bureau un cabinet de curiosité, avec un ésprit très special et positif.

Un ringraziamento particolare va anche alla collega e concittadina Giulia Mazzeo, con la quale ho condiviso questo percorso trovando in lei una persona su cui contare.

Se ho avuto la possibilità di fare un dottorato all'Ecole Centrale de Lyon, é stato grazie al mio professore e tutor all'Università di Napoli Federico II, Francesco Marulo. È stato, é, e sarà, la figura professionale alla quale ispirarmi. Ringrazio egualmente Tiziano Polito e Michele Guida, per avermi accolto nel laboratorio di San Giovanni come un amico, con una simpatia e umanità uniche che contraddistinguono il loro gruppo di ricerca. I ricordi di quei pochi mesi passati lì con Antonio Sorrentino e Giuseppe Petrone, ad imparare ad amare la ricerca, sono indelebili. Come la mia prima conferenza ad ISMA2018, dove il gruppo si riunì come una famiglia.

Ringrazio anche il Prof. Sergio De Rosa il quale ha contribuito a farmi sentire parte della

realtà napoletana, anche se a distanza.

Infine ringrazio la mia famiglia, a cui questo lavoro, come tutto il mio percorso di studi, é dedicato. Loro sono l'origine e il fine di tutto ciò che di buono ho fatto.

Abstract

Boundary treatment for noise mitigation has long been targeted by both passive and active noise control strategies. Applications range from building and vehicle sound comfort, to the more challenging reduction of the noise radiated from aircraft engines. On the one hand the passive absorbing materials are not affected by stability problems but are usually bulky and not much performant in sufficiently large bandwidths in the low-frequency range. On the other hand, classical active noise control systems are very much affected by modification of the external acoustic environments, such as changes in the furniture of a room, or variation of the flow-speed and incident angle in an aircraft nacelle. In this perspective, the impedance control strategy provides an efficient way to assure stability independently from the external acoustic environment. In this thesis, the impedance control concept is deeply investigated and enlarged.

The first chapter is an introduction on the boundary treatment theoretical problem and state-of-art technologies (both passive and active). This introduction helps in the understanding of both limitations and spaces for improvements. Special attention is given to the problem of noise attenuation by boundary treatment of the parietal walls of an acoustic waveguide, as one bug industrial objective of this thesis is to provide an alternative solution to liners for the new generation of ultra-high-bypass-ratio (UHBR) turbofans. The second chapter analyses the potentialities of the pressure-based, current-driven impedance control technique to overcome the passive absorbing material limitations. The stability constraints of such impedance control are investigated analytically, numerically and experimentally, especially with respect to the inevitable time delay, and a practical solution to enlarge the stability margins is provided. The chapter ends with two broadening perspectives for such impedance control technique: the H_∞ automatic control synthesis approach, and a real-time innovative implementation featuring tunable non-linear behaviour of the absorber at low excitation amplitudes. The third chapter deals with a non-local boundary control capable of enhancing the isolation performances of the (local) impedance control, and of achieving non-reciprocal propagation in guided media. Such strategy is an enlargement of the classical impedance control, featuring convection of the surface reaction in a prescribed direction along the boundary itself. Analytical tools, along with numerical simulations are developed to fully characterize both performances and limitations of such boundary control concept. Finally, experimental tests validate its non-reciprocal character, its high isolation capabilities, as well as its stability constraints.

Keywords: active noise control, impedance control, non-linear absorber, active metamaterials, acoustic non-reciprocity.

Résumé

Le traitement aux bornes pour l'atténuation du bruit a longtemps été ciblé par les stratégies de contrôle du bruit. Les applications vont du confort sonore des bâtiments et des véhicules au réduction plus pénible du bruit émis par les moteurs d'avions. D'une part, les matériaux absorbants passifs ne sont pas affectés par des problèmes de stabilité mais sont généralement volumineux et pas très performant dans des bandes suffisamment larges dans la gamme des basses fréquences. D'autre part, les systèmes classiques de contrôle actif du bruit sont fortement influencés par la modification des environnements acoustiques externes, tels que les modifications du mobilier d'une pièce, ou la variation de la vitesse et de l'angle d'incidence dans une nacelle d'avion. Dans cette perspective, la stratégie de contrôle d'impédance offre un moyen efficace pour assurer la stabilité indépendamment de l'environnement acoustique. Dans cette thèse, le concept de contrôle d'impédance est approfondi et élargi.
Le premier chapitre est une introduction au problème théorique du traitement aux bornes et à l'état de l'art des technologies existantes (à la fois passives et actives). Cette introduction aide à comprendre soit les limites soit les espaces pour améliorer. Une attention particulière est accordée au problème d'atténuation du bruit par traitement aux bornes des parois d'un guide d'ondes acoustique, vu que l'objectif industriel de cette thèse est de proposer une solution alternative aux liners pour les nouveaux génération de turboréacteurs à ultra-grand taux de des dilution (UHBR). Le deuxième chapitre analyse les potentialités de la technique de contrôle d'impédance pilotée par le courant et basée sur la pression pour surmonter les limites des matériaux absorbants passifs. Les contraintes de stabilité d'un tel contrôle d'impédance sont étudiés analytiquement, numériquement et expérimentalement, en particulier en ce qui concerne l'inévitable retard, et une solution pratique pour élargir les marges de stabilité est fournie. Le chapitre se termine par deux perspectives qui élargissent telle technique de contrôle d'impédance: l'approche H_∞ de synthèse de contrôle automatique, et une implémentation en temps réel innovante qui permet d'atteindre comportement non linéaire réglable de l'absorbeur à faibles amplitudes de l'excitation. Le troisième chapitre traite d'un contrôle au bornes non local capable d'améliorer les performances d'isolation par rapport à la commande d'impédance (locale), et d'obtenir une propagation non réciproque dans des milieux guidés. Une telle stratégie est un élargissement du contrôle d'impédance classique, avec convection de la réaction de surface dans une direction prescrite le long de la frontière elle-même. Outils analytiques, ainsi que des simulations numériques sont développées pour caractériser pleinement les performances et limites d'un tel concept de contrôle de frontière. Enfin, des tests expérimentaux valident son caractère non-réciproque, ses capacités d'isolation élevées, ainsi que ses contraintes de stabilité.

Mots-clés: contrôle actif du bruit, contrôle d'impédance, absorbeur non linéaire, méta-matériaux actifs, non-réciprocité acoustique.

Contents

Chapter 1

Introduction

The thesis has been funded by the European Commission's Framework Program "Horizon 2020" through the Marie Sklodowska-Curie Innovative Training Networks (ITN) "SmartAnswer - Smart mitigation of flow-induced acoustic radiation and transmission" grant agreement No. 722401. The present thesis project aims at providing innovative solutions for the acoustic liner treatments of the new generation of Ultra-high bypass ratios (UHBR) turbofan engines, which are expected to equip the next generation of aircraft to maximise efficiency and reduce fuel consumption. The noise generated by these engines will concern lower frequencies compared to existing engine technologies. Also, with a thinner nacelle, absorption performances are expected to drop at low frequencies and, with a shorter nacelle, less surface area will be available for acoustic treatments, see Figure 1.1. Hence, UHBR engine technologies represent significant challenges for the design of next-generation acoustic treatments. Electro-active membranes (such as loudspeakers) driven by digital control architectures, provide promising solutions to overcome the limitations of traditional liners at the inlet and bypass regions of the nacelle, see Figure 1.2. In this thesis, an impedance control technique is deeply investigated both in its achievable performances and stability constraints. Also, the impedance control potential is broadened by investigating optimal corrector synthesis and non-linear target dynamics of the loudspeaker. Then, the locally reacting boundary concept is expanded to produce an unconventional non-local (advective) reaction of the liner, which proves both to enhance the isolation and to break the reciprocity principle of acoustic propagation in guided media. As such noise control techniques very much interest also other fields, such as room acoustics, an eye is kept both on the so-called "grazing-incidence" problem (concerning liner applications) and on the room acoustics application. Though, the main focus is on the grazing incidence one, envisaging the implementation of such technologies in the turbofan nacelles.

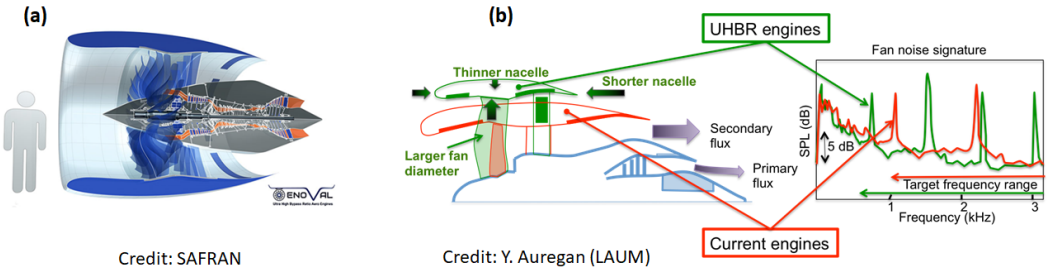

Figure 1.1: Size of the UHBR turbofan compared to an average man in **(a)**, and nacelle length evolution along with the noise signature shift in **(b)**.

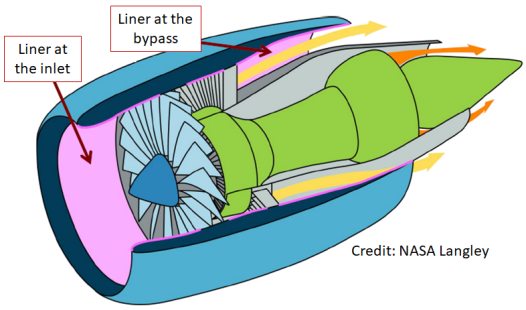

Figure 1.2: Sketch of the interior of a turbofan engine with inlet and bypass liners in pink.

1.1 The theoretical problem of boundary treatment for noise mitigation

The wave control by treating the boundaries of propagative domains is a large area of research encompassing all fields from electromagnetics to solid mechanics and acoustics. In this work we are dedicated to acoustics, but some concepts could be applied to other fields as long as the interdisciplinary analogies are properly defined.

In acoustics a typical boundary treatment problem is the room modal equalization, where the objective is to damp the acoustic modes in an enclosed cavity. P. Morse [87], in 1939, provided analytical solutions for the modes in an enclosed cavity with walls uniformly treated with materials characterized by the so-called *normal surface impedance*. Morse affirms that such quantity univocally identifies the absorptive properties of a surface, as it "depends only on the material and not on the incident wave (except for the variation with frequency)" [87]. The surface normal acoustic impedance $Z(\omega)$, is a complex quantity defined as the ratio between the local acoustic pressure $p(\omega)$ and the local normal acoustic velocity $v_n(\omega)$ in the frequency domain (ω being the angular frequency). Morse was analysing so-called locally-reacting surfaces, whose reaction depends only on the local sound pressure, and can therefore be characterized by the surface normal impedance. But Morse identified the concept of locally reacting wall as a degeneration of a more general case, where propagation could happen inside the wall, according to an anisotropic wave propagation equation with normal and tangential phase speeds (or refractive indexes) different from each other. Observe that the equivalence with anisotropic media in electromagnetics is straightforward. By reducing the tangential phase speed to zero, the propagation inside the wall would produce

a locally-reacting behaviour at the wall interface with air, represented by the normal surface impedance. A non-zero tangential phase speed "inside the wall", characterizes the so-called *non-locally reactive* surfaces, where the wall reaction does not depend only upon the local pressure, but also upon its spatial distribution. Typical non-locally reacting surfaces are indeed the interfaces with porous materials, which can be modelled as propagative homogeneous media in the equivalent fluid formulations [1].
The approximate analytical solutions in [87] related the modal damping factors to the wall impedances, providing an important background for optimization of boundary treatment in room acoustics and room modal equalization. Nevertheless, when the walls are only partially treated, the problem becomes far more complicated. Different geometries, position of the absorbing walls, presence of furniture, further increase this complexity. Recently, a plane wave approximation of the cavity modes [85] has inspired a fast technique to reconstruct the pressure field in rooms [118]. Both the plane wave decomposition and the fast sound field reconstruction techniques allow to envisage interesting optimizations of boundary treatments in room acoustics.
Another typical boundary treatment problem in acoustics is the noise transmission mitigation in an open duct, by treating its parietal walls with the so-called liners. A great deal of this thesis has been carried out by targeting such type of implementation with our boundary control techniques. Examples of industrial fields where this problem is particularly felt are the Heating and Ventilation Air-Conditioning Systems (HVAC) and the aircraft turbofan engines. The latter field in particular, on the one hand has to face significant restrictions on fuel consumptions and pollutant emissions, and on the other hand is tightened by the increasingly restrictive regulations on noise pollution. These two constraints are unfortunately in conflict with each other. As the fuel restrictions demand larger turbofan diameters, less number of blades and higher by-pass-ratios, the engine noise signature is shifted toward lower frequencies, which are much more challenging to mitigate by parietal treatments than high frequencies, as it is explained in the following sections. It is the case for the Ultra-High-By-Pass-Ratio turbofans, depicted in Figure 1.1. Though it constitutes a significant simplification of the actual industrial implementations of the noise transmission mitigation techniques in waveguides, the hypothesis of no-flow will be taken all along this thesis. The theoretical and experimental preliminary study of an acoustic waveguide without flow is common practice [116] as liners are usually meant to modify the acoustic field without significantly impacting on the aerodynamic one. Such hypothesis is nowadays very much debated [28], and in any case theoretical and experimental testing with flow constitutes an important successive step for the industrial implementation of any liner technology.

The greatest difficulty for the parietal treatment of a waveguide is, antonomastically, that it applies on the parietal walls $\partial\mathcal{A}$ (see Figure 1.3), whereas the noise propagates along the longitudinal axis x which is clearly parallel to $\partial\mathcal{A}$. Such problem is usually referred to as *grazing incidence* problem. It is very well known that if a plane wave field is incident on an infinite surface with an elevation angle $\bar{\theta} \in (0, \pi)$, where $\bar{\theta}$ is taken from the tangential boundary coordinate (see Figure 1.4), then perfect absorption is achieved when the surface acoustic impedance is $Z = \rho_0 c_0 / \sin\bar{\theta}$, where ρ_0 and c_0 are the air density and sound speed in the steady state. For $Z = \rho_0 c_0 / \sin\bar{\theta}$, a plane wave propagating at a certain angle θ_i, *sees*

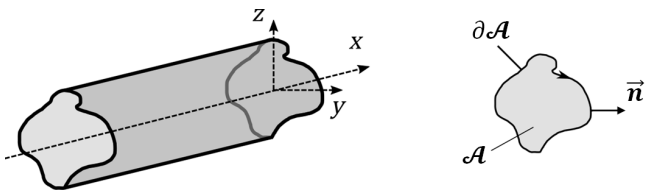

Figure 1.3: A cylindrical waveguide along coordinate x, with cross section of arbitrary shape $\mathcal{A}$. Left: overview of the waveguide. Right: detail of the cross-section and its contour $\partial\mathcal{A}$. $\vec{n}$ is the local exterior normal at each point of the contour.

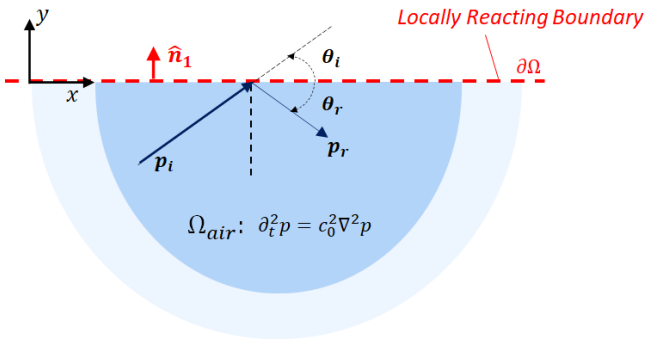

Figure 1.4: Semi-infinite acoustic domain Ω_{air}, expanding indefinitely along $\pm x$ and $-y$, bounded on $y = 0$ by a locally-reacting boundary $\partial\Omega$, and definition of the incidence and reflection angles according to the convention adopted in this text.

a frontal impedance $Z_f = \rho_0 c_0 sin\bar{\theta}/\sin\theta_i$ along its propagation direction, when it impacts the boundary. Therefore, if $\theta_i = \pm\bar{\theta}$ the frontal impedance encountered by the wave is equal to the characteristic impedance of air $\rho_0 c_0$, and no reflection occurs.
The problem arises when $\theta_i = 0$ or π. C. Bardos, G. Lebeau and J. Rauch [7] demonstrated that a sufficient condition for the boundary to fully control the wave propagation is that every ray of the acoustic field must interact with the boundary. But in case of the *grazing incidence* problem, i.e. in case of an acoustic field propagating in a waveguide, there will always be some rays not directly interacting with the boundary, therefore not *controllable*. This is also the reason why the effectiveness of any liner in noise transmission attenuation, degrades if the cross-section area of the waveguide increases, as less number of acoustic rays will directly interact with the boundary.

Nevertheless, even if the "grazing incidence problem" is not fully controllable, it should still be possible to determine an optimal liner behaviour which achieves the maximum noise transmission attenuation. The first work in this sense was done by L. Cremer [24] who searched for the optimal *local impedance* $Z_{cre}(\omega)$ producing the highest attenuation rate of the *least-attenuated* duct mode in a 2D infinite acoustic waveguide lined on one side, see Figure 1.5. His

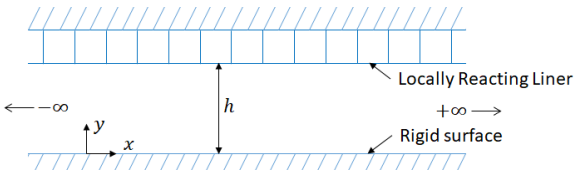

Figure 1.5: Infinite 2D lined duct considered in Cremer's work [24].

work is indeed rooted in the so-called duct-modes solution, i.e. the solution of the dispersion problem in terms of axial wavenumbers $k_{x,m}(\omega)$ and duct modes $\psi_m(y,z)$, corresponding to the eigenvalues and eigenfunctions of the transverse Laplace operator reduced to the waveguide cross section, as explained in Section 3.2.

Such optimal impedance is the one providing the coalescence of the first two duct modes, which means that for $Z(\omega) = Z_{cre}(\omega)$ the first and second wavenumber solutions of the dispersion problem merge. For $Z(\omega)$ slightly varied with respect to $Z_{cre}(\omega)$, either the first or the second duct mode presents an attenuation rate which is lower with respect to the case of $Z_{cre}(\omega)$. The duct modes are arranged in "first", "second", "third", etc. according to the number of node lines in the shape of $\psi_m(y,z)$, in ascending order.

In an infinite waveguide, the transmission between two points along the longitudinal axis is fully determined by the attenuation rate (of each duct mode involved in the noise propagation) times the distance between the two points. As the first duct modes are the ones presenting the lowest attenuation rate $\mathrm{Im}\{k_x(\omega)\}$, by maximizing it then the transmission will be minimized.

Nevertheless, the actual waveguides are not infinite, neither the first two duct modes are always the ones mainly excited by the external sources or the ones which radiate more acoustic energy outside the waveguide. B. Tester [116] reformulated the optimization problem based upon a non-conventional Green's function, allowing to slightly correct the Cremer value, and to determine the optimal impedances not only for the first couple of modes, but also for higher order couples of modes and for different geometries of the duct cross section. The tube was still considered as infinite and the optimal impedances were still producing the coalescence of the couple of modes to be mostly attenuated.

Such impedances found both by Cremer and Tester have all the same form: $Z_{opt}(\omega) = \rho_0 c_0 (a - \mathrm{j}b) k_0 h/\pi$, where a and b are constant positive real numbers, $k_0 = \omega/c_0$ is the wavenumber of the plane mode in hard-walled ducts and h is a characteristic dimension of the duct cross-section, normal to the liner. It is interesting to notice that while for free plane waves with an angle of incidence $\theta_i \in (0,\pi)$, the optimal impedance is purely resistive, for grazing incidence ($\theta_i = 0$ or π), $Z_{opt}(\omega)$ has a reactive component which has the same order of magnitude as the resistive one. Tester [117] provided a physical qualitative explanation for the specific value obtained for $Z_{opt}(\omega)$, by considering a line source applied along the centre longitudinal axis of the waveguide. He found that "the optimum impedance is roughly that value which allows the amplitude and phase of the singly-reflected field to cause the most efficient destructive interference with the direct field". It becomes then more understandable the importance of the phase change of the reflected field with respect to the incident one, produced by a complex impedance.

The only issue of such optimal complex impedance function $Z_{opt}(\omega)$ is that its inverse Fourier transform does not correspond to any real function in time domain, as it does not satisfy the so-called *reality condition* $Z^*(\omega) = Z(-\omega)$. This is so because the real part of $Z_{opt}(\omega)$ is not a pair function, which means that such optimal impedance is not physically realisable if not for single target frequencies $\omega = \omega_{target}$, but not on a continuous frequency span.

Another approach was instead investigated by M. Collet et al. [22], who presented an interesting technique to find the boundary operator assuring total absorption for any angle of incidence of impinging waves, see Chapter 3. As Morse, also Collet considered the boundary

as an interface with a secondary fictitious propagative medium, whose presence is *simulated* by the boundary condition at the interface. Therefore, he evaluated the boundary operator to apply in order to *simulate* the presence of a fully propagative domain behind, with both normal and tangential phase speeds equal to the air one, c_0. This way, as a plane wave propagates in air with any angle θ_i, in impacting such boundary, it does not even *realize* the presence of the boundary itself, and no reflection occurs. The derived boundary operator is non-local both in time and space (as non-local is the propagative domain *to be simulated* in behind). Though unrealistic to be implemented by active control systems (because of the number and complexity of calculations required), such boundary operator inspired the conceiving of another non-local operator which is the so-called Boundary Advection law in [22], whose implementation is a central argument of this manuscript.
The total absorption condition has been extensively investigated also in the field of computational physics, in order to simulate unbounded domains. An interesting boundary condition (B.C.) was provided by R. Higdon [53], which assured total absorption for multiple incident angles. For a single angle $\bar{\theta}$ (and its specular one) of total absorption, such B.C. degenerates to the local real impedance $Z = \rho_0 c_0 / \sin\bar{\theta}$ that we already discussed above. As soon as the total absorption must be achieved for more than one couple of specular angles of impingement, a non-local character of the boundary is required.
Nevertheless, though with no doubt such perfect absorption operators are of great interest for both room and duct acoustics, it is not sure that they would provide the best isolation performances in the grazing incidence problem. We have just mentioned that, in the restricted case of locally-reacting boundaries, the optimal impedance for the grazing incidence problem should take the form proposed by Cremer [24] and Tester [116], where actually the reflected field plays a more important role than the absorbed one. In any case, we have no certainty about the ideal Non-Local B.C. for the grazing incidence problem. Moreover, as both the Cremer optimal local impedance and the perfect-absorption non-local operator break down faced with their physical realisability, further investigation is required in the quest of physically admissible boundary controls for noise attenuation, both in their local and non-local connotations.

As this thesis focuses on the implementation of an active control to achieve higher performances with respect to the current state-of-art in both room-acoustics and grazing incidence problems, the following section goes through the evolution of the available technologies in boundary treatments for both these fields, with greater attention spent for the liner applications. Moreover, as our advection boundary law presents the special feature of *reciprocity breaking*, such field of research is also introduced in a separate section.

1.2 Passive Boundary treatments for noise mitigation

The problem of noise attenuation can be addressed by two main general philosophies: one is to trap or reflect the sound energy by means of some resonant element, and the other one is to dissipate it through viscous and heat conduction mechanisms at the solid-air interface. Clearly, the first idea does not exclude the second one, as dissipation inevitably occurs in passive systems, but, in resonant devices, dissipation is a secondary phenomenon respect to

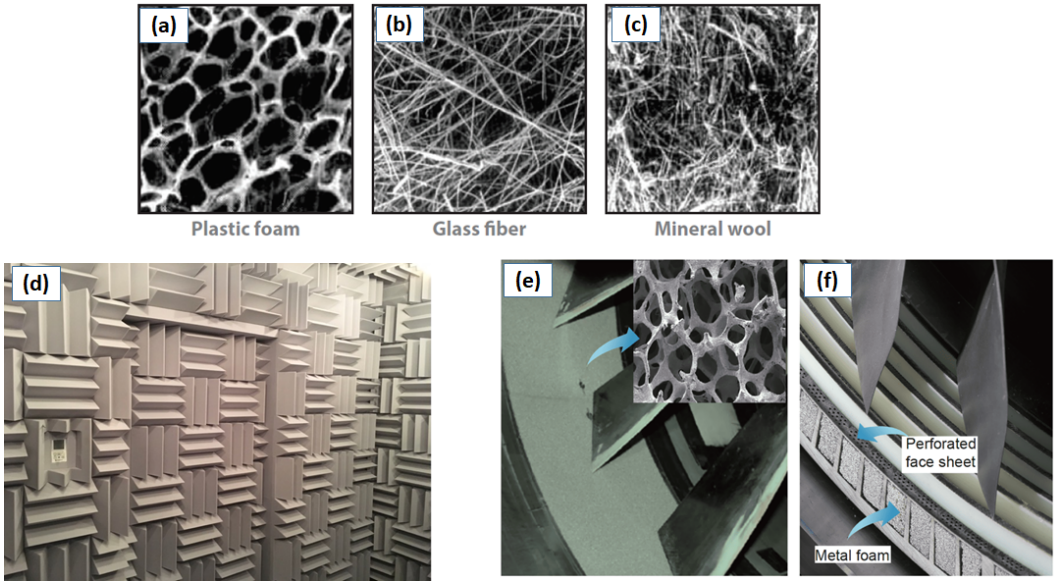

Figure 1.6: Types of porous materials microstructures: plastic foam **(a)**, glass fiber **(b)** and mineral wool **(c)**, from [123]. Applications of porous media in room acoustics (absorbing wedges in an anechoic chamber **(d)**) and in turbofan over-the-rotor nacelle (liner of metal foam **(e)**, with groves **(f)** to keep the aerodynamic performances, from [77])

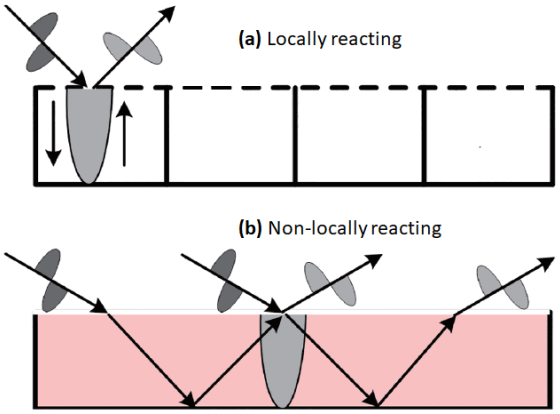

Figure 1.7: Sketch of locally-reacting **(a)** and non-locally reacting **(b)** liner (from [77])

resonance itself. The two phenomena of sound attenuation have also been targeted at the same time in order to exploit each other advantages.

Porous materials are renowned for the significant sound absorption they can achieve especially at high frequencies. Thanks to the large air-solid interface area obtained by fibrous and permeable microstructures (see Figures 1.6a,b,c), the viscosity and heat conduction mechanisms produce large dissipation. As dissipative forces vary linearly with the rate (e.g. viscous acoustic damping force is proportional to velocity), it follows that sound dissipation is a quadratic function of frequency. For this reason, the porous materials tend to improve their sound absorption potential as frequency increases. Moreover, as the dissipative forces mainly depend upon the acoustic velocity, the absorption is maximum at a $\lambda/4$ (λ being the wavelength of sound waves) distance from a rigid back-wall (where the acoustic velocity becomes zero). This explains the very large space required by the so-called absorbing wedges, clas-

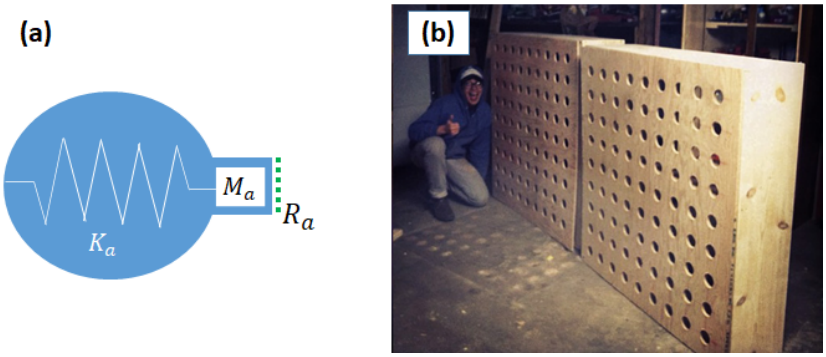

Figure 1.8: Sketch of a Helmholtz resonator in **(a)** with the mechanical mass-spring-resistance in-series analogy, with the equivalent acoustical mass M_a (given by the air in the neck), equivalent acoustical spring K_a (the compressibility of the cavity) and resistance R_a (given by an additional perforated sheet place at the inlet, and/or by the visco-thermal exchanges in the narrow neck). Typical application of the Helmholtz resonator in room acoustics **(b)**, from www.andymacdoor.com.

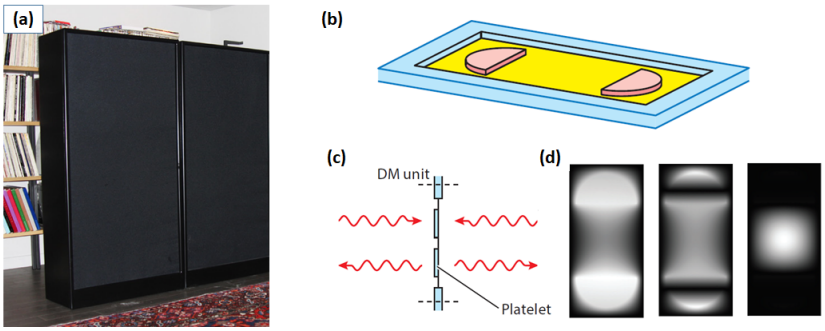

Figure 1.9: Membrane bass-trap for room acoustics **(a)** from www.andymacdoor.com; sketches of the decorated membrane (DM) **(b)**, **(c)** with the additional masses (platelets), providing the multimodal behaviour **(d)**, from [123].

sically used in room acoustics applications (see Figure 1.6d). Rigid porous materials, such as metal foams, are currently under investigation for applications as acoustic liners also in a harsh environment as the over-the-rotor region of the nacelle (see Figure 1.6e,f). Because of high percentage of void into their structure, porous materials allow sound propagation into their volume in both normal and tangential directions with respect to the interface with air. For this reason, they are defined as *non-locally* or *bulk* reacting liners, as opposed to the locally-reacting ones (see Figure 1.7).

Another classical sound-proofing device is the perforated, and micro-perforated, plate. It consists of a thin, rigid (usually metallic) plate with straight holes, usually backed by a cavity in order to increase the wave amplitude at the perforated plate location through the constructing interference effect. The sound energy dissipation mechanisms through the holes are indeed the same as in porous materials.

The classical sound-proofing device based upon the resonance principle is the famous Helmholtz resonator which is composed of a thin neck connecting the interface with a back-cavity. The air in the narrow neck moves as a whole, as if it were a mass, which is connected to a spring given by the back-cavity compressibility. Slight dissipative effects occurs in the neck. Another basic resonant absorber is the membrane, which is classically applied in room acoustics, where it takes the name of bass-trap (see Figure 1.9a).

All such resonant-based acoustic devices mainly suffer from the narrowness of the efficient absorption bandwidth.

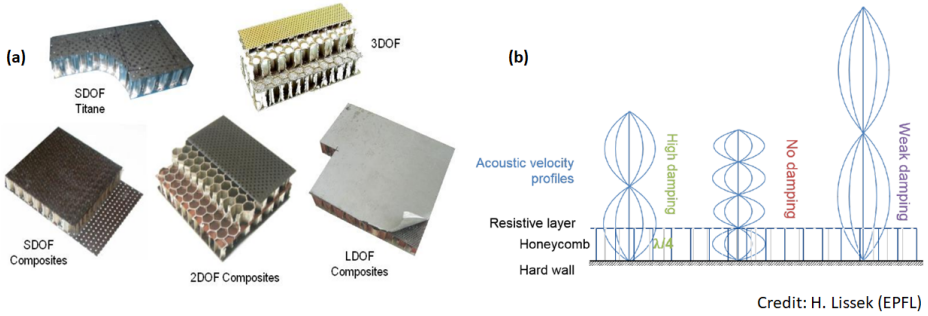

Figure 1.10: Single and multi-degree-of-freedom liners **(a)**, whose functioning is based upon the quarter-wavelength principle **(b)**.

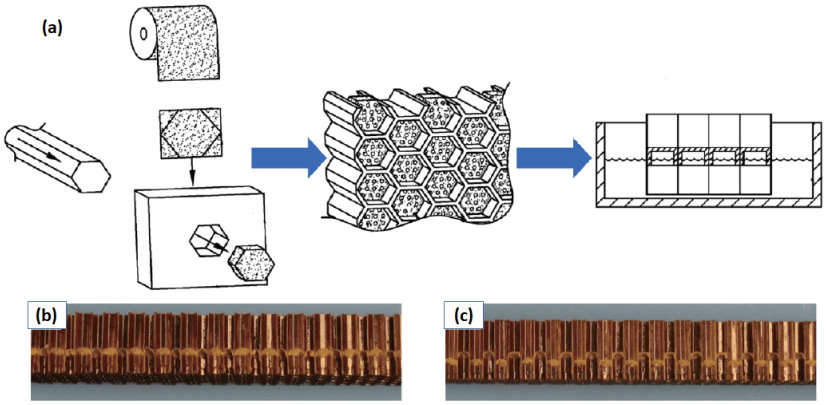

Figure 1.11: Schematics of manufacturing procedures **(a)** and photographs of mesh-cap honeycomb with **(b)** uniform depth and **(c)** variable depth, from [77].

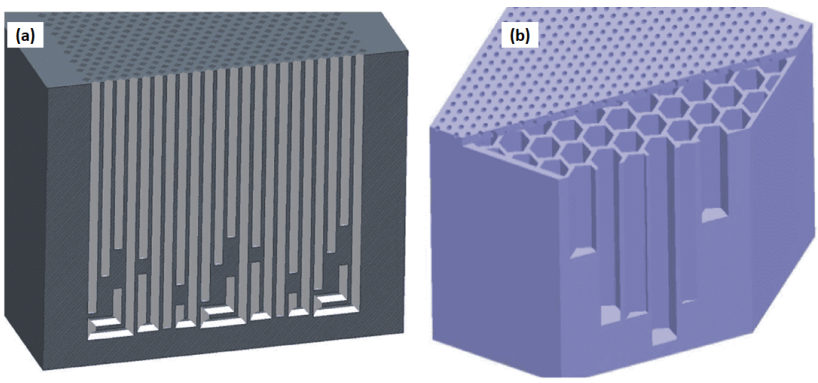

Figure 1.12: Sketch of variable-depth liners with narrow **(a)** and wide chambers **(b)**, from [77].

The traditional acoustic liner technology still applied nowadays for noise transmission attenuation at the inlet and outlet portions of turbofan engines is the so-called Single-Degree-of-Freedom (SDOF) liner. It is made of a closed honeycomb structure and a perforated plate which is used to provide the dissipative effect, to add mass in order to decrease the resonance

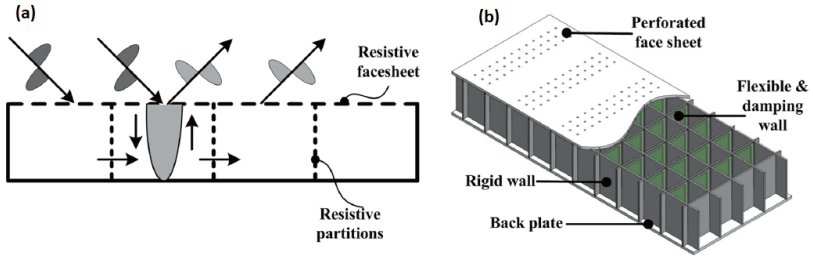

Figure 1.13: Sketch of hybrid locally/non-locally reacting liners with perforated **(a)** and flexible **(b)** cavity walls, from [77].

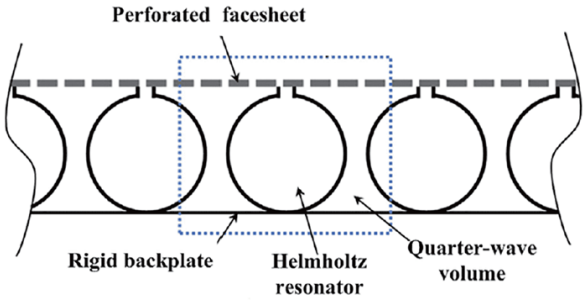

Figure 1.14: Double resonant liner [8].

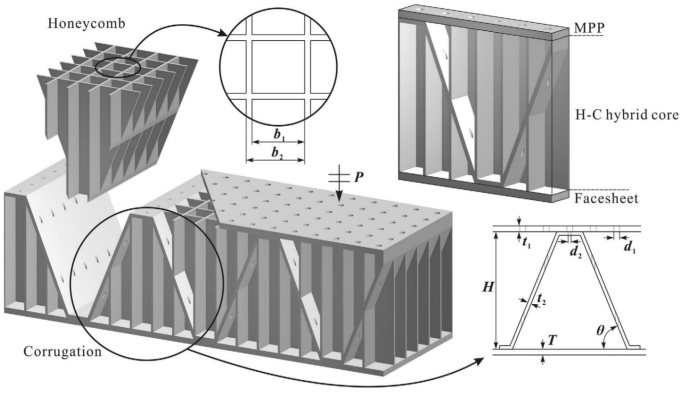

Figure 1.15: Liner with inclined microporous septa in the honeycomb, producing the so-called honeycomb-corrugation hybrid structure, but with microperforations on both top facesheet and corrugations [115].

frequency, and also to maintain the aerodynamic flow as smooth as possible on the internal wall of the nacelle. As the honeycomb structure is impervious, propagation is prevented transversely to the wall, therefore it can be considered as *locally reacting* as long as the incident field wavelength is much larger than the size of the honeycomb cells. The traditional SDOF liner is a quarter-wavelength resonator with a narrow absorption spectrum around $\lambda/4$, see Figure 1.10. Guess [48] has provided a method in three steps to evaluate the geometrical parameters of a SDOF liner, from a specified acoustic resistance and reactance, which can be tuned, for example, to the Cremer's values at a target frequency. The difficulty stays in the fact that the SDOF liner parameters affect both the resistance and reactance terms at the same time, making the tuning not so straightforward.

In order to broaden the noise absorption bandwidth, a septum is used to separate the honeycomb into two or more parts, forming the so-called double (DDOF) or multi-degree-of-freedom

(MDOF) configurations. They provide on the one hand larger bandwidth, but on the other excessive weight and bulky structures. Other improvements of the SDOF liner technologies have been developed, such as the mesh-cap liner [77] where porous sheets were inserted into the honeycomb cavities, see Figure 1.11. Compared to the integral septum in traditional MDOF liners, the mesh caps were only anchored to the cavity walls. Different number and types of mesh caps (with various resistances) could placed at different depths, in order to adjust the liner impedance. Another variant of the SDOF liner is the variable depth liner, with either narrow or wide chambers [94], see Figure 1.12. In order to exploit the benefits of a non-local reaction, the hybrid acoustic liner was conceived, where the cavity walls of the SDOF liner were substituted by perforated panels (see Figure 1.13). Another proposed alternative was to use flexible walls as partitions in order to profit from the visco-elastic dissipation.

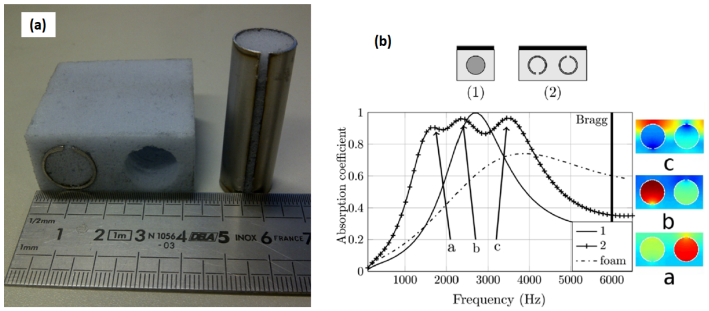

Figure 1.16: Meta-porous with resonant-inclusions photo **(a)** and normal absorption performances **(b)** [67].

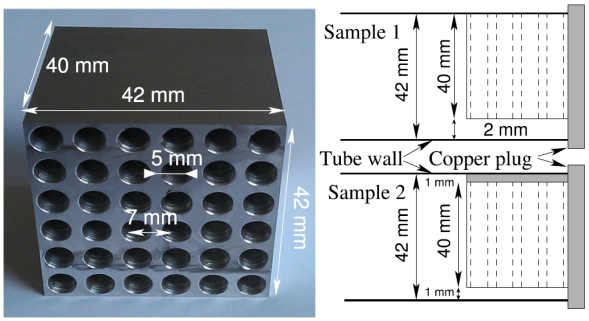

Figure 1.17: Slow-sound absorber by periodical structure of narrow slits with quarter-wavelength inclusions [47].

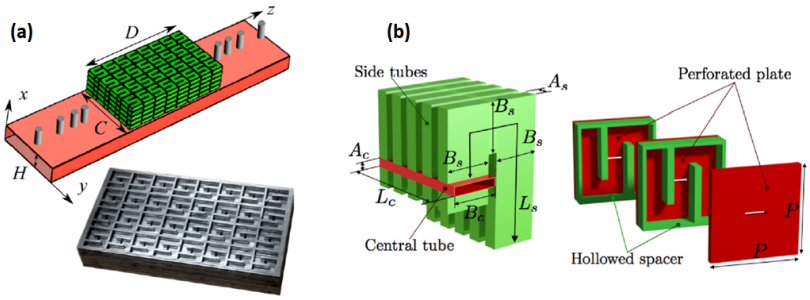

Figure 1.18: Slow-sound liner **(a)** with folded branches obtained by hollowed plates **(b)**, [3].

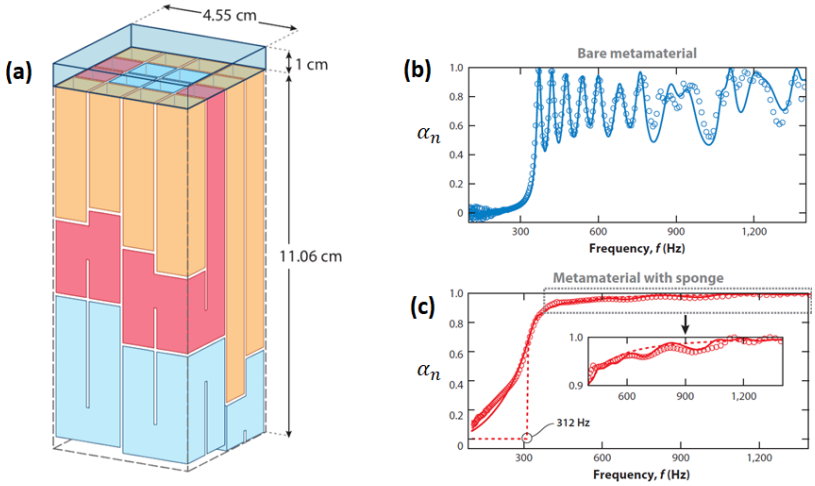

Figure 1.19: Optimal absorber designed by [122], made of an array of channel-resonators **(a)**, and its normal absorption α_n performance without **(b)** and with **(c)** the addition of a sponge layer 1 cm thick.

Apart from the challenging environments that liners for turbofans applications must confront with, the main issue of classical boundary treatments, both for grazing incidence or room acoustics problems, are the low frequencies, especially among 100 and 1000 Hz, where the traditional soundproofing techniques described above would require excessive thickness. From here, it comes the great interest for acoustic metamaterials, and their quest toward *subwavelength* dimensions, i.e. to achieve picks of noise attenuation with thicknesses as much as possible below the quarter-wavelength. Most of such metamaterials combine together different traditional absorbers (such as porous materials, Helmholtz and/or quarter-wavelength resonators and membranes) in such a way to improve the overall performance. Beck et al. [8] has improved the SDOF traditional liner with the inclusion of a Helmholtz resonator in the honeycomb cavity, which produced an additional low-frequency resonance, see Figure 1.14. Tang et al. [115] have inserted inclined microporous septa in the honeycomb, producing the so-called honeycomb-corrugation hybrid structure, but with microperforations on both top facesheet and corrugations, see Figure 1.15. The asset of such metamaterial is its high mechanical stiffness and a broader low-frequency bandwidth respect to traditional quarter-wavelength absorbers.

The insertion of resonators inside porous materials has given rise to the so-called meta-porous absorbers [67] (see Figure 1.16). Another interesting perspective is the design of porous microstructures in order to achieve targeted acoustic performances [18], [91]. While very well suited for room acoustics applications though, porous non-rigid materials would hardly resist harsh environments such as the nacelle of turbofans.

The problem of lowering the frequency of maximum absorption (usually around $c_0/4d$ with d the thickness of the absorber) have also been tackled by targeting the reduction of the *effective sound speed* in the material. In traditional porous materials the sound speed is usually the same as in air, as it tends asymptotically to $c_0/\sqrt{\alpha_\infty}$, with α_∞ the so-called tortuosity of the porous material which is around unity. In [47] a periodic structure composed by narrow slits with quarter-wavelength inclusions reduces the effective sound speed. By properly designing the slow-sound effect along with the associated dissipation, subwavelength absorption performance could be achieved (see Figure 1.17). The slow-sound effect can be obtained

also by folding branch tubes as proposed in the subwavelength liner of [3], see Figure 1.18. The space-coiling is indeed a very much pursued technique to achieve the quarter-wavelength performance with subwavelength thickness. Li et al. [71] combined a perforated plate with a coiled coplanar quarter-wavelength resonator allowing to match the air impedance at one frequency, while Chen et al. [19] coiled two tubes, axially coupled in series, with different diameters, allowing to reproduce the subwavelength equivalent of a DDOF resonator.
Also membranes have been exploited in order to produce subwavelength metamaterial absorbers. The team of Hong Kong University of Science, Department of Physics, has provided several contributions to the so-called decorated-membrane (DM) metamaterial [124], [81], [76]. A DM comprises an elastic membrane with one or more rigid weights attached on its surface, as in Figure 1.9b. Rigid platelets were added to the membrane in [81] leading to flapping modes of the DM under normally incident plane waves. These flapping modes are responsible of high energy concentration along the perimeter of the platelets. As such modes couple only to evanescent acoustic modes in the plane wave regime, the incident wave energy is dissipated in the displacement profile of the DM. The performance of the DM has then been improved by placing an air-cavity cushion behind, leading to the so-called "hybrid" DM [76] allowing to match the normal incidence air impedance at several frequencies.

Nevertheless, all passive absorbers must satisfy the integral constraint, demonstrated by Yang et al. in [122] and reported here:

$$d \geq \frac{B_{eff}}{\pi \rho_0 c_0} \left| \int_0^\infty \frac{1}{\omega^2} \ln |R(\omega)| d\omega \right|, \tag{1.1}$$

where $|R|$ is the absolute value of the reflection coefficient spectrum, B_{eff} is the effective Bulk Modulus (inverse of compressibility) and d is the thickness of the absorber. Such inequality states that for a certain bandwidth of efficient absorption a minimum thickness is required. As the integrand in Eq. (1.1) presents ω^2 at the denominator, the constraint becomes even more stringent at lower frequencies, explaining the narrowness of the absorption bandwidth achieved even by the metamaterial absorbers. From such constraint [122], Yang et al. devised a strategy to produce an optimum absorber (in the sense of minimum thickness given by the right-hand-side of Eq. (1.1)), and proposed a broadband absorber by means of an array of channel-resonators in parallel with each other, covered by a thin porous layer, shown in Figure 1.19. In Section 2.2 such integral constraint will be extended to the electro-active Electroacoustic Absorber (EA).

1.3 Active Boundary treatments for noise mitigation

Active acoustical devices can be defined as those requiring some "active component", i.e. an external energy source, in order to achieve a certain desired acoustic behaviour. In [128] active devices are split into two categories according to weather the external source provides energy to the acoustic domain or not. The latter can therefore be defined as acoustically active, the former as acoustically passive [59].
The reason for employing some active device is to overcome the limitations of the passive ones. First of all, a passive device performance is fixed by its own geometry and material.

As the noise frequency range of aero-engines significantly varies with the flight phases (such as take-off, climb, cruise, approach and landing), it could be very advantageous if the target frequency bandwidth for noise mitigation could adapt accordingly. In addition, the aforementioned challenges presented by the new ultra-high bypass ratio (UHBR) turbofan engines (smaller thickness and less surface area available for acoustic treatments along with low frequency noise signature) conflicts with the integral constraint relating bandwidth and thickness demonstrated by [122]. Therefore, several active strategies have been proposed in the attempt to better *adapt* the liner behaviour to the desired acoustic performance, meanwhile satisfying stricter spatial constraints at low frequencies.

1.3.1 Adaptive resonators

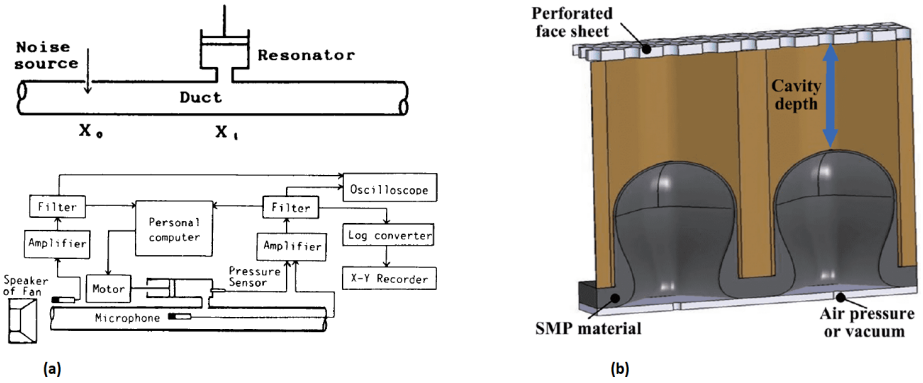

Figure 1.20: Helmholtz resonator liner examples with variable cavity volume: the "semi-active" control concept proposed by [79] **(a)**, and the "morphing resonator" by shape-memory-polymer of [52] **(b)**.

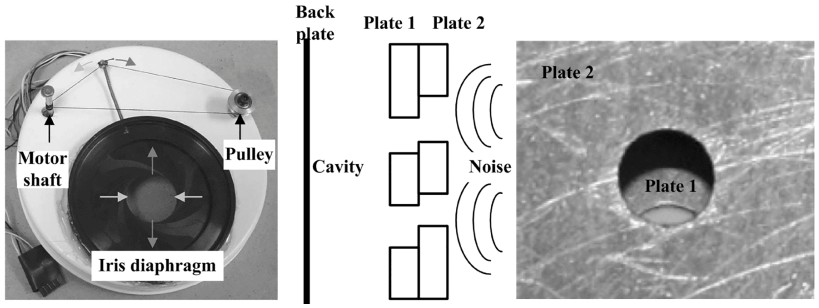

Figure 1.21: Helmholtz resonator with variable orifice area of the neck, controlling an iris diaphragm [34].

The most intuitive *active* solution might be to simply adjust the geometry of classical resonant absorbers in order to change the resonance frequency per the need. This has been accomplished by varying either the acoustic stiffness, i.e. the cavity ([80], [79], [26], [66], [64], [52]), see Figure 1.20, or the acoustic mass (i.e. the orifice area , [73], [65], [89], [58], [34] etc.) of Helmholtz resonators, see Figure 1.21, but both these techniques tended to present complex structure, excessive weight and high energy consumption [77]. In [93], an adaptive Helmholtz resonator liner segment was used with the objective to scatter or redistribute energy among modes, so that to maximize the effectiveness of a neighbour passive liner segment.
An alternative to geometry adjustment, is to couple the Helmholtz resonator in series with

a compliant piezoelectric composite diaphragm which substituted the rigid back plate. This way, a Double-Degree-Of-Freedom (DDOF) resonator was obtained ([54], [75]), and the piezoelectric could also work as energy harvester [96].

1.3.2 Active Noise Control: from the secondary source to the impedance control concept

Instead of adjusting the Helmholtz resonator acoustic behaviour, Active Noise Control (ANC) researchers proposed to make use of an electro-mechano-acoustical system (a loudspeaker for example) as either a *secondary source*, therefore acoustically active, or as an *Electroacoustic Absorber* (EA) which is supposed to feature acoustical passivity. The objective of the *secondary source* was to achieve a "quite zone", i.e. a zero (or minimum) sound pressure at one specific location (or in a certain area), by the destructive interference principle (or upon a "total acoustic potential energy" minimization) [32]. Such techniques made use of one or several sensors (microphones) coupled with one or more actuators (loudspeakers) by a feedback and/or feedforward control. The main difference between the feedforward and the feedback approaches is that in the first case a separate reference signal, well correlated with the primary noise meant to be cancelled, is used to drive the secondary source. The destabilizing elements of the secondary source strategy (either feedback or feedforward), might be resumed and simplified in: unexpected and undesired behaviours of the acoustic surrounding environment and/or of the control architecture itself. Examples of unexpected behaviour of the acoustic environment are: modifications of the primary source contents and position, changes in the geometry of surrounding cavity, presence of flow-induced measurement noise, insufficient spatial modelling of the acoustic domain where noise reduction must be achieved, etc. Undesired conditions of the control architecture are: unexpected loudspeaker dynamics, time-delay (if digital) and other signal perturbations. All these issues of the secondary source approach, concern the so-called *secondary path*, which is the path travelled by the signal from the secondary source input, to the microphone output [32]. The secondary path differs from the primary one as the latter is the one travelled by the signal from the primary noise source to the microphone. In the simplest Single-Input-Single-Output digital feedback control architecture for example, the transfer function between the disturbance (coming from the primary source) $D(s)$ and the error signal $E(s)$ (see Figure 1.22), is:

$$\frac{E(s)}{D(s)} = \frac{1}{1 - C(s)H(s)}, \tag{1.2}$$

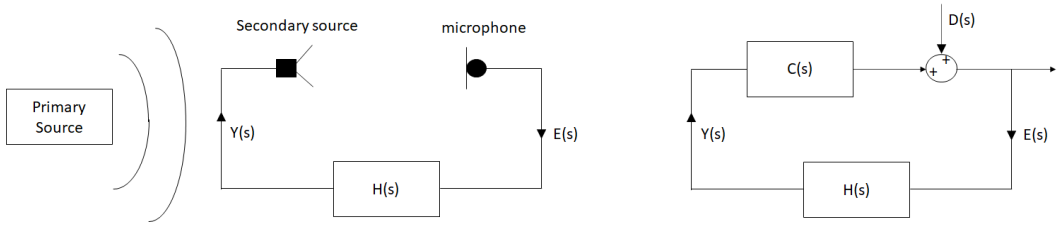

Figure 1.22: Idealised physical illustration (left) and its equivalent block diagram (right) of a SISO feedback secondary source approach, from [32].

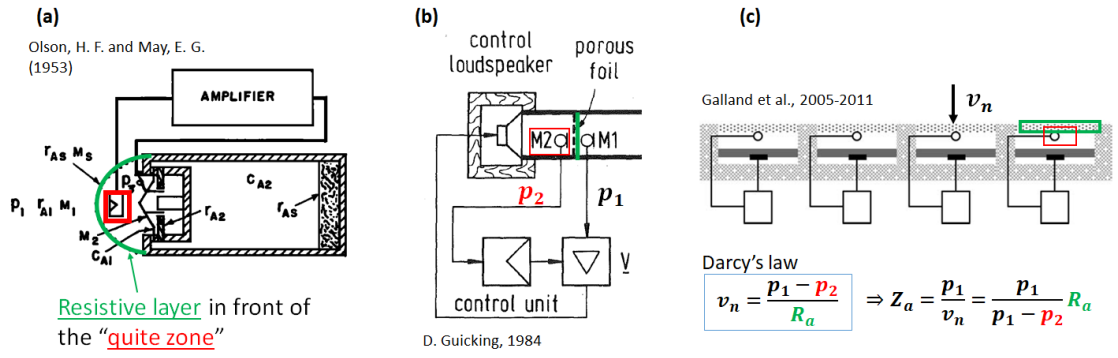

Figure 1.23: Evolution of the "hybrid" strategy (secondary source behind a resistive layer) for impedance control: the "electronic sound absorber" of [90] and [74] **(a)**, the "active equivalent of the quarter wavelength resonator" of [50] **(b)**, and the "hybrid" liner controlling the pressure behind the porous layer [43], to achieve a target impedance Z_a [11] **(c)**.

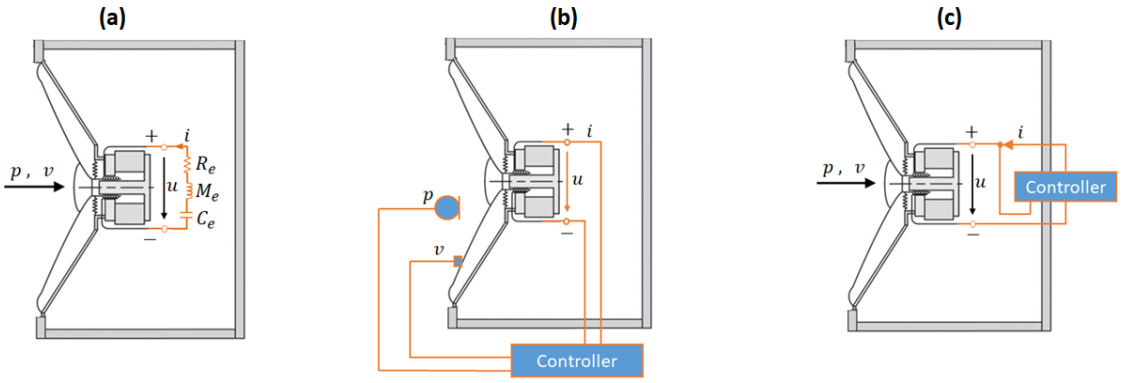

Figure 1.24: Evolution of the Electroacoustic Absorber (EA) concept for impedance control: the shunting techniques of [37], **(a)**, the direct impedance control of [41] **(b)**, and the self-sensing strategy of [70] and [15] **(c)**.

where s is the Laplace variable, $H(s)$ is the corrector and $C(s)$ is the secondary path transfer function. From Eq. (1.2), a high phase shift introduced by $C(s)$, can impact the stability margin, according to the well-known Nyquist criterion [27].
In order to improve global noise reduction in acoustic cavities, *compensating filters* [32], such as phase correction [20] and velocity compensation [68], have been introduced in the feedback controllers. Adaptive filters, on the other hand, rapidly evolving thanks to the digital technology, very much supported the feedforward strategies [84].

Already in the first paper on Active Noise Control, Olson and May [90] suggested to collocate sensor and actuator in order to reduce the risk of having constructive, instead of destructive, interference. The collocation of sensor and actuator, and the idea to use a resistance in front of their "spot type noise reducer" (see Figure 1.23a), was seminal in the active *impedance control* strategy. Guicking first [50], and then Galland [43], developed the idea of [90] of an "active equivalent of the quarter wavelength resonance absorber" in normal and grazing incidence respectively (see Figure 1.23b,c). The "quite zone" (of zero pressure) behind a resistive layer allowed to increase the pressure gradient across the layer and improve the effective-

ness of the porous material at lower frequencies. A FX-LMS adaptive filter was employed in order to achieve such hybrid behaviour in [43]. Analogously to the adaptive Helmholtz resonators of Section 1.3.1, where active means were used to adjust the resonator behaviour, here a secondary source was used to modify the effectiveness of a quarter wavelength resonator equipped with a resistive layer. The same technique was slightly modified by [11] in the attempt to reproduce the Cremer's liner optimal impedance for the first duct modes pair [24], [116] (see Figure 1.23c). As the optimal impedance could not be achieved in a broadband sense, this interesting approach remained limited to monotonal applications.
These are examples of impedance control achieved through secondary source approaches combined with passive liners, but the collocation of sensor and actuator suggested also another avenue: the modification of the actuator (loudspeaker or else) own mechano-acoustical impedance.

Instead of using the loudspeaker as a secondary source, or to use active means to adjust the impedance of a passive absorber, one can envisage to adjust the loudspeaker own mechano-acoustical response by controlling its electrical dynamics. The objective shifts from creating a "quite zone" at a certain location, to achieving an optimal impedance on the loudspeaker diaphragm. That is why this concept can be referred to as Electroacoustic Absorption [74]. Clearly, the electroacoustic absorption becomes equivalent to the secondary source approach in case of collocation between sensor and actuator, with a target impedance set to zero [61].

Electroacoustic absorption can either be realized by electrically shunting the loudspeaker terminals, therefore modifying the electrical dynamics through passive analogical circuits (see Figure 1.24a), or by using one or more sensor information (on pressure and/or velocity) to feed into a control algorithm [74] (see Figure 1.24b). Electrical shunting techniques were investigated by [37] and [74] among others. The main advantage of the electrical shunting strategy is the assurance of *acoustical passivity* (and therefore stability [6]) as the acoustic energy was transferred through the loudspeaker diaphragm vibration, to the electrical passive shunted circuit and dissipated in heat. The so-called direct-impedance control instead, was based upon the direct measurement of both pressure and velocity on the loudspeaker diaphragm. The measured impedance then could be adjusted to the desired one, by minimizing the error signal [41]. Equivalently, a certain reflection coefficient was targeted thanks to the two-microphone-method in [49] and [92]. The addition of intrusive and bulky sensors, such as accelerometers or frontal microphones, and the complexities related to the necessary adaptive filters, make these direct impedance control techniques not ideal for compact and light implementations, such as liners.
An alternative to the use of external sensors was offered by self-sensing strategies (see Figure 1.24c), as in [12], [70], [108], [103] and [15]. [74] introduced an unified formulation of the EA by demonstrating the equivalence between direct impedance control (based upon pressure and velocity sensing) and the shunting techniques. They highlighted how, on the one hand, the direct impedance control strongly depends upon the neutralization of the loudspeaker electrical impedance, therefore is limited by stability issues coming from wrong modelling of the electrical inductance. On the other hand, the electrical shunting equivalent, even though always stable, is often not easily realizable.

The idea was then to increase the flexibility of the EA by substituting the electrical shunt with a synthesized digital corrector in [37] and [104]. In particular, [104] proposed a mechanical-model-inversion-based control architecture. It detected pressure by one or more microphones placed as close as possible to the loudspeaker to achieve quasi-collocation, and drove the current (thanks to a Howland current pump [95]) in order to equal out the own mechanical dynamics of the loudspeaker, and reproduce a desired acoustical impedance at the speaker diaphragm. The Howland current pump on the one hand, and the use of a microphone on the other, allowed to restrict the model inversion to the mechanical dynamics only, getting rid of the electrical inductance modelling issues of the direct impedance control, at the same time providing a flexible controller thanks to the digital implementation. As the mechanical model uncertainties are much less critical than the electrical ones, it was possible to enlarge the frequency bandwidth of absorption. This control architecture proved great versatility and it has been employed in various applications. Rivet et al. [104], [106] proved the efficiency of such EA concept for room modal equalization. The target impedance was set to a SDOF resonator or to the equivalent impedance of a MDOF resonator composed by more SDOFs in parallel. Such EA strategy was originally designed in order to achieve the characteristic impedance of air $\rho_0 c_0$ in an as large as possible frequency bandwidth, for total absorption in normal incidence. In order to optimize the target impedance assigned on the EAs for room modal equalization, a numerical study has been conducted in [105] by considering purely resistive impedances and discarding the effect of the EA reactance. A plane wave approximation of the cavity modes [85] has recently inspired a fast technique to reconstruct the pressure field in rooms [118] which could be adopted to envisage more physically-grounded optimizations of the EA target impedance, taking into account both its resistance and reactance.
In [14] the EA strategy has been implemented in a liner made up of small unit cells, and tested in an acoustic waveguide with and without flow. The main interest of such EA-liner is its tunability which makes it particularly attractive for reducing noise radiation from turbofan engines during different flight phases. The nacelle parietal walls at the inlet and bypass regions (see Figure 1.1) are the most suitable for such electro-active treatments.
The same control strategy has also been proposed to obtain a phase gradient reflection coefficient, by grading the complex target impedance on an array of EAs, so that to control the reflected wavefront direction [33]. The interest in wave-steering ranges from carpet cloaking to noise transmission reduction for grazing incidence in an acoustic waveguide.

All the aforementioned implementations of the impedance control, target locally reacting behaviours of the treated boundaries. Nevertheless, both room acoustics and grazing incidence problems might benefit from a *non-local* character of the controlled boundary, whose potential is yet to be fully understood. As mentioned in Chapter 1, B.C.s assuring total absorption at more than one angle of incidence might be very interesting for room modal equalization. The field of computational physics has provided, among many, an intriguing so-called Higdon B.C. [53], assuring total absorption for multiple incident angles. It is interesting to notice how such B.C. could be achieved by controlling the EA velocity based upon the local pressure and its tangential derivatives of increasing order, which invest the boundary with a non-local character. To the limit, the B.C. assuring total absorption of waves for any angle of incidence is a pseudo-differential operator non-local both in time and space but not physically imple-

mentable because requiring an infinite amount of data storage [22]. In [22], Collet et al. have proposed a first-order non-local differential operator, here called as *boundary advection law*, which provided interesting results for noise transmission attenuation in grazing incidence.
The boundary advection law has proven to feature broadband non-reciprocal propagation [59] (a hot topic in the metamaterial field), thanks to a completely innovative bias-mechanism. Next section provides a quick overview of the reciprocity-breaking state-of-art, needed in order to appreciate the following numerical and experimental demonstrations of the acoustical non-reciprocity realized by the boundary advection law, presented later in this manuscript.

1.4 Reciprocity breaking

Reyleigh has been the first formulating the reciprocity theorem for sound in [113] and demonstrating it in [114]. It states that exciting acoustic waves at any point A of an acoustic medium at rest (possibly inhomogeneous as represented by the darker purple region in Figure 1.25), "the resulting velocity potential at a second point B is the same both in magnitude and in phase, as it would have been at A, had B been the source of sound". We remark that this result holds even in the presence of absorption losses and in arbitrarily inhomogeneous media. Such property is widely exploited in measurement techniques, for instance in scattering and radiation patterns measurements and transducer calibration. Nevertheless, nonreciprocal wave propagation might be convenient for energy concentration and harvesting, communications and imaging systems, signal processing or even thermal management [38].
The reciprocity theorem can be formulated for many physical systems supporting wave propagation, such as electromagnetics (the Lorentz theorem) or solid structures (the Betti-Maxwell theorem). A sufficient condition for reciprocity is the Onsager-Casimir principle of microscopic reversibility, i.e. the invariance of the medium behaviour and properties under time reversal [17]. Mathematically speaking, time reversal (TR) is represented by the operator $\mathfrak{I}$ [17], which, applied to a process $\phi(t)$, writes:

$$\mathfrak{I}[(\phi(t))] = \phi'(-t). \tag{1.3}$$

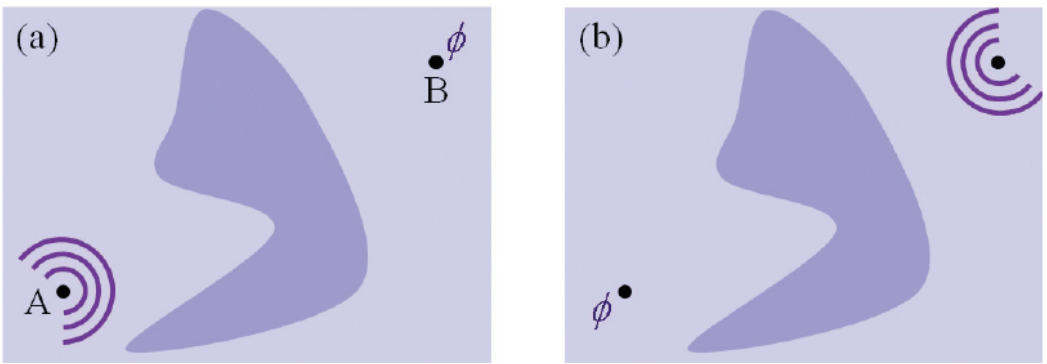

Figure 1.25: Rayleigh reciprocity theorem in acoustics from [38]. The velocity potential ϕ at the receiver point B for a sound source placed in A **(a)**, is equal to the velocity potential at the point A for a source at point B **(b)**.

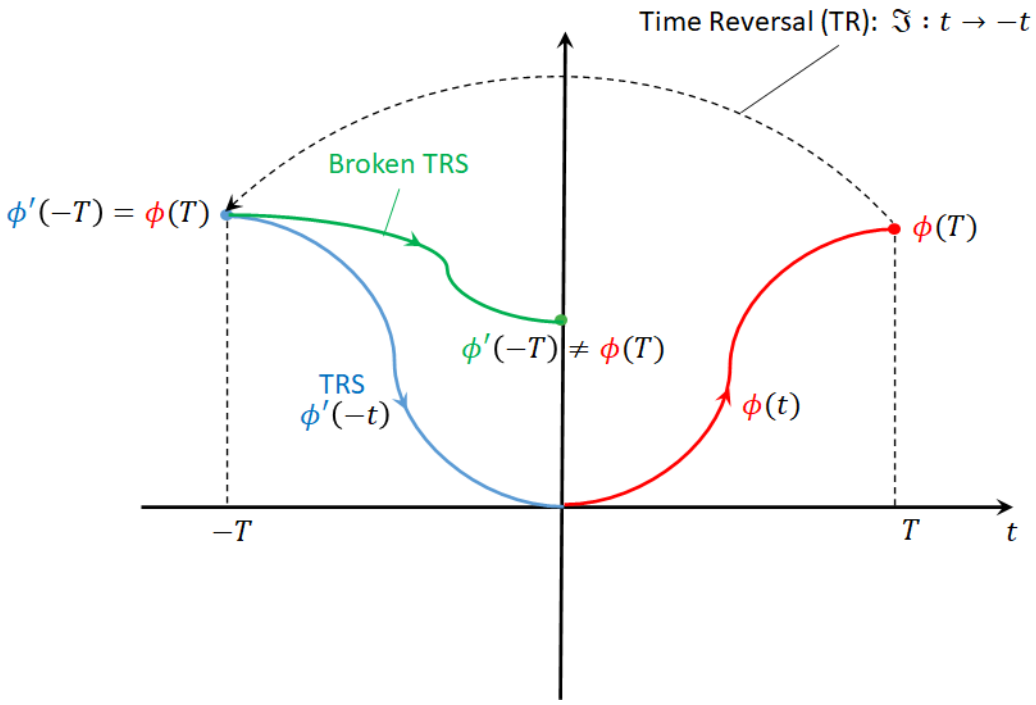

Figure 1.26: Time reversal (TR) operation applied on the process $\phi(t)$ in red. The blue curve describes the case where the time-reversal symmetry (TRS) holds, in green the case when the TRS is broken (from [17]).

If $\phi'(-t) = \phi(t)$, then the system is called "time-reversal symmetric", vice versa, if $\phi'(-t) \neq \phi(t)$ the system is said "time-reversal asymmetric". Figure 1.26, from [17], shows a case of "time-reversal symmetry" (TRS) (blue and red curves), and a case of broken time-reversal symmetry (BTR) (red and green curves).

The invariance of the medium under time reversal is satisfied for linear time-invariant (LTI) media, whose properties does not depend on parameters (let us call them $\mathbf{B}$) which are oddly symmetric under time reversal ($\mathbf{B}(-t) = -\mathbf{B}(t)$).
Hence, in order to allow for non-reciprocity to manifest, one of the hypotheses of time-reversal symmetry must be broken: either linearity, time-invariance or the absence of oddly symmetric parameters under time reversal.
Liang et al. [72] demonstrated that nonreciprocal isolation could be achieved by pairing a nonlinear acoustic medium, playing the role of higher harmonic generator, with a sonic crystal, playing the role of a frequency selective mirror, as in Figure 1.27. Thanks to its periodic structure, the sonic crystal reflects any harmonic signal of frequency f in its bandgap $[f_1, f_2]$. The nonlinear medium is juxtaposed on the right of the sonic crystal. When the signal at frequency $f \in [f_1, f_2]$ enters the device from the right, it encounters the nonlinear medium which partially converts it to higher harmonics (second harmonics in [72]). If the bandgap of the sonic crystal is so designed such that $2f \notin [f_1, f_2]$, some energy traverses the crystal and is transmitted downstream, so the transmission coefficient right-to-left $t_{R\to L}$ is different from 0. Observe that, in this case, the transmission coefficient should refer to the total transmitted power, not its frequency spectrum, as the frequency content of the transmitted signal is different from the incident one's. The other way around, a signal entering

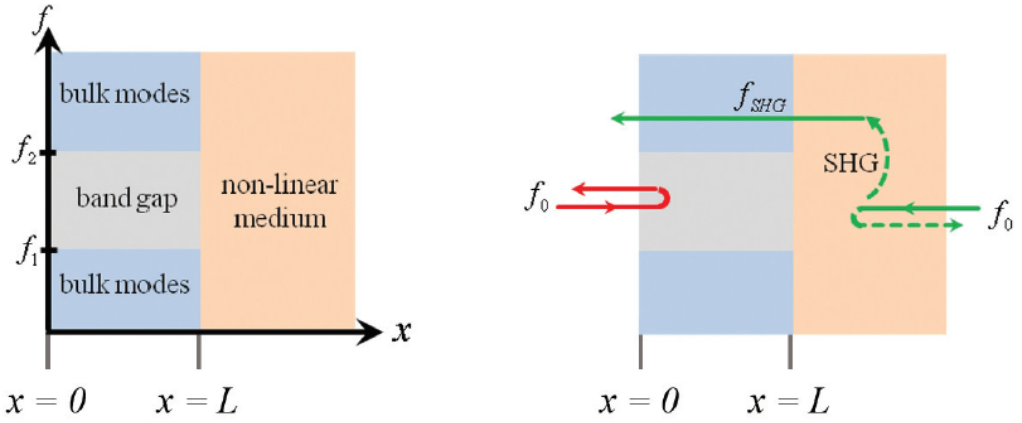

Figure 1.27: Non-linear isolator principle pairing a frequency-selective mirror (sonic crystal) and a non-linear medium capable of second-harmonic generation (SHG), from [38].

the device from the left at the same frequency $f \in [f_1, f_2]$, encounters first the sonic crystal which will reflect it upstream, so the transmission coefficient left-to-right $t_{L\to R}$ is almost 0. Thanks to the excellent reflection properties of the sonic crystal, the nonlinear nonreciprocal device achieves high values of the isolation coefficient $IS = 20\log_{10}(|t_{R\to L}/t_{L\to R}|)$, which is the metrics adopted to quantify the transmission contrast and non-reciprocal performance. Nevertheless, the transmission in the passing sense $t_{R\to L}$ is relatively small, depending on the efficiency of the higher-harmonic generations of the nonlinear medium, other than the losses both in the nonlinear medium and the sonic crystal.

Nonreciprocal devices (also called isolators) based upon coupling nonlinear medium and sonic crystals, present some drawbacks for practical applications. First, they require high levels of incident acoustic power to trigger the nonlinear behaviour. Second, they are typically bulky as the thickness of the sonic crystal must be much larger than the wavelength of the incoming acoustic wave, making such devices inadequate for audio and low frequency applications. In order to cope with such shortcoming, Popa and Cummer [97] proposed a different approach, based upon a piezoelectric membrane driven by a nonlinear electronic circuit which amplifies and convert the pressure signal to twice its frequency. Such electroacoustic transducer was placed between two Helmholtz resonators. Such resonators ($r1$ and $r2$) presented different hole diameters d_1 and d_2 to resonate at different frequencies f_1 and $f_2 = 2f_1$, respectively. Incident sound waves at frequency f_1 strongly couple with the resonator r_1, which in turn efficiently excites the membrane. The second-harmonic-generation (SHG) of the nonlinear electronic circuit, converts the signal at f_1 to a signal at $f_2 = 2f_1$, which in turn strongly couples with the resonator r_2 placed on the other side of the membrane. This is the transmit sense. On the other hand, when the same incident wave (at f_1) impinges from the opposite direction, it weakly couples with the resonator r_2, and even less with the resonator r_1 because its neck is facing the opposite direction. This way, acoustical reciprocity was broken with a device of subwavelength thickness. Though, as it is based upon Helmholtz resonators, the bandwidth of efficient isolation is narrow. A third inevitable drawback of nonlinear isolators is that they very much rely on the frequency conversion accomplished by the nonlinear medium, which significantly alters the incident acoustic signal. Nevertheless, they are still relevant for some applications, such as the protection of systems from incident acoustic power

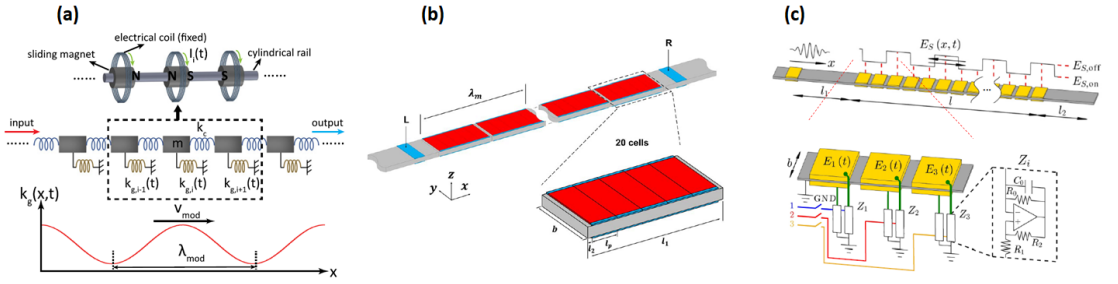

Figure 1.28: Examples of non-reciprocal propagation in elastic media: equivalent mass-spring lattice with spatio-temporally modulated springs [120] **(a)**; spatio-temporal modulation of beam stiffness by piezoelectric patches [125] **(b)**, [78] **(c)**.

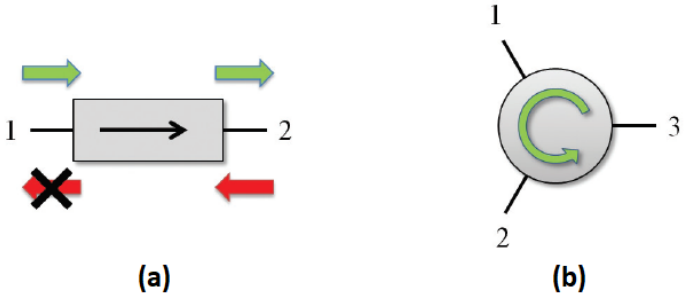

Figure 1.29: Schematics of the isolator allowing transmission from port 1 to 2 but not vice versa **(a)**, and of the circulator allowing transmission between ports in an unirotational fashion **(b)**, from [38].

beyond a given threshold.

The second hypothesis of reciprocity is time-invariance. Time-dependent modulation breaking reciprocity in electromagnetics is analysed in [111]. An example of non-reciprocal propagation in elastic medium is in [120], where a chain of repelling magnets is modulated by externally driven coils, producing an equivalent mass-spring lattice with spatio-temporally modulated springs, see Figure 1.28a. In [125] and [78], non-reciprocal propagation is achieved by spatio-temporal modulation of the stiffness profile of a beam, thanks to piezoelectric patches, see Figures 1.28b,c.

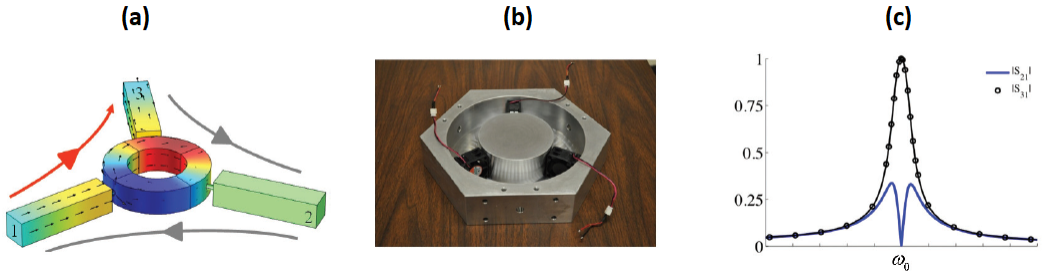

Figure 1.30: Acoustic circulator based upon biasing fluid flow, proposed in [40]: schematics of the one-way circulation of the acoustic wave (from port 1 to port 3) **(a)**; experimental realization with internal fans **(b)**; achievable isolation in terms of transmission coefficients amplitude between port 1 and 3 $|S_{31}|$ and between port 1 and 2 $|S_{21}|$ **(b)**.

Finally, the last available hypothesis to be broken to achieve non-reciprocal propagation, is to conceive a medium having some parameter which is oddly symmetric under time reversal, i.e. whose sign flips under time reversal. In electromagnetics, a typical example of such parameter is a static magnetic field bias. A magnetic field result from the motion of electrical charges along circular paths. If the circular motion of charges is reversed as by time reversal, the sign of the magnetic field flips. Magnetic fields can indeed break electromagnetic reciprocity in ferrites [69] and acoustic reciprocity of ultrasonic waves in magnetoelastic crystals [63]. Applications of such electromagnetic non-reciprocal devices employing magnetic bias, are isolators and circulators, which have long been used in the magnetic and photonics industry [98]. Isolators are two-port devices allowing signal transmission in only one direction, see Figure 1.29a. They are used to protect sources from unwanted reflections or to connect different circuits together in a modular way such that interference with reflected signals is minimized. Circulators combine three isolators into a three-port network that allows signal transmission in an unirotational fashion, see Figure 1.29b. As they allow both a receiver and a transmitter to be connected to the same antenna, they are essential parts of radar systems, and they are becoming crucial components to enable full duplex operation in the next generation of communication devices [38].
In order to produce the acoustic analogue of a circulator, Fleury et al. [40] employed fluid flow as the biasing factor, by making use of three small fans, see Figure 1.30. It is the analogue of the electronic Zeeman effect [21] on an "acoustic meta-atom" (a ring filled with air), where the magnetic bias is substituted by fluid flow which splits the azimuthal resonant modes of the ring. In other words, the azimuthal mode of the ring, gets separated in two counter-propagating modes with different resonance frequencies. By controlling the fan speeds attached to the ring, it is possible to excite the clockwise or anticlockwise azimuthal modes, hence realizing a tunable circulator. An alternative to fluid flow bias to impart the angular momentum biasing, was also proposed by Fleury et al. [39] via spatio-temporal modulation, see Figure 1.31. It was conceived in order to design a circulator for ultrasonic purposes, where a fluid bias would have been unpractical given the small size of the cavity required. The spatio-temporal modulation was applied to three cavity volumes, symmetrically coupled to each other through small channels and to external waveguides. The modulating function, on each cavity volume, have a fixed frequency and a phase difference of $2\pi/3$ between neighbouring cavities.
Observe that the border line between spatio-temporal modulation strategy, and the biasing technique, is very thin, as spatio-temporal modulation usually induces a bias. By the way, in both cases external energy supply is required, which constitutes the actual *biasing source* needed to break reciprocity in linear systems. We also remark that both [40] and [39] circulators, rely on resonance phenomena, hence the isolation achieved has a narrow bandwidth.

In Chapter 3, a novel reciprocity-breaking strategy is proposed, based upon the potential of *programmable B.C.s.* In [22], Collet et al. first implemented a first-order advection equation on the boundary of an acoustic waveguide, making use of electro-acoustic transducers. The same law has been retrieved in [59], to demonstrate its potentialities to accomplish broadband non-reciprocal propagation, and its efficiency has been experimentally validated beyond the resonance frequency of the actuators (loudspeakers), see Figure 1.32. Here the *biasing source*

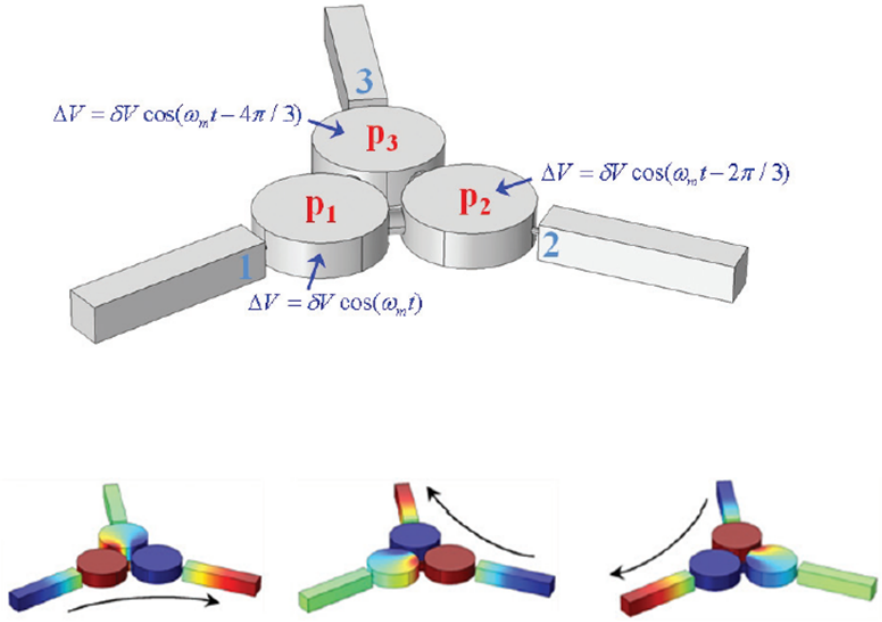

Figure 1.31: Ultrasonic circulator based upon volumes spatio-temporal modulation proposed in [39]. Top: schematics of three interconnected cavities whose volume is dynamically modulated **(a)**; experimental realization with internal fans **(b)**. Bottom: colour field plots showing the one way achievable propagation.

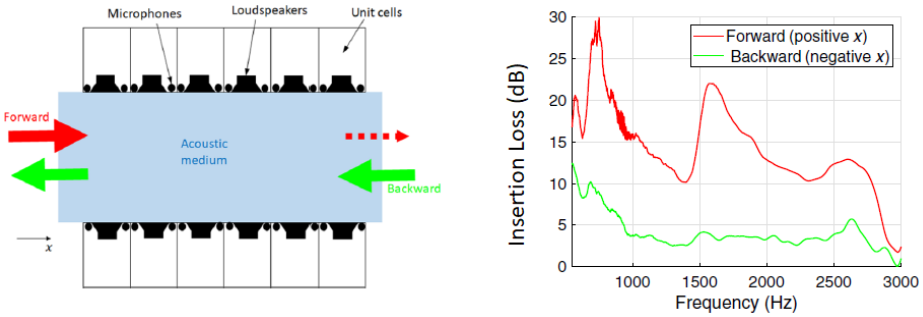

Figure 1.32: Two-dimensional sketch of the waveguide lined by electroactive devices reproducing the advection B.C. (left) and insertion-loss measurements (right) relative to incident waves directed towards the positive x direction (forward) and towards the negative x direction (backward), from [59].

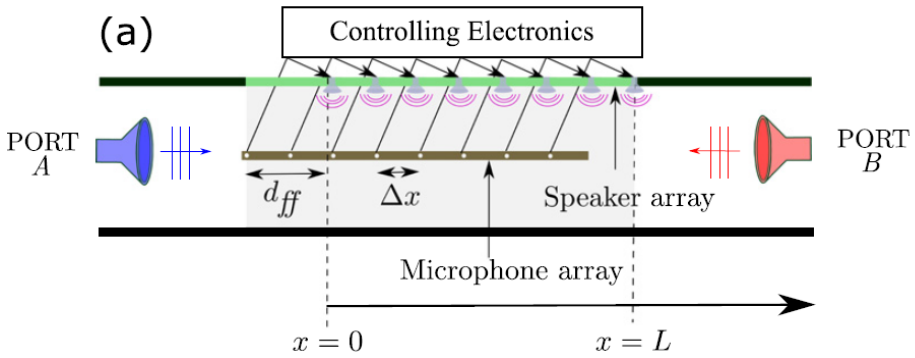

Figure 1.33: Sketch of the non-reciprocal system proposed by [109]: the sensors (microphones) and actuators (speakers) are arrayed along the waveguide and the output of each sensor is fed forward a distance d_{ff} to its corresponding actuator, from [109].

(electrical energy) is employed to modify the response of the boundary, achieving a *convection* of the local boundary reaction in an exclusive sense (either forward or backward). Such *advective* boundary could be seen as a non-locally reacting liner, whose non-local behaviour happens solely along one sense of propagation. The sense of propagation is given by the convection speed defined in the B.C.. If such convection speed is set equal to the speed of sound c_0, then high isolation levels can be accomplished. We highlight that, in contrast with the circulating fluid of [40], or the spatio-temporal modulation of [39], no biasing fields or momentum are induced in the acoustic domain if the boundary is not excited. Moreover, such non-reciprocal B.C. does not rely on resonance phenomena, so that it can potentially achieve large bandwidth of efficient isolation. The actual limitations to its operative bandwidth only depends upon the complexities related to the control systems.
Finally, it is interesting to note how such a *non-local* strategy has been later re-proposed in a simplified fashion by [109]. Nevertheless, in [109] the *unidirectional* non-locality is simply achieved by using loudspeakers emitting sound proportional to upstream pressure signals, see Figure 1.33. The analogy to the boundary advection law of [22] is evident as both introduce a boundary behaviour which is either in phase advance (in the non-passing sense of propagation) or in phase delay (in the passing sense) respect to the local value of the incident pressure wave. In other words, placing microphones upstream respect to the actuators in [109], plays an analogous role of the boundary advection speed in the control law implemented in [22]. Hence, the non-reciprocal device proposed in [109] can be seen as an extreme simplification of the advection boundary law, where the phenomenon of transport of the local reaction is reduced to just a gain factor between each loudspeaker vibration and the corresponding upstream microphone. By doing so, [109] fails to provide any physical interpretation of the non-reciprocal effect, and prevents to take into account many important features as acoustical passivity.
In Chapter 3, the boundary advection law is investigated deeply, from its theoretical conception to its practical implementation, passing through numerical simulations of increasing complexities. Its experimental implementation is renovated with respect to both [22] and [59], allowing to target frequencies around the resonance of the loudspeakers. All the aspects and results related to the non-reciprocal propagation achieved by the advective B.C. are highlighted throughout Chapter 3.

1.5 Thesis Overview

Here is a brief overview of the following chapters.

In Chapter 2, the pressure-based current-driven control architecture, firstly proposed in [104], is investigated in terms of its performances, limitations and further potentialities. In Section 2.1, the model inversion control strategy is analysed in details, paying special attention to its acoustical-passivity, jeopardized at high frequencies by the physiological time-delay of the digital control. Analytical, numerical and experimental tests correlate the effect of time-delay on passivity and thereby stability, to finally propose a *passivating* technique capable to restore the high-frequency acoustical passivity. In Section 2.2, an integral constraint on the absorption performance of the EA is analytical derived from complex integration, which

enlarges the constraint for passive absorber previously found by Yang et al. [122], to the electro-active impedance control through EAs. In Section 2.3, the impedance control problem in the pressure-based current-driven architecture, is formulated in the H_∞ formalism, taking into account the acoustical passivity requirement. The simulated performances of the H_∞ synthesized corrector confirms the relationship between operating frequency range, electrical current required, and passivity, deduced by the integral constraint found in Section 2.2. In Section 2.4, an innovative real-time implementation of the corrector is proposed (based upon a Runge-Kutta scheme, rather than the classical Infinite-Impulse-Response 5 technique), in order to feature a non-linear EA dynamics. The performances achieved by such control scheme are simulated both for a linear target impedance and a cubic (Duffing) desired EA dynamics. The non-linear EA is compared to the linear EA, by numerical tests both in stationary and transient regimes.

In Chapter 3, a non-local (advective) boundary condition studied. Such boundary law degenerates to a purely locally-reacting boundary (described by its acoustical impedance) in case of zero advection speed. Hence, the (non-advective) local impedance results will be included in this chapter analyses and tests as a degenerated case. In Section 3.1, the advective B.C. is investigated analytically by evaluating the non-grazing reflection coefficient in a semi-infinite domain, leading to a first acoustical passivity criterion and condition to be respected by the advective boundary. In Section 3.2, the duct mode analysis is carried out in a 2D waveguide lined on both sides by the advective B.C., showing the non-reciprocal propagation achieved by the advective boundary and partially correlating with the analytical passivity criterion found in Section 3.1. The relative scattering performances simulations, in the plane wave regime, are showed in Section 3.3. The results correlate with the duct mode analysis and give a further insight on both the performance and acoustical passivity of such innovative boundary law. In Section 3.4, the same scattering performances are conducted in a 3D waveguide with the boundaries lined by discrete disks, simulating the EAs behaviour. The control functions needed by the pressure-based, current-driven control architecture to achieve the advective B.C. are presented and simulated on each EA. These simulations allow to examine the effect of the B.C. discretization, as well as to estimate the required electrical current needed by the array of EAs. Finally, in Section 3.5 the experimental implementation of such electro-acoustic liner is presented and analysed in terms of its scattering performances on a test-bench tube with EAs prototypes. The non-reciprocal propagation is confirmed.
Finally, in Chapter 4, the main contributions of this thesis are highlighted and future developments are proposed.

Chapter 2

The Impedance Control by Digitally Adaptive Loudspeaker based upon pressure sensing and driven by electrical current

As mentioned in Section 1.3.2, the pressure sensing by one or more quasi-collocated microphones, fed into the controller, in turn driving the current in the loudspeaker coil thanks to a Howland pump, has so far proven to be the best architecture for the active impedance control [106]. The possibility to use one or more external microphones and the use of electrical current as controller, allowed to break free from the electrical dynamics model of the loudspeaker and its related issues. Nevertheless, as the impedance control aims at controlling the ratio between two variables (acoustic pressure and velocity), sensing only the acoustic pressure inevitably brings about the characteristics of a feedforward-like system. Above all, the use of the *model-inversion* to achieve the target acoustic velocity producing the desired impedance value.
In the next section, much attention is paid on the acoustical passivity which, as mentioned in 1.3.2, is the real asset of the impedance control techniques based upon adaptive actuators.

2.1 A model-inversion control

In this section, the model-inversion approach proposed in [104] is investigated analytically, numerically and experimentally. Let us consider a closed box loudspeaker as in Figure 2.1, used as a membrane absorber, thanks to a pressure-based current-driven impedance control scheme [104]. In this configuration, the corrector transfer function between the pressure input and the control variable (the electrical current in the loudspeaker coil) is defined based upon the assumption of knowing the mechano-acoustical dynamics of the loudspeaker. The model assumed for the loudspeaker corresponds to the classical SDOF piston-mode approximation [10], and is reported in Eq. (2.1).

$$Z_{m0}(s)v(s) = S_d\, p(s) - Bl\, i(s), \tag{2.1}$$

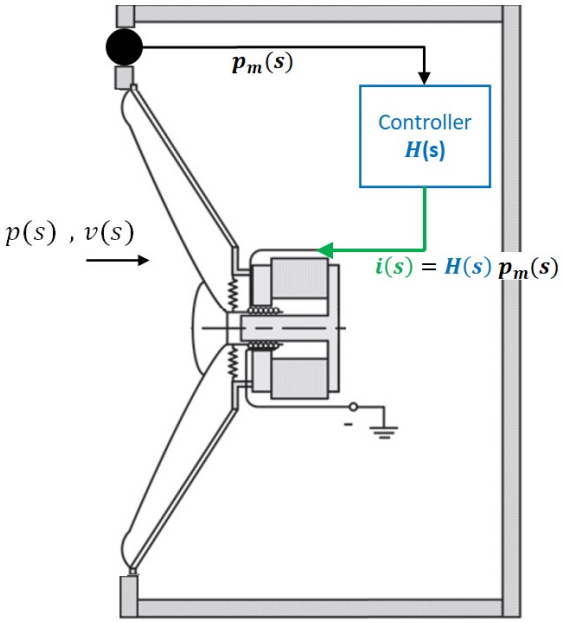

Figure 2.1: Schematic representation of the closed-box electrodynamic loudspeaker. $p(s)$ and $v(s)$ are the acoustic pressure and inward velocity, respectively, on the speaker diaphragm; $i(s)$ is the electrical current in the loudspeaker coil; $H(s)$ is the corrector transfer function which applies to the measured pressure $p_m(s)$.

where s is the Laplace variable, $v(s)$ is the mechanical inward velocity of the loudspeaker diaphragm (check Figure 2.1), $p(s)$ is the sound pressure on the diaphragm front face, S_d is the equivalent piston area (also called effective area), Bl is the force factor of the moving coil, $i(s)$ is the current circulating in the moving coil. $Z_{m0}(s)$ is the mechanical impedance of the SDOF loudspeaker model in open circuit configuration, and it writes $Z_{m0}(s) = M_{m0}s + R_{m0} + \frac{K_{m0}}{s}$, where M_{m0}, R_{m0} and K_{m0} are the mechanical mass, resistance and stiffness of the SDOF loudspeaker model respectively. The stiffness K_{m0} (inverse of the compliance C_{m0}) takes into account also the effect of the backing enclosure. In the following stationary regime analysis, s is exchangeable with $\mathrm{j}\omega$, where $\omega = 2\pi f$ is the angular frequency (in rad/seconds) and f is the ordinary frequency (in Hz).
As we are interested in the acoustic behaviour, it is more convenient and intuitive to divide all the terms of Eq. (2.1) by S_d so that to obtain:

$$Z_{a0}(s)v(s) = \; p(s) - \frac{Bl}{S_d}\, i(s), \tag{2.2}$$

where $Z_{a0}(s) = M_{a0}s + R_{a0} + \frac{K_{a0}}{s}$ is the acoustical impedance of the EA in open circuit. Looking at Eq. (2.2), and supposing that the pressure measured by the microphone $p_m(s)$ be equal to the pressure on the speaker diaphragm, it is easy to derive the corrector transfer function $H(s)$ between $p(s)$ and $i(s)$, in order to achieve a target impedance $Z_{at}(s)$ on the loudspeaker diaphragm, see Eq. (2.3):

$$H(s) = \frac{i(s)}{p(s)} = \frac{S_d}{Bl}\left(1 - \frac{\zeta_{a0}(s)}{\zeta_{at}(s)}\right) = \frac{S_d}{Bl}\left(1 - \frac{\eta_{at}(s)}{\eta_{a0}(s)}\right) \tag{2.3}$$

In Eq. (2.3), we called $\zeta_{a0/t} = Z_{a0/t}/\rho_0 c_0$ the normalized impedances, and $\eta_{a0/t} = 1/\zeta_{a0/t}$ the corresponding normalized mobilities. The last expression on the right-hand-side (rhs) of Eq.

Thiele-Small parameters	M_{m0}	R_{m0}	K_{m0}	Bl	S_d
Units	kg	$\mathrm{N.sm^{-1}}$	$\mathrm{m.N^{-1}}$	$\mathrm{N.A^{-1}}$	$\mathrm{m^2}$
Values	4.45×10^{-4}	0.173	3.85×10^{3}	1.10	1.30×10^{-3}

Table 2.1: Thiele-Small parameters of the EA.

(2.3), where η_{a0} is at the denominator, manifests in formula the concept of model-inversion. The so-called Thiele-Small parameters appearing in Eq. (2.1) and (2.3) must be estimated with some technique, taking advantage of electrical and/or acoustic measurements in different configurations [106]. The Thiele-Small parameters of the EA taken into account for the following simulations, have been estimated by the technique described in Appendix A, and are reported in Table 2.1.

We remind that the model of Eq. (2.1) corresponds to the piston mode approximation, and higher order mechanical modes of the loudspeaker are not taken into account in the control law (2.3). This can lead to spill-over effects, which also can contribute to the stability of the entire system. Nevertheless, in this analysis we focus on the effect of the time-delay, and the piston-mode approximation of Eq. (2.1) is considered as representing the full dynamics of the loudspeaker in our simulations.

The objective of [104] was to attain an acoustic resistance on the loudspeaker diaphragm in an as-wide-as-possible frequency range. The target impedance $Z_{at}(s)$ was then chosen as a target resistance R_{at} equal to the characteristic impedance of air $\rho_0 c_0$ ($\zeta_{at} = \eta_{at} = 1$) to have perfect absorption for normally incident plane waves. In other applications, such as the lining configuration in duct acoustics, or room acoustics, the optimal value for R_{at} becomes a more difficult choice (see [24] and [106]).

In any case, a Z_{at} simply equal to the target resistance R_{at}, would bring a non-proper [45] transfer function $H(s)$, and indefinitely increasing electrical current at lower and higher frequencies. Therefore, for causality and energy limits, in the expression of $Z_{at}(s)$ a reactive part was added to R_{at}, see Eq. (2.4):

$$Z_{at}(s) = M_{at}s + R_{at} + \frac{K_{at}}{s}, \tag{2.4}$$

where M_{at} and K_{at} are the target mass and resistance. Such terms can be written in terms of the acoustic mass and stiffness of the EA in open circuit: $M_{at} = \mu_M M_{a0}$ and $K_{at} = \mu_K K_{a0}$. By doing so, the coefficients μ_M and μ_K indicate how far the target acoustical mass and stiffness differ from the case of open circuit. By varying their ratio, it is possible to set the resonance frequency f_{at} of $Z_{at}(s)$ at different values than the open-circuited EA natural frequency f_0, see Eq. (2.5).

$$f_{at} = \sqrt{\frac{\mu_K}{\mu_M}} f_0 = \sqrt{\frac{\mu_K}{\mu_M}} \frac{1}{2\pi} \sqrt{\frac{K_{m0}}{M_{m0}}} \tag{2.5}$$

The target impedance (2.4) is the one of a SDOF resonator, with the mass, stiffness and damping elements in series as the loudspeaker piston-mode in open circuit, which is the model to be inverted by the corrector (2.3). Nevertheless, other target impedances can be targeted, for example by considering some elements in parallel (instead of in series), producing

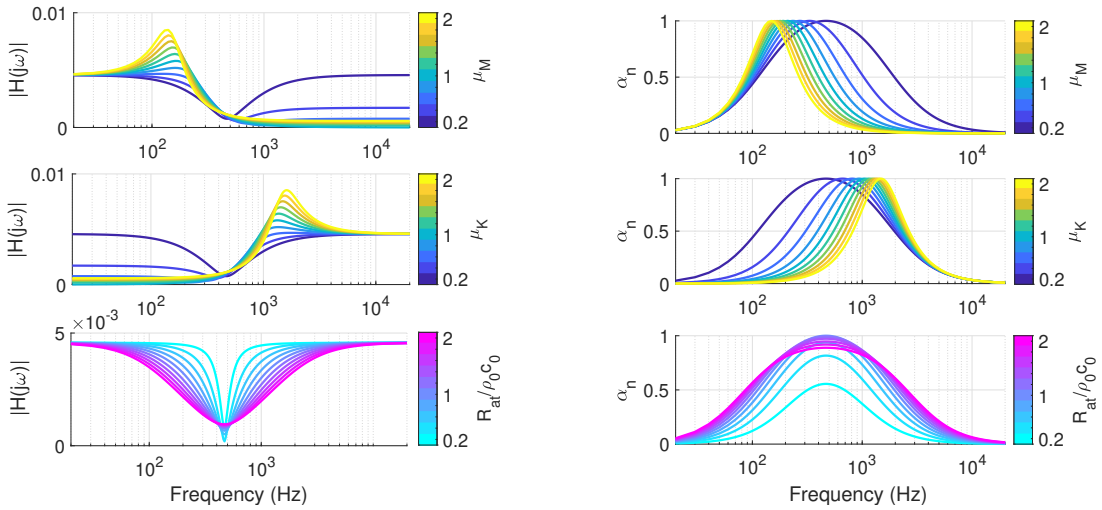

Figure 2.2: Variation of the amplitude of corrector $H(\omega)$ (left) and normal absorption coefficient $\alpha_n(\omega)$ (right) with respect to each of the target impedance parameters μ_M, μ_K and R_{at}. The default values are $\mu_M = 0.2$, $\mu_K = 0.2$ and $R_{at} = \rho_0 c_0$ respectively.

interesting results which is the subject of an ongoing research.

The influence of each tunable parameter μ_M, μ_K and R_{at} of the target impedance (2.4) on the absolute value of the corrector $|H(s)|$, and on the normal absorption coefficient are simulated on Figure 2.2. The parametric variation of the bandwidth of efficient normal absorption is simulated on Figure 2.3. From Figure 2.2, it is evident the effect of varying the ratio μ_K/μ_M on the peak of absorption of the EA. The absolute bandwidth Δf on the ordinate of Figure 2.3 (left) is the frequency range such that $\alpha \geq \alpha_{th}$, where $\alpha_{th} = 1 - (\sqrt{2} - 1)^2$ corresponds to the case where the total sound intensity on the loudspeaker diaphragm is less than twice the sound intensity of the normal incident wave [106]. From Figure 2.3 (both left and right) we can notice that the main impact on the bandwidth is given by the μ_M coefficient (in logarithmic scale on the y-axis), i.e. by the mass term, as the bandwidth significantly enlarges when μ_M is reduced. Despite what was reported in [106] and [104], we remark that also μ_K (the stiffness term) affects the efficient absorption bandwidth: the absolute bandwidth Δf is slightly enlarged, whereas the relative bandwidth $\Delta \mathrm{f}/f_{0_{at}}$ is slightly reduced when μ_K is augmented. Hence, shifting the resonance frequency f_{at} toward higher values (increasing μ_K or decreasing μ_M), brings about a larger absolute, but lower relative, bandwidth. Even keeping f_{at} unchanged, both the absolute and relative bandwidth can still be expanded by reducing both μ_M and μ_K proportionally, as the effect of decreasing μ_M is more important than the one induced by diminishing μ_K. Concerning R_{at} there is an optimal value (which is more than $\rho_0 c_0$) achieving the largest bandwidth.

Ideally, the impedance on the loudspeaker diaphragm realised by the controller (2.3) is exactly the target impedance $Z_{at}(s)$ as reported in Figures 2.2 and 2.3. However, this is never the case because of model uncertainties (errors or changes in the Thiele-Small parameters), dynamic uncertainties (neglected modes outside the operating bandwidth) and time delay in the control chain. In the following, the effect of time delay is discussed with respect to acoustical passivity and stability. Experimental measurements are shown to confirm the correlation between time delay and acoustical passivity and stability.

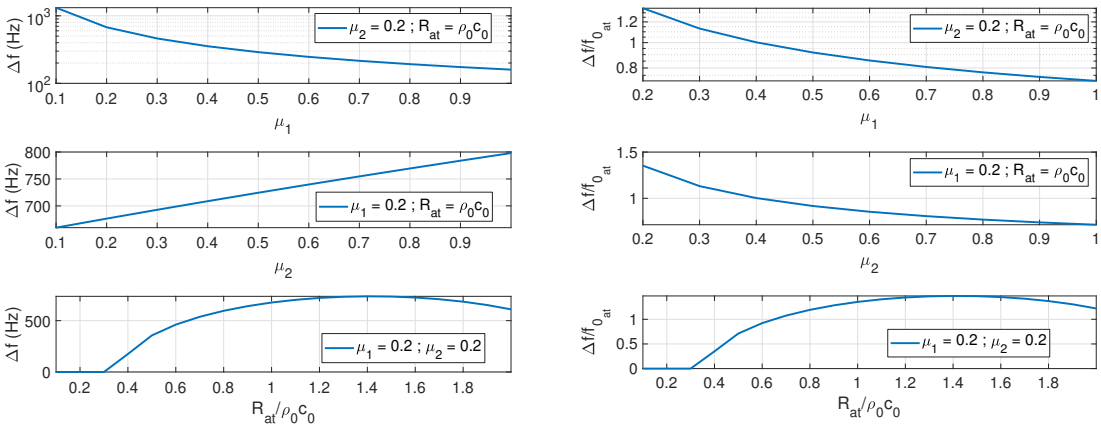

Figure 2.3: Variation of the absolute bandwidth Δf (left) and of the relative bandwidth ($\Delta f/f_{0_{at}}$) (right) of efficient normal absorption, with respect to each of the control parameters (μ_M, μ_K and R_{at}), separately. The default values are $\mu_M = 0.2$, $\mu_K = 0.2$ and $R_{at} = \rho_0 c_0$ respectively.

2.1.1 Effect of time delay on passivity

As any digital control system, a certain time delay happens between the input and the output of the control loop. The time delay in the control chain corresponds to an exponential transfer function $e^{-s\tau}$ in the Laplace domain, multiplying the controller $H(s)$ of Eq. (2.3). Supposing $p_m(s) = p(s)$, the acoustic mobility $Y_a(s)$ achieved on the loudspeaker diaphragm is:

$$Y_a(s) = \frac{v(s)}{p_m(s)} = \frac{1}{Z_{m0}(s)}\left(S_d - Bl\ H(s)\ e^{-s\tau}\right) \tag{2.6}$$

Because of the time delay, $Y_a(s)$ achieved on the loudspeaker diaphragm is different from the target one ($1/Z_{at}(s)$).

In Figure 2.4 we simulate the variation of the normal absorption with respect to the target impedance parameters as in Figure 2.2, but with a control latency of $\tau = 2 \times 10^{-5}$ seconds applied, according to the delay estimation reported in [106]. Figure 2.4 shows that time delay significantly affects the acoustical passivity both around f_0 (about 500 Hz) and at higher frequencies. A locally-reacting surface can be defined as passive if the $\mathrm{Re}\{Y_a(\mathrm{j}\omega)\}$ is positive, that is if $\alpha_n(\omega) \geq 0$ for every ω. A negative absorption indicates that more acoustic energy is reflected than the incident one (the reflection coefficient becomes $|R(\mathrm{j}\omega)| \geq 1$). The ratio of the energy injected by a non-passive locally reacting surface, to the incident one, at a certain frequency ω, is given by the negative value of $\alpha_n(\omega)$. The impact of time delay around f_0 is as more important as farer we push f_{at} away from f_0. The high-frequency loss of acoustical passivity on the other hand, gets more critical as the corrector gain increases at those frequencies, as expected. As the high-frequency gain of $H(s)$ is given by the target acoustic mass, i.e. by the factor μ_M (see Figure 2.2 left), the high-frequency enlargement of the bandwidth of efficient absorption is paid by a so-called *shortage* of acoustical passivity at the forthcoming frequencies.

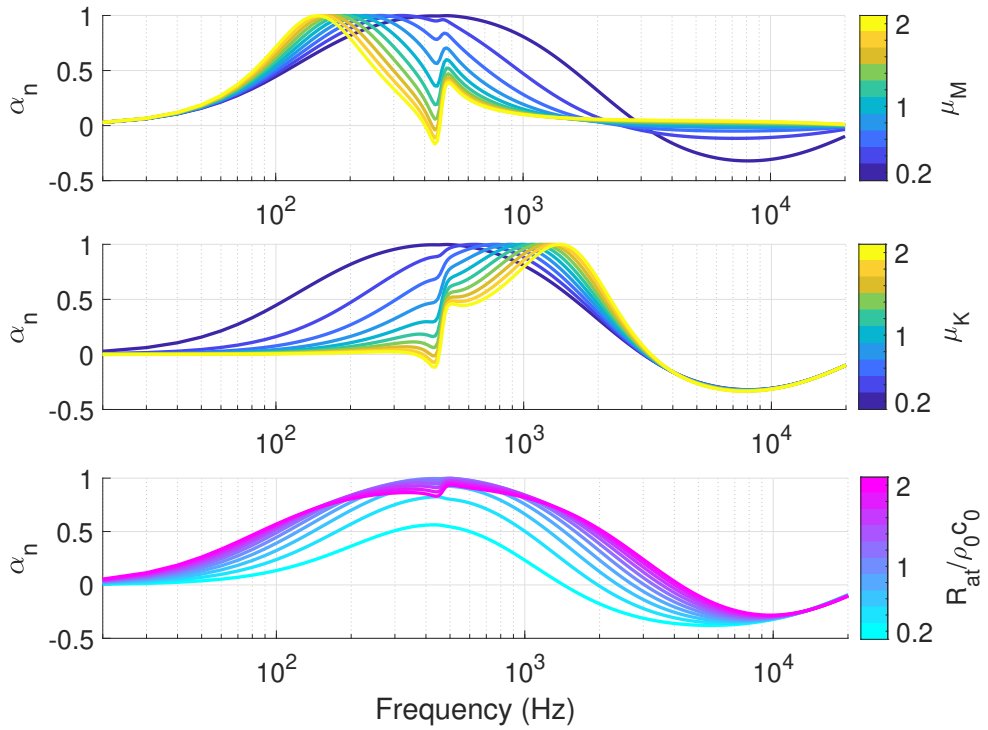

Figure 2.4: Variation of the normal absorption coefficient $\alpha_n(\omega)$ with respect to the control parameters, in case of a delay in the control loop equal to $\tau = 2 \times 10^{-5}$ seconds. The default values chosen for the target impedance parameters are $\mu_M = 0.2$, $\mu_K = 0.2$ and $R_{at} = \rho_0 c_0$.

In classical control schemes, the problem of non-passive systems manifests itself when a feedback is applied between the output and the input. This is also the case here, with the peculiarity that the feedback between the output velocity and the input pressure is given by the acoustic domain in which the controlled loudspeaker is placed. Indeed, as the control system becomes *acoustically non-passive* at high frequencies, the problem of acoustic feedback of the secondary path, typical of ANC techniques (especially feedforward), comes back into the scenario.

2.1.2 Stability analysis

Coupling an acoustically *non-passive* device with a conservative acoustic cavity inevitably leads to instability. In Appendix B, it is briefly recalled the solution of a 1D acoustic hard-walled cavity with a rigid termination on one side, and a generic acoustic element characterized by a reflection coefficient $R(s)$ on the other. It is shown how a reflection coefficient such that $|R(s_p)| > 1$ (where s_p is a pole of the entire system) causes $\mathrm{Re}\{s_p\} > 0$, i.e. instability. In the current section, the stability is analysed by an equivalent approach dearer to control engineers: the poles calculation. By evaluating the poles of the closed-loop transfer function of the entire system coupling our EA with a 1D hard-walled rigidly terminated acoustic waveguide, we verify that the effect of each control parameter on the unstable poles is in accordance with the results of Section 2.1.1. In the following analyses, the time delay is assumed as $\tau = 2 \times 10^{-5}$ seconds, if not specified differently.
In Figure 2.5 the block diagram relative to the pressure-based, current-driven impedance

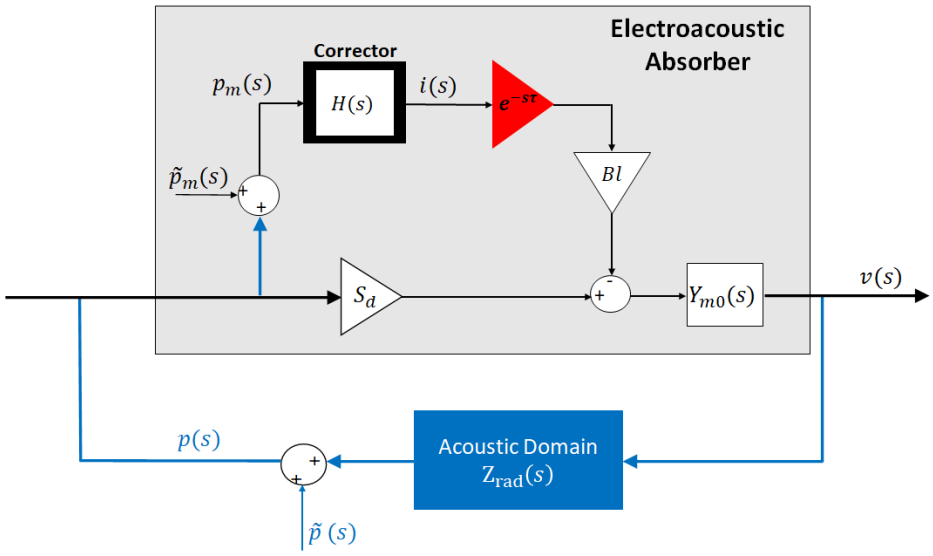

Figure 2.5: Block diagram of the pressure-based, current-driven impedance control.

control is depicted, where $p_m(s)$ is the pressure sensed by the microphone; $v(s)$ and $p(s)$ are, respectively, the velocity and pressure on the loudspeaker diaphragm; $Z_{rad}(s)$ is the radiation impedance of the acoustic domain where the loudspeaker is placed; $\tilde{p}(s)$ and $\tilde{p}_m(s)$ are, respectively, the perturbations upon the pressure on the speaker (due for example to a secondary source), and on the measured pressure at the microphone location (due to measurement noise and/or non-collocation effects); $Y_{m0}(s)$ is the mechanical mobility of the loudspeaker in open circuit $Y_{m0}(s) = 1/Z_{m0}(s)$. The block of the time-delay transfer function $e^{-s\tau}$ multiplies the current output of the corrector.

We highlight that it is not possible to incorporate the radiation impedance $Z_{rad}(s)$ into $Z_{m0}(s)$ (as proposed in [104] and [13]), because the transfer function $Z_{rad}(s)$ plays the role of a feedback term in the closed loop of our controlled system.

The system will be stable against perturbations (either on the measurement or on the external field) if the transfer function of the closed loop of Figure 2.5 is stable. The closed loop transfer function between the pressure perturbation on the speaker $\tilde{p}(s)$ and the diaphragm velocity is given by:

$$\frac{v(s)}{\tilde{p}(s)} = \frac{Y_a(s)}{1 - Y_a(s)Z_{rad}(s)}, \tag{2.7}$$

whereas the closed loop transfer function between the pressure perturbation on the measurement $\tilde{p}_m(s)$ and the diaphragm velocity, is $v(s)/\tilde{p}_m(s) = -Y_m(s)BlH(s)e^{-s\tau}/(1-Y_a(s)Z_{rad}(s))$. In both cases the stability margin is given by the product $Y_a(s)Z_{rad}(s)$ with respect to the unstable point $+1$, as reported in [106]. If the open loop (i.e. open field) transfer function between the measured pressure $p_m(s)$ and the speaker diaphragm velocity $v(s)$ is passive, being the feedback operator $Z_{rad}(s)$ always passive, then the entire closed loop will also be passive as passivity is preserved under feedback interconnections [6]. Since passivity is a sufficient condition for stability [6], then the closed loop will be unconditionally stable.

In the plane wave assumption, the acoustic load relative to a rigidly-terminated hard-walled duct of length L corresponds to the transfer function reported in Eq. (2.8), which is derived

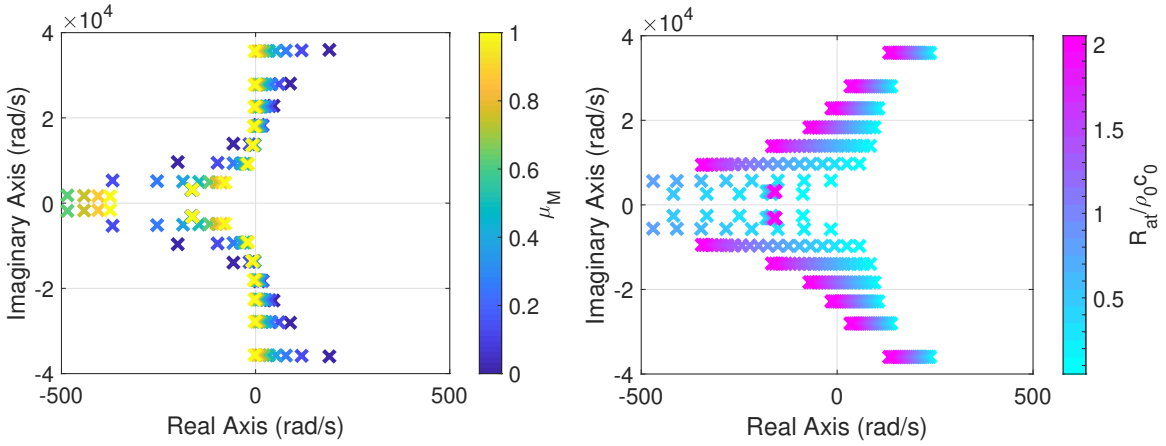

Figure 2.6: Closed loop poles migration with varying control parameters: μ_M (left), R_{at} (right).

from the plane wave decomposition (thus supposing to stay below the cut-off frequency of the rigid duct).

$$Z_{rad}(s) = -\rho_0 c_0 \frac{e^{sL/c_0} + R_{term} e^{-sL/c0}}{e^{sL/c0} - R_{term} e^{-sL/c0}}. \tag{2.8}$$

In the formula of Eq. (2.8), R_{term} is the reflection coefficient of the termination, which is taken equal to 1 in what follows. In order to analyse the stability, we choose to calculate the poles rather than to evaluate the Nyquist diagram as the latter becomes laboured in case of resonances in the feedback term.
The presence of the exponentials in Eq. (2.7), makes it a transcendental equation. Therefore, for the poles calculation, we need to approximate it with a rational proper transfer function. In order to do that, it is common practice to approximate the complex exponentials appearing in Eq. (2.6) and (2.8) by the Padé ratio of polynomials [5]. In Figure 2.6 we compute the migration in the complex plane of the poles of the closed loop transfer function (2.7) with $L = 0.24$ m, by varying the control parameters. The nominal values of μ_M, μ_K and R_{at} are the same as the ones of Section 2.1. From Figure 2.6 it is visible how reducing μ_M causes the unstable poles to increase their positive real-part significantly, which means quicker divergence of pressure. Decreasing R_{at} also appreciably move the unstable poles toward the rhp. The trends shown by the unstable poles with the parameters variation of Figures 2.6 are coherent with their effects on passivity presented in Section 2.1.1.

Both in this section and in Appendix B, we have supposed a conservative acoustic cavity in front of the EA. Similar computations can be carried out by simulating the actual damping present in the cavity, in order to assess weather the coupled system is actually stable or not. In the latter case, an obvious remedy is to add some damping into the system. The next section proposes such simple solution to restore the acoustical passivity of the EA at high frequencies. If we are able to achieve acoustical passivity at any frequency, then the system will be stable whatever the acoustic cavity where the EA is placed.

2.1.3 Acoustic passivation

In order to enlarge the frequency bandwidth without becoming unstable, it is necessary in some way to restore the acoustical passivity at high frequencies. In [60] four general possible *passivation* methods are presented: series, feedback, feedforward and hybrid compensation. These methods are classically used in order to passivate a (non-passive) plant before applying the controller, therefore exploiting the robust stability properties of passivity-based control laws [60]. In our case, it is the entire plant+controller system which has to be acoustically passivated, and it presents a time delay in series with the control itself. Therefore, a series passivation, generally through alternating poles and zeros (such as high frequencies phase-lead or lead-lag compensators, as the ones proposed in [13]) does not solve the problem. Indeed, a series passivation allowing passivity over a larger frequency range (leading to what Kelkar calls "Band-Limited Positive Real systems" [60]) expanding towards higher frequencies, would also bring about a larger impact of the time-delay de-phasing effect, and hence a more serious loss of passivity at the forthcoming frequencies. Not even feedback compensation can passivate a non-minimum-phase system [60], and in any case our architecture does not provide for a fully-feedback control (which entails the measurement of both pressure and velocity). A possible solution could be to adopt feedforward compensation, that is a transfer function between the input pressure and the output velocity which would add up to the system transfer function $Y_a(s)$ [60]. Nevertheless, it is hard, if not impossible, to conceive a feedforward acoustical passivation through an electrical network or controller, acting directly on current without deteriorating the performance at the operating frequencies and, mostly, being devoid of time delay.

A more straightforward and intuitive solution is instead to physically apply a porous layer in front of the loudspeaker membrane. Porous materials are renown for their good absorptive properties at high frequencies, allowing to compensate for the *shortage of acoustical passivity* of our EA at those frequencies. In Figure 2.7 an example of application of a porous layer in front of the speaker is depicted. The porous layer must be attached on the support of the loudspeaker so that there is never a contact between the speaker's diaphragm in vibration and the porous treatment. The acoustic impedance of the EA (the cell) with a porous layer in front has been evaluated thanks to the Impedance Translation Theorem [1], for which

$$Z_2(\mathrm{j}\omega) = \frac{p_2(\mathrm{j}\omega)}{v_2(\mathrm{j}\omega)} = z_c(\mathrm{j}\omega)\frac{\mathrm{j}Z_1(\mathrm{j}\omega)\cot(k_c(\mathrm{j}\omega)d) + z_c(\mathrm{j}\omega)}{Z_1(\mathrm{j}\omega) - \mathrm{j}z_c(\mathrm{j}\omega)\cot(k_c(\mathrm{j}\omega)d)} \tag{2.9}$$

where $Z_2(\mathrm{j}\omega)$ is the acoustic impedance of the EA with porous layer applied; $Z_1(\mathrm{j}\omega) = 1/Y_a(\mathrm{j}\omega)$ is the acoustic impedance of the EA without porous layer; $k_c(\mathrm{j}\omega)$ and $z_c(\mathrm{j}\omega)$ are the wave number and the characteristic impedance of the porous medium in the equivalent-fluid modelling [1], obtained by the Miki semi-empirical power laws [83] based upon the flow resistivity.

In Figure 2.8 we simulate the normal absorption coefficient (on the left) and the poles of the closed loop transfer function (on the right) of the EA (in blue) and of the EA with a porous layer applied (in red). The porous layer has thickness $d = 1.2$ cm and flow resistivity $\sigma = 4 \times 10^3$ rayl/m (these are the characteristics of the foam used in the experimental tests of Section 2.1.4). The mobility of the EA with porous layer applied $Y_2(\mathrm{j}\omega) = 1/Z_2(\mathrm{j}\omega)$ has a transcendental expression, thus $Y_2(\mathrm{j}\omega)$ has been substituted by a proper rational transfer

function which perfectly fits the actual $Y_2(\mathrm{j}\omega)$ in all the frequency range of interest (not shown here), in order to evaluate the poles of the closed loop of Eq. (2.7) (in Eq. (2.7) read $Y_2(s)$ instead of $Y_a(s)$ in case of porous layer applied).

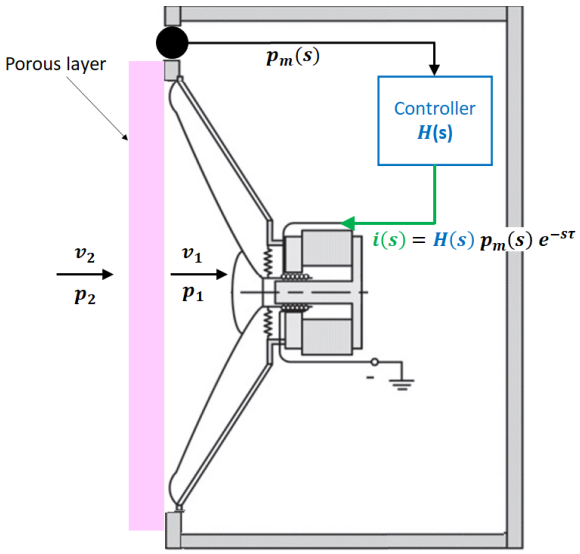

Figure 2.7: Sketch of the porous layer arrangement on the EA.

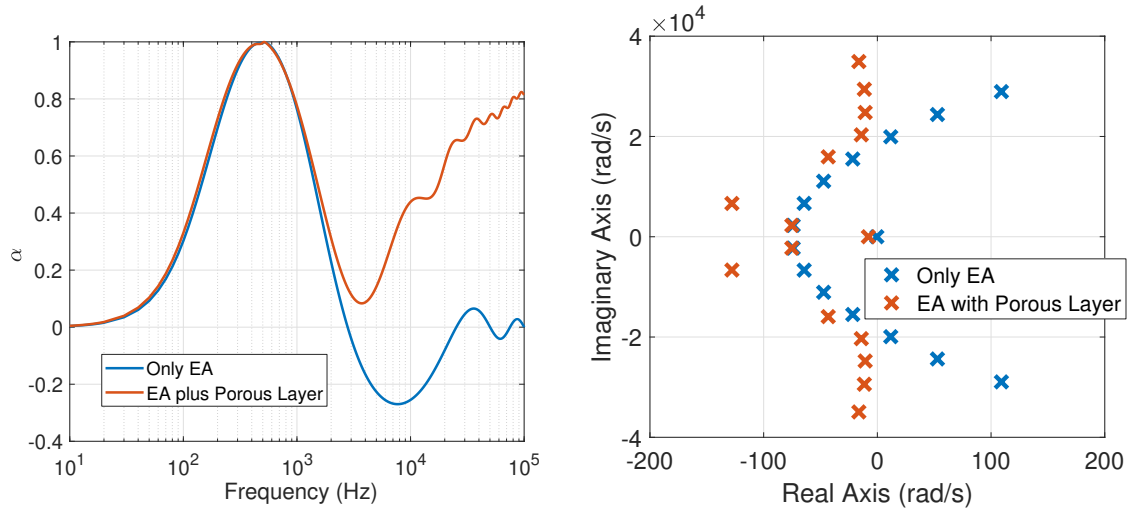

Figure 2.8: Simulated absorption coefficient (left) and poles of the closed loop transfer function (right), in case of simple EA (blue) and EA plus porous layer (red). The control parameters for the EA are set to: $\mu_M = \mu_K = 0.2$, $R_{at} = \rho_0 c_0$. The porous layer has a thickness of 12 mm and flow resistivity $\sigma = 4 \times 10^3$ rayl/m.

From the simulations of Figure 2.8, the porous sheet has the effect of restoring the passivity and therefore the stability, without practically affecting the performance of the EA in the operating frequency range (around the resonance of the loudspeaker).
The application of the porous sheet can be seen as a passivation through an input-output transformation matrix M, as the one proposed by Xia et al. [121]. In our case, M is the Transmission Matrix relative to the porous medium described in Eq. (2.10) where p_1 and v_1 are, respectively, the input pressure and output velocity of the EA system, while p_2 and v_2

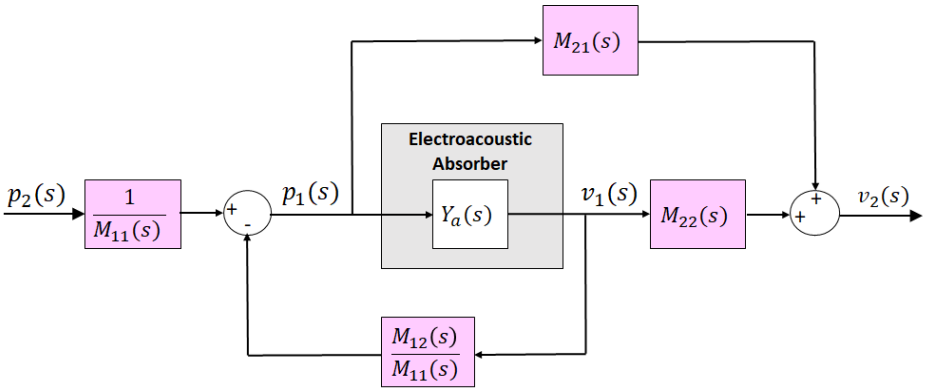

Figure 2.9: Block diagram of the input-output transformation matrix for passivation applied to our controlled EA.

are, respectively, the input pressure and output velocity of the entire EA plus porous layer system (see Figure 2.7).

$$\begin{bmatrix} p_2 \\ v_2 \end{bmatrix} = \begin{bmatrix} M_{11} & M_{12} \\ M_{21} & M_{22} \end{bmatrix} \begin{bmatrix} p_1 \\ v_1 \end{bmatrix} = \begin{bmatrix} \cos(k_c d) & -\mathrm{j} z_c \sin(k_c d) \\ -\mathrm{j} z_c^{-1} \sin(k_c d) & \cos(k_c d) \end{bmatrix} \begin{bmatrix} p_1 \\ v_1 \end{bmatrix} \tag{2.10}$$

The terms of the passivating Transformation Matrix are introduced in the block diagram of Figure 2.9, where the EA is represented by its acoustic mobility $Y_a(s)$.
We remind that the higher the delay, or the lower the μ_M or R_{at} parameters, the more serious will be the *shortage of passivity*. Therefore, to attain full passivation (to re-establish a positive "passivity index" [121]), we need a more performant (in terms of high frequency absorption) porous layer, which usually means a thicker sample and/or a higher flow resistivity. Another possible improvement for the acoustic passivation, is to add a thin air-gap between the EA and the porous layer, so as to increase high frequency viscous dissipation at the porous location [1], as simulated in Figure 2.10. To calculate the resulting acoustic impedance in front the porous layer, the Impedance Translation Theorem has been applied recursively as described in [1]. The air-gap thickness is an additional variable which could be adjusted for the optimal design of the acoustic passivation.
We underline that this passivation technique should not be confused with a hybrid impedance control as the one proposed by [43], because in our case the porous element has the only scope of restoring passivity at high frequencies, without *directly* affecting the performance of the EA at the operating frequency range.

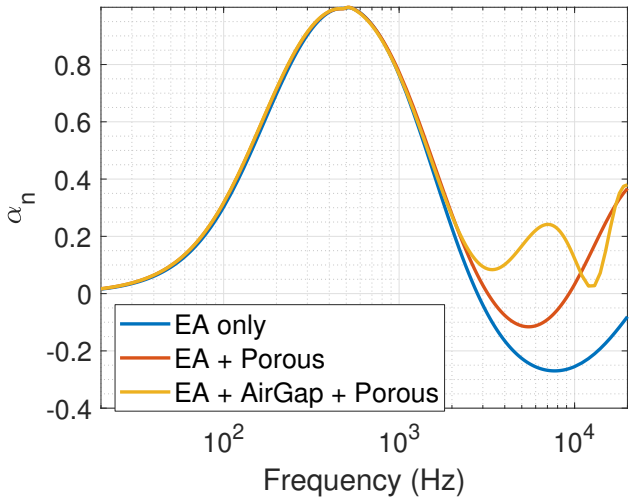

Figure 2.10: Simulated normal absorption of the EA only (in blue), of the EA plus a porous layer (in red) and of the EA plus a porous layer with a 1 cm air-gap between them. The EA control parameters are: $\mu_M = \mu_K = 0.2$, $R_{at} = \rho_0 c_0$; the porous layer thickness considered is 1 cm with a flow resistivity $\sigma = 4 \times 10^3$ rayl/m.

2.1.4 Normal incidence experimental tests

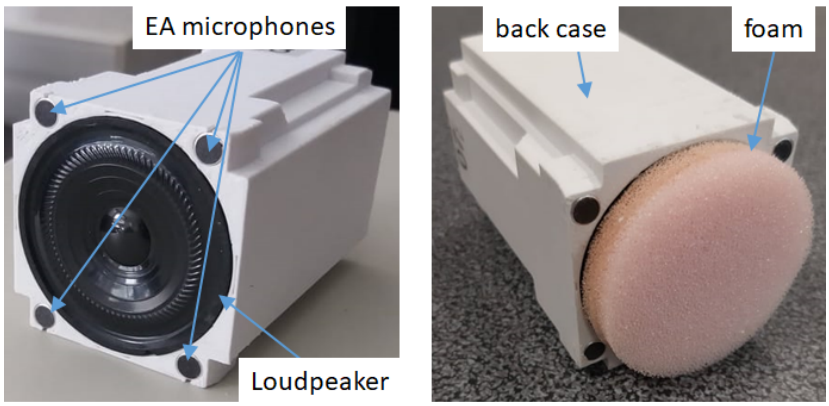

Figure 2.11: Our EA, before (left) and after (right) the application of the porous layer.

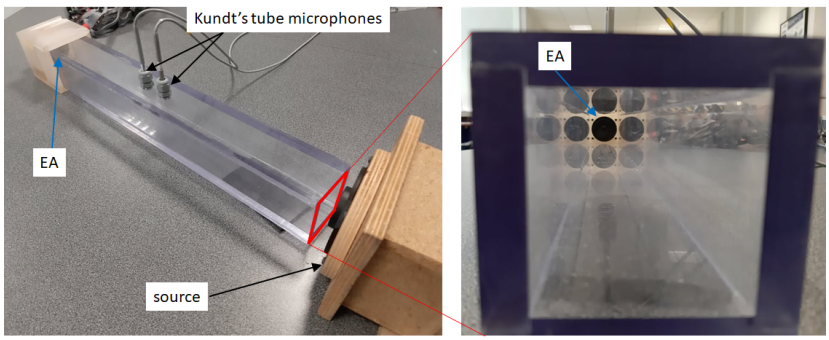

Figure 2.12: Kundt's tube.

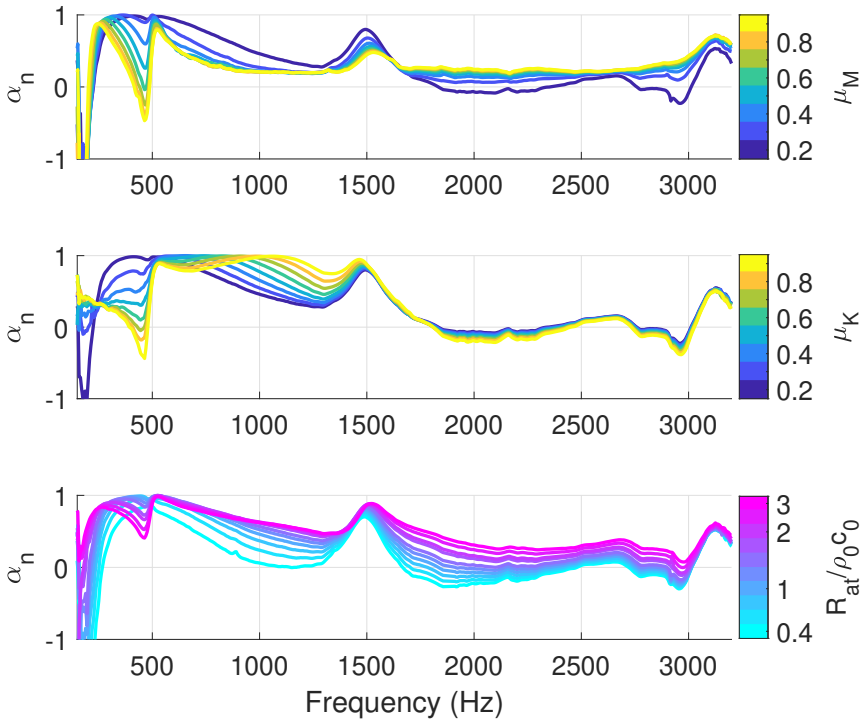

Figure 2.13: Variation of the measured normal absorption coefficient α with respect to the control parameters, in case of a delay in the control loop equal to $\tau = 2 \times 10^{-5}$ seconds. The default values chosen for the control parameters are $\mu_M = 0.2$, $\mu_K = 0.2$ and $R_{at} = \rho_0 c_0$.

In this section, the EA is experimentally tested in order to verify the effect of the time delay on passivity and stability simulated in the previous sections. In Figure 2.11 there is a picture of the EA produced in FEMTO-ST Institute, Department of Applied Mechanics, of Besançon. The EA is composed by a loudspeaker and four microphones at the corners used to estimate an averaged pressure on the speaker diaphragm. The back case accommodates the necessary electronics. In Figure 2.11 on the right, a layer of 12 mm of melamine foam is applied in front of the loudspeaker, in keeping with the sketch of Figure 2.7. In Figure 2.12, the Kundt's tube adopted for the normal absorption measurements is photographed. The tube is made by plexiglass and supposed rigid, it is 60 cm long and has a squared cross-section of $D = 53$ mm side (cut-off frequency $f_{cut-on} = c_0/2D = 3.2$ kHz). The two microphones for the Two-Microphone Method (2MM) [112] are spaced by 4 cm along the tube and the distance between the EA and the centre of the closest microphone is 28 cm. The source is an external loudspeaker reproducing a swept-sine noise signal from 150 Hz to 3.2 kHz. The EA is allocated on the other end of the duct, thanks to an appropriate parallelepiped casing where to clasp our EA. On the right of Figure 2.12 there is the internal view of the tube.

The absorption coefficient is retrieved according to the ASTM [112], to check the high-frequency behaviour induced by time delay and verify the contribution of each control parameter on the high-frequency passivity. Figure 2.13 illustrates the variation of the absorption coefficient with the control parameters, as in the simulations of Figure 2.4.

In the actual EA, the piston-mode modelled by Eq. (2.1) and taken into account in our

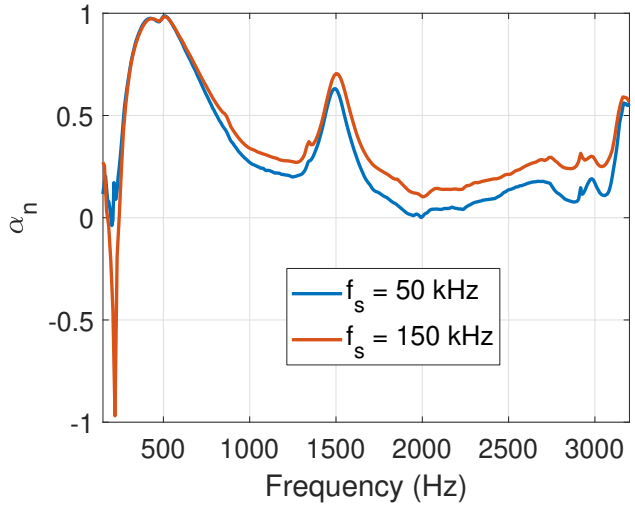

Figure 2.14: Measured normal absorption coefficient α for two different sampling frequencies f_s and consequent time delays. The control parameters are $\mu_M = 0.3$, $\mu_K = 0.3$ and $R_{at} = \rho_0 c_0$.

control law (2.3), is only valid around the resonance frequency f_0 (which is about 500 Hz) of the open-circuited EA. At about 1.5 kHz, another mode appears in Figure 2.13, which anyway seems to be either amplified or weakened in a concordant way with the piston-mode. An unexpected shortage of passivity appears at lower frequencies between 150 and 225 Hz, which is attenuated for higher values of μ_K and R_{at}. This effect is not due to the time delay but it might be related to dynamic uncertainties and spill-over effects [27] on a low-frequency mode of the speaker which is not taken into account in our control law, or to acoustic leakage inside the loudspeaker box. Another unwanted behaviour happens around the resonance frequency f_0 of the loudspeaker: the absorption coefficient presents a dip just before f_0, which critically descends toward the negative axis of α the more we shift the resonance frequency f_{at} of the EA with respect to f_0 (see Eq. (2.5)). This must be caused mainly by a time delay which is higher than the one reported in [106]. Other contributions might come from uncertainties in the Thiele-Small parameters along with the participation of the low/high frequency unexpected modes which are excited away from f_0. Both dynamics and parameter incertitudes are the price to pay by a *model-inversion based* control. These effects and their coupling with the time delay shall be investigated in a future contribution; in here we focus on the time delay effect at the high frequencies. Figure 2.13 confirms that increasing μ_M raises the high-frequency absorption (above 1.7 kHz), reducing μ_K also slightly improves high-frequency passivity, while if R_{at} is significantly augmented an *excess of passivity* is promoted. These experimental trends are in agreement with the simulations of Section 2.1.1.

In Figure 2.14 the absorption coefficient is measured for two different time delays. By reducing the number of microphones adopted by the EA (from four to two), it was possible to increase the sampling frequency f_s in the digital implementation, and consequently reduce the time delay which is directly linked to f_s. It is apparent the improvement of high-frequency acoustical passivity obtained thanks to a shorter time delay. We also note that reducing the number of microphones adopted by the EA has no impact on the performance for normally incident plane waves, except for the low-frequency loss of passivity. This might be explained

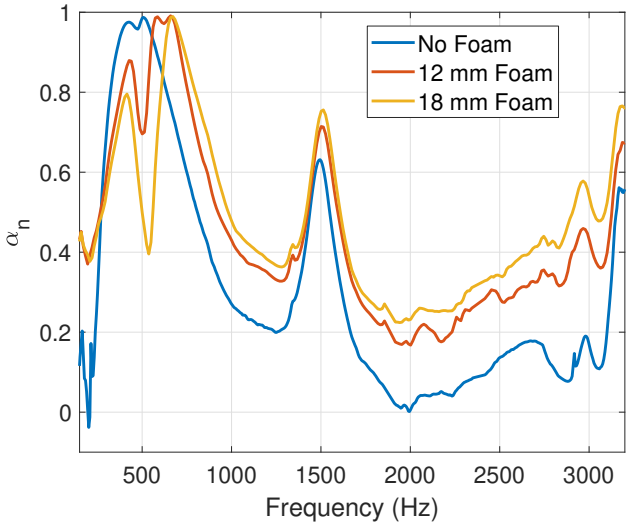

Figure 2.15: Measured normal absorption coefficient α in case of a layer of melamine foam applied of varying thickness.

by an accentuation of the spill-over effect in using only two microphones instead of four, and probably suggests that the low-frequency mode of the loudspeaker (between 150 and 225 Hz) is asymmetric. In Figure 2.15 the measured normal absorption of the EA, with $\mu_M = \mu_K = 0.3$ and $R_{at} = \rho_0 c_0$, is compared with the case of the layer of melamine foam applied in front of the speaker. The thicker the porous layer, the more passivity is gained at high frequencies, whereas the EA performance at the resonance gets modified. This significant effect at resonance was not predicted by the simulations of Figure 2.8, probably due to the inaccurate model of the porous material adopted in Section 2.1.3, especially at lower frequencies.
An unexpected positive effect of the foam is the restoring of acoustical passivity at the lower frequencies. The interaction between the EA low-frequency mode and the porous layer should be investigated further.

Now we propose to experimentally assess the effect of the control parameters and the porous layer on the instability induced by time-delay. Presenting experimental results about the instability of a system, is not such a trivial task. Here, we use the time histories of sound pressure recorded in a hard-walled duct with the EA on one side and a rigid termination on the other, at the upsurge of instability. In Figure 2.16 the experimental setup for the stability tests is shown. A Brüel and Kjaer impedance tube has been employed as hard-walled duct. The rigid termination is given by the rigid piston of the Brüel and Kjaer equipment. The EA is allocated on the right end side of the duct thanks to an appropriate cylindrical casing where to clasp our EA. The distance between the EA and the rigid termination is 0.24 m and the diameter of the duct is 0.1 m. In Figure 2.17, the time history of the recorded sound pressure inside the cavity is plotted in case of EA with (red curve) and without (blue curve) the foam layer applied. The control parameters adopted are $\mu_M = \mu_K = 0.15$, $R_{at} = 3\rho_0 c_0$. As expected, with the porous layer the imaginary part of the unstable poles are lower (slower divergence of the time signal), i.e. the reflection coefficient is reduced (see Appendix B), as

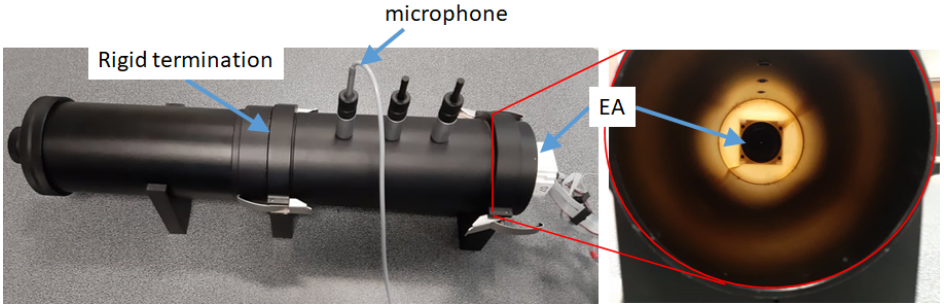

Figure 2.16: Experimental setup for stability tests. Brüel and Kjaer tube with rigid piston termination on the left and EA on the right.

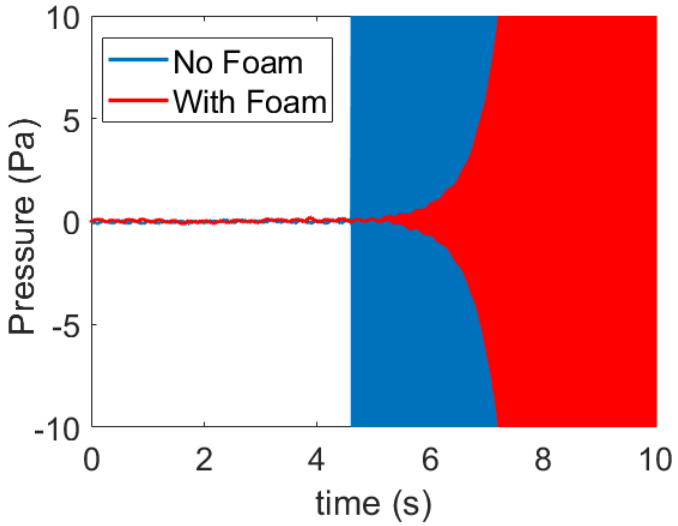

Figure 2.17: Time history of the pressure signal recorded at the upsurge of instability, in case of absence (blue curve) and presence (red curve) of the 12 mm foam layer.

predicted by Figure 2.8.

In Figure 2.18, we recorded the time histories for different values of $\mu_M = \mu_K$ and of R_{at}, with the foam layer applied. The nominal values of the control parameters are: $\mu_M = \mu_K = 0.15$ for the R_{at} variation, and $R_{at} = \rho_0 c_0$ for the $\mu_M = \mu_K$ variation. We can see that augmenting $\mu_M = \mu_K$, as well as increasing R_{at} reduces the imaginary part of the unstable poles, as expected. For $\mu_M = \mu_K = 0.24$ and $R_{at} = \rho_0 c_0$, the system is stable.

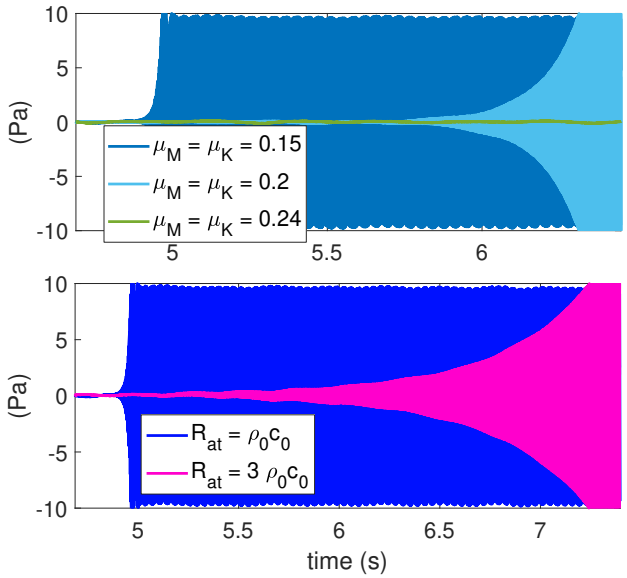

Figure 2.18: Time history of the pressure signal recorded at the upsurge of instability, for different values of $\mu_M = \mu_K$ and of R_{at}, with the foam layer applied.

2.2 Integral constraints on reflection and transmission coefficients of the EA

In order to give a further insight in the EA behaviour, both with respect to passivity and absorptive performance, an integral constraint has been derived in Appendix C. Exploiting the theorems of complex analysis, it is possible to arrive at a relationship between a frequency integral of the normal reflection coefficient spectrum $R_n(\omega)$, the open-circuit acoustical stiffness of the speaker K_{a0}, the static corrector transfer function $H(s \to 0)$, and the "unstable zeros" of the reflection coefficient transfer function $R_n(s)$, i.e. the zeros of $R_n(s)$ with positive real part. The relationship derived in Appendix C is reported below:

$$-\int_0^\infty \frac{1}{\omega^2} \ln|R_n(\omega)| d\omega = \frac{\pi \rho_0 c_0}{K_{a0}} \left(1 - \frac{Bl}{S_d} \lim_{s\to 0} H(s)\right) - \pi \sum_n \frac{\mathrm{Re}\{s_n\}}{|s_n|^2}, \tag{2.11}$$

where s_n are the "unstable zeros" of the normal incidence reflection coefficient transfer function $R_n(s)$, i.e. the zeros with positive real part. For $\lim_{s\to 0} H(s) = 0$ we retrieve the integral constraint for purely passive absorbers provided by Yang [122], reported in Eq. (2.12)

$$-\int_0^\infty \frac{1}{\omega^2} \ln|R_n(\omega)| d\omega = \frac{\pi \rho_0 c_0 d}{B_{eff}} - \pi \sum_n \frac{\mathrm{Re}\{s_n\}}{|s_n|^2}, \tag{2.12}$$

where the acoustic stiffness of the loudspeaker in the open-circuit configuration K_{a0} is substituted by the effective bulk modulus B_{eff} divided by the thickness of the sample d.
Imposing the acoustical passivity condition, then $-\int_0^\infty \frac{1}{\omega^2} \ln|R_n(\omega)| d\omega = |\int_0^\infty \frac{1}{\omega^2} \ln|R_n(\omega)| d\omega|$ (because $|R_n(\omega)| \leq 1$). Since $\mathrm{Re}\{s_n\}) \geq 0$, a constraint on the minimum thickness for a fixed bandwidth of efficient absorption was derived [122]:

$$d \geq \frac{B_{eff}}{\pi \rho_0 c_0} \left| \int_0^\infty \frac{1}{\omega^2} \ln|R_n(\omega)| d\omega \right|. \tag{2.13}$$

Analogously, for a SDOF-in-series resonator which is purely passive, or having a null static controller $H(s \to 0) = 0$, there is a minimum value of the acoustical compliance needed in order to achieve a certain bandwidth of efficient absorption:

$$C_{a0} \geq \frac{1}{\pi \rho_0 c_0} \left| \int_0^\infty \frac{1}{\omega^2} \ln |R_n(\omega)| d\omega \right|. \tag{2.14}$$

Eq. (2.13) and (2.14) imply that high absorption in purely passive absorbers (such as porous materials or Helmholtz and quarter-wavelength resonators) is not possible for any finite thickness or finite compliance, especially at lower frequencies (look at the expression of the integrand) if not for narrow peaks [122].
If the pressure-based, current-driven control architecture is applied on a SDOF-in-series resonator like a loudspeaker instead, Eq. (2.11) holds. If the controller is supposed to keep the acoustical passivity of the system, then once again $-\int_0^\infty \frac{1}{\omega^2} \ln |R_n(\omega)| d\omega = |\int_0^\infty \frac{1}{\omega^2} \ln |R_n(\omega)| d\omega|$, and we get:

$$-H(0) \geq \frac{S_d}{Bl} \frac{K_{a0}}{\pi \rho_0 c_0} \left| \int_0^\infty \frac{1}{\omega^2} \ln |R_n(\omega)| d\omega \right|. \tag{2.15}$$

Therefore, $H(0)$ must be a negative real number with a minimum absolute value depending upon the frequency bandwidth of efficient absorption and upon the acoustic stiffness K_{a0} of the passive resonator under control, as well as the ratio S_d/Bl. Indeed, $-H(0)S_d/Bl$ is the contribution of the control architecture on the loudspeaker first mode compliance term. This means that, for any acoustic stiffness (or compliance) of the passive resonator, it is possible to keep the acoustical passivity of the resonator with the control applied, and to achieve a desired bandwidth of efficient absorption, as long as sufficient electrical current is supplied at the static limit.
In case of the control transfer function (2.3), $H(0) = Sd/Bl(1 - 1/\mu_K)$, and the *effective* compliance is $1/\mu_K K_a$.
From the integral constraint (2.11), it is clear that there is a strong relationship between the frequency bandwidth of efficient absorption, the low-frequency controller transfer function (which means electrical energy supply), and the acoustical passivity. In Section 2.3, such interdependence becomes evident in the attempt to conceive an optimized filter through the H_∞ automatic control synthesis approach.

Observe that such integral constraint on the reflection coefficient for normal incidence, remains valid for any angle of incidence as long as R_n is substituted by

$$R_\theta(\omega) = \frac{\zeta(\omega)/\sin\theta - 1}{\zeta(\omega)/\sin\theta + 1}, \tag{2.16}$$

where $\zeta(\omega)$ is the normalized acoustic impedance of the EA and θ is the angle of incidence, i.e. the angle between the incident pressure field and the tangent to the boundary (normal incidence is for $\theta = \pi/2$). For $\theta \neq \pi/2$ then, Eq. (2.11) still holds, with s_n being the zeros of $R_\theta(s)$.

The question arises about the existence of an integral constraint for the grazing incidence transmission coefficient of the EA (see Figure 2.19). The transmission coefficient in grazing

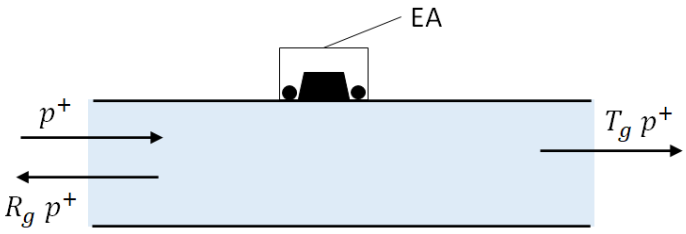

Figure 2.19: Sketch defining the scattering coefficients (transmission T_g and reflection R_g) of a single EA in grazing incidence.

incidence of a single locally reacting device, characterized by the acoustic mobility $Y_{EA}(\omega)$, is described by:

$$T_g(\omega) = \frac{1}{1 + \frac{S_d}{2S}\rho_0 c_0 Y_{EA}(\omega)}, \tag{2.17}$$

where S_d is the size of the locally-reacting device (in our case, S_d is the equivalent piston area of the loudspeaker) supposed to be much lower than the wavelength, and S is the duct cross section area. Eq. (2.17) can be easily derived from the transmission matrix of an impedance $Z_{EA}(\omega) = 1/Y_{EA}(\omega)$ in parallel with the direction of propagation of the incoming wave p^+ (i.e. in grazing incidence). We can notice that the transmission coefficient of Eq. (2.17) has the same expression as the sensitivity transfer function of a classical feedback control loop:

$$S(s) = \frac{1}{1 + H_{ol}(s)}, \tag{2.18}$$

where $H_{ol}(s)$ is a generic open loop transfer function. The equivalence with Eq. (2.17) is evident, with $H_{ol}(s)$ substituted by $\frac{S_d}{2S}\rho_0 c_0 Y_{EA}(s)$. According to the Bode integral constraint on sensitivity [45], for a SDOF stable control loop, with $H_{ol}(s)$ of relative degree $n_r > 0$, it is:

$$\int_0^\infty \ln|S(\mathrm{j}\omega)|d\omega = -\frac{\pi}{2}\lim_{s\to\infty} sH_{ol}(s). \tag{2.19}$$

We are only left to prove the hypothesis of the Bode integral constraint and evaluate the limit appearing on the rhs of Eq. (2.19) in the equivalence explained above, to find the integral constraint for the transmission coefficient $T_g(\omega)$.

The hypothesis of stable control loop, means that the transfer function $T_g(s)$ (obtained substituting ω with s in Eq. (2.17)) does not have unstable poles. As long as $Y_{EA}(s)$ represents a passive acoustical device (true if we suppose no time delay in the EA), then the feedback loop is stable and the first hypothesis is fulfilled.

The second hypothesis is the relative degree $n_r > 0$ of $H_{ol}(s)$ which means, in our equivalence, that the denominator of the transfer function $Y_{EA}(s)$ must be of higher degree than the numerator. This is so for our EA, by looking at the expression of the acoustical mobility in Eq. (2.6), as long as the controller $H(s)$ is a proper rational transfer function. Finally, the limit appearing on the rhs of Eq. (2.19) corresponds to:

$$\lim_{s\to\infty} sY_{EA}(s) = \lim_{s\to\infty} Y_{a0}(s)\left(1 - \frac{Bl}{S_d}H(s)\right) = \frac{1}{M_{a0}}, \tag{2.20}$$

where $Y_{a0}(s) = 1/Z_{a0}(s)$ is the acoustical mobility of the EA in case of open circuit. The last equality in Eq. (2.20) holds if $\lim_{s\to\infty} H(s) = 0$, which is always true as long as high-frequency noise must be cut-off (it is the so-called *roll-off rule*). We can finally state the following integral constraint on the transmission coefficient of the EA:

$$\int_0^\infty \ln|T_g(\omega)|d\omega = -\frac{\pi}{2}\frac{S_d}{S}\frac{\rho_0 c_0}{M_{a0}}. \tag{2.21}$$

Observe that Eq. (2.21) holds for any proper controller transfer function $H(s)$ respecting the roll-off condition. It is interesting to highlight that while the integral constraint on the normal incidence reflection coefficient is ruled by the EA acoustic stiffness, the integral constraint on the grazing incidence transmission coefficient is determined by the open-circuit acoustic mass.

For what just said, a local impedance control of the EAs entails specific limits on both the normal incidence absorption and the grazing incidence transmission.

A non-local conception for the boundary control, as the boundary advection law presented in Chapter 3, might allow to break free from such physical constraints which limit the performances of locally-reacting EAs.

2.3 H_∞ control synthesis: problem setting and simulations

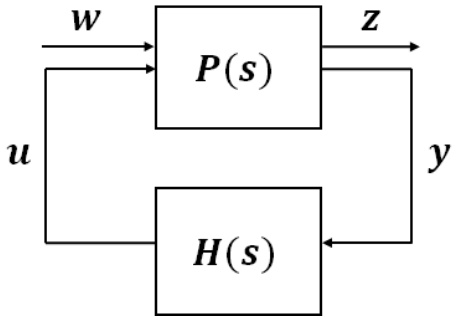

Figure 2.20: Block diagram of the "Standard Problem".

In Section 2.1, the corrector $H(s)$ is synthesized based upon a model-inversion approach. Nevertheless, an optimal control synthesis technique might be adopted as well. In this section the H_∞ problem is formulated for the impedance control of a pressure-based, current-driven architecture of the EA. The results in terms of simulated normal absorption coefficient are compared with the model-inversion-based control. The mutual constraints between bandwidth of efficient absorption, low-frequency energy-supply and acoustical passivity, found by the integral constraint of Eq. (2.11), becomes evident in the H_∞ approach.

The origins of the H_∞ problem dates back to the 1960s when Zames enunciated the small gain theorem [126], but he formally posed it only 20 years later [127]. The name of such approach comes from the use of weighted H_∞ norms for the frequency response transfer functions, to be minimized in order to achieve the problem specifications.

The H_∞ automatic control synthesis approach makes use of the notion of "Standard Problem". The relative block diagram is displayed in Figure 2.20, where $H(s)$ is the controller and $P(s)$ is the matrix transfer function (so-called "Plant") between two sets of entries and

two sets of outputs: the vector w represents external entries, u represents the commands, the signals z are chosen to characterise the good functioning of the control, and y is the vector of available measurements to elaborate the controller. The corresponding matrix equation is in Eq.s (2.22).

$$\begin{bmatrix} z \\ y \end{bmatrix} = \begin{bmatrix} P_{wz} & P_{uz} \\ P_{wy} & P_{uy} \end{bmatrix} \begin{bmatrix} w \\ u \end{bmatrix} \tag{2.22a}$$

$$u = H(s)y \tag{2.22b}$$

The H_∞ approach aims at synthesizing the corrector $H(s)$ such that the matrix transfer function between w and z, usually called $P(s) \star K(s)$ (where $\star$ indicates the so-called Rhedeffer product) or $\mathcal{F}_l(P(s), K(s))$ (where $\mathcal{F}_l$ indicates the so-called Linear Fractional Transformation) is asymptotically stable (poles have strictly negative real part) and the inequality $||P(s) \star K(s)||_\infty < \gamma$ holds. The correctors assuring the smallest value of γ are called "optimal". The matrix transfer function $P(s) \star K(s)$ is expanded in Eq. (2.23) for the general standard problem defined in Eq. (2.22).

$$z(s) = \Big[P(s) \star K(s)\Big] w(s) = \Big[P_{wz}(s) + P_{uz}(s)H(s)\Big(I - P_{uy}(s)H(s)\Big)^{-1} P_{wy}(s)\Big] w(s). \tag{2.23}$$

Two methods are available to solve such problem: the simplest one based upon solving a series of Riccati equations, requires the fulfilment of numerous hypotheses which are not necessaries for the H_∞ standard problem to admit a solution. A second approach allows to reduce the number of hypothesis, at the price of an increased computational complexity. The latter is based upon a convex optimization problem under certain constraints of Linear Matrix Inequalities (LMIs), and was first solved in [42].

To write the standard problem for the local impedance control, first thing to do is to define the specifications. The local impedance control aims at achieving a target impedance in a certain frequency bandwidth, expressed in terms of a target normalized acoustic mobility $\eta_{at}(\mathrm{j}\omega)$, which means to reproduce a target acoustic velocity $v_{at}(\mathrm{j}\omega) = \rho_0 c_0 \eta_{at}(\mathrm{j}\omega) p(\mathrm{j}\omega)$ for any acoustic pressure, on the loudspeaker diaphragm in case of an EA. Therefore, we can define a velocity error function $\epsilon_v(\mathrm{j}\omega) = v(\mathrm{j}\omega) - v_{at}(\mathrm{j}\omega)$, where $v(\mathrm{j}\omega)$ is the actual acoustic speed on the loudspeaker diaphragm. In terms of the mobility transfer functions, the error reads:

$$\epsilon_v(\mathrm{j}\omega) = \rho_0 c_0 [\eta_a(\mathrm{j}\omega) - \eta_{at}(\mathrm{j}\omega)] p(\mathrm{j}\omega), \tag{2.24}$$

where $\eta_a(\mathrm{j}\omega)$ is the actual normalized mobility.
The objective in terms of performance is to minimize the transfer function $\epsilon_\eta(\omega) = \eta_a(\omega) - \eta_{at}(\omega)$, that is:

$$|\epsilon_\eta(\mathrm{j}\omega)| = |\eta_a(\mathrm{j}\omega) - \eta_{at}(\mathrm{j}\omega)| \leq \epsilon_{max}, \tag{2.25}$$

where ϵ_{max} is the maximum tolerated error. Since the inequality (2.25) must to be achieved in a fixed frequency range, then it is useful to substitute the real value ϵ_{max} with a frequency

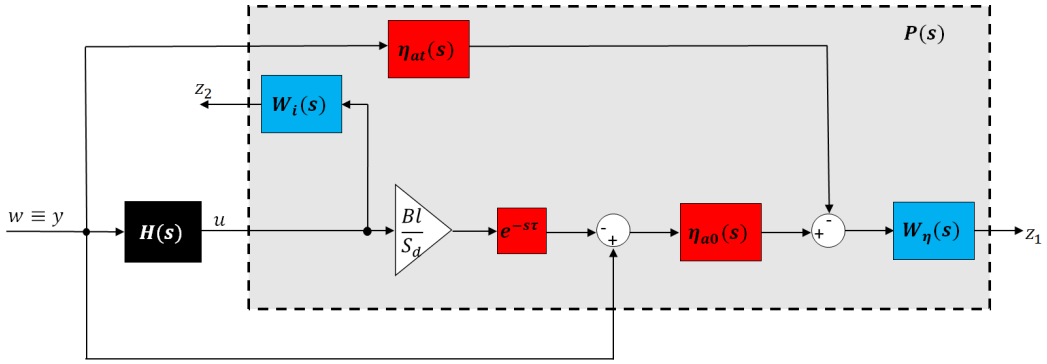

Figure 2.21: Block diagram of the EA problem with weighting filters for specifications of performance and current limit.

transfer function which would *constrain* $|\epsilon_\eta(\mathrm{j}\omega)|$ only in the frequency bandwidth of interest for the attainment of the targeted mobility. In this sense, it is convenient to introduce the definition of *weighting* transfer function $W_s(\mathrm{j}\omega)$ which characterises a set of generic signals $s(t)$ such that $|s(\mathrm{j}\omega)| \leq 1/W_s(\mathrm{j}\omega)$. Hence, Eq. (2.25) can be rewritten as:

$$|\epsilon_\eta(\mathrm{j}\omega)| \leq \frac{1}{|W_\eta(\mathrm{j}\omega)|}. \tag{2.26}$$

If $W_\epsilon(\mathrm{j}\omega)$ is both stable and inversely stable, then Eq. (2.25) is equivalent to:

$$||W_\eta(\mathrm{j}\omega)\epsilon_\eta(\mathrm{j}\omega)||_\infty \leq 1. \tag{2.27}$$

Eq. (2.27) involving the H_∞ norm, translates into a constraint on the transfer function $\eta_a(\mathrm{j}\omega)$ of the EA in a certain frequency bandwidth where the target mobility $\eta_{at}(\mathrm{j}\omega)$ is desired and where $1/|W_\eta|$ has its minimum equal to the tolerance ϵ_{max}.
One of the greatest advantages of the optimal synthesis approaches is the possibility to write a mathematical formulation of the control problem which would take into account various specifications. After having written the performance specification through a weighted H_∞ norm of the mobility transfer function, let us introduce another typical specification which is the limit on energy demand. For a current-driven control architecture, such specification expresses itself in terms of a constraint on the absolute value of the controller transfer function $H(\mathrm{j}\omega)$. As done in Eq. (2.27), a constraint on the electrical current can be written in terms of a weighted H_∞ norm, as:

$$||W_i(\mathrm{j}\omega)H(\mathrm{j}\omega)||_\infty \leq 1. \tag{2.28}$$

We are now ready to write the "Standard" form (displayed in Figure 2.20) of the impedance control problem, with specifications in terms of performance and energy limit, for the current-driven, pressure-based architecture. So, the only available measurement y is the sound pressure and the command u is the electrical current. The vector z contains 2 signals: the acoustic velocity on the speaker diaphragm and the command (the electrical current) after being filtered by the constraint (2.28). The block-diagram of the EA with the weighting filters $W_\epsilon(s)$ and $W_i(s)$ applied, and the corresponding *standard matrix problem*, are reported in Figure 2.21 and in Eq.s 2.29 respectively.

$$\begin{bmatrix} z_1 \\ z_2 \\ y \end{bmatrix} = \begin{bmatrix} W_\eta(s)(\eta_{a0}(s) - \eta_{at}(s)) & -W_\eta(s)\frac{Bl}{S_d}e^{-s\tau} \\ 0 & W_i(s) \\ 1 & 0 \end{bmatrix} \begin{bmatrix} w \\ u \end{bmatrix} \tag{2.29a}$$

$$u = H(s)y \tag{2.29b}$$

Note that the transfer function $P_{uy}(s)$ is zero as for the feed-forward scheme.
Having written the impedance control in the standard shape, we can derive the expression of the transfer matrix between $w(s)$ and $z(s)$:

$$\begin{bmatrix} z_1 \\ z_2 \end{bmatrix} = \begin{bmatrix} W_\eta(s)(\eta_{a0}(s) - \eta_{at}(s) - \frac{Bl}{S_d}H(s)e^{-s\tau}) \\ W_i(s)H(s) \end{bmatrix} w \tag{2.30}$$

Hence, the synthesized controller $H(s)$ must be such that the transfer matrix of Eq. (2.30) must fulfil the inequality:

$$\left\| \begin{matrix} W_\eta(s)(\eta_a(s) - \eta_{at}(s)) \\ W_i(s)H(s) \end{matrix} \right\|_\infty < \gamma. \tag{2.31}$$

From the properties of the H_∞ norm, the inequality (2.31) is a sufficient condition for the inequalities (2.27) and (2.28), but not a necessary condition, which means that there could be solutions to the inequalities (2.27) and (2.28), which do not satisfy Eq. (2.31).
Below, we resume the fundamental steps to synthesize a control by the H_∞ formulation:

1. Define the specifications, in terms of performance and energy limits at least.
2. Define the weighting functions constraining the transfer functions of interest ($W_\eta(s)$ and $W_i(s)$ for example).
3. Identify the variables of the standard problem formulation: w, u, z, y.
4. Build the block diagram of the system with the weighting functions and the standard variables.
5. Verify that the standard problem retrieves the constraints on the transfer functions of interest, according to the specifications.
6. Solve the problem.
7. Check if the specifications are met satisfactorily. If required, tailor the weighting functions to better fulfil specifications and reach a lower value of γ (closer to 1).

Let us consider a practical example of impedance control synthesis through the H_∞. So, first step is the outline of the specifications in terms of performance and electrical current limit, to stay in the framework presented above.
Let us consider the simplest boundary problem, that is the case of a normally incident plane wave field, for which the normalized target mobility is simply $\eta_{at} = 1$. The relative frequency bandwidth where such target should be attained can be set between 100 and 1000 Hz, in order to avoid the controller to *spill-over* the second mode of the EA prototypes appearing in Section 2.1.4. The Thiele-Small parameters relative to such EA are taken into account.

Hence, we can now set the weighting function $W_\eta(s)$, which should be such that $1/|W_\eta(s)|$ constrained $|\eta_a(s) - \eta_{at}|$ below 1 in the range $100 - 1000$ Hz. Therefore, a band-pass filter could be employed for $W_\eta(s)$:

$$W_\eta(s) = g_\eta \left(\frac{s}{\frac{s}{\omega_{HP,\eta}} + 1} \right) \left(\frac{1}{\frac{s}{\omega_{LP,\eta}} + 1} \right), \tag{2.32}$$

where $\omega_{HP,\eta}$ and $\omega_{LP,\eta}$ are respectively the high-pass and low-pass angular frequencies, and g_η is the static gain adopted in $W_\eta(s)$. Different transfer functions could be adopted for $W_\eta(s)$, of any order, as long as they are proper and inversely stable. We should keep in mind that higher order weightings imply higher order synthesized correctors $H(s)$, which keep the same order as the plant $P(s)$, i.e. of the system to be controlled, plus the introduced weighting filters. Nevertheless, a model reduction could be easily carried out a-posteriori as we show in the following.

The second typical requirement concerns the energy demand, for which we can set an upper limit on the amplitude of the controller $|H(s)|$ as already said above. Clearly, the electrical current demand will depend upon the sound pressure excitation level. In addition, it is very important to cut the high-frequencies in $H(s)$, that is to reduce the gain of the controller at such frequencies in order not to amplify measurement noises (typically of high-frequency content, it is the roll-off principle mentioned in Section 2.2), other perturbations, and also to reduce the risk of spilling-over higher order modes. In order to do that, $W_i(s)$ should be such that $1/|W_i(s)|$ would constrain $|H(s)|$ at high frequencies. As both $W_i(s)$ and its inverse should be stable transfer functions, a possible form of $W_i(s)$ is:

$$W_i(s) = g_i \frac{1 + \frac{s}{\omega_{LP,i}}}{1 + \frac{s}{\omega_{hf}}}, \tag{2.33}$$

where g_i is the static gain, $\omega_{LP,i}$ is the cut-off angular frequency prescribed for $|H(s)|$, and ω_{hf} is a pole placed as higher as possible on the imaginary axis. The latter serves uniquely to obtain a proper transfer function for $W_i(s)$. The static gain could be adjusted to the limit on electrical current according to the predicted sound pressure level.

Once the system, the target and weighting functions are all defined, the H_∞ problem can be solved with one of the method mentioned above (based upon Riccati or LMI solvers). Nevertheless, usually it is never a "one time shot", as the tailoring of the weighting filters is an iterative process which requires the hand of the control designer to properly adjust them in such a way to achieve the minimum value of γ (see Eq. (2.30)). The a-posteriori simulation of the controlled system behaviour against the prescribed specifications is an important step for assessing their fulfilment, and consequently adjusting the weighting filters. The solutions presented below have been obtained thanks to the code and the collaborative help gently offered by Prof. G. Scorletti and A. Korniienko of the Ampère Laboratory of the Ecole Centrale de Lyon.

A solution to the above H_∞ problem is presented in Figures 2.22 and 2.23. The synthesized corrector $H(s)$ has the same order as the plant $P(s)$ which includes $\eta_{a0}(s)$ and the weighting filters $W_\eta(s)$ and $W_i(s)$. If the weighting functions of Eq.s (2.32) and (2.33) are taken into account, then $H(s)$ is synthesized as a fifth order filter. Nevertheless, the corrector size can be reduced by evaluating the singular values of the Gramian of the balanced realization of

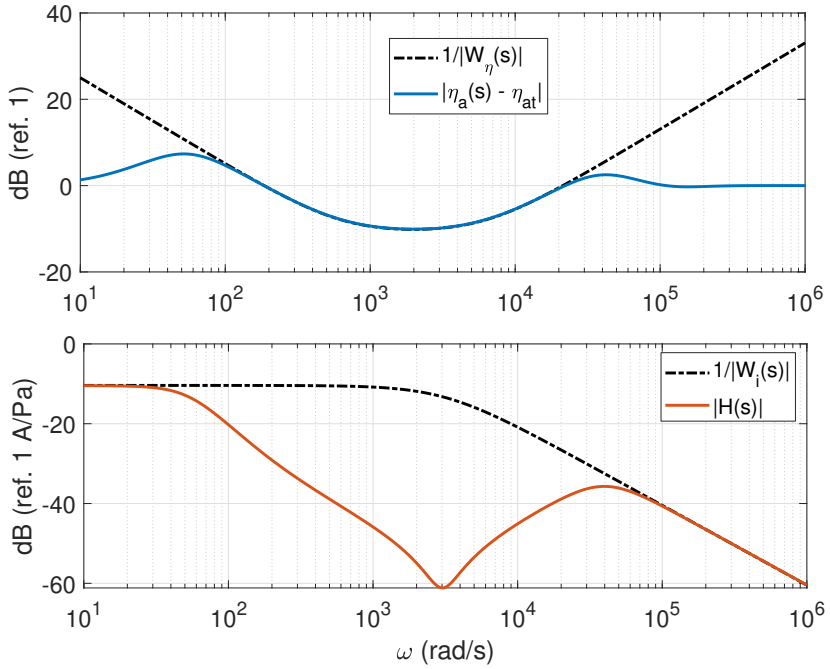

Figure 2.22: Amplitudes of the inverse of the weighting filters and corresponding (constrained) system transfer functions.

the corrector state-space representation. The balanced realization of the state space representation of $H(s)$ is obtained thanks to the controllability and observability Gramians [31]. In the balanced realization, the observability and controllability Gramians coincide, and their singular values, so-called Hankel singular values, are the indicators of both observability and controllability of the corresponding components in the state vector of the state-space representation of $H(s)$. Therefore, the components presenting the lowest Hankel singular values could be eliminated in order to reduce the order of $H(s)$. In Matlab the balanced realization is obtained by the command "balreal", while the model reduction through the function "modred". The impact of such model reduction is to be investigated by a-posteriori simulations as well.
From Figure 2.22, it is evident that the specifications are fulfilled, even in a wider frequency bandwidth than expected for the performance specification. The matrix inequality of Eq. (2.30) is indeed solved with γ very close to 1. From the normal absorption coefficient though, showed on the right of Figure 2.23, it must be remarked the high frequency significant loss of acoustical passivity. Indeed, no constraint was imposed upon acoustical passivity, and a wide bandwidth of absorption far beyond the natural frequency of the loudspeaker, which is around 500 Hz, is bound to produce a significant shift in the phase and a consequent huge loss of acoustical passivity at high frequencies due to the time delay (as verified in Section 2.1.1).

For coping with such a passivity problem, either we can work to better tailor the weighting transfer functions, or we introduce another specification which is indeed the acoustical passivity requirement. In the first case, $W_\eta(s)$ should be adjusted in order to reduce the effective bandwidth, by confining it more to lower frequencies, while for $W_i(s)$ a higher order low-pass

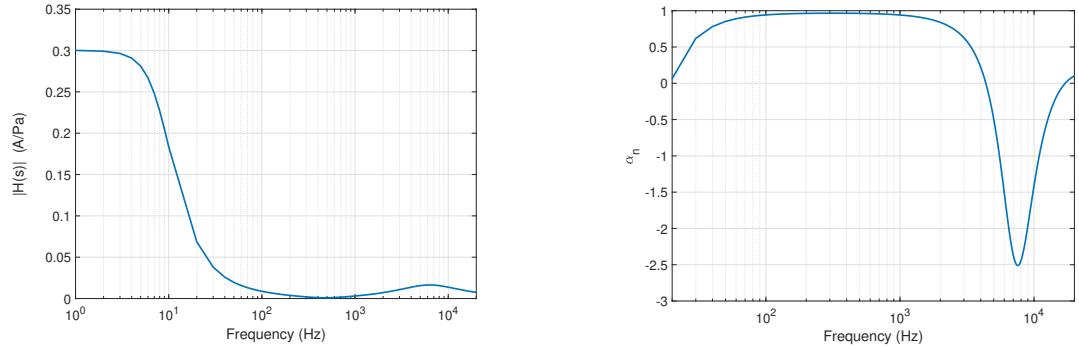

Figure 2.23: Amplitude of the controller transfer function $|H(s)|$ on the left, and simulated absorption coefficient for normal incidence α_n on the right.

filter could be adopted to further cut $|H(s)|$ at high frequencies. Such approach has resulted quite time consuming. In the following, we propose a technique to introduce a constraint on acoustical passivity, which stems from the properties of the bilinear transform. The bilinear transform, usually known for the digital implementation of controller (see Appendix D), can also be defined for a generic transfer function $q(s)$ as:

$$Q(s) = \mathfrak{B}[q(s)] = \frac{q(s)-1}{q(s)+1}. \tag{2.34}$$

The bilinear transform $\mathfrak{B}[q(s)]$ maps the left half of the complex $q(s)$-plane to the interior of the unit circle in the complex $Q(s)$-plane.
Note that the reflection coefficient $R(s) = \frac{1-\eta_a(s)}{1+\eta_a(s)}$ is nothing else than a bilinear transform of the transfer function $\eta_a(s)$, with reversed sign. Therefore, the passivity condition $\eta_a(s) > 0$ is equivalent to $|R(s)| < 1$. Moreover, if $\eta_a(s)$ is passive, then $\beta\eta_a(s)$ also is passive, for any real value β. In order to obtain a transfer function of the type $(1-\beta\eta_a(s))/(1+\beta\eta_a)$, a fictitious feedback gain β has been inserted between the output of the controlled system and the input of the corrector in the block diagram of Figure 2.24.

The signal at point A is $w\eta_a(s)/(1+\beta\eta_a)$. The entry in $W_R(s)$ is therefore $y-\beta w\eta_a(s)/(1+\beta\eta_a(s))$, which gives the bilinear transform of $\beta\eta_a(s)$ with reversed sign.
Therefore, the specification on acoustical passivity can be enforced by the weighting $W_R(s)$, giving in output an additional output signal z_3.
In order to keep the performance specification unaltered, the target normalized mobility $\eta_{at}(s)$ has been substituted by $\eta_{at}(s)/(1+\beta\eta_{at})$. The standard problem becomes as reported in Eq.s (2.35), and the inequality to be fulfilled by the synthesized corrector is in Eq. (2.36).

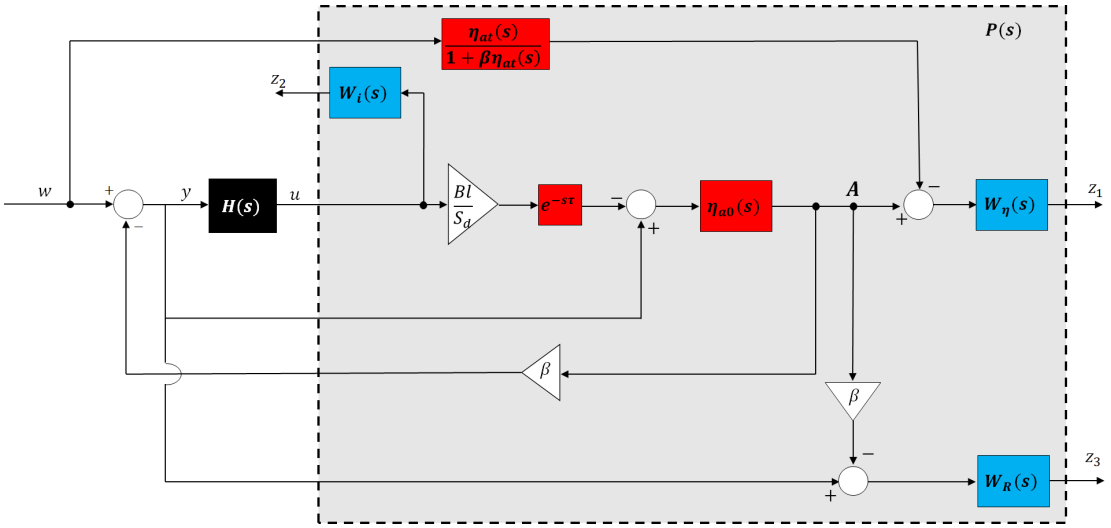

Figure 2.24: Block diagram of the EA problem with weighting filters for specifications of performance, current limit and acoustical passivity constraint.

$$\begin{bmatrix} z_1 \\ z_2 \\ z_3 \\ y \end{bmatrix} = \begin{bmatrix} W_\eta(s)\left(\frac{\eta_{a0}(s)}{1+\beta\eta_{a0}(s)} - \frac{\eta_{at}(s)}{1+\beta\eta_{at}(s)}\right) & -W_\eta(s)\frac{Bl}{S_d}e^{-s\tau}\frac{\eta_{a0}(s)}{1+\beta\eta_{a0}(s)} \\ 0 & W_i(s) \\ W_R(s)\left(\frac{1-\beta\eta_{a0}(s)}{1+\beta\eta_{a0}(s)}\right) & W_R(s)\left(\frac{1-\beta\eta_{a0}(s)}{1+\beta\eta_{a0}(s)}+1\right)\beta\eta_{a0}(s)\frac{Bl}{S_d}e^{-s\tau} \\ \frac{1}{1+\beta\eta_{a0}(s)} & \frac{\beta\eta_{a0}(s)}{1+\beta\eta_{a0}(s)}\frac{Bl}{S_d}e^{-s\tau} \end{bmatrix} \begin{bmatrix} w \\ u \end{bmatrix} \tag{2.35a}$$

$$u = H(s)y \tag{2.35b}$$

$$\left\| \begin{matrix} W_\eta(s)\left(\frac{\eta_a(s)}{1+\beta\eta_a(s)} - \frac{\eta_{at}(s)}{1+\beta\eta_{at}(s)}\right) \\ W_i(s)H(s)\frac{1}{1+\beta\eta_a(s)} \\ W_R(s)\frac{1-\beta\eta_a(s)}{1+\beta\eta_a(s)} \end{matrix} \right\|_\infty < \gamma, \tag{2.36}$$

The performance specification (first line in Eq. (2.36)) is satisfied for $\eta_a(s)$ approaching $\eta_{at}(s)$, while the passivity specification (third line in Eq. (2.36)) is satisfied as long as $|W_R(s)| \geq 1$, because $\min\{\gamma\} \approx 1$.

We highlight that the specification on the limit of $|H(s)|$ (second line in Eq. (2.36)) gets inevitably altered by the new feedback configuration built in Figure 2.24, and that should be kept in mind during weighting filter tailoring and a-posteriori testing. Nevertheless, by keeping β sufficiently small the undesired implications of such fictitious feedback can be contained.

The weighting filters have been modified respect to the previous case, in order to facilitate the passivity condition. Indeed, as demonstrated in Section 2.2 the frequency bandwidth (i.e. the

performance), the static corrector (second specification) and the acoustical passivity (third specification) are very much related to each other by the integral constraint of Eq. (2.11).
In Figure 2.25, the inverse amplitude of the weighting filters are plotted along with the corresponding constrained transfer functions. On the left, the standard system of block diagram of Figure 2.21 is taken into account (therefore without "fictitious feedback" for passivity constraint), while on the right the filtering is applied to the modified block diagram of Figure 2.24. Both the filter for performance $W_\eta(s)$ and the one for current limit $W_i(s)$ are kept the same to synthesize the corrector both in the standard and modified configurations. $W_\eta(s)$ aims at constraining the normalized mobility at very low frequencies, in order not to enhance the high frequency phase shift due to time-delay. For the same reason, $W_i(s)$ is such that to cut the high frequencies. We remind once again that high frequencies are problematical also for the presence of higher order modes of the speaker, which are not taken into account neither in these simulations nor in the control synthesis. In addition, the low-frequency limit of $|W_i(s)|$ has been very much unleashed respect to the previous synthesis, in order to allow the corrector to reach the minimum value in case of an acoustically passive system, given by the integral constraint in Eq. (2.15).
The weighting filter $W_R(s)$ for the passivity enforcement, constrains the transfer function $\frac{1-\beta\eta_a(s)}{1+\beta\eta_a(s)}$ to be lower than 1 beyond the natural resonance of the loudspeaker (which is around 500 Hz), where the phase-shift induced by time-delay particularly endangers passivity. The coefficient β has been set to 1×10^{-3}.
Observe in Figure 2.25 the gap between the inverse amplitude of the weighting filters and the system transfer functions modulus, which is due to the strong interdependence between each of the system transfer functions. Indeed, as written in Eq. (2.35a), there is just one input signal w for 3 output weighted signals z_1, z_2 and z_3. Therefore, it results inevitable that all the transfer functions interested by the weighting process are very much linked to each other. The possibility to add another input w_2, such as an estimation of the speaker diaphragm displacement (as proposed in [51]), could loosen up the interdependence between the system transfer functions of interest.
Nevertheless, the absorption coefficients plotted in Figure 2.26 show the effectiveness of the passivity constraint achieved thanks to the "fictitious feedback technique" showed in the block diagram of Figure 2.24. As expected, enforcing the high-frequency passivity leads to a shift of the efficient absorption bandwidth to lower frequencies.
In Figure 2.27, two different weighting filters have been adopted to constrain the system acoustical passivity.

No experimental investigation has been conducted with the correctors synthesized by the H_∞ approach, as they exceeded the limit on the filter order for the control architecture provided by FEMTO-St Research Institute. Nevertheless, the main interest of the H_∞ approach is the possibility to improve the system robustness in performance and passivity, with respect to both parameters and dynamic incertitudes, i.e. with respect to errors in the SDOF identified model, and with respect to un-modelled higher order dynamics. In order to take into account such uncertainties, other constraints should be applied in the plant $P(s)$, which means further increase in the order of the synthesized filters. For this reason, optimal real-time implementations of the digital filters could result very helpful in reducing the sensitivity

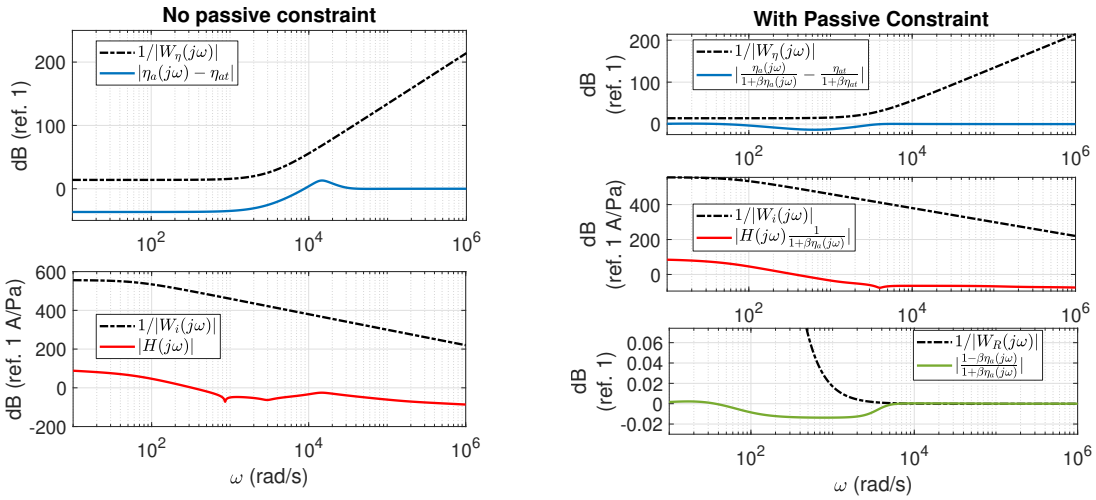

Figure 2.25: Amplitudes of the inverse of the weighting filters and corresponding (constrained) transfer functions modulus relative to system of Figure 2.21 (on the left) and 2.24 (on the right). The weighting filters $W_\eta(s)$ and $W_i(s)$ are the same between right and left plots.

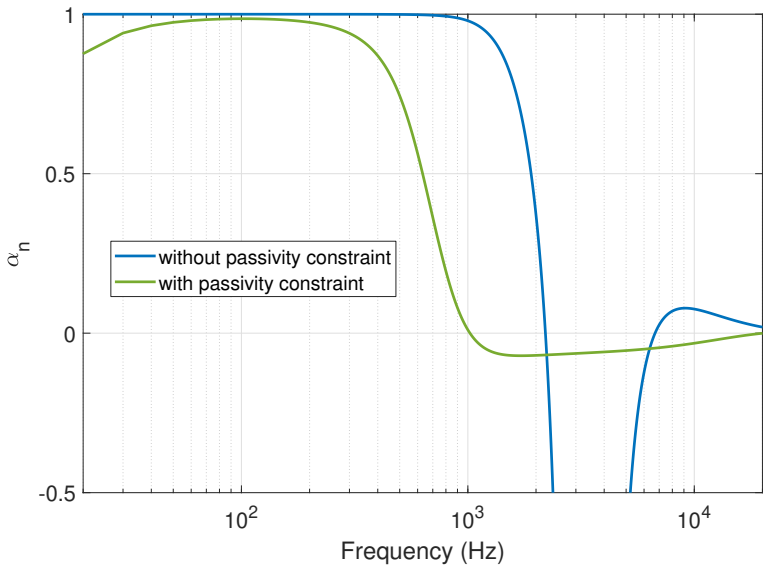

Figure 2.26: Simulated normal absorption coefficient before and after the application of the passivity constraint. The weighting filters $W_\eta(s)$ and $W_i(s)$ are the same.

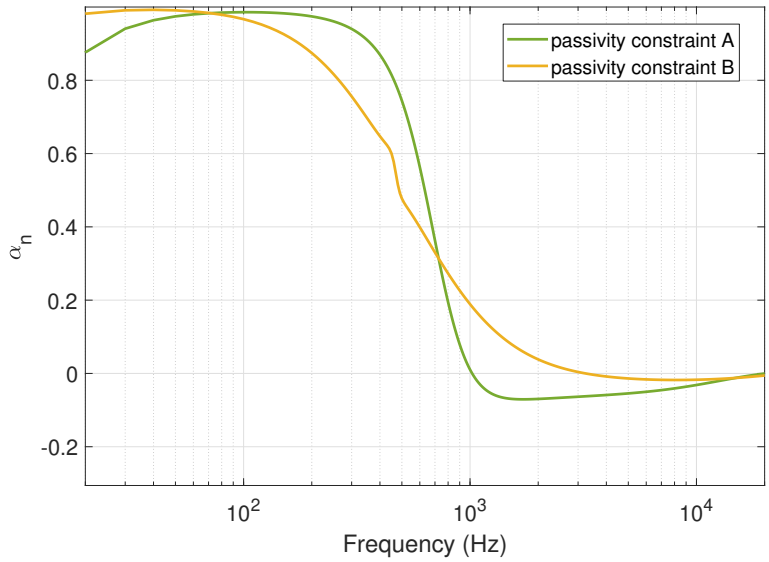

Figure 2.27: Simulated normal absorption coefficients obtained by applying different passivity constraints.

of the Infinite-Impulse-Response (IIR) iterative algorithm to round-off numerical errors (as described in Appendix D). The H_∞ problem can also be written in terms of the Tustin transforms of the discrete transfer functions involved, so that the high-frequency de-phasing introduced by the discretization is automatically taken into account in the H_∞ synthesis. The Tustin transform is a bilinear transform of the Laplace variable s used to approximate the Laplace transform of the discrete time signals, as described in Appendix D.

To sum up, in this section we have formulated the impedance control problem for a pressure-based, current-driven electroacoustic absorber, in the automatic synthesis formulation of the H_∞ method. Other than performance and energy limit specifications, we have provided a way to enforce also a passivity requirement thanks to a "fictitious feedback" in the system block diagram. The correctors obtained by solving the H_∞ problem confirm that, in order to enforce high-frequency passivity, the bandwidth of efficient absorption must shift toward low frequencies. The interdependence of the weighting filters employed for performance, energy limit and acoustical passivity, validates the outcome of the integral relationship found in Section 2.2.

We end up by proposing another possible employment of the H_∞ technique: the identification of an optimal causal local impedance for the grazing incidence problem, and its corresponding corrector synthesis. Faced with the "unreality" of the Cremer optimal local impedance for the grazing incidence, an H_∞ standard problem might be set first for searching an optimal local impedance with respect to a transmission minimization criteria. For this purpose the 1D reduced model of Appendix G could turn to be helpful for an easy (approximative) relationship between the boundary impedance and the achieved transmission coefficient. In a second moment, once an optimal causal impedance has been identified, the H_∞ technique could be exploited to synthesize the corresponding corrector to be implemented in the EA. As the optimal control synthesis for normal absorption problem was very much affected by

the integral constraint of Eq. (2.11), an optimal control synthesis for the grazing incidence problem would be affected by the integral constraint given in Eq. (2.21) in case of locally reacting EAs.

2.4 Model-inversion control strategy featuring Non-Linear dynamics at low excitation amplitudes

As wittily noted by Detroux et al. [29], there is an increasing trend toward the exploitation of nonlinear dynamical phenomena, instead of avoiding them. In solid dynamics, the nonlinear absorber, consisting of a mass with a nonlinear spring, coupled to a linear primary structure, can produce an irreversible energy transfer, from the primary structure to the absorber. Such phenomenon is usually referred to as targeted energy transfer, energy pumping or non-linear energy sink (NES), whose dynamics was firstly described in [44] and [119]. The NES concept has also been adopted for noise absorption using a membrane in its non-linear working regime, weakly coupled with a tube. Readers should refer to the extensive work of the team of the Laboratoire de Mécanique et d'Acoustique de Marseille, in France, such as [9]. A major accomplishment of [9] is the possibility for the membrane absorber to tune itself to different resonance frequencies. Though, one of the drawbacks of nonlinear absorbers is the fact that a certain energy threshold must be reached before the nonlinear phenomena occur.
Recently, Guo et al. [51] have targeted a Duffing behaviour for the EA by sensing the pressure inside the back-cavity of the EA such that to retrieve a measurement directly proportional to the diaphragm displacement at low frequencies. The main interest resided into the tunability of the non-linear absorber as well as in the possibility of accomplishing cubic dynamics for low excitation amplitudes. In [51] the control variable, the current, is defined as:

$$i(t) = i_L(t) + i_{NL}(t). \tag{2.37}$$

In Eq. (2.37), $i_L(t)$ is the current relative to the IIR implementation of the linear model-inversion impedance control law, described by Eq. (2.38). The non-linear character is given by the term $i_{NL}(t)$, which is cubic function of the pressure measured inside the EA back-case, in turn directly proportional to the diaphragm displacement, hence we can write $i_{NL}(t) = \beta w^3(t)$.

$$i_L(t_n) = \sum_{m=0}^{N_b} b_m p(t_{n-m}) - \sum_{k=1}^{N_a} a_k i_L(t_{n-k}), \tag{2.38}$$

In Eq. (2.38), b_m and a_k are the numerator and denominator coefficients of the Z transform of $H_{loc}(s)$ as described in Appendix D. Clearly, $i(t_{n-k})$ must not comprise the non-linear contributions i_{NL} at the instants t_{n-k}. Hence it is very important to separate the linear from the non-linear contribution to the total current in the control implementation, as the IIR comes from an approximation of the convolution integral valid only for linear systems (as described in Appendix D).

Here we investigate the possibility of achieving a Duffing behaviour of the EA at low excitation amplitudes (where classical absorbers normally exhibit linear behaviour), by exploiting the same pressure-based current-driven architecture as the one treated so far, but without the addition on a microphone in the EA back-case. In order to do so, we had to substitute the IIR real-time implementation with a Runge-Kutta (RK) scheme which is able to feature non-linear mechano-acoustical behaviour. Numerical simulations, both in the harmonic and in transient regimes advocate this approach to achieve non-linear EA dynamics, looking forward future numerical studies and experimental campaigns to finally validate it.

Before getting into the proposed non-linear control algorithm, let us first look at the model-inversion-based corrector $H_{loc}(s)$ (presented in Section 2.1), from another point of view. The controller reads:

$$\begin{aligned} i(s) =& H_{loc}(s)p(s) = \frac{S_d}{Bl}\left(1 - \frac{Z_{a0}(s)}{Z_{at}(s)}\right)p(s) \\ =& \frac{S_d}{Bl}\left(p(s) - \frac{Z_{a0}(s)}{Z_{at}(s)}p(s)\right), \end{aligned} \tag{2.39}$$

which has the objective to substitute the mechanical own dynamics of the loudspeaker with a target relationship between the acoustic velocity and pressure, given by:

$$v_{at}(s) = \frac{p(s)}{Z_{at}(s)}, \tag{2.40}$$

where $v_{at}(s)$ is the target inward velocity on the speaker diaphragm. Hence, Eq. (2.39) can also be rewritten as:

$$i(s) = \frac{S_d}{Bl}\left(p(s) - Z_{a0}(s)v_{at}(s)\right), \tag{2.41}$$

where $Z_{a0}(s) = M_{a0}s + R_{a0} + K_{a0}/s$ is the normalized impedance on the diaphragm in case of open-circuited loudspeaker terminals. The equivalent expression of $i(s)$ in the time domain is then:

$$i(t) = \frac{S_d}{Bl}\left[p(t) - \left(M_{a0}\ddot{w}_{at}(t) + R_{a0}\dot{w}_{at}(t) + K_{a0}w_{at}(t)\right)\right], \tag{2.42}$$

where $w_{at}(t)$ is the target displacement corresponding to the Laplace velocity expression of Eq. (2.40), and the upper dot indicates the time derivative. The expression (2.42) is indeed approximated by an IIR system obtained through a zero-order-holder or Tustin discretization of $H(s)$, as described in Appendix D.
Nevertheless, Eq. (2.42) gives us the freedom to define any type of impedance operator, also non-linear, based upon the evaluation of the target displacement $w_{at}(t)$ solution of any ordinary differential operator of the type $\mathcal{F}[p(t), w_{at}(t)] = 0$. Based upon the real-time measurement of pressure $p(t)$, $w_{at}(t)$ can be retrieved by a solver method for ordinary differential

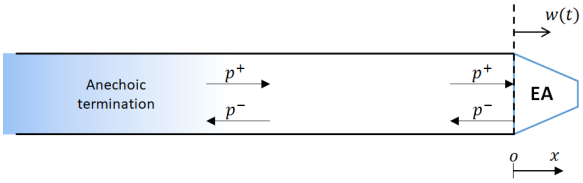

Figure 2.28: Normal incidence problem, with anechoic termination on one side and EA on the other (see Appendix E).

equations, like a 4^{th} order Runge-Kutta. For example, the EA control presented in Section 2.1, considers as target operator $\mathcal{F}[p(t), w_{at}(t)] = 0$, the relationship:

$$p(t) = M_{at}\ddot{w}_{at}(t) + R_{at}\dot{w}_{at}(t) + K_{at}w_{at}(t), \tag{2.43}$$

where M_{at}, R_{at} and K_{at} can be adjusted at will, for example putting them equal to $\mu_M M_{a0}$, $\rho_0 c_0$ and $\mu_K K_{a0}$ respectively. The recursive control algorithm would be:

1. Time step t_n: evaluate $\ddot{w}_{at}(t_n)$ from Eq. (2.43), where $p(t_n)$ is the measured pressure, while $w_{at}(t_n)$ and $\dot{w}_{at}(t_n)$ are computed at the previous time-step.

2. Time step t_n: once $w_{at}(t_n)$, $\dot{w}_{at}(t_n)$ and $\ddot{w}_{at}(t_n)$ are known, compute the electrical current $i(t_n)$ from Eq. (2.42), and inject it into the loudspeaker coil.

3. Time step t_{n+1}: solve Eq. (2.43) with the measured pressure $p(t_{n+1})$ to find $w_{at}(t_{n+1})$ and $\dot{w}_{at}(t_{n+1})$, by 4^{th} order Runge-Kutta scheme.

4. Restart from point 1., with $t_n = t_{n+1}$.

Such control algorithm can be defined as Runge-Kutta (RK)-based as opposed to the IIR recursive implementation usually adopted for correctors synthesized in the Laplace domain. For comparing the two control algorithms, a time-simulation is carried out on the simplest case-study of normally incident harmonic plane waves. The problem is described in Appendix E: the EA is placed at one end of an acoustic waveguide which has an anechoic termination on the other end as in Figure 2.28.
In the plane wave regime, it is a 1D problem. Because of the anechoic termination, we can fix the incident plane wave $p^+(t)$ on the EA. The reflected wave $p^-(t)$ is written in terms of the EA normal inward velocity $\dot{w}(t)$, so that the total sound pressure on the EA is $p(t) = 2p^+(t) - \rho_0 c_0 \dot{w}(t)$.
Because of the inevitable time delay, the sound pressure $p(t)$ in Eq. (D.9) or Eq. (2.42) to find the controller $i(t)$, must be evaluated at a number of time steps, given by the time delay divided the time steps size, before the present one. The electrical current (either coming from the IIR or RK algorithms) is then inserted in the actual mechanical dynamics equation of the loudspeaker:

$$M_{a0}\ddot{w}(t) + R_{a0}\dot{w}(t) + K_{a0}w(t) = p(t) - \frac{Bl}{S_d}i(t), \tag{2.44}$$

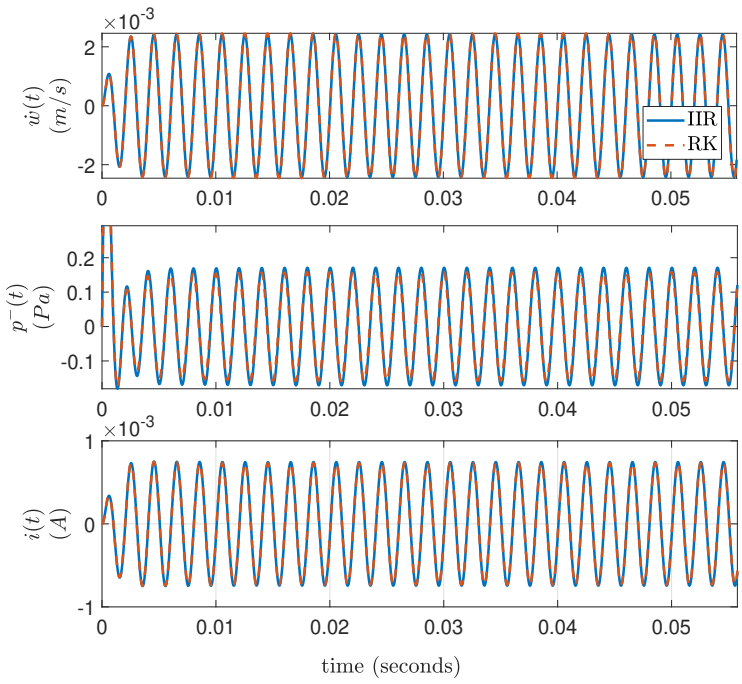

Figure 2.29: Simulated time histories of EA velocity $\dot{w}(t)$, reflected pressure $p^-(t)$ and electrical current signals $i(t)$, for harmonic incident pressure $p^+(t)$ of amplitude 1 Pa at 500 Hz, in case of IIR (in solid blue) and RK (in dashed red) controller implementations.

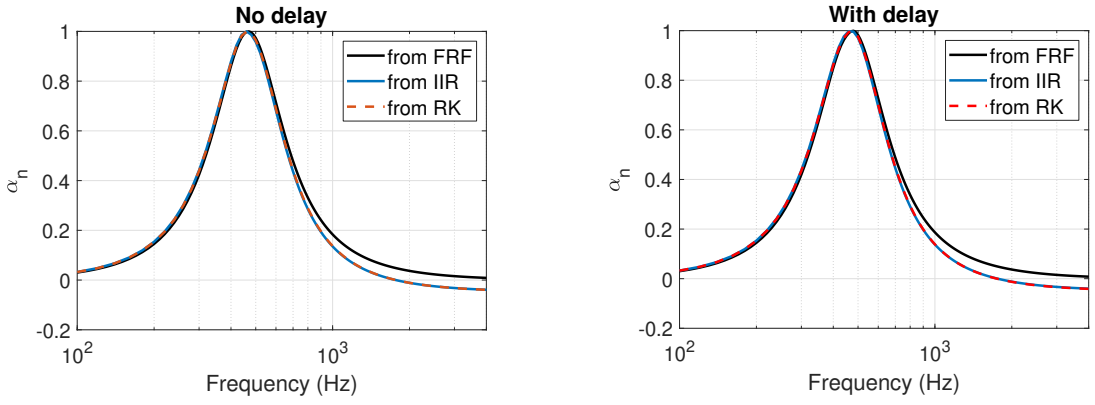

Figure 2.30: Simulated normal absorption coefficients obtained directly in frequency domain from $H(\mathrm{j}\omega)$ (in black) compared with the values obtained by the IIR (in blue) and RK (in dashed red) time implementations of the controller. On the left no time delay is assumed while on the right a time delay of 2×10^{-5} seconds is considered. The target impedance operator is set with values: $\mu_M = \mu_K = 1$ and $R_{at} = \rho_0 c_0$.

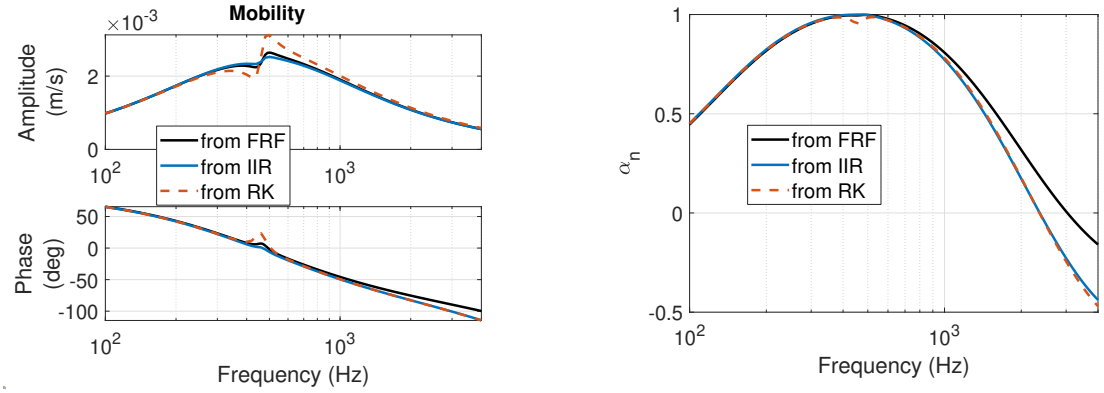

Figure 2.31: Simulated acoustic mobility (on the left) and normal absorption coefficient (on the right) obtained directly from $H(\mathrm{j}\omega)$ (in black), and retrieved from the time-response either with the IIR or RK algorithm. The target impedance operator is set with values: $\mu_M = \mu_K = 0.2$ and $R_{at} = \rho_0 c_0$. The time delay is 2×10^{-5} seconds.

where $p(t)$ must be evaluated at the present time. For harmonic incident waves $p^+(t)$, the reflection $R(\omega)$ and absorption $\alpha(\omega)$ coefficients spectra can be retrieved by taking the Discrete-Fourier-Transform (DFT) of the incident and reflected signals. In Figure 2.29 the time histories of the EA velocity, the reflected pressure $p^-(t)$ and electrical current $i(t)$, for harmonic incident pressure $p^+(t)$ at 500 Hz of amplitude 1 Pa, in case of IIR and RK control strategies. The normal incidence problem in time, described in Appendix E, is solved by a 4^{th}-order Runge-Kutta algorithm, both for the IIR and RK controllers. In Figure 2.30, we show the normal absorption coefficients retrieved computing the DFT of the incident and reflected pressures signals after the transient, in case of IIR and RK control implementation, as well as the curve of $\alpha_n(\omega)$ obtained directly from the Frequency-Response-Functions (FRFs) of the EA acoustic mobility as done in Section 2.1. The FRFs though, are here evaluated by taking the Tustin transform of the discrete corrector $H(z)$ in order to obtain $H(s)$, so that the transfer function $H(s)$ (i.e. $H(\mathrm{j}\omega)$) be equivalent to $H(z)$ in the sense described in Appendix D.

The target acoustic impedance operator is the same SDOF-in-series as considered in Section 2.1 and in Eq. 2.43, with $\mu_M = \mu_M = 1$ and $R_{at} = \rho_0 c_0$.

The two real-time implementation strategies (IIR or RK-based) look equivalent both in Figure 2.29 and 2.30. Figure 2.30 shows that the Runge-Kutta algorithm for the resolution of the normal incidence problem in time domain, produces a phase-shift, due to numerical errors, which grows up in frequency. Indeed, such a phase shift is present independently of delayed or perfectly synchronized controllers, as showed in Figure 2.30. Therefore, the loss of acoustical passivity displayed by $\alpha_n(\omega)$ from 2 kHz and above, must be related to truncation errors of the numerical scheme, which is more important as the frequency increases, for a fixed time resolution.

In Figures 2.31, 2.32 and 2.33, the RK strategy has been compared to the IIR implementation, as well as to the values obtained directly in the frequency domain from the FRF of $H(\mathrm{j}\omega)$. Both acoustic mobility and normal absorption coefficient are showed, for a target impedance operator with target resonance frequency equal to the loudspeaker natural one, but with a lower quality factor ($\mu_M = \mu_K = 0.2$, in Figure 2.31), or with a resonance frequency twice

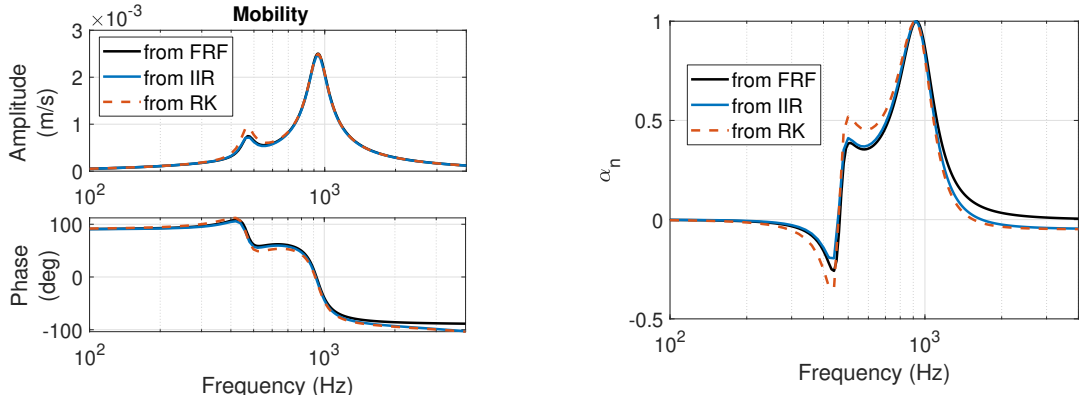

Figure 2.32: Simulated acoustic mobility (on the left) and normal absorption coefficient (on the right) obtained directly from $H(\mathrm{j}\omega)$ (in black), and retrieved from the time-response either with the IIR or RK algorithm. The target impedance operator is set with values: $\mu_M = 1$, $\mu_K = 4$ and $R_{at} = \rho_0 c_0$. The time delay is 2×10^{-5} seconds.

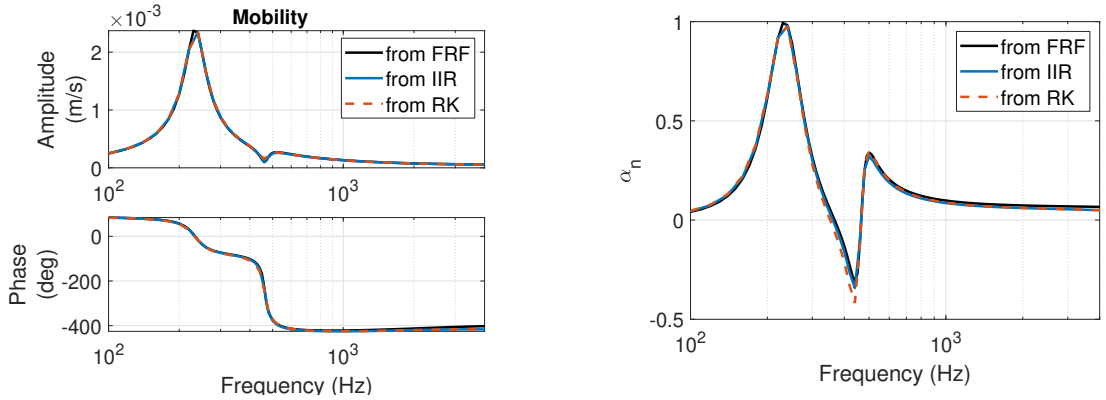

Figure 2.33: Simulated acoustic mobility (on the left) and normal absorption coefficient (on the right) obtained directly from $H(\mathrm{j}\omega)$ (in black), and retrieved from the time-response either with the IIR or RK algorithm. The target impedance operator is set with values: $\mu_M = 1$, $\mu_K = 4$ and $R_{at} = \rho_0 c_0$. The time delay is 2×10^{-5} seconds.

the natural one ($\mu_M = 1$ and $\mu_K = 4$ in Figure 2.32), or with a resonance frequency half the natural one ($\mu_M = 4$ and $\mu_K = 1$ in Figure 2.33).
These Figures, show that the RK strategy slightly enhances the effect of the time delay around resonance (see Section 2.1.1) respect to the IIR implementation. The high-frequency is indeed not significantly impacted by the RK respect to the classical IIR, and the loss of acoustical passivity above resonance in Figures 2.31 and 2.32 is due to the truncation errors in the numerical simulation of the time-response. Nevertheless, we stress here that the RK applies a Runge-Kutta scheme at each time step, in real time, which might require higher computational time than the IIR, which in turn might increase the time delay of the entire digital control architecture. In the simulations here, the time delay has been considered as constant (equal to 2×10^{-5} seconds). Nonetheless, as already mentioned before, the RK technique seems to be currently the main way for implementing a non-linear "impedance operator" with a pressure-based, current-driven control architecture.

Let us now investigate the implementability of a cubic (Duffing) target dynamics, as the one in Eq. (2.45):

$$p(t) = M_{at}\ddot{w}_{at}(t) + R_{at}\dot{w}_{at}(t) + K_{at}\Big(\beta_L w_{at}(t) + \beta_{NL} w_{at}^3(t)\Big), \tag{2.45}$$

where β_L, always kept equal to 1 in the following, multiplies the target displacement $w_{at}(t)$, while the coefficient β_{NL} multiplies the cubic of the target displacement $w_{at}^3(t)$, and has therefore the dimensions of m^{-2}.
Figure 2.34 shows the DFTs at the fundamental harmonics, of the EA simulated responses for a harmonic normal incident plane wave of amplitude 1 Pa, on the EA placed at one end, and anechoic termination on the other (as in Figure 2.28), obtained through the same scheme described in Appendix E. The electrical current, acoustic mobility and normal absorption coefficient are plotted in case of $\mu_K = \mu_M = 1$ and $R_{at} = \rho_0 c_0$, and for different β_{NL}. Figure 2.34 shows the typical "hardening spring" effect of Duffing dynamics [82]. Each increase of β_{NL} of a factor 10, approximately triples the required electrical current at the pick.
Observe that the DFTs of current and mobility, as well as the absorption coefficient, in Figure 2.34 are relative to the fundamental harmonics of the responses, while sub- or super-harmonics scattered by the non-linear absorber, are not taken into account here.
The time-histories relative to the linear $\beta_{NL} = 0$ and cubic $\beta_{NL} = 1 \times 10^{13}$ m^{-2} dynamics are reported in Figure 2.35a and 2.35b for incident harmonic pressure waves at 500 Hz and 800 Hz respectively. While 500 Hz is about the resonance frequency of the linear EA (with $\mu_M = \mu_K$), 800 Hz is the frequency relative to the pick of both mobility and normal absorption coefficient fundamental harmonics of the cubic EA. Therefore, the reflected pressure wave amplitude is minimum for excitation at $f_{pick} = 800$ Hz in case of $\beta_{NL} = 1 \times 10^{13}$ m^{-2}. Figure 2.35b clearly shows a multi-harmonic response of the EA.
Figures 2.36a and 2.36b show the effect of varying the reactive and resistance, respectively, in the EA target dynamics. The tunability of the RK-control strategy is demonstrated also for a non-linear (Duffing) target dynamics of the EA: reducing the reactive terms enlarges the bandwidth, while decreasing the resistive term sharpens the pick of EA response. Let us now check the effect of time delay on such non-linearly controlled EA.

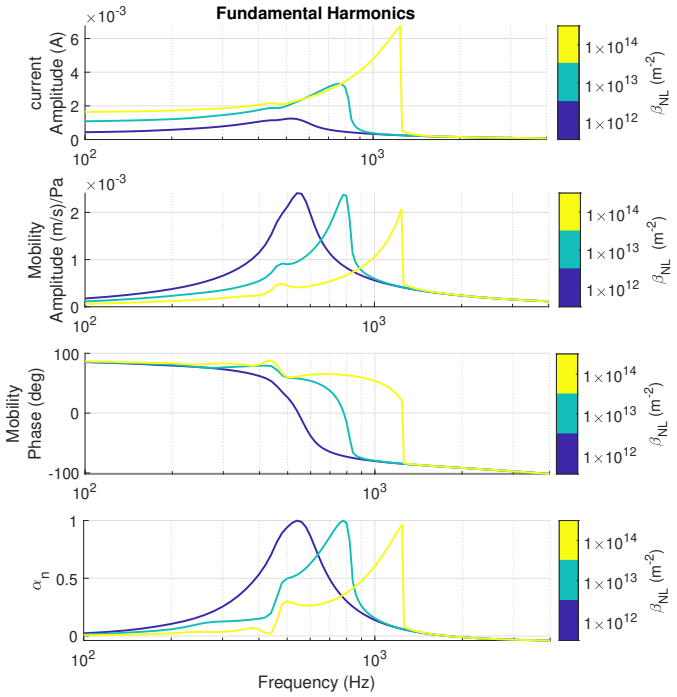

Figure 2.34: DFTs of the stationary harmonic responses of the EA, in terms of electrical current, acoustic mobility v/p and normal absorption coefficient, relative to the fundamental harmonics, in case of $\mu_M = \mu_K = 1$, $R_{at} = \rho_0 c_0$ and with varying β_{NL} (dimensions m^{-2}).

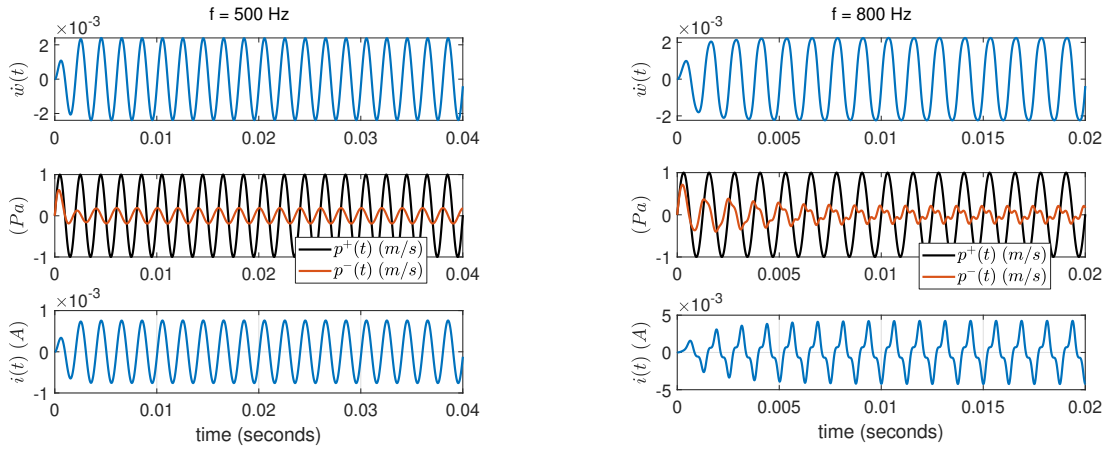

(a) (b)

Figure 2.35: Time histories of the electrical current $i(t)$, the reflected $p^-(t)$ pressure wave amplitude, and EA velocity $v(t)$ for an harmonic incident pressure wave, in case of linear EA (with $\mu_M = \mu_K = 1$ and $R_{at} = \rho_0 c_0$) at 500 Hz **(a)** and Duffing EA (with $\mu_M = \mu_K = 1$, $R_{at} = \rho_0 c_0$ and $\beta_{NL} = 1 \times 10^{13}$ m^{-2}) at 800 Hz **(b)**.

Figure 2.37 shows the effect of time delay on the normal absorption coefficient α_n relative to the fundamental harmonics scattered by the non-linear EA with $\mu_M = \mu_K = 1$, $R_{at} = \rho_0 c_0$ and $\beta_{NL} = 1 \times 10^{13}$ m^{-2}. Apparently, a time delay of $\tau = 2 \times 10^{-5}$ seconds can induce the loss of acoustical passivity before $f_0 \approx 500$ Hz. We must remark though, that a RK-scheme time-implementation might require a bigger time delay, as more computations must be car-

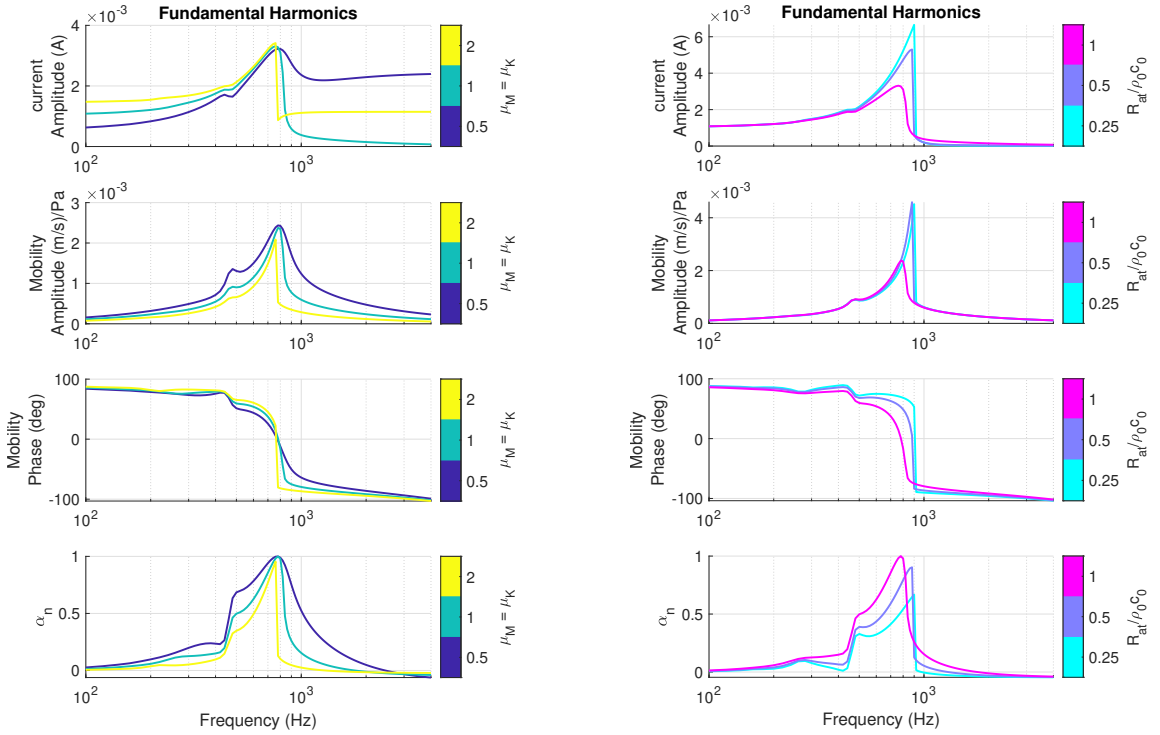

(a) (b)

Figure 2.36: DFTs of the simulated stationary harmonic responses of the EA, in terms of electrical current, acoustic mobility v/p and normal absorption coefficient, relative to the fundamental harmonics, in case of varying $\mu_M = \mu_K$ and $R_{at} = \rho_0 c_0$ **(a)**, or with $\mu_M = \mu_K$ and varying R_{at} **(b)**, and $\beta_{NL} = 1 \times 10^{13}$ m^{-2}.

ried out at each time step.

A major interest for the non-linear dynamic vibration (or sound) absorbers resides into the possibility to accelerate the time-decay of vibration (or sound) levels in the primary linear system, respect to the classical linear absorbers [9]. For this reason, we examined the transient response in a 1D acoustic cavity, simulating the response in a tube around its first resonance $f_{res,tube} = c_0/(2L)$ (in case of enclosed tube with rigid end walls), with L the length of the 1D cavity. In Figure 2.38, the 1D cavity is represented by a segment connecting a pressure source p_s at one end, and the nonlinear EA at the other. In order to place the resonant frequency of the 1D cavity at the pick of absorption of the non-linear EA, the tube length has been set equal to $L = c_0/(2f_{pick})$, where f_{pick} is the frequency where the acoustical mobility, relative to the fundamental harmonics of the EA, approximately reaches the pick value of $1/(\rho_0 c_0)$. Choosing $\mu_M = \mu_K = 1$ and $R_{at} = \rho_0 c_0$, Figure 2.34 shows that the pick of mobility and α_n (relative to the fundamental harmonics) is at about $f_{pick} = 800$ Hz. Hence, the length of the duct is set to $L = 0.21$ m, such that $f_{res,tube} = c_0/(2L) \approx f_{pick}$.
In Figure 2.39 the fundamental-harmonics of electrical current, acoustical mobility and normal absorption coefficient of the non-linear EA, are compared to a linear EA control. The linear EA used for the comparison, has $\mu_M = 1$, $R_{at} = \rho_0 c_0$ and $\mu_K = \mu_M \frac{f_{pick}^2}{f_0^2}$, where $f_{pick} = 800$ Hz, such that also the linear EA presents the pick at 800 Hz.

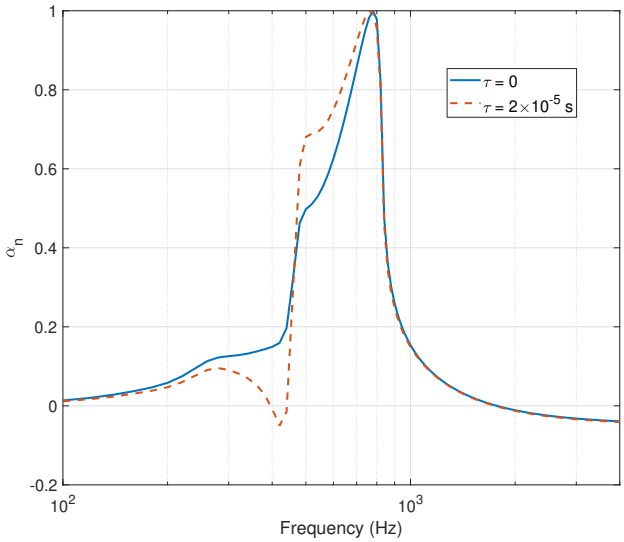

Figure 2.37: Effect of time delay τ on the normal absorption coefficient α_n relative to the fundamental harmonics scattered by the non-linear EA with $\mu_M = \mu_K = 1$, $R_{at} = \rho_0 c_0$ and $\beta_{NL} = 1 \times 10^{13}$ m^{-2}.

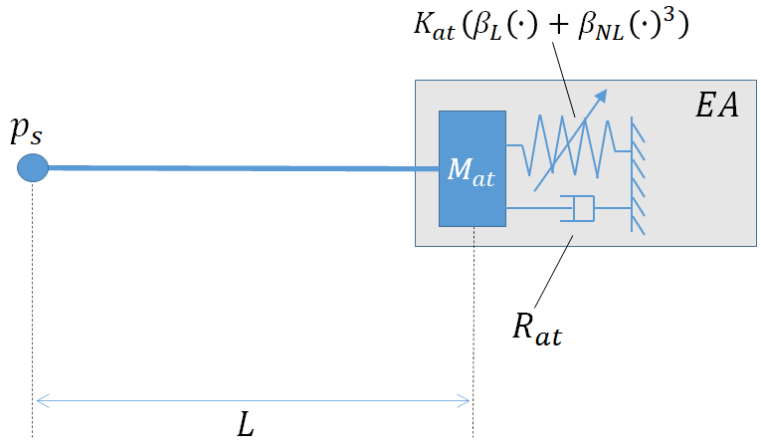

Figure 2.38: Sketch of the 1D problem used for simulations: at the left end the pressure source p_s and at the right end the EA whose target dynamics is described by its equivalent mechanical SDOF system. The SDOF absorber is characterized by a target acoustical mass M_{at}, a resistance R_{at} and a Duffing stiffness operator $K_{at}\left(\beta_L(\bullet) + \beta_{NL}(\bullet)^3\right)$.

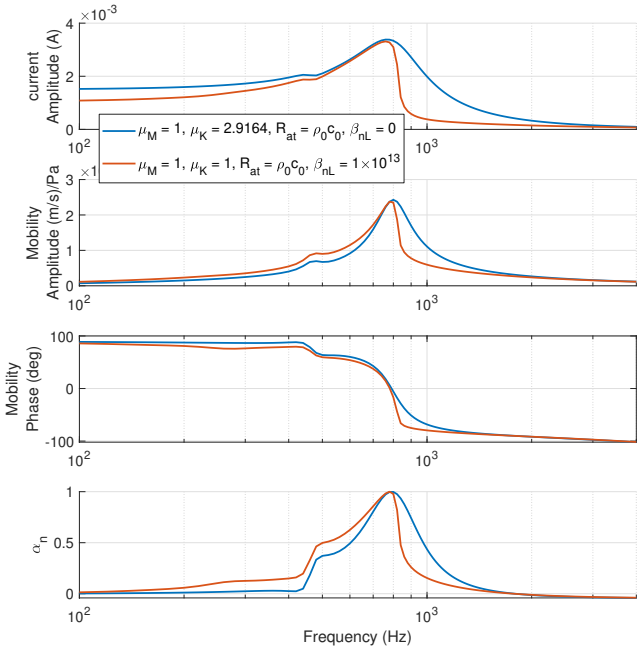

Figure 2.39: DFTs of the stationary harmonic responses of the EA, in terms of electrical current, acoustic mobility v/p and normal absorption coefficient, relative to the fundamental harmonics, in case of linear EA with $\mu_M = 1$, $\mu_K = 2.9$ and $R_{at} = \rho_0 c_0$, and non-linear EA with $\mu_M = \mu_K = 1$, $R_{at} = \rho_0 c_0$ and $\beta_{NL} = 1 \times 10^{13}$ m^{-2}.

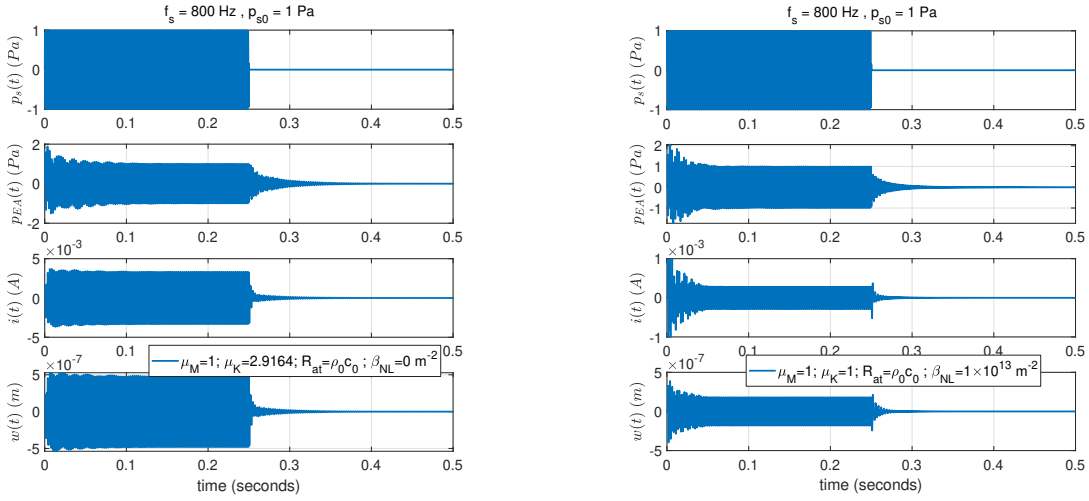

(a) (b)

Figure 2.40: Time histories of the pressure at the source $p_s(t)$, of the pressure at the EA location $p_{EA}(t)$, electrical current in the EA $i(t)$ and diaphragm displacement $w(t)$ in case of linear control law (with $\mu_M = 1$, $\mu_K = 2.92$ and $R_{at} = \rho_0 c_0$) **(a)** and in case of linear control law (with $\mu_M = 1$, $\mu_K = 1$, $R_{at} = \rho_0 c_0$ and $\beta_{NL} = 1 \times 10^{13}$ m^{-2}) **(b)**.

The pressure excitation has been set to $p_s(t) = p_{s0}\mathrm{Heav}(t) sin(2\pi f_{res,tube} t)$, where $\mathrm{Heav}(t)$ is the Heaviside step-function applied between t=0 and t=0.25 seconds. The time-simulation is run up to 0.5 seconds to detect the transient regime when $p_s(t) = 0$.

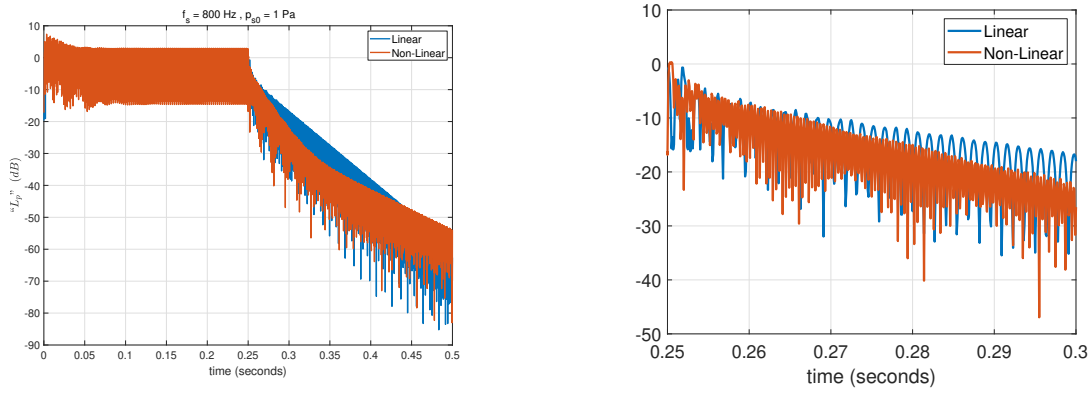

(a) (b)

Figure 2.41: "L_p" $= 10\log_{10}\left(\frac{\int_0^L p^2(t,x)dx}{\int_0^L p_{rms}^2(x)dx}\right)$ for Linear (with $\mu_M = 1$, $\mu_K = 2.92$ and $R_{at} = \rho_0 c_0$) and Non-Linear (with $\mu_M = 1$, $\mu_K = 1$, $R_{at} = \rho_0 c_0$ and $\beta_{NL} = 1 \times 10^{13}$ m^{-2}) control law, between 0 and 0.5 seconds in **(a)**. In **(b)** a zoom between 0.25 and 0.3 seconds highlights the decay trends at the first transient stage.

In Figure 2.40, we report the time histories of the simulations carried out in COMSOL of the Finite Element (FE) model of Figure 2.38. The pressure at the source $p_s(t)$ is plotted along with the pressure at the EA location $p_{EA}(t)$, the displacement of the EA membrane $w(t)$ and the necessary electrical current $i(t)$ in case of the linear and non-linear controls. The non-linear plots present stationary responses (between 0.1 and 0.24 seconds) with lower amplitudes than the linear case. When the source is put to 0 ($p_s(t) = 0$), for $t > 0.25$ seconds, there is a sudden increase of the non-linear EA responses before the decay.
In order to compare the decay of the overall sound pressure level in the 1D cavity, achieved by the non-linear absorber respect to the linear one, the following quantity has been taken into account:

$$\text{“}L_p(t)\text{”} = 10\log_{10}\left(\frac{\int_0^L p^2(t,x)dx}{\int_0^L p_{rms}^2(x)dx}\right), \tag{2.46}$$

where $p_{rms}(x)$ is the root-mean-square (rms) value at each point x along the 1D cavity (of length L). The rms is evaluated in the stationary-regime, which is considered to be attained between around 0.1 and 0.24 seconds.
Figure 2.41a clearly highlights the faster decay at the first stage of the transient regime achieved by the non-linear EA (between 0.25 and 0.3 seconds, see Figure 2.41b), respect to the exponential (linear in dB) descent obtained by the linear control. After this first transient stage, the nonlinear phenomenon is less efficient and the decay is classically exponential as in the linear control. This is a classical behavior of NES observed with mechanical NES resonators [46].

Finally, it must be said that sensing the speaker displacement or velocity, by a microphone in the EA back-case, as well as by any other external sensor, such as a laser doppler velocimeter (LDV), and then feed such measurement into the RK scheme, would surely improve the robustness of the RK approach, at the price of a relatively bulkier control system.

2.5 Conclusions

In this chapter, we studied the model-inversion control strategy in the pressure-based current-driven EA architecture. First, the model-inversion control strategy originally proposed in [104] has been analysed in both its performance and stability aspects in Section 2.1. The effect of time-delay on passivity and therefore stability has been assessed by both simulations and experimental tests. A practical solution to acoustically passivate the system has been adopted, by applying a porous layer in front of the EA. This remedy can be considered as an input-output transformation-matrix passivating technique [121]. Nevertheless, the elements of the transformation matrix for the porous layer, cannot be written as causal transfer functions, therefore limiting the possibility to find an electrical equivalent to the porous passivation. An optimal passive element can be searched in order to achieve the best high-frequency passivation, which would allow to enlarge the operative bandwidth of the EA, faced with the shortage of acoustical passivity due to time-delay as well as to spill-over.
An integral constraint has been analytically determined in Section 2.2 which generalizes the one of Yang [122] for passive absorbers, to the impedance control of EAs. It applies for any proper rational correctors in the pressure-based, current-driven impedance control architecture and imposes a compromise between frequency bandwidth, high-frequency passivity and low-frequency energy supply.
The pressure-based, current-driven impedance control problem has been formulated in the H_∞ formalism in Section 2.3. In addition to the normal-absorption performance and current limitations, a passivity specification has been enforced thanks to the analogy between the bilinear transform of a transfer function and the reflection coefficient of a surface impedance. The outcomes of the H_∞ syntheses highlight the tight inter-dependence between the bandwidth of efficient absorption, the acoustical passivity and the low-frequency limit of the corrector amplitude.
Then, a real-time implementation alternative to the classical IIR, has been proposed in Section 2.4. It is based upon a Runge-Kutta solution scheme, which allows to feature non-linear target dynamics of the EA.

2.6 Next steps

Concerning the future developments, we highlight that the normal absorption testing showed the need for a dedicated analysis upon the system robustness with respect to parameters and dynamic uncertainties, as to be expected for model-inversion control strategies. The mechanical dynamics of the loudspeaker taken into account in the control syntheses, has been restricted to the first piston-like mode, where the loudspeaker behaves as a SDOF mechanical system, excited by the external pressure force $S_d p(t)$ and the driving electromechanical force $Bli(t)$. Clearly, such model is accurate only around the natural frequency where the loudspeaker features such mode. A controller conceived in such a way, might induce spill-over effects [27] around the natural frequencies of other mechanical modes of the loudspeaker. Usually the piston-like mode is the first mode, and higher order modes are sufficiently far in frequency.

The spill-over is one of the most important factor which limits the achievable operational bandwidth of this controller, not simply because the corrector $H(s)$ might be inefficient far from the controlled mode, but especially because it might destabilise the system at the higher order natural modes of the loudspeaker. In order to cope with such drawback, one possible strategy could be to try to integrate higher-order modes in the controller synthesis, which would bring about more challenging identification processes than the ones presented in Appendix A on the one hand, and higher order filters for the control transfer function on the other. Increasing the filter order means also increasing the time delay, which has equal, if not higher impact than the spill-over, on stability.

In order to face possible parameters uncertainties in the piston model, it might be useful to employ the measurement of the speaker diaphragm velocity in the control law, without invoking the electrical dynamics. By doing so, the feedforward (pressure-based) impedance control would combine with a velocity *feedback* which can improve the robustness with respect to model uncertainties [30]. An interesting idea in this sense, is presented in [51], where an additional microphone is placed inside the back cavity of the loudspeaker enclosure. As the back cavity behaves as a compliant/stiffness element, then the acoustic pressure is directly proportional to the displacement of the speaker diaphragm. This way, both the acoustic variables interested in the impedance control would be sensed, and a corrector could potentially be synthesised in such a way to reduce the impact of the errors in the loudspeaker mechanical dynamics model. Nevertheless, this approach is still limited to the bandwidth of the first natural mode of the loudspeaker, as far from it the higher order modes of the speaker would impact the back-cavity dynamics, and the simple compliance/stiffness model assumed for the back-cavity would become inaccurate. We can also foresee the use of properly designed loudspeakers, or even different types of actuators, which would present a simpler dynamics, described by a simple mechanical model in a wider frequency range.

To sum up, we demonstrated that an optimization of the entire system entails the need to take into account the acoustical passivity from the very early design stage. The H_∞ synthesis approach can indeed give the basis for next optimization processes targeting robustness, such as the so-called μ-strategy [31].

Concerning the non-linear EA concept, a deeper numerical analysis is required to optimize the NES phenomenon.

Both the H_∞ approach and the non-linear EA concept, look forward to their experimental validation.

Chapter 3

The boundary advection law

As already mentioned at the beginning of Chapter 1.1, Morse [87] in 1939 introduced the locally reacting surface as a particular case of a general interface $\partial\Omega$ (see Figure 3.1) between two propagative media: one Ω_{air} characterized by the wave equation in air, the other one Ω_{fict} (fictitious) represented by an anisotropic wave equation, of the type:

$$c_y^2\partial_y^2 p + c_t^2(\partial_x^2 p + \partial_z^2 p) = \partial_t^2 p \tag{3.1}$$

where c_y was the phase speed along the normal y to the surface, and c_t the "tangential" phase speed parallel to the surface. Such anisotropic wave equation could even be more generalized by considering the possibility of different phase speeds along x and z (where z is the out-of-plane direction in Figure 3.1), as well as the presence of a *convection speed* $\vec{V}_c$:

$$c_x^2\partial_x^2 p + c_y^2\partial_y^2 p + c_z^2\partial_z^2 p = (\partial_t + \vec{V}_c \cdot \vec{\nabla})^2 p \tag{3.2}$$

According to Morse, a *locally reacting surface* could be interpreted as the interface between air and a domain Ω_{fict}, characterized by Eq. (3.2) with $c_x = c_z = \vec{V}_c = 0$. This way, Eq. (3.2) *degenerates* into a 1D wave equation, where wave propagation in Ω_{fict} is allowed only along the normal direction y to the surface $\partial\Omega$, with a phase speed equal to c_y. The boundary $\partial\Omega$ would then be seen as a locally-reacting surface by Ω_{air}, with characteristic impedance

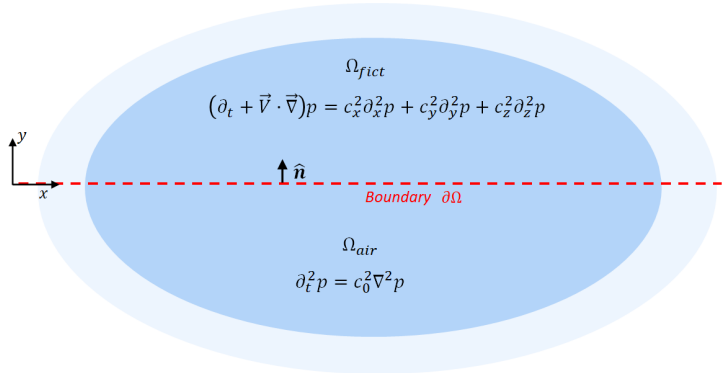

Figure 3.1: Interface $\partial\Omega$ between two semi-infinite domains: Ω_{air} and Ω_{fict}. Ω_{air} is filled with still air, and extends indefinitely toward $\pm x$ and $-y$. Ω_{fict} extends indefinitely toward $\pm x$ and $+y$, and is an anisotropic acoustic medium characterized by Eq. (3.2).

$\rho_{fict}c_y$, with ρ_{fict} the density in Ω_{fict}. For Ω_{fict} extending to infinity along the $+y$ direction, then the characteristic impedance becomes the surface impedance of the locally-reacting surface $\partial\Omega$. By contemplating complex values of c_y and/or ρ_{fict}, complex impedances would be reproduced on the interface $\partial\Omega$. Such considerations are retrieved in the equivalent fluid model for porous media [1].
Non-locally reacting surfaces can be attained if c_x and/or c_z are different from 0 in Eq. (3.2). It is the case of non-locally reacting liners for example, where the y-dimension of Ω_{fict} is bounded by a rigid back wall [56]. In the following discussion, Ω_{fict} will be considered always as extending indefinitely from the boundary $\partial\Omega$ toward all three coordinate directions ($\pm x$,$\pm z$,$+y$), as showed in Figure 3.1 for the 2D case.

In [22], Collet et al. presented a Fourier-space-based approach in order to provide the boundary operator (applying on $\partial\Omega$) corresponding to a propagative domain Ω_{fict} behind. In particular, Collet was interested in a boundary operator, i.e. a relationship between the pressure and velocity, assuring total absorption for any angle of incidence, as mentioned at the beginning of Chapter 1.1. In order to do that, he considered a Ω_{fict} characterized by the same wave equation as Ω_{air}, i.e. $c_0^2\nabla^2 p = \partial_t^2 p$ in the absence of convection, and imposed on the interface $\partial\Omega$ the continuity of pressure and its y-derivative:

$$\begin{aligned} p &= p_{fict} \quad \text{on } \partial\Omega \\ \partial_y p &= \partial_y p_{fict} \quad \text{on } \partial\Omega, \end{aligned} \tag{3.3}$$

where p_{fict} is the acoustic variable defined in the fictitious domain Ω_{fict}. Hence, the boundary operator, i.e. the relationship between $\partial_y p$ and p, presented in [22], is:

$$c_0\partial_y p = -\left(\sqrt{\partial_t^2 - (c_0^2\partial_x^2 + c_0^2\partial_z^2)}\right)p \quad \text{on } \partial\Omega. \tag{3.4}$$

The result of Eq. (3.4) is quite intuitive, and is derived here formally, without getting into the details of Fourier transform of non-integer operators [86]. Supposing no boundary at all, but simply an infinite domain Ω_{air}, and operating the Fourier transform for both the time and space variables of the wave equation (which is equivalent to assuming the wave function ansatz $p = p_0 e^{\mathrm{j}\omega t - \mathrm{j}k_x x - \mathrm{j}k_y y}$, and inserting it into the wave equation), we get the well-known wave number equation in air:

$$(\mathrm{j}\omega)^2 = c_0^2(-\mathrm{j}k_x)^2 + c_0^2(-\mathrm{j}k_y)^2 + c_0^2(-\mathrm{j}k_z))^2 \quad \text{on } \partial\Omega. \tag{3.5}$$

Isolating the k_y term, we get:

$$-c_0\mathrm{j}k_y = \pm\sqrt{\mathrm{j}\omega - c_0^2(-\mathrm{j}k_x)^2 - c_0^2(-\mathrm{j}k_z)^2} \quad \text{on } \partial\Omega. \tag{3.6}$$

In order to attain a passive boundary (absorbing and not radiating), only the minus sign should be accounted for, in Eq. (3.6) (this can be easily verified if we suppose a locally-reacting boundary). Re-transforming Eq. (3.6) in the time-space domain, we get Eq. (3.4).

By imposing Eq. (3.4) on the surface $\partial\Omega$, such boundary would become transparent, i.e. totally absorbing, for waves coming from Ω_{air}, for any angle of incidence.
The reasoning can be generalized to evaluate the boundary operator relative to an Ω_{fict} (behind the boundary) characterized by the anisotropic and convected wave equation (3.2), with advection speed taken as $\vec{V_c} = c_a\vec{x}$ (the subscript in c_a stays for *advection*):

$$c_y\partial_y p = -\left[\sqrt{(\partial_t + c_a\partial_x)^2 - (c_x^2\partial_x^2 + c_z^2\partial_z^2)}\right]p \quad \text{on } \partial\Omega. \tag{3.7}$$

The operator appearing on the rhs of Eq.s (3.4) and (3.7) is of fractional order, non-local both in time and space, hence requiring huge computational efforts, as mentioned in Section 1.1. Nevertheless, for $c_x = c_z = c_a = 0$ such B.C. degenerates to the one relative to a locally reactive surface. We remark that Ω_{fict} is a fictitious domain, therefore it can be assumed that the field in Ω_{fict}, governed by Eq. (3.2) is purely potential and inviscid. Therefore, even though a convection is considered in Ω_{fict}, no vortex sheet has to be expected at the interface with the actual air domain Ω_{air}, and the continuity of normal velocity, that is of normal pressure gradient (in our case $\partial_y p$), is still valid as long as there is no airflow in Ω_{air} [55].

Supposing $c_x = c_z = 0$, Eq. (3.7) degenerates into:

$$c_y\partial_y p = -(\partial_t + c_a\partial_x)p \quad \text{on } \partial\Omega. \tag{3.8}$$

Eq. (3.8) is the advection B.C. law first reported in [22].
Hence, we can finally define the *advection law* as the boundary operator simulating the interface with a domain Ω_{fict} governed by an anisotropic convected equation of the type of Eq. (3.2) with convection speed $\vec{V_c} = c_a\vec{x}$, and phase speeds c_x and c_z degenerating to 0.
Therefore, the *advection boundary law* simulates the interface with a fictitious domain Ω_{fict} where wave propagation is allowed only along the direction y normal to the boundary as for locally reacting surfaces, but where such propagation is convected along $\text{sign}(c_a)\vec{x}$. Note that in [22], c_y is taken as equal to c_a and Eq. (3.8) is not derived from the general boundary operator (3.7) simulating the interface with an anisotropic propagative and convective fictitious domain Ω_{fict}.
In terms of the normal velocity at the boundary, Eq. (3.8) reads:

$$\rho_0 c_y\partial_t v_y = \partial_t p + c_a\partial_x p \quad \text{on } \partial\Omega. \tag{3.9}$$

Observe that for $c_a = 0$, Eq. (3.9) retrieves a locally reacting boundary of surface acoustic impedance $Z_{Loc} = \rho_0 c_y$. In order to take into account a general complex local impedance $Z_{Loc}(\mathrm{j}\omega)$, Eq. (3.9) is to be rewritten in terms of the differential operator $Z_{Loc}[\bullet]$ corresponding to the complex-valued $Z_{Loc}(\mathrm{j}\omega)$ in the Fourier ω-space, applied to the normal acceleration:

$$Z_{Loc}[\partial_t v_y] = \partial_t p + c_a\partial_x p = D_t|_{c_a} p \quad \text{on } \partial\Omega. \tag{3.10}$$

In Eq. (3.10) $D_t|_{c_a}$ is the Lagrangian derivative with respect to a convection speed c_a, indicating that the boundary *local reaction* is convected by a *boundary advection speed* equal to c_a. Defining the boundary plane as $y = 0$, as in Figure 3.1, the trajectory $\vec{x}(t) = (x(t), y(t))$ given by:

$$\begin{aligned} y(t) &= 0, \\ x(t) &= x_0 + c_a t, \end{aligned} \tag{3.11}$$

with x_0 any initial x-position, defines a *characteristic line* of the transport equation (3.10). Indeed, along $\vec{x}(t)$, the advective B.C. (3.10) becomes:

$$Z_{Loc}[\partial_t v_y(\vec{x}(t))] = \partial_t p(\vec{x}(t)), \tag{3.12}$$

or, by defining the mobility operator $Y_{Loc}[\bullet] = 1/Z_{Loc}[\bullet]$:

$$\partial_t v_y(\vec{x}(t)) = Y_{Loc}[\partial_t p(\vec{x}(t))]. \tag{3.13}$$

Eq. (3.13) clearly shows that the local reaction (given by the operator $Y_{Loc}[\bullet]$), is convected along the characteristic line $x(t) = x_0 + c_a t$ on the boundary.

In the following, the effects of such B.C. are investigated first analytically on a semi-infinite domain Ω_{air}, and then also numerically and experimentally in an acoustic waveguide.

3.1 Advection boundary law on a semi-infinite domain

In order to investigate the performance and passivity of such advection boundary law, an immediate proposition could be to evaluate the reflection coefficient of free plane-waves on an infinite surface characterized by the B.C. (3.10), according to the 2D ray acoustics theory of Appendix F. For an angle of incidence θ_i, defined in Figure 3.2, the reflection coefficient produced by the advection law is:

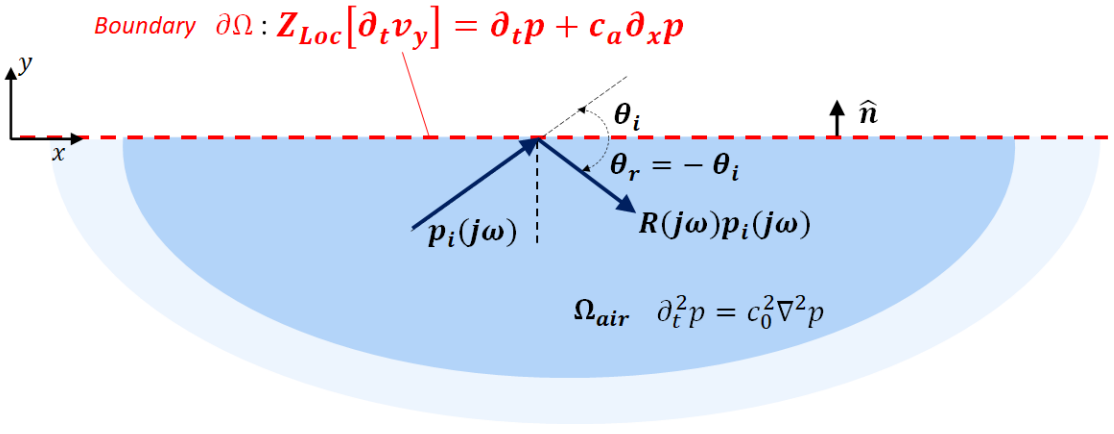

Figure 3.2: .

$$R(\mathrm{j}\omega) = \frac{\zeta_{Loc}(\mathrm{j}\omega)\sin\theta_i - (1 - \frac{c_a}{c_0}\cos\theta_i)}{\zeta_{Loc}(\mathrm{j}\omega)\sin\theta_i + (1 - \frac{c_a}{c_0}\cos\theta_i)}, \tag{3.14}$$

where $\zeta_{Loc}(\mathrm{j}\omega) = Z_{Loc}(\mathrm{j}\omega)/\rho_0 c_0$. In Appendix F the steps bringing to Eq. (3.14) are given. We remind that Eq. (3.14) is valid for free plane incident waves, in a semi-infinite domain bounded on top by the advection law, as in Figure 3.2.

Supposing a purely real local impedance ζ_{Loc}, the reflection coefficient R becomes independent of the frequency. We can therefore plot $|R|$ versus the angle of incidence θ_i in Figure 3.3, where it is assumed $\zeta_{Loc} = 1$. Therefore, $|R| = 0$ for $\theta_i = 90$ deg, for any value of c_a. Notice also that the reflection is not the same for specular angles with respect to 90 deg, as it is the case for locally reacting surfaces. In addition, for $|c_a| < c_0$ there is another minimum of $|R|$ different from 90 degree. For $c_a > c_0$, we have $|R| > 1$ and the advection boundary law becomes non-passive in the sense described in Section 2.1.1.

In Figure 3.4, the local normalized impedance is set to $\zeta_{Loc} = 0.5$, therefore there is no longer a real angle of perfect absorption in case of locally reacting surface (for $c_a = 0$), as $\zeta_{Loc} < 1$. Instead, in Figure 3.5, $\zeta_{Loc} = 2$ and the angles of perfect absorption becomes two, specular with respect to 90 deg, as $\zeta_{Loc} > 1$. The non-passive behaviour for $c_a > c_0$ is kept for any ζ_{Loc}.

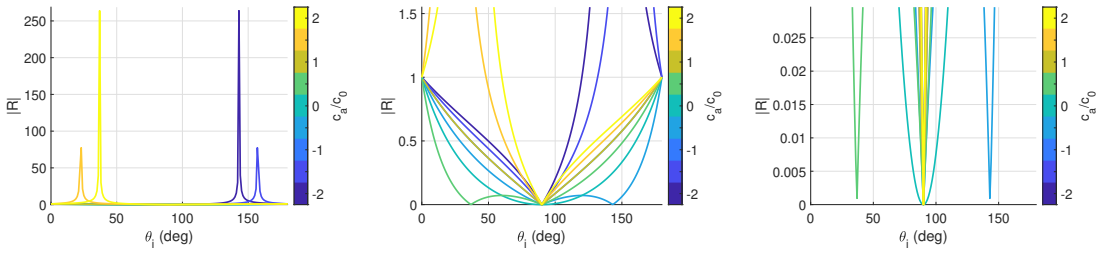

Figure 3.3: Reflection coefficient modulus $|R|$ versus the angle of incidence θ_i for $\zeta_{Loc} = 1$, and varying boundary advection speed c_a. The three plots from left to right increasingly zoom toward $|R| = 0$.

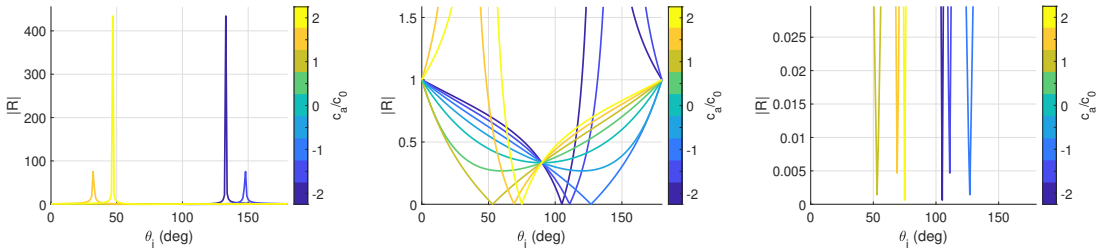

Figure 3.4: Reflection coefficient modulus $|R|$ versus the angle of incidence θ_i for $\zeta_{Loc} = 0.5$, and for varying boundary advection speed c_a. The three plots from left to right increasingly zoom toward $|R| = 0$.

In the next section, the acoustical passivity is interpreted from another point of view, which allows to assess the acoustical passivity of a B.C. by solving a dispersion problem.

3.1.1 Passivity and wave-number angles

It is well known in structural mechanics [25] that the solution of the dispersion problem in a semi-infinite domain as represented in Figure 1.4, bounded by a plate travelled by a bending

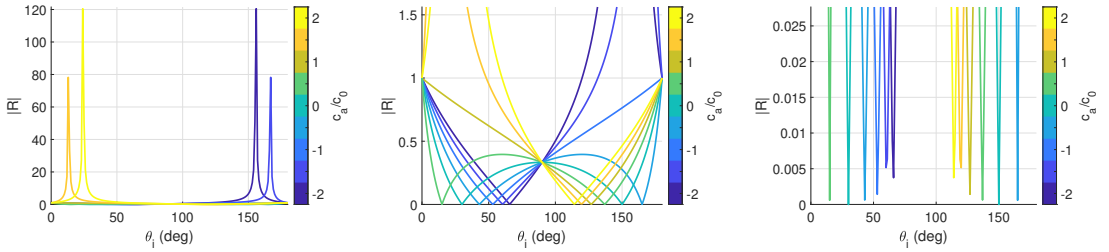

Figure 3.5: Reflection coefficient modulus $|R|$ versus the angle of incidence θ_i for $\zeta_{Loc} = 2$, and for varying boundary advection speed c_a. The three plots from left to right increasingly zoom toward $|R| = 0$.

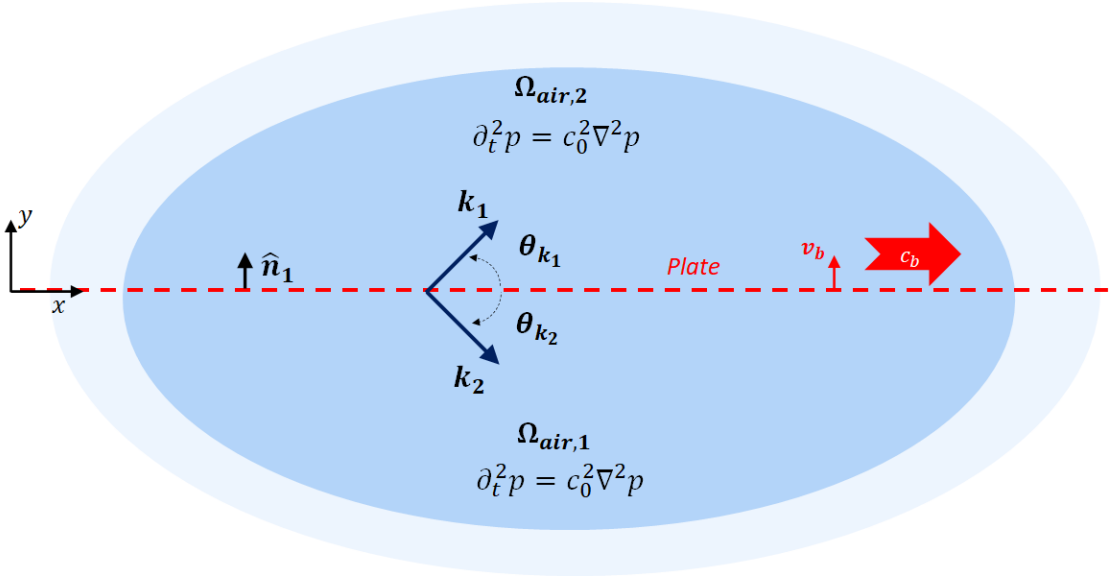

Figure 3.6: Bending plate separating two propagative domains filled with air: $\Omega_{air,1}$ and $\Omega_{air,2}$. Wavenumbers k_1 and k_2 are the dispersion solutions giving the radiation angles $\theta_{k,1}$ and $\theta_{k,2}$.

wave, gives the condition for the bending wave to be *radiative*, leading to the definition of *coincidence frequency*. Let us retrieve such result in the domain of Figure 3.6, where a plate separates two semi-infinite domains, $\Omega_{air,1}$ and $\Omega_{air,1}$, each of them propagative and filled with air. The plate is supposed of negligible thickness

The bending wave on the plate is described by the transversal velocity field $v_b(x,t) = v_{b0}e^{\mathrm{j}\omega t - \mathrm{j}k_{x,b}x}$, where v_b is the velocity along y, $k_{x,b} = \omega/c_b$ is the wave number of the boundary wave and c_b is the corresponding phase speed.

The acoustic field radiated by the bending wave, both in $\Omega_{air,1}$ and $\Omega_{air,2}$, can be written as $p(x,y) = p_0 e^{\mathrm{j}\omega t - \mathrm{j}k_x x - \mathrm{j}k_y y}$, with k_x and k_y the wave number components. From the Euler equation, the acoustic velocity v_a is:

$$v_a(x,y,t) = -\frac{1}{\rho_0 \mathrm{j}\omega}\partial_y p(x,y,t) = \frac{1}{\rho_0 c_0}\frac{k_y}{k_0}p(x,y,t) \tag{3.15}$$

The continuity condition imposes the equality of velocity at the interface both with $\Omega_{air,1}$ and $\Omega_{air,2}$, hence:

$$v_a(x, y=0, t) = v_{b0}(x,t) \tag{3.16}$$

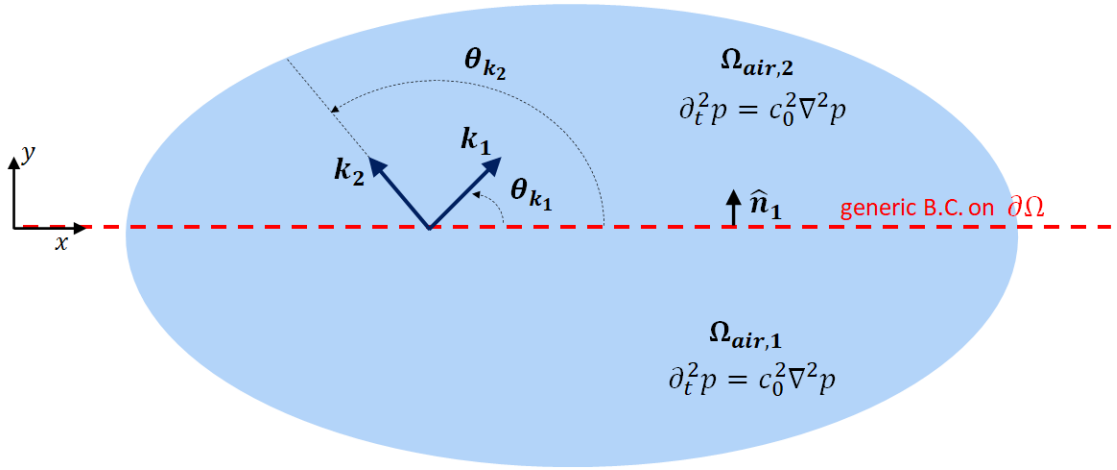

Figure 3.7: Boundary $\partial\Omega$ separating two propagative domains filled with air: $\Omega_{air,1}$ and $\Omega_{air,2}$. Wavenumbers k_1 and k_2 are the dispersion solutions for a generic B.C. which is acoustically passive in $\Omega_{air,1}$.

$$\Rightarrow \quad \frac{1}{\rho_0 c_0}\frac{k_y}{k_0} p_0 e^{\mathrm{j}\omega t - \mathrm{j}k_x x} = v_{b0} e^{\mathrm{j}\omega t - \mathrm{j}k_{x,b} x} \tag{3.17}$$

Since the equality of Eq. (3.17) must hold for any x [36], then:

$$p_0 = v_0 \rho_0 c_0 \frac{k_0}{k_y}, \tag{3.18}$$

$$k_x = k_{x,b}. \tag{3.19}$$

From the wave equation $k_x^2 + k_y^2 = k_0^2$, the wavenumbers relative to the acoustic wave propagating in $\Omega_{air,1}$ and $\Omega_{air,2}$, write:

$$k_{y,1,2} = \pm k_0 \sqrt{1 - \frac{c_0}{c_b}}, \tag{3.20}$$

where the plus sign correspond to the wave propagating in $\Omega_{air,2}$ and the minus sign to the wave propagating in $\Omega_{air,1}$. If $c_b < c_0$ both waves are evanescent, whereas if $c_b \geq c_0$, the radiated waves propagate in $\Omega_{air,2}$ and $\Omega_{air,1}$ with angles $\theta_{k_1} = \mathrm{atan2}\Big(\mathrm{Re}\{k_x\}, \mathrm{Re}\{k_{y,1}\}\Big)$ and $\theta_{k_2} = \mathrm{atan2}\Big(\mathrm{Re}\{k_x\}, \mathrm{Re}\{k_{y,2}\}\Big)$ respectively. The angles $\theta_{k_{1,2}}$ are labelled here as *wave-number angles*, as they define the wave-number directions.
As for flexural waves c_b grows with $\sqrt{\omega}$ (*dispersive* behaviour), the *coincidence frequency* is defined as the frequency for which $c_b = c_0$ [25] and the flexural wave becomes radiative. In general, supersonic boundary waves of the transversal velocity v_b are propagative.

Let us keep the same system of Figure 3.6 and follow the same reasoning also for a generic B.C. at the interface between $\Omega_{air,1}$ and $\Omega_{air,2}$, as in Figure 3.7. First, let us consider a locally-reacting boundary in order to start with a well-understood case. A locally-reacting boundary can be defined by the relationship between pressure and normal velocity:

$$\vec{n}_1 \cdot \vec{v}(x,\omega) = \frac{\eta(\omega)}{\rho_0 c_0} p(x, y=0, \omega), \tag{3.21}$$

where $\eta(\omega)$ is the normalized acoustic mobility on the boundary surface. Observe that $\vec{n}_1$ is the normal to $\partial\Omega$, inward with respect to the domain $\Omega_{air,2}$, and outward with respect to $\Omega_{air,1}$. This means that, if $\mathrm{Re}\{\eta(\omega)\} > 0$, the boundary $\partial\Omega$ is passive with respect to $\Omega_{air,1}$, i.e. if sound waves in $\Omega_{air,1}$ impinges the boundary $\partial\Omega$, the reflected acoustic energy is lower than the incident one. On the other hand, for sound waves impinging the boundary coming from $\Omega_{air,2}$, than $\partial\Omega$ is non-passive.

Defining the radiated pressure field $p(x,y) = p_0 e^{\mathrm{j}\omega t - \mathrm{j}k_x x - \mathrm{j}k_y y}$ as before, and imposing the continuity of velocity at the interface with both acoustic domains $\Omega_{air,1}$ and $\Omega_{air,2}$, we get:

$$\frac{k_y}{k_0} = \eta. \tag{3.22}$$

Notice that y coincides with $\vec{n}_1$.
From the wave equation, we retrieve k_x:

$$\frac{k_x}{k_0} = \pm\sqrt{1-\eta^2} \tag{3.23}$$

The wave-number angles are therefore:

$$\theta_{k_{1,2}} = \mathrm{atan2}\Big(\mathrm{Re}\{k_x\}, \mathrm{Re}\{k_y\}\Big) = \mathrm{atan2}\Big(\mathrm{Re}\{\eta\}, \pm\mathrm{Re}\{\sqrt{1-[\mathrm{Re}\{\eta\}]^2}\}\Big), \tag{3.24}$$

where atan2 is the arctangent on the four quadrants. From Eq. (3.24), $\theta_{k_{1,2}} \in (0, 180)$ if $\mathrm{Re}\{\eta\}$ is positive. Reminding, from Eq. (3.21), that a $\mathrm{Re}\{\eta\} > 0$ means passive boundary with respect to $\Omega_{air,1}$, and non-passive boundary with respect to $\Omega_{air,2}$, then we conclude that the passivity condition with respect to $\Omega_{air,1}$ is met as long as $\theta_{k_{1,2}} \in (0, \pi)$. Vice versa, the boundary $\partial\Omega$ is passive with respect to $\Omega_{air,2}$, as long as $\theta_{k_{1,2}} \in (\pi, 2\pi)$.
Moreover, we know that a purely real normalized mobility $0 < \eta \leq 1$ provides total absorption for waves with angle of incidence $\theta_{\alpha_{tot}} = \pm\sin^{-1}\eta$, see Appendix F. Looking at Eq. (3.24), we realize that, for $0 < \eta \leq 1$, the wave-number angles coincide with the angles of total absorption for waves coming from $\Omega_{air,1}$. It is easy to verify that for non-passive locally-reacting surface, i.e. for $\mathrm{Re}\{\eta\} < 0$, the wave-number angles correspond to the angles of highest (greater than 1) reflection coefficient amplitudes (check the following).
Notice also that, while for the travelling bending wave of Figure 3.6, the wave-number angles gave the direction of radiation from the plate to the acoustic domains $\Omega_{air,1}$ and $\Omega_{air,2}$, for a locally-reacting surface $\partial\Omega$, the wave-number angles give the directions of highest absorption or highest reflection depending upon weather the boundary is passive or not.
The relationship between passivity and wave-number angles just found for a locally-reacting boundary, can be extended to general (possibly non-locally) reacting boundaries, where the relationship between pressure and normal velocity is not simply definable by a mobility η. We can indeed state the following *acoustical passivity criterion* for general (locally or non-locally) reacting boundaries on the semi-infinite domain $\Omega_{air,1}$:

$$\text{Acoustical Passivity} \quad \Leftrightarrow \quad \theta_{k_{1,2}} = \mathrm{atan2}(\mathrm{Re}\{k_x\}, \mathrm{Re}\{k_y\}) \ \in \ (0, 180) \tag{3.25}$$

So let us consider the advection boundary law of Eq. (3.10), which, in frequency domain, writes:

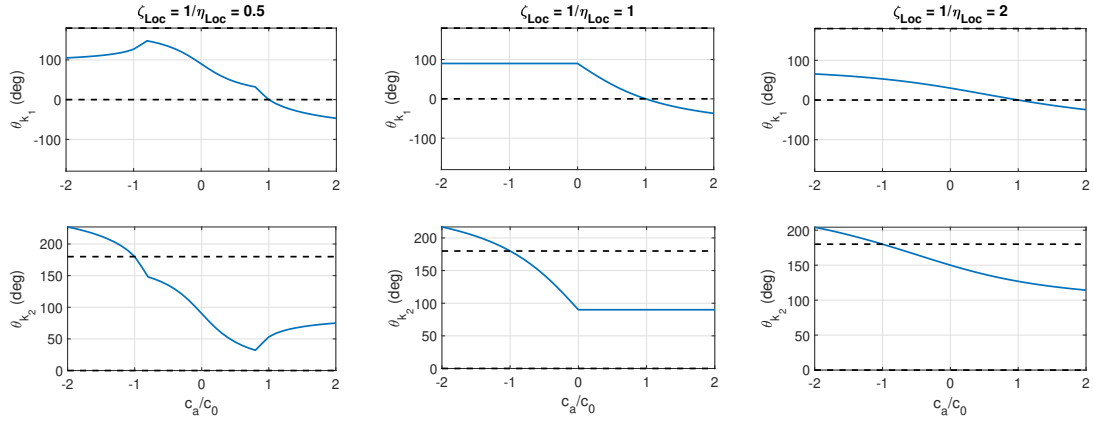

Figure 3.8: Wave-number angles relative to the boundary advection law, varying c_a, for three different values of $\zeta_{Loc} = 1/\eta_{Loc}$: 0.5 (left), 1 (middle) and 2(right).

$$v_n(x,\omega) = \frac{\eta_{Loc}(\mathrm{j}\omega)}{\rho_0 c_0}\left(p + \frac{c_a}{\mathrm{j}\omega}\partial_x p(x,\omega)\right), \tag{3.26}$$

where $v_n = \vec{n}_1 \cdot \vec{v}$ and $\eta_{Loc}(\mathrm{j}\omega) = \rho_0 c_0 / Z_{Loc}(\mathrm{j}\omega)$. Once again, defining the radiated pressure field $p(x,y) = p_0 e^{\mathrm{j}\omega t - \mathrm{j}k_x x - \mathrm{j}k_y y}$ as before, and imposing the continuity of velocity at the interface with both acoustic domains $\Omega_{air,1}$ and $\Omega_{air,2}$, we get:

$$\frac{k_y}{k_0} = \eta_{Loc}\left(1 - \frac{c_a}{c_0}\frac{k_x}{k_0}\right) \tag{3.27}$$

From the wave equation, the dispersion relation in terms of k_x is found as in Eq. (3.28), where the normalized quantities $\hat{k}_x = k_x/k_0$ and $\hat{c}_a = c_a/c_0$ have been adopted.

$$\hat{k}_x^2\left(1 + \hat{c}_a\eta_{Loc}^2\right) - 2\hat{c}_a\eta_{Loc}^2\hat{k}_x + \eta_{Loc}^2 - 1 = 0 \tag{3.28}$$

Solving this simple quadratic equation in $\hat{k}_x$, and substituting $\hat{k}_x$ in Eq. (3.27) allows to evaluate the radiation/absorption angle and check the passivity of such non-locally reacting boundary, according to the acoustical passivity criterion of Eq. (3.25).

In Figure 3.8, the radiation angles are plotted for the boundary advection law, with $\zeta_{Loc} = 1/\eta_{Loc} = 0.5$ (left), $\zeta_{Loc} = 1/\eta_{Loc} = 1$ (middle) and $\zeta_{Loc} = 1/\eta_{Loc} = 2$ (right), and varying c_a. It can be verified, by comparing Figure 3.8 with Figures 3.4, 3.3 and 3.5, that each wave-number angle coincides with the angle of maximum absorption (of minimum $|R| < 1$) when it $\in (0, 180)$, while it corresponds to the angle of maximum reflection $|R| > 1$ when it $\in (-180, 0)$ (or equivalently $\in (180, 360)$). Observe that the angles on the x-axis of the reflection coefficient plots 3.4 to 3.5, are the angles of the incident wave, related to the reflection angle by $\theta_r = 2\pi - \theta_i$ in the convention adopted in Figures 3.8.

Figures 3.9 to 3.11 better shows that the wave-number angles coincide either with the incident angles of highest absorption, or with the opposite of the incident angles of highest reflection. Figures 3.9a to 3.11a retrieve the same plots of the reflection coefficient amplitude versus the incident angle, for $\zeta_{Loc} = 1$, and varying c_a in $(-2c_0, -c_0)$, $[-c_0, c_0]$ and $(c_0, 2c_0)$ respectively. Figures 3.9b to 3.11b give the contour plot of $|R|$ versus θ_i and c_a/c_0. The curves of $\theta_{k_{1,2}}$ versus c_a/c_0 are also traced to show that they coincide with the incident angles of highest absorption

or reflection. For $c_a \in [-c_0, c_0]$, the advective B.C. is passive, hence the wavenumber angles $\theta_{k_{1,2}} \in (0, 180)$ and they both correspond to incident angles θ_i of minimum reflection. For $c_a \in (-2c_0, -c_0)$, the advective B.C. is non-passive: $\theta_{k_1} = 90$ degrees corresponds to the incident angle of minimum reflection, while $\theta_{k_2} \in (-180, 0)$ corresponds to the reflection angle $\theta_r = -\theta_i$ of maximum reflection $|R| > 1$. Conversely, for $c_a \in (c_0, 2c_0)$, $\theta_{k_2} = 90$ degrees corresponds to the incident angle of minimum reflection, while $\theta_{k_1} \in (-180, 0)$ corresponds to the reflection angle $\theta_r = -\theta_i$ of maximum reflection $|R| > 1$.
We state once again the result just demonstrated: **the wavenumber solutions of the dispersion problem of a B.C. applied on a semi-infinite domain, indicate the directions of highest absorption if the B.C. is passive. On the contrary, if the B.C. is non-passive, at least one wavenumber solution must indicate the direction of highest reflection** $|R| > 1$. Such assertion does not depend on weather the B.C. is locally or non-locally reacting.

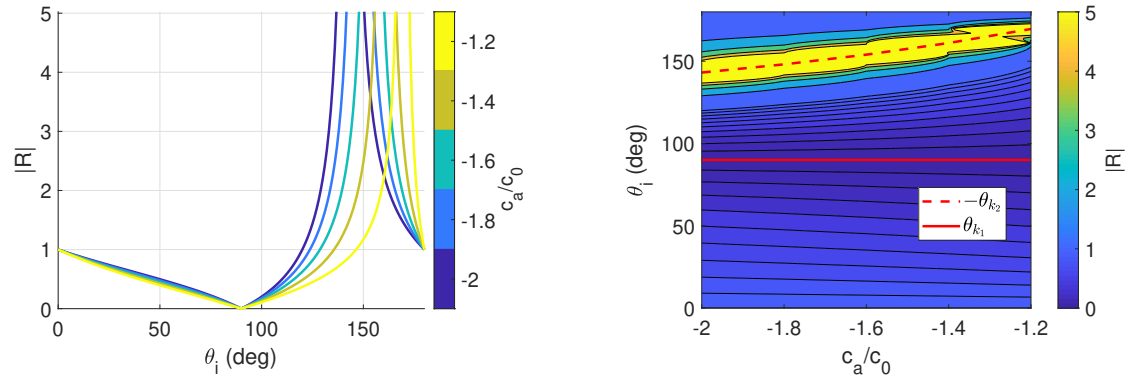

(a) (b)

Figure 3.9: **(a)**: reflection coefficient amplitude $|R|$ versus incidence angle θ_i, varying c_a in $[-2c_0, -1c_0]$; **(b)**: contour plot of $|R|$ versus θ_i and c_a/c_0, along with the wavenumber angles θ_{k_1} and θ_{k_2} plots versus c_a/c_0 in $[-2c_0, -c_0]$. The value of ζ_{Loc} is set to 1.

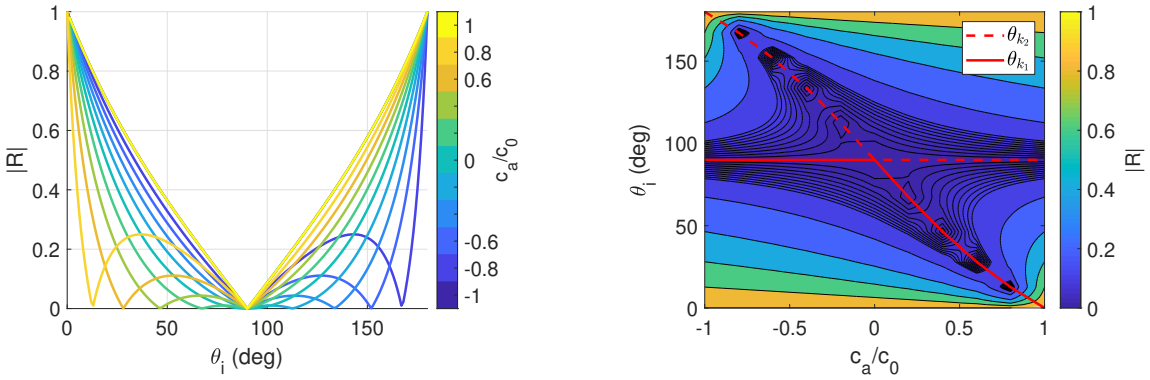

(a) (b)

Figure 3.10: **(a)**: reflection coefficient amplitude $|R|$ versus incidence angle θ_i, varying c_a in $[-c_0, c_0]$; **(b)**: contour plot of $|R|$ versus θ_i and c_a/c_0, along with the wavenumber angles θ_{k_1} and θ_{k_2} plots versus c_a/c_0 in $[-c_0, c_0]$. The value of ζ_{Loc} is set to 1.

In Figure 3.12, the acoustical passivity condition as reported in Section 2.1.1 is compared

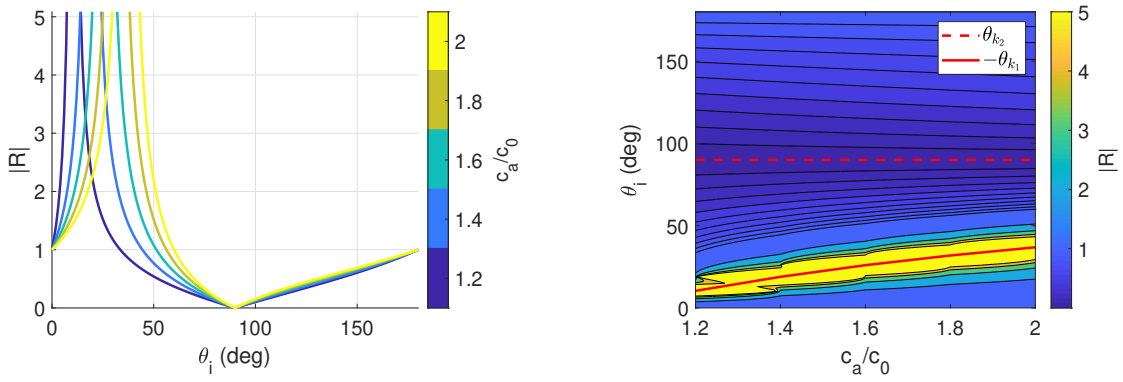

(a) (b)

Figure 3.11: **(a)**: reflection coefficient amplitude $|R|$ versus incidence angle θ_i, varying c_a in $[c_0, 2c_0]$; **(b)**: contour plot of $|R|$ versus θ_i and c_a/c_0, along with the wavenumber angles θ_{k_1} and θ_{k_2} plots versus c_a/c_0 in $[c_0, 2c_0]$. The value of ζ_{Loc} is set to 1.

to the acoustical passivity criterion (3.25). At the boundary it is considered the acoustical mobility obtained by the application of the local control defined in Section 2.1, including the physiological time delay. Observe that now the B.C. corresponds to a locally reacting surface of complex impedance. The normal absorption coefficient spectrum is plotted along with the wavenumber angles θ_{k_1} and θ_{k_2} corresponding to the two wavenumber solutions of Eq. (3.28). Apparently, both θ_{k_1} and θ_{k_2} does not satisfy the criterion (3.25) in the frequency range where the normal absorption coefficient becomes negative.

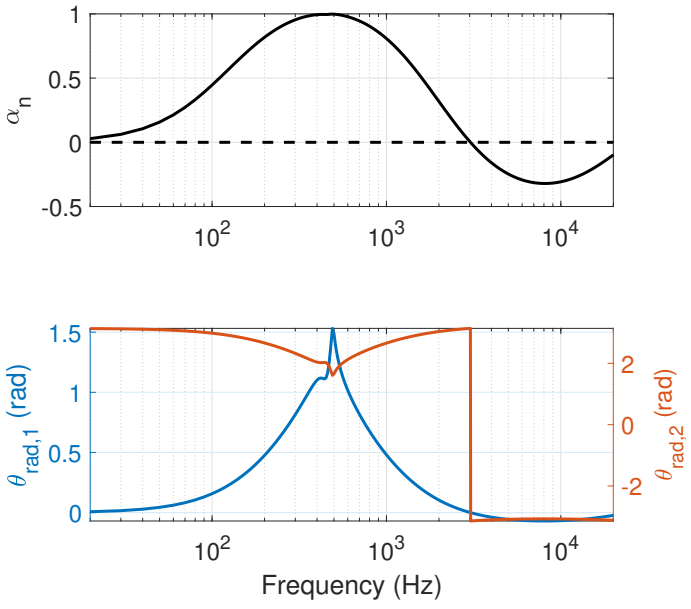

Figure 3.12: Acoustical passivity of a Local Impedance Control with $\mu_M = \mu_K = 0.2$ and $R_{at} = \rho_0 c_0$, examined in terms of the normal absorption coefficient α and radiation angles $\theta_{k,1}$ and $\theta_{k,2}$. The time delay is taken as 2×10^{-5} seconds.

Clearly, the passivity criterion of Eq. (3.25) is equivalent to the one based upon weather the

reflection coefficient amplitude is higher or lower than 1. Both the computation of $|R|$ and of the wavenumber angles, assess that the advective B.C. is non passive if $|c_a| > c_0$, in an analogous way to the *radiativity* condition for a plate travelled by a bending wave. We have to remark that such passivity condition is always respected as long as $|c_a| \leq c_0$, independently from the values (real or complex) of $\zeta_{Loc} = 1/\eta_{Loc}$.
In the next section though, we show how a complex local impedance ζ_{Loc}, lining an acoustic waveguide, can bring about amplifications of sound even for $|c_a| \leq c_0$, at some frequencies. This might seem in contrast with the results of the present section. Nevertheless, one important hypothesis of the above conclusions is removed: the semi-infinity of the acoustic domain.

3.2 Duct modes analysis in 2D waveguide

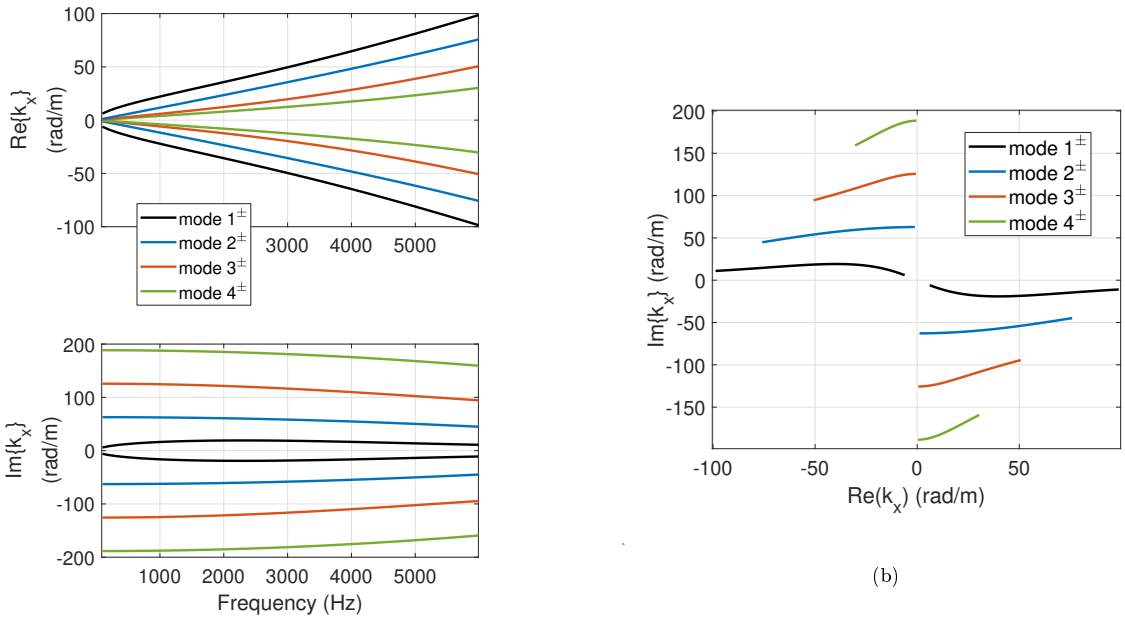

(a) (b)

Figure 3.13: Dispersion plots for the wavenumbers relative to the first four duct modes propagating in both senses, in case of purely resistive boundary, with resistance $\rho_0 c_0$.

After having discussed the acoustical passivity of the boundary advection law, let us investigate its performance into an acoustic waveguide starting from the duct mode analysis. Duct modes are fundamental to understand the propagation characteristics in a waveguide. Consider an infinite duct of constant cross-section $\mathcal{A}$ in the plane y, z (as in Figure 1.3) with boundary $\partial\mathcal{A}$ and normal $\vec{n}$. Assuming a time-harmonic sound field in the usual complex notation $(+\mathrm{j}\omega t)$ in the duct: $p(x, y, z, t) = p(x, y, z, \omega)e^{\mathrm{j}\omega t}$ the wave equation reduces to the Helmholtz equation:

$$\nabla^2 p + k_0^2 p = 0. \tag{3.29}$$

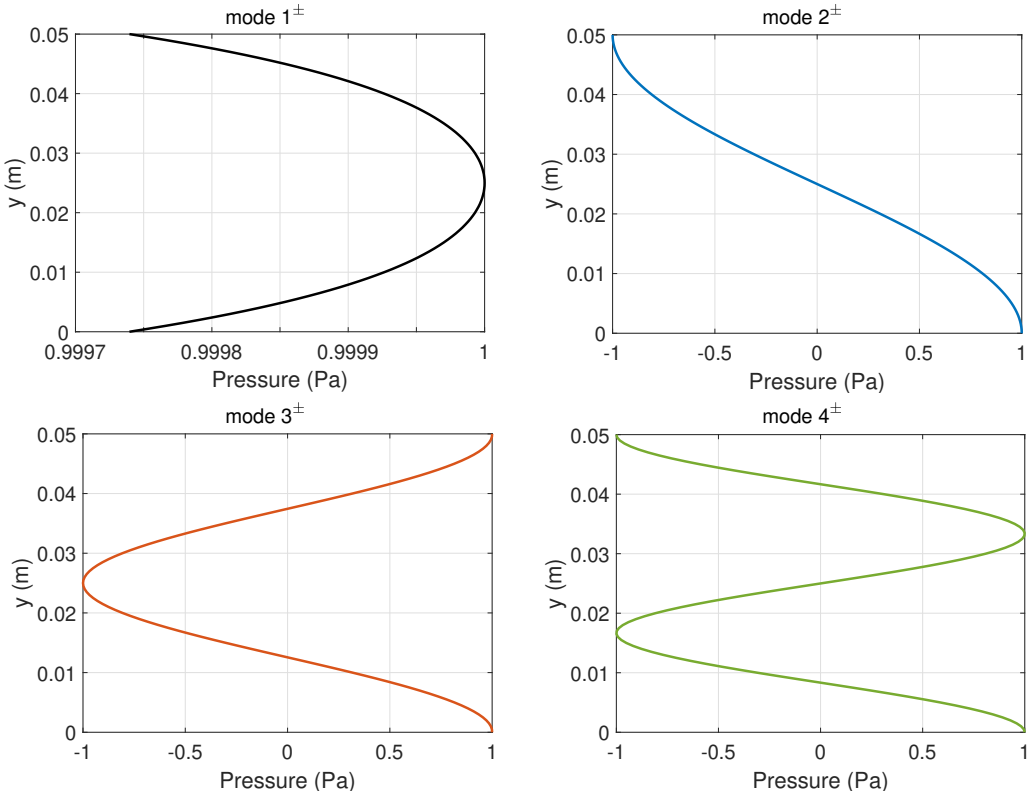

Figure 3.14: First four mode shapes $\psi_m(y)$ normalized with respect to the maximum value, in case of purely resistive boundary, of impedance $\rho_0 c_0$.

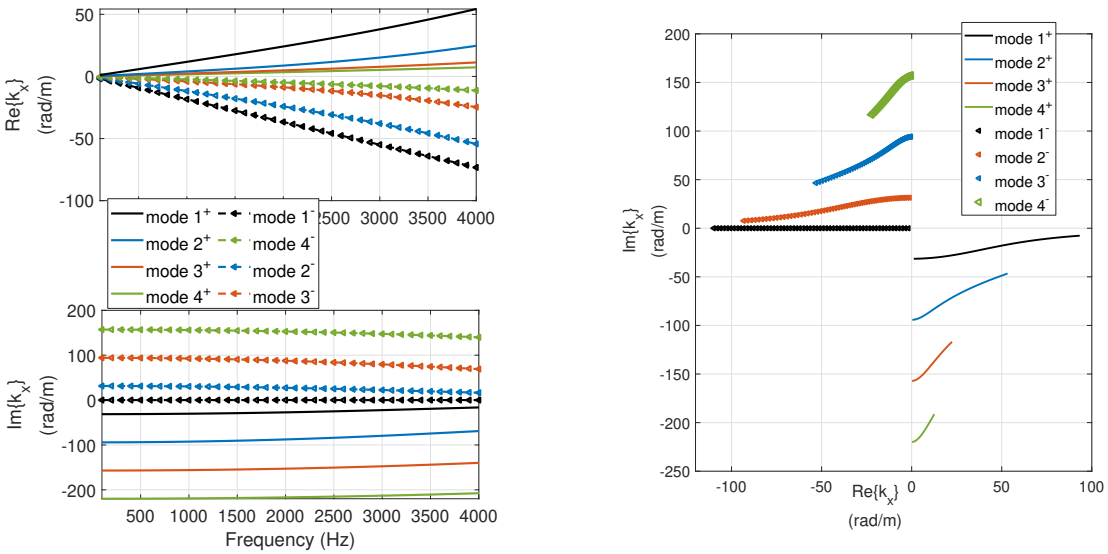

(a)

(b)

Figure 3.15: Dispersion plots for the wavenumbers relative to the first four duct modes propagating in both senses, in case of boundary advection law with $\zeta_{Loc} = R_{at}/\rho_0 c_0 = 1$ and $c_a = -c_0$.

Such sound field must also satisfy the generic B.C. $\mathcal{B}(p) = 0$ on the wall $\partial\mathcal{A}$. The solution to this problem can be written as:

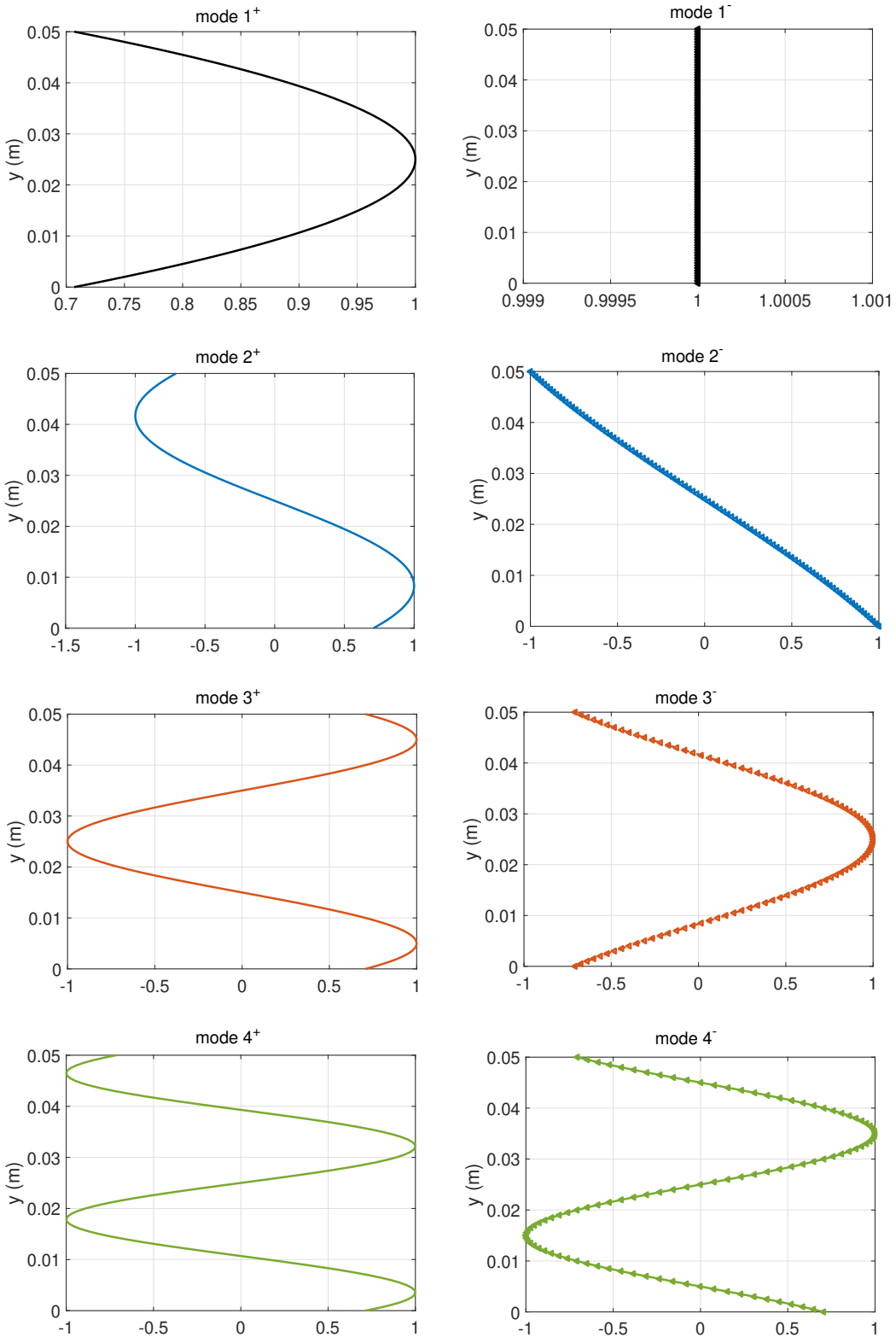

Figure 3.16: First four mode shapes $\psi_m(y)$ normalized with respect to the maximum value.

$$p(x,y,z) = \sum_{m=0}^{\infty} C_m \psi_m(y,z) e^{-\mathrm{j}k_{x,m}x}, \tag{3.30}$$

where $\psi_m(y,z)$, the so-called *duct modes*, are the eigenfunctions of the transverse Laplace operator reduced to $\mathcal{A}$ satisfying the B.C. $\mathcal{B}[p] = 0$ on $\partial\mathcal{A}$, i.e. they are solution of the eigenvalue problem:

$$\begin{aligned} &\nabla_\perp^2 \psi_m(y,z) + (k_0^2 - k_{x,m}^2)\psi_m(y,z) = 0 \quad \text{fory, z} \in \mathcal{A} \\ &\mathcal{B}[\psi_m(y,z), k_{x,m}] = 0 \quad \text{fory, z} \in \partial\mathcal{A}, \end{aligned} \tag{3.31}$$

with eigenvalues $k_0^2 - k_{x,m}^2$. The axial wavenumbers relative to each duct mode is therefore given by the eigenvalue of Eq. (3.31). Observe that for classical boundaries the B.C. does not involve the axial wavenumber $k_{x,m}$.
The sense of propagation and the attenuation of a duct mode $\psi_m(y,z)$ along its propagation are given by the group velocity $c_{g,m}$ [23] and $\mathrm{Im}\{k_{x,m}\}$ respectively. The group velocity for each duct mode can be defined as:

$$c_{g,m} = \frac{I_m}{E_m}, \tag{3.32}$$

where I_m and E_m are the acoustic intensity and twice the kinetic energy of the mode m, respectively, whose expressions are below:

$$\begin{aligned} I_m &= \int_0^h \mathrm{Re}\Big(p_m(x,y,t) v_{x,m}(x,y,t)^*\Big) dy \\ E_m &= \int_0^h \rho_0 |v_{x,m}(x,y,t)|^2 dy \end{aligned} \tag{3.33}$$

where p_m is the acoustic pressure and $v_{x,m}$ is the acoustic velocity along the longitudinal axis of the duct, of mode m as shown in Eq.s (3.34). The width of the 2D duct has been called h.

$$\begin{aligned} p_m(x,y,t) &= C_m \psi_m(y) e^{\mathrm{j}\omega t - \mathrm{j}k_{x,m}x} \\ v_{x,m}(x,y,t) &= -\frac{1}{\rho_0 \mathrm{j}\omega}\partial_x p = \frac{k_{x,m}}{\rho_0\omega} C_m \psi_m(y) e^{\mathrm{j}\omega t - \mathrm{j}k_{x,m}x}, \end{aligned} \tag{3.34}$$

Hence, the complex conjugate of $v_{x,m}$ is:

$$v_{x,m}^*(x,y,t) = \frac{k_{x,m}^*}{\rho_0\omega} C_m^* \psi_m^*(y) e^{-\mathrm{j}\omega t + \mathrm{j}k_{x,m}^* x}, \tag{3.35}$$

where the superscript "$*$" indicates the complex conjugate. We can now write the expressions for I_m and E_m appearing in the definition of the group velocity.

$$\begin{aligned} I_m =& \mathrm{Re}\Big(e^{-\mathrm{j}(k_{x,m} - k_{x,m}^*)x} \frac{k_{x,m}^*}{\rho_0\omega}\Big) C_m^2 \int_0^h |\psi_m(y)|^2 dy = \\ =& e^{2\mathrm{Im}\{k_{x,m}\}x} \frac{\mathrm{Re}\{k_{x,m}\}}{\rho_0\omega} C_m^2 \int_0^h |\psi_m(y)|^2 dy = \end{aligned} \tag{3.36}$$

$$E_m = e^{2\mathrm{Im}\{k_{x,m}\}x} \frac{|k_{x,m}|^2}{\rho_0 \omega^2} C_m^2 \int_0^h |\psi_m(y)|^2 dy \tag{3.37}$$

And finally:

$$c_{g,m} = \frac{I_m}{E_m} = \frac{\mathrm{Re}\{k_{x,m}\}\omega}{|k_{x,m}|^2} \tag{3.38}$$

Since the sign of $c_{g,m}$ depends only on $\mathrm{Re}\{k_{x,m}\}$, a $\mathrm{Re}\{k_{x,m}\} > 0$ means a $+x$ sense of propagation, and $\mathrm{Im}\{k_{x,m}\} < 0$ means an attenuation of the duct mode amplitude along its propagation.

Here we report and discuss the solution of the duct mode problem in case of the boundary advection law as B.C., in which the purely locally reacting liner is a special case (for $c_a = 0$). The duct-modes eigenvalue problem writes:

$$\begin{aligned} &\nabla_\perp^2 \psi_m(y) - (k_0^2 - k_{x,m}^2)\psi_m(y) = 0 \quad \text{for} \quad \mathrm{y} \in \mathcal{A} \\ &\vec{n} \cdot \vec{\nabla} \psi_m(y) = -\mathrm{j}\eta_{Loc} \left(k_0 - \frac{c_a}{c_0} k_{x,m} \right) \psi_m(y) \quad \text{for} \quad \mathrm{y} \in \partial\mathcal{A}. \end{aligned} \tag{3.39}$$

Notice the non-standard character of such eigenvalue problem, where the eigenvalue appears in the B.C. as well. Solutions for such eigenvalue problem have been found by Finite Elements (FE) in COMSOL where the presence of an eigenvalue-dependent B.C. has been enforced directly in the weak-formulation, by a so-called "weak-contribution". The weak formulation of the eigenvalue problem of Eq.s (3.39) is reported in Eq.s (3.40) following the steps of integration by parts (application of Green formula) 3.40b till the final expression 3.40c with the assimilation of the B.C..

$$\int_{\mathcal{A}} \hat{\psi} \nabla_\perp^2 \psi_m \, dydz + (k_0^2 - k_{x,m}^2) \int_{\mathcal{A}} \hat{\psi} \psi_m \, dydz = 0 \tag{3.40a}$$

$$\int_{\partial\mathcal{A}} \hat{\psi} \partial_n \psi_m \, dydz - \int_{\mathcal{A}} \vec{\nabla}_\perp \hat{\psi} \cdot \vec{\nabla}_\perp \psi_m \, dydz + (k_0^2 - k_{x,m}^2) \int_{\mathcal{A}} \hat{\psi} \psi_m \, dydz = 0 \tag{3.40b}$$

$$-\mathrm{j}\eta_{Loc} \left(k_0 - \frac{c_a}{c_0} k_{x,m} \right) \int_{\partial\mathcal{A}} \hat{\psi} \psi_m \, dydz - \int_{\mathcal{A}} \vec{\nabla}_\perp \hat{\psi} \cdot \vec{\nabla}_\perp \psi_m \, dydz + (k_0^2 - k_{x,m}^2) \int_{\mathcal{A}} \hat{\psi} \psi_m \, dydz = 0 \tag{3.40c}$$

The "weak contribution" is the first term on the lhs of Eq. 3.40c.

The duct modes solutions discussed here are for a 2D (x,y) waveguide with cross section width $h = 0.05$ m, hence with a cut-on frequency of higher-order duct modes in case of rigid boundaries $f_{cut-on} = c_0/2h = 3430$ Hz. The upper and lower boundaries of the duct are lined. First, the solutions relative to a purely resistive boundary, with $\eta_{Loc} = 1$ (and $c_a = 0$) are displayed in Figures 3.13. In Figure 3.13a the dispersion plots of the first four duct modes are shown, while in 3.13b the wavenumbers are plotted in the complex plane. Figure 3.14 shows the corresponding mode shapes. Such solutions relative to a locally-reacting (in this

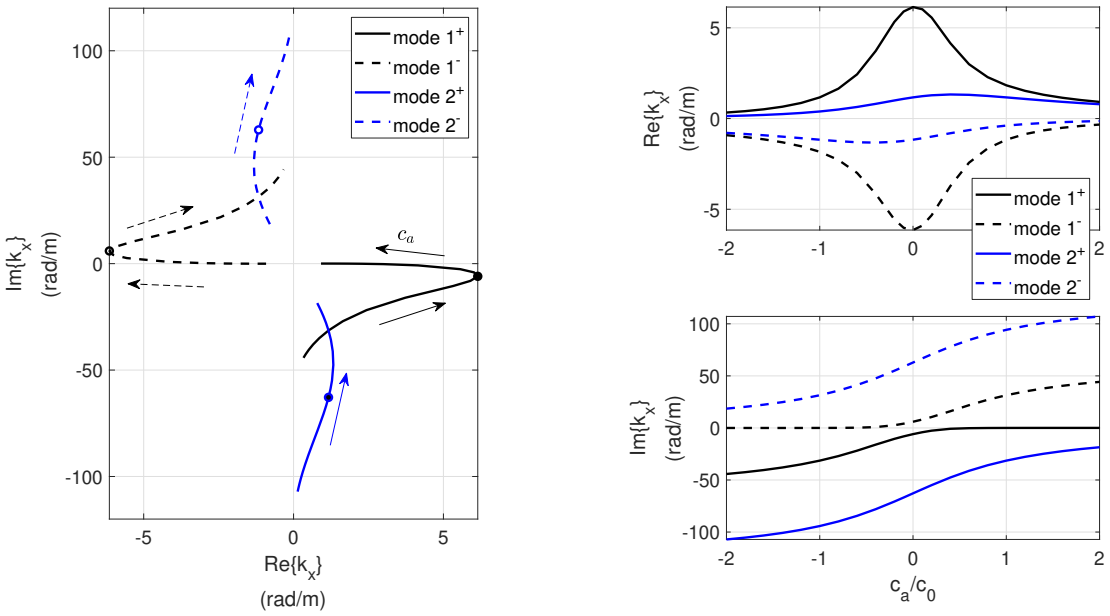

(a) (b)

Figure 3.17: Complex plane plot **(a)** of the first two positive and negative propagating modes, with varying c_a/c_0 from -2 to 2, at $f = 100$ Hz. The values for $c_a = 0$ are identified with "o" symbols. In **(b)** the $\mathrm{Re}\{k_x\}$ and $\mathrm{Im}\{k_x\}$ are plotted versus c_a/c_0 for $f = 100$ Hz.

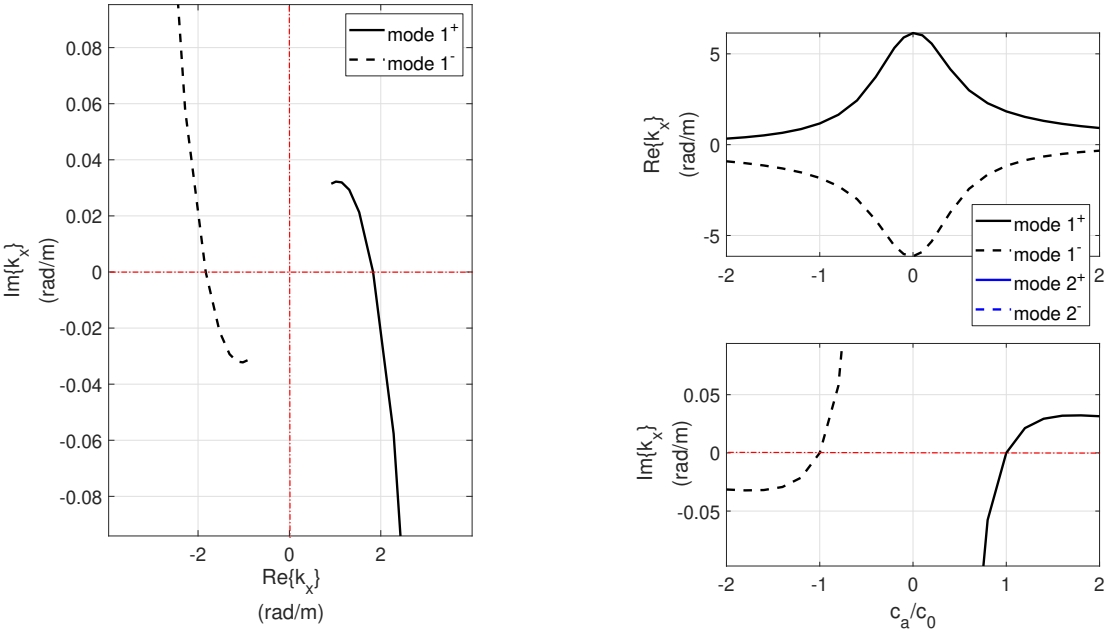

(a) (b)

Figure 3.18: Zoom of complex plane plot **(a)** of the first positive and negative propagating modes, with varying c_a around ± 1, at $f = 100$ Hz. In **(b)** the $\mathrm{Re}\{k_x\}$ and $\mathrm{Im}\{k_x\}$ are plotted versus c_a/c_0 for $f = 100$ Hz, with zoom of the $\mathrm{Im}\{k_x\}$ around the zero axis.

case purely resistive) liner will be used as basis for comparison with the case of advective B.C.s.

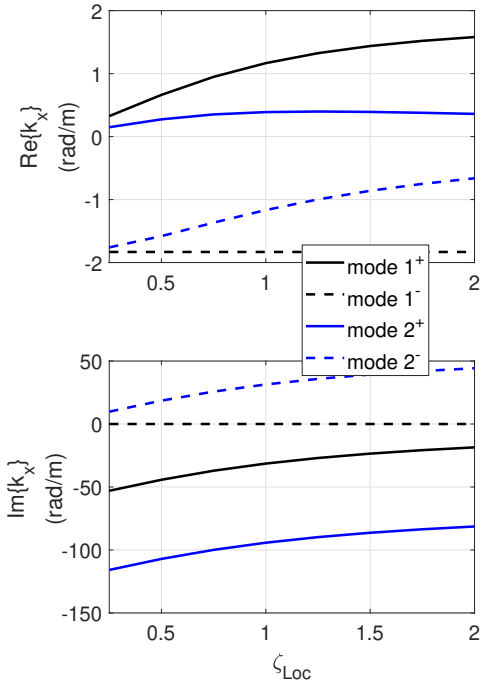

(a)

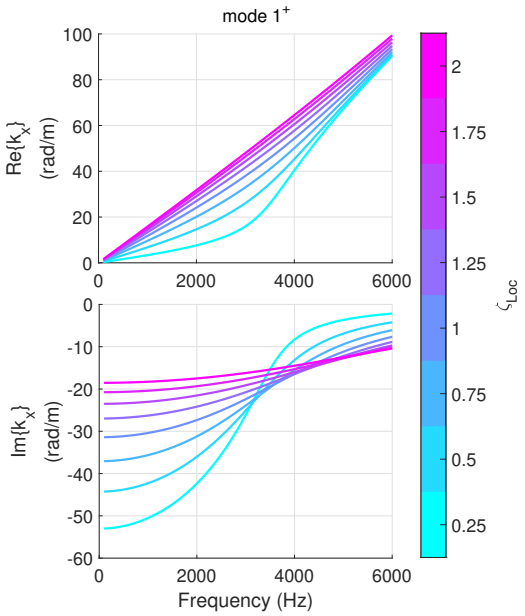

(b)

Figure 3.19: In **(a)** the $\mathrm{Re}\{k_x\}$ and $\mathrm{Im}\{k_x\}$ of the first two positive and negative propagating modes at $f = 100$ Hz, are plotted versus ζ_{Loc} from $\zeta_{Loc} = 0.25$ to $\zeta_{Loc} = 2$. In **(b)** the $\mathrm{Re}\{k_x\}$ and $\mathrm{Im}\{k_x\}$ of the first positive propagating mode, is plotted versus the frequency, for various ζ_{Loc} from $\zeta_{Loc} = 0.25$ to $\zeta_{Loc} = 2$. In both **(a)** and **(b)** a boundary advection law is considered, with $c_a = -c_0$ and purely resistive ζ_{Loc}.

The case of advection law, with $\eta_{Loc} = 1$ and $c_a = -c_0$, applied on both boundaries of the acoustic waveguide, is illustrated in Figures 3.15. It is evident a plane wave mode solution (mode 1^-) propagating toward $-x$. Indeed, both sides of the boundary advection law Eq. 3.9 are identically equal to zero for a plane mode propagating toward $\mathrm{sign}(c_a)x$. *The reciprocity of the system is broken* and the mode shapes are not the same if propagating toward $+x$ or $-x$.

Let us now investigate the variation of the duct modes solutions with respect to the advection speed c_a. In Figure 3.17a the wavenumber solutions of the first and second duct modes propagating in both senses are plotted in the complex plane for c_a varying from $-2c_0$ to $+2c_0$. In Figure 3.17b the real and imaginary parts of k_x are plotted separately versus c_a/c_0. Zooming around $\mathrm{Im}\{k_x\} = 0$ gives Figure 3.18, showing how the first duct mode propagating toward $+x$ becomes unstable for $c_a > c_0$, while the first duct mode propagating toward $-x$ becomes unstable for $c_a < -c_0$. This is so, because $\mathrm{Im}\{k_x\}$ assumes the same sign as $\mathrm{Re}\{k_x\}$ when $|c_a| > c_0$, meaning amplification of the mode along its sense of propagation.
Hence, the duct modes analysis confirms the result on passivity of Section 3.1.1, i.e. *the boundary advection law is non passive if* $|c_a| > 1$.
Notice also that increasing the boundary advection speed c_a produces higher $\mathrm{Im}\{k_x\}$. Looking at the mode 1^+ in Figure 3.17, for negative values of c_a, a higher $|c_a|$ brings about higher attenuations, that is the $\mathrm{Im}\{k_x\}$ is negative and augments in absolute value. Since for $|c_a| > c_0$ either mode 1^+ (for $c_a > 0$) or 1^- (for $c_a < 0$) becomes unstable, we deduce the maximum

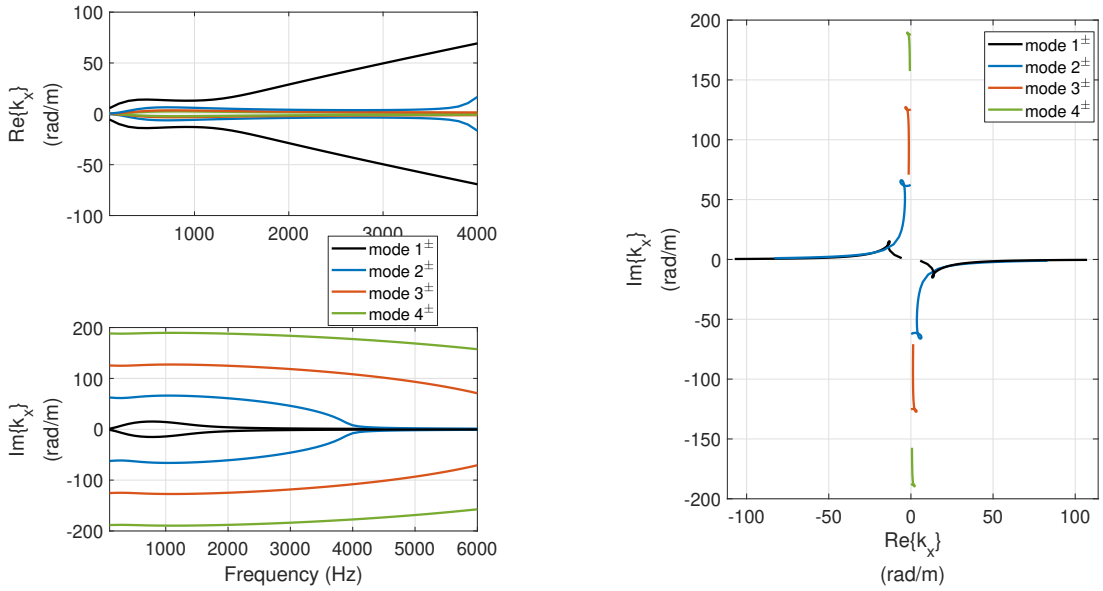

(a) (b)

Figure 3.20: Dispersion plots relative to the first four duct modes propagating in both senses, in case of locally reacting boundary with complex impedance ζ_{Loc} of Eq. (3.41), with $\mu_M = \mu_K = 0.2$ and $R_{at} = \rho_0 c_0$.

attenuation of the least attenuated mode is achieved when c_a is equal to $-c_0$ or $+c_0$, for positive or negative propagation respectively.
After having analysed the effect of the boundary advection speed, let us now check the influence of the local resistive impedance $\zeta_{Loc} = R_{at}/\rho_0 c_0$. Figure 3.19a shows the evolution of the first two least attenuated modes propagating toward $+x$ and $-x$, for $c_a = -c_0$ and varying the resistive ζ_{Loc}. Figure 3.19a shows that the negative propagating plane mode 1^- is not affected by the variation of ζ_{Loc}. Both Figures 3.19a and 3.19b show that lower values of ζ_{Loc} brings greater attenuation at lower frequencies for mode 1^+. Such tendency is inverted at higher frequencies. We bring the attention over the mode 1^+ as it is the least attenuated one for positive sense of propagation, therefore decisive for the transmission loss (TL) performance below f_{cut-on}. From these figures, we conclude that low ζ_{Loc} and a $c_a = -c_0$ leads to significant attenuation of the least attenuated mode propagating toward $+x$.

The results just assessed by the duct mode analysis, in case of purely real ζ_{Loc}, are summarized below:

1. An advection speed $c_a \neq 0$ introduces an asymmetrical propagation between forward and backward propagating modes.

2. For $c_a = -c_0$, duct mode 1^+ is highly attenuated, while mode 1^- is a plane wave. Hence *the acoustical reciprocity is strongly broken* for $f < f_{cut-on}$. Also higher forward-propagating duct modes present larger attenuation than the backward propagating ones, assuring non-reciprocal propagation also for $f \geq f_{cut-on}$. The contrary happens for $c_a = c_0$ (forward duct modes less attenuated than backward duct modes).

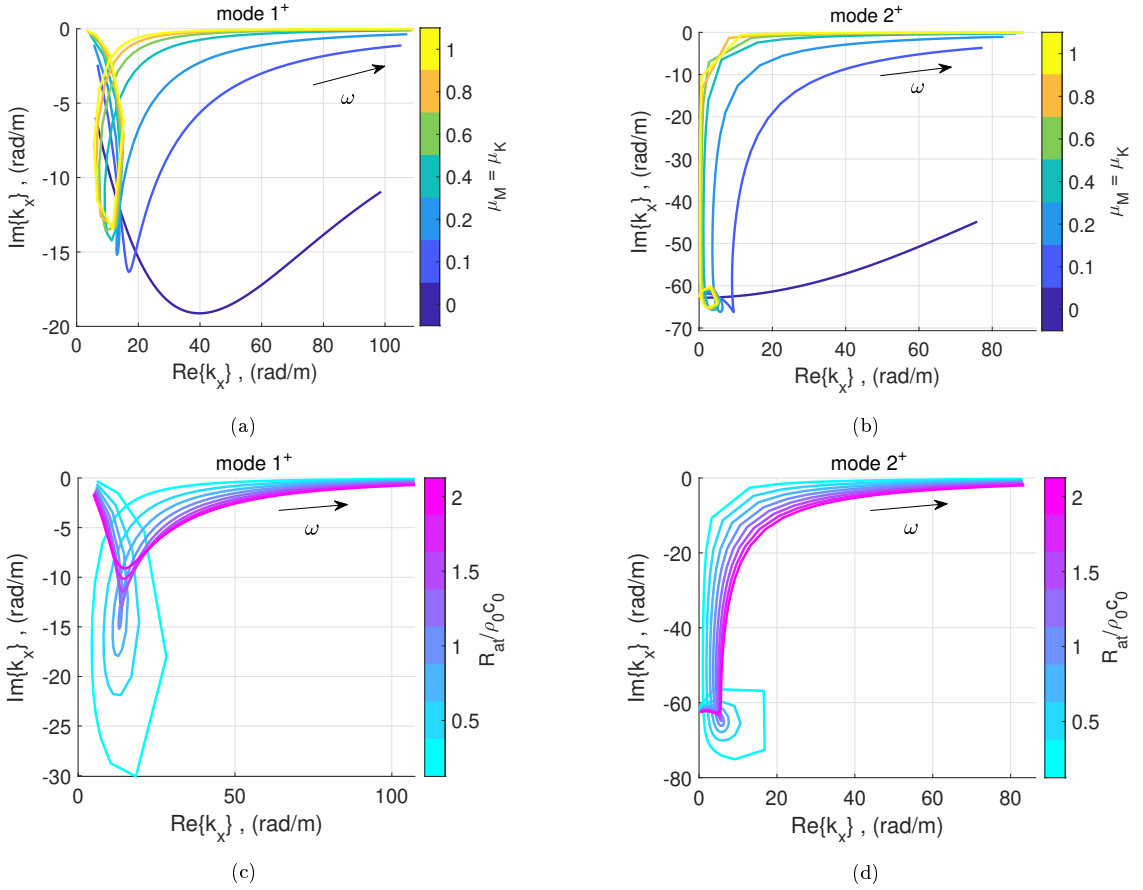

Figure 3.21: Dispersion plots in complex plane, relative to the first two duct modes, in case of complex boundary impedance $\zeta_{Loc}(\mathrm{j}\omega)$ of Eq. (3.41), with $\mu_M = \mu_K = 0.2$ and R_{at} varying from $0.25\rho_0 c_0$ to $2\rho_0 c_0$.

3. Increasing $|c_a|$ augments the attenuation of modes propagating toward $-\mathrm{sign}(c_a)x$.

4. For $|c_a| > c_0$ mode $1^{\mathrm{sign}(c_a)}$ becomes unstable, as the $\mathrm{Im}\{k_x\}$ changes its sign and becomes concordant with $\mathrm{Re}\{k_x\}$. Hence, the highest forward attenuation achievable before duct-mode instability is obtained for $c_a = -c_0$.

5. Reducing ζ_{Loc} also increases attenuation at low frequencies, up to f_{cut-on} approximately.

Unfortunately, a purely real local impedance is not physically realisable. Hence, let us analyse the duct modes solutions for a complex ζ_{Loc} which has the classical shape of a SDOF resonator, to maintain consistency with Section 2.1. With such a scope, the mass and stiffness reactive parts of ζ_{Loc} will be taken as proportional to the acoustic mass and stiffness of the EA in open circuit, as presented in Section 2.1. Keeping the same formalism then:

$$\zeta_{Loc}(\mathrm{j}\omega) = \frac{1}{\rho_0 c_0}\left(M_{at}\mathrm{j}\omega + R_{at} + \frac{K_{at}}{\mathrm{j}\omega}\right), \tag{3.41}$$

where $M_{at} = \mu_M M_{a0}$ and $K_{at} = \mu_K K_{a0}$ as in Section 2.1.
Following the same procedure of analysis as above, let us start with the duct modes solutions in case of locally-reacting boundary, i.e. for $c_a = 0$, but this time with the complex $\zeta_{Loc}(\mathrm{j}\omega)$

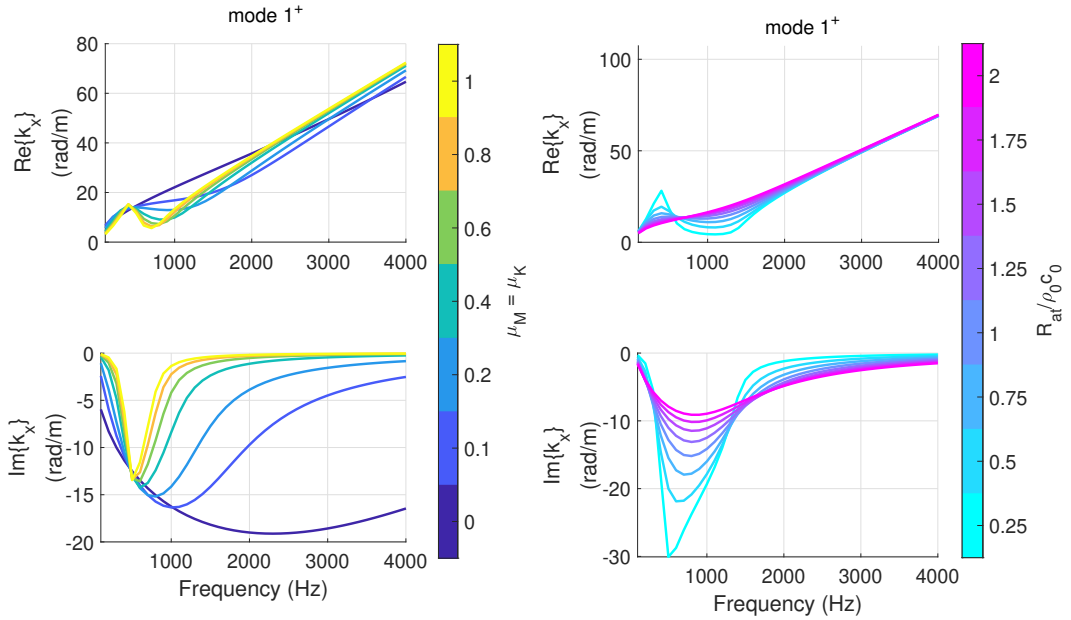

(a) (b)

Figure 3.22: Plot of $k_x(\omega)$ in its real and imaginary part, of the mode $1a$ relative to complex locally reacting boundaries, with $R_{at} = \rho_0 c_0$ and varying $\mu_M = \mu_K = 0.2$ (a), or with $\mu_M = \mu_K = 0.2$ and varying R_{at} (b).

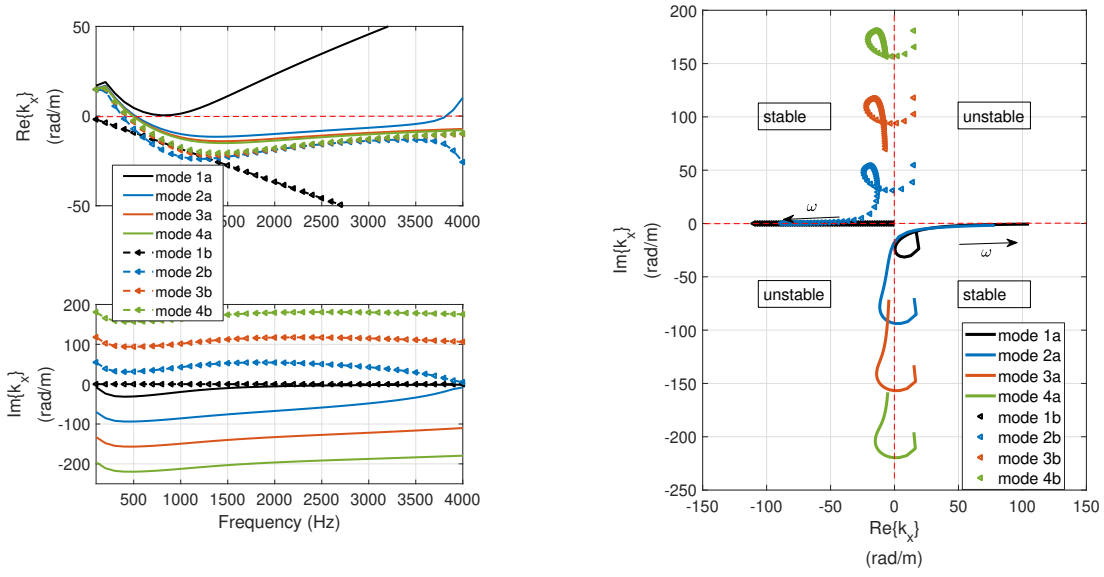

(a) (b)

Figure 3.23: Dispersion plots relative to the first eight duct modes in case of advection boundary law Eq. (3.9), with complex local SDOF impedance $\zeta_{Loc}(\mathrm{j}\omega)$ of Eq. (3.41), with $\mu_M = \mu_K = 0.2$ and $R_{at} = \rho_0 c_0$, and with $c_a = -c_0$.

of Eq. (3.41). Figures 3.20 show the dispersion plots relative to the case of $R_{at} = \rho_0 c_0$ and $\mu_K = \mu_M = 0.2$. In Figures 3.21a, 3.21b the wavenumbers of the first two positive propagating duct modes (the other two propagating toward $-x$ have specular plots with respect to the origin of the complex plane) are plotted with $R_{at} = \rho_0 c_0$, and varying $\mu_M = \mu_K$ from 0 to

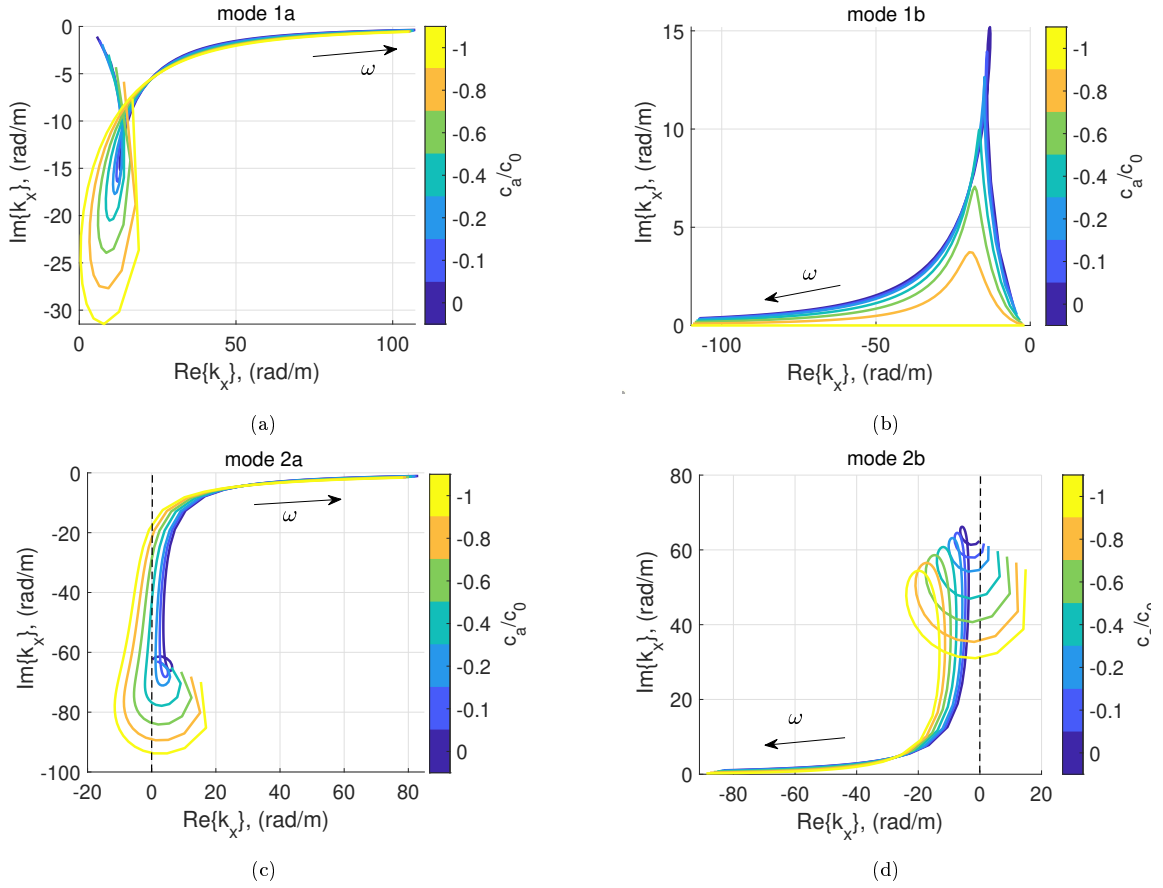

Figure 3.24: Dispersion plots in complex plane, relative to the first four duct modes, in case of boundary advection law of Eq. (3.9), with $R_{at} = \rho_0 c_0$, $\mu_M = \mu_K = 0.2$ and varying c_a from 0 to -1.

1. In Figures 3.21c and 3.21d the wavenumbers of the first two positive propagating duct modes are plotted with $\mu_M = \mu_K = 0.2$ and varying R_{at} from $\rho_0 c_0/4$ to $2\rho_0 c_0$. Figures 3.21 show that by increasing the reactive components with respect to the resistive one, the dissipation, given by $\mathrm{Im}\{k_x\}$, gets concentrated around the resonance of $\zeta_{Loc}(\mathrm{j}\omega)$ (about 500 Hz for $\mu_K = \mu_M$). Observe also that the maximum of $|\mathrm{Im}\{k_x\}|$ reduces, and the bell around resonance narrowed, for higher reactive as well as higher resistive components. Figure 3.22a displays the $\mathrm{Re}\{k_x\}$ and $\mathrm{Im}\{k_x\}$ for the first duct mode, in frequency, with varying $\mu_M = \mu_K$. This plot reveals how by increasing the reactive component (by making the resonance more evident), the pick of $\mathrm{Im}\{k_x\}$ moves toward lower frequencies (toward the resonance). Same plot, but by varying R_{at} is displayed in Figure 3.22b, making it clear that by reducing R_{at} higher attenuation is achieved around resonance.

Before, introducing an advection speed $c_a \neq 0$, let us resume the effects of each term of a SDOF in-series impedance on the duct modes:

1. Increasing the quality factor (augmenting the reactive with respective to the resistive components) of $\zeta_{Loc}(\mathrm{j}\omega)$, the attenuation of each duct mode gets concentrated around resonance.

2. Increasing $\mu_M = \mu_K$ and/or decreasing R_{at} reduces the pick value of attenuation for mode 1, and shifts it toward lower frequencies.

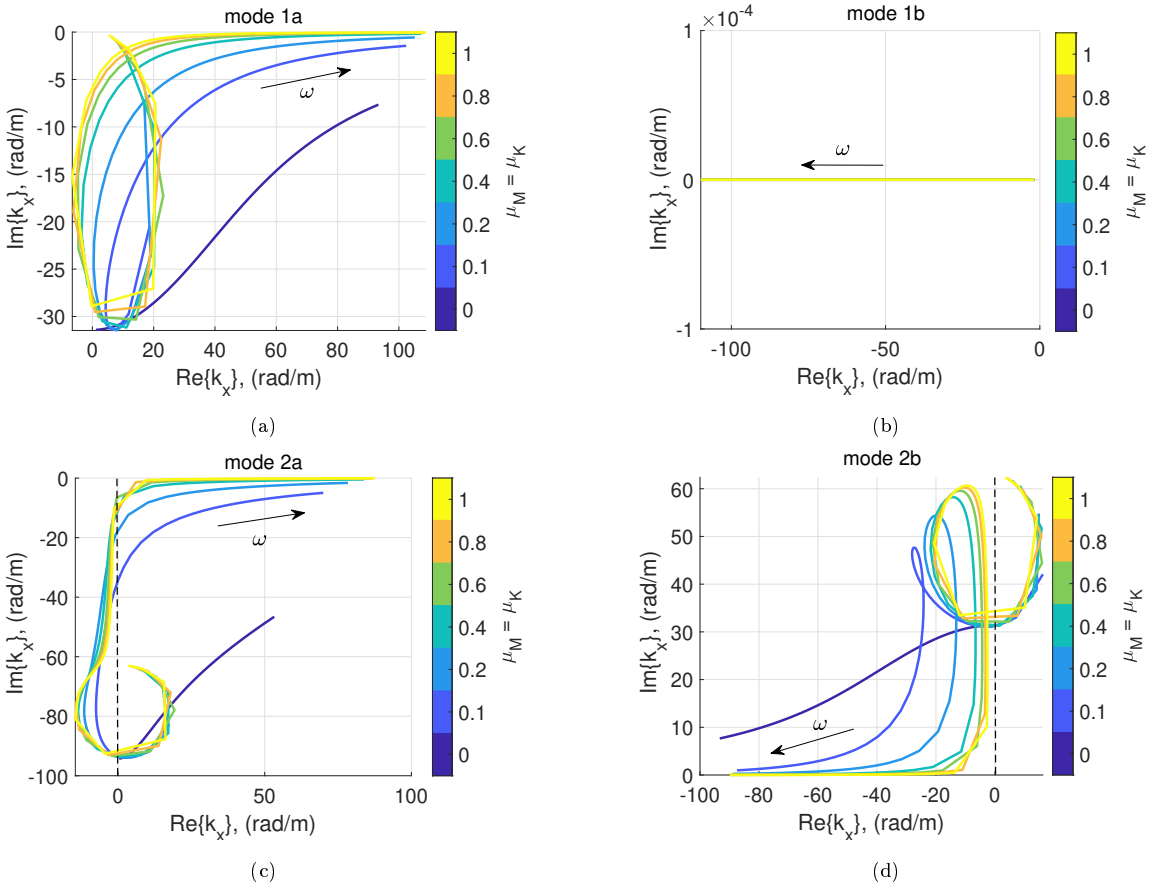

Figure 3.25: Dispersion plots in complex plane, relative to the first four duct modes, in case of boundary advection law of Eq. (3.9), with $R_{at} = \rho_0 c_0$, $c_a = -c_0$ and varying $\mu_M = \mu_K$ from 0 to 1.

Once the effect of each component of a locally reacting SDOF impedance on the dispersion of the first duct modes has been assessed, we can now investigate the case of boundaries lined with the advection law Eq. (3.9). Figures 3.23 shows the dispersion plots of $k_x(\omega)$ for $\mu_M = \mu_K = 0.2$ and $R_{at} = \rho_0 c_0$. The modes are not labelled referring to their sense of propagation (positive or negative) as the $\mathrm{Re}\{k_x\}$ happens to change its sign with frequency, while sign of $\mathrm{Im}\{k_x\}$ is unaltered. Mode 1b corresponds to the plane wave always present for $c_a = \pm c_0$, here propagating backward as $\mathrm{sign}(c_a) < 0$. Mode $1a$ is the first mode propagating toward $+x$. Nevertheless, the $\mathrm{Re}\{k_x\}$ of mode $1a$ approaches zero very closely just above resonance, prospecting a possible change of sign (and a reversed sense of propagation) for some parameter variation. We will see in the following that increasing the quality factor (reducing R_{at} or augmenting the reactive coefficients μ_M and μ_K) can make $k_{x,1a}$ to change its sign above resonance.

All other modes present a change of sign of $\mathrm{Re}\{k_x\}$ at a frequency around resonance. Either below or above such frequency, $\mathrm{Re}\{k_x\}$ and $\mathrm{Im}\{k_x\}$ present the same sign, which means unstable propagation in the present convention. Notice that such unstable behaviour was not displayed in case of boundary advection law with purely resistive ζ_{Loc} (i.e. for $\mu_M = \mu_K = 0$), neither was detected by the passivity discussion of Section 3.1.1. Indeed, in Section 3.1.1 the concept of passivity was presented for a boundary over a semi-infinite propagative domain. In case of a duct, the opposite wall can affect the stability of duct modes propagation if one, or

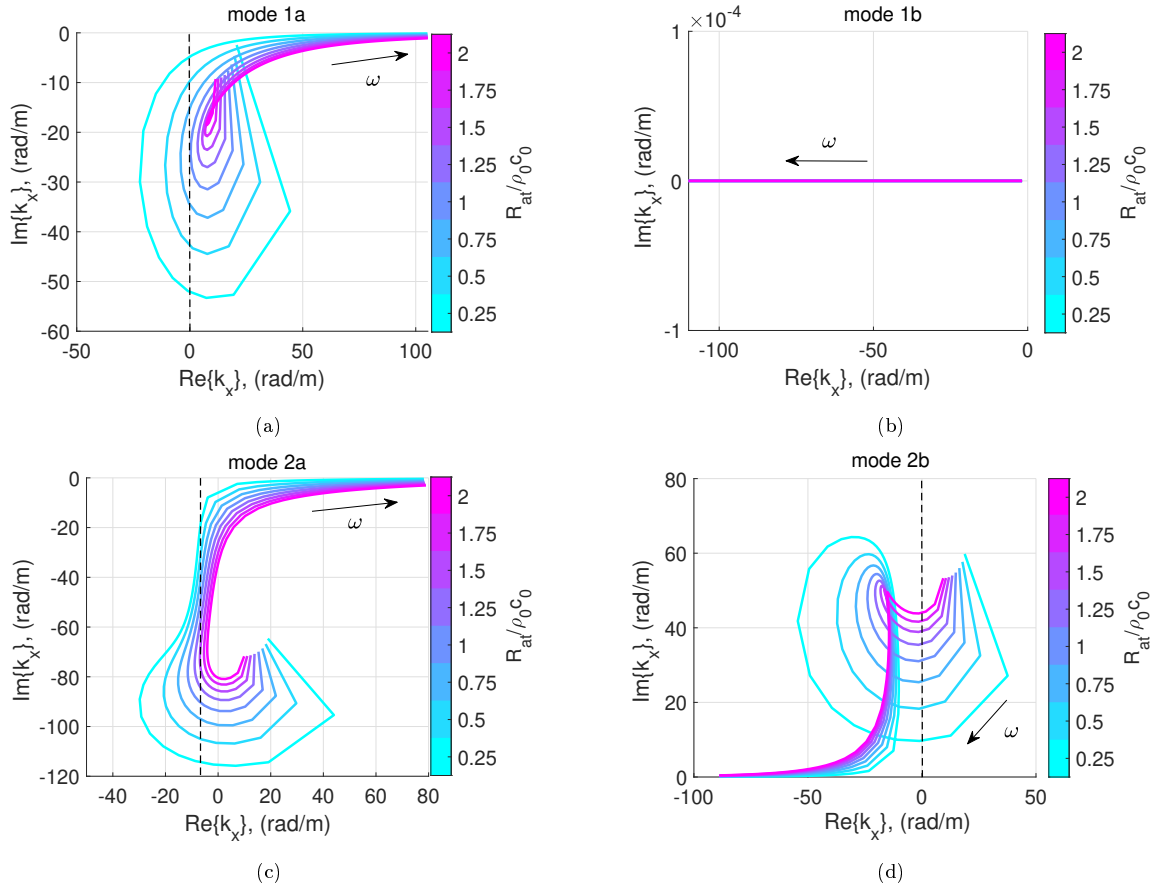

Figure 3.26: Dispersion plots in complex plane, relative to the first four duct modes, in case of boundary advection law of Eq. (3.9), with $\mu_M = \mu_K = 0.2$, $c_a = -c_0$ and R_{at} varying from $0.25\rho_0 c_0$ to $2\rho_0 c_0$.

both boundaries are treated with an advection law. Therefore, we expect such phenomenon to dwindle by reducing either the *reactive* or the *advective* character of the B.C., or by increasing the duct section width h.

In Figures 3.24 we report the dispersion plots in complex plane of the first four duct modes (1a, 1b, 2a, 2b), with $\mu_M = \mu_K = 0.2$, $R_{at} = \rho_0 c_0$ and varying advection speed c_a from 0 to $-c_0$. Mode $2a$ is unstable for a wide frequency range as both $\mathrm{Re}\{k_x\}$ and $\mathrm{Im}\{k_x\}$ are negative, meaning a duct mode propagating toward $-x$ with an increasing amplitude. Mode $2b$ instead, presents unstable propagation at lower frequencies where both $\mathrm{Re}\{k_x\}$ and $\mathrm{Im}\{k_x\}$ are positive. Mode $1a$ does not show instability but for $c_a = -c_0$, $\mathrm{Re}\{k_x\}$ becomes zero at a certain frequency, suggesting that either by increasing $|c_a|$ or the reactive components of $\zeta_{Loc}(\mathrm{j}\omega)$ will lead to instability.

Figures 3.25 and 3.26 show the effect of varying $\mu_K = \mu_M$ and R_{at} respectively, on the dispersion plots of the first four modes. Nominal values of $\mu_K = \mu_M$ and R_{at} are, as usual, set to 0.2 and $\rho_0 c_0$ respectively. Mode 1b is not affected by the variation of either the reactive or the resistive components of $\zeta_{Loc}(\mathrm{j}\omega)$ as expected. Increasing the quality factor of $\zeta_{Loc}(\mathrm{j}\omega)$, i.e. augmenting $\mu_K = \mu_M$ and/or reducing R_{at}, enhances the dissipation at resonance but pushes $\mathrm{Re}\{k_x\}$ toward negative values, therefore possibly causing unstable propagation for

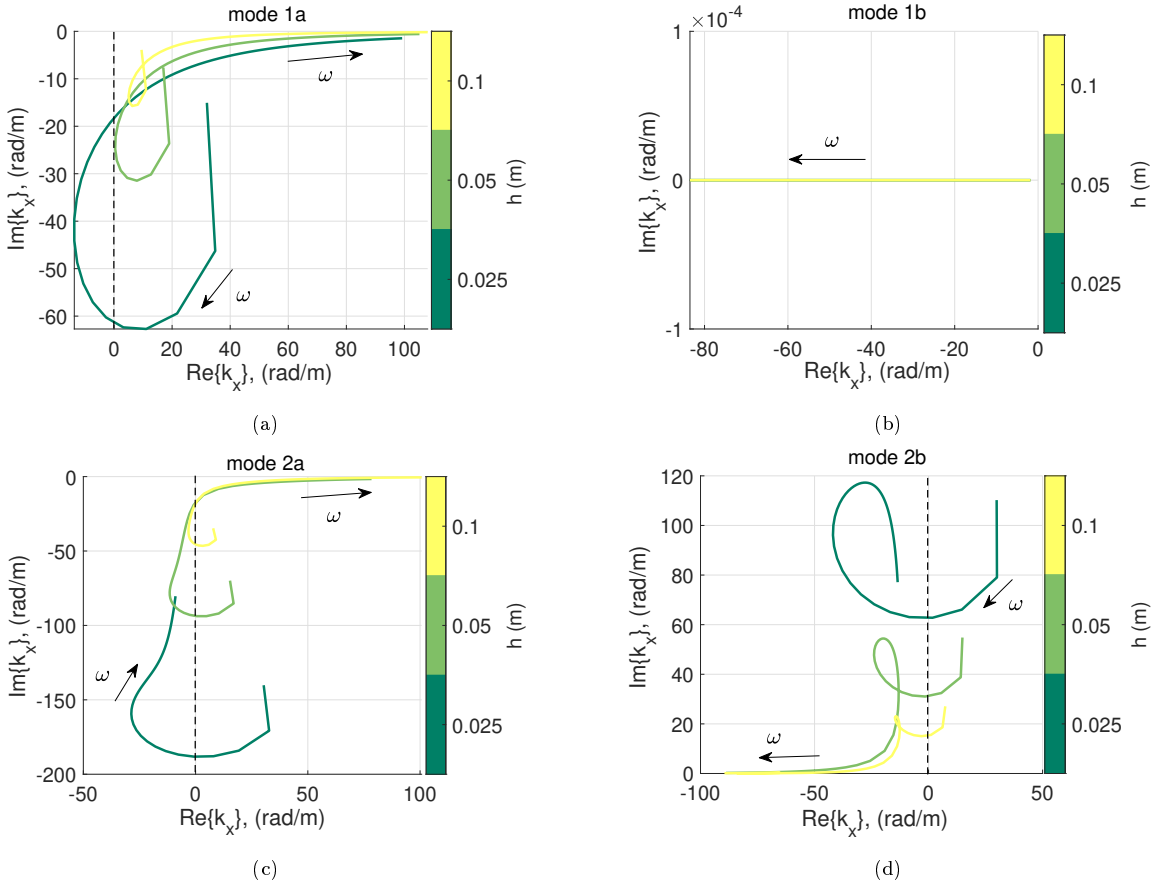

Figure 3.27: Dispersion plots in complex plane, relative to the first four duct modes, in case of boundary advection law of Eq. (3.9), with $\mu_M = \mu_K = 0.2$, $R_{at} = \rho_0 c_0$ and $c_a = -c_0$, with varying duct cross section width h from 0.025 to 0.1 m.

mode 1a. A similar effect is on modes 2a and 2b which comes back to the stable condition (Re$\{k_x\}$ and Im$\{k_x\}$ with opposite signs) for sufficiently low values of the reactance and/or sufficiently high values of the resistance in $\zeta_{Loc}(\mathrm{j}\omega)$.

Figure 3.27 shows the effect of varying the duct width h on modes 1a, 1b, 2a and 2b. As expected, larger cross sections reduces the unstable character of mode 1a around resonance, and of modes 2a and 2b at low frequencies, while mode 1b looks unaffected. In Figures 3.28a, 3.28b, 3.28c and 3.28d, we focus on the dispersion curves in frequency, of mode 1a. Figure 3.28a confirms that for $c_a = -c_0$ the Re$\{k_x\}$ is about to change its sign above resonance, while sign of Im$\{k_x\}$ is unaltered. Figures 3.28b and 3.28c demonstrate how increasing the quality factor can lead to unstable propagation around resonance. Finally, Figure 3.28d, certifies the role of the duct cross section width h on stability of the duct mode 1a, illustrating how instability withdraws for larger duct sections.

In order to fully understand the physical mechanism underlying such unstable propagation, deeper analyses are required, and for that scope, we believe that inspiration might be found in the discussion on duct modes instabilities in case of another type of convection: a mean flow in the duct [99], [100], [101], [16], [102]. An advection of the boundary reaction means a phase travelling along the wall. Each point of the advective boundary has therefore two contributions to its phase, one given by the local reaction and the other given by the travelling

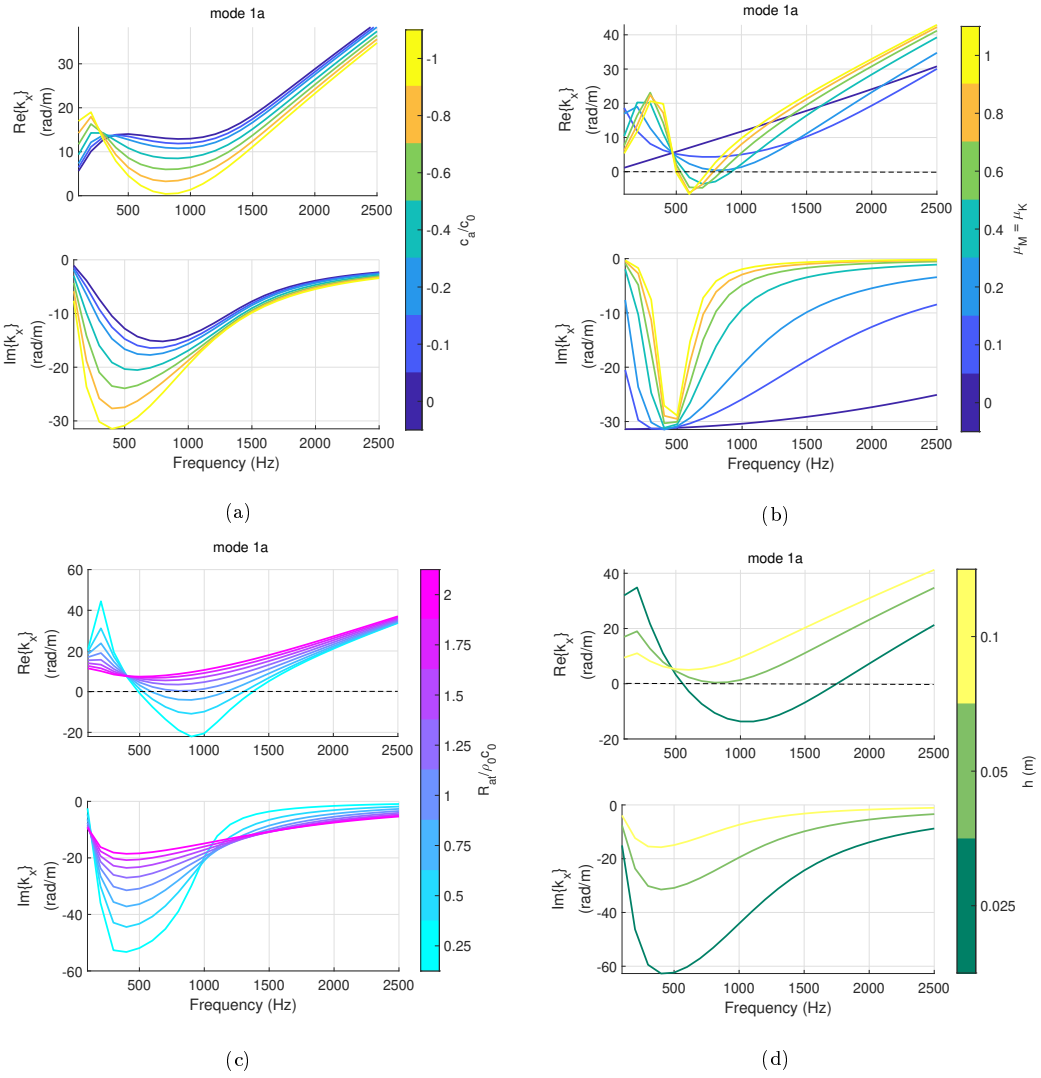

Figure 3.28: Plot of $k_x(\omega)$ in its real and imaginary part, of the mode $1a$ relative to boundaries lined with the advection B.C. Eq. (3.9), with **(a)** varying c_a, **(b)** varying $\mu_M = \mu_K$, **(c)** varying R_{at} and **(d)** varying the duct cross section width h. The nominal values are $\mu_M = \mu_K = 0.2$, $R_{at} = \rho_0 c_0$ and $c_a = -c_0$ and $h = 0.05$ m.

boundary wave. We are brought to imagine that the presence of a reflecting wall in front of a boundary advection law, the de-phasing introduced by a complex $\zeta_{Loc}(\mathrm{j}\omega)$, and a sufficiently high wall advection speed, can cause the amplification of the waves reflected from the facing wall to the advected boundary.

Let us resume the outcomes of the duct-modes simulation in case of complex $\zeta_{Loc}(\mathrm{j}\omega)$:

1. For non-zero reactive terms ($\mu_M \neq 0$ and/or $\mu_K \neq 0$) all duct modes can become unstable even for values of $|c_a| < c_0$, except mode $1b$ (plane wave propagating toward $\mathrm{sign}(c_a)x$). The duct-modes instability is related to a change of sign of the $\mathrm{Re}\{k_x\}$, i.e. a flip in the sense of propagation of the duct modes.

2. The duct modes, except mode 1b, propagating toward $\mathrm{sign}(c_a)x$ can be unstable at low frequencies (below resonance). Modes propagating toward $-\mathrm{sign}(c_a)x$ can be unstable above resonance.

3. Increasing the quality factor of $\zeta_{Loc}(\mathrm{j}\omega)$ enhances the duct-modes instability. For sufficiently low quality factors, the stability of duct mode 1a can be restored.

4. For sufficiently large duct cross section, the stability of duct mode 1a can be restored, highlighting the role of the finiteness of the transversal dimension of the acoustic domain (not taken into account in Section 3.1) in such instability phenomenon.

The reader is invited to look at Appendix G to verify the possibility to obtain the duct mode solutions for the first positive and negative propagating modes by a 1D reduced model. The interest of such 1D solutions is that they can be computed analytically, as the lined waveguide is treated as a medium with different propagation characteristics, analogously to the porous equivalent fluid models and the effective properties in periodic media.
The duct mode analysis carried out in this section will be very helpful in the interpretation of the scattering performances in a waveguide, which are presented in the following.

3.3 Scattering simulations in 2D waveguide

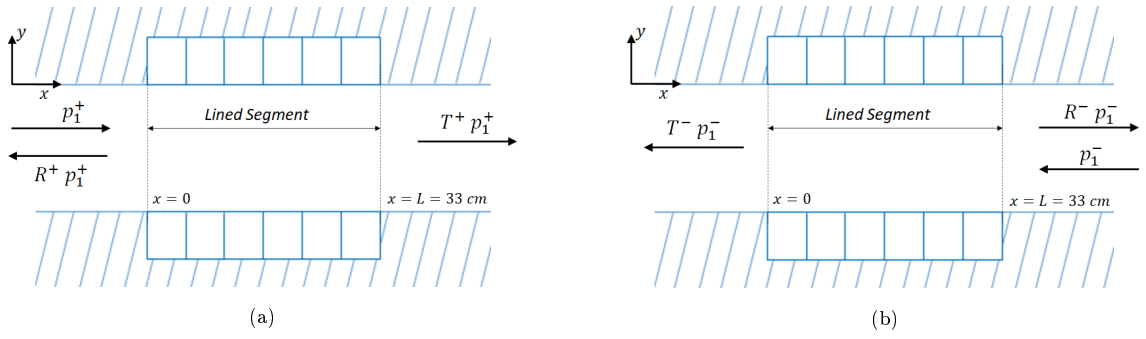

Figure 3.29: Lining segment and scattering coefficients definition in a 2D waveguide lined on both sides.

$$\begin{bmatrix} p_2^+ \\ p_1^- \end{bmatrix} = \begin{bmatrix} T^+ & R^- \\ R^+ & T^- \end{bmatrix} \begin{bmatrix} p_1^+ \\ p_2^- \end{bmatrix} \tag{3.42}$$

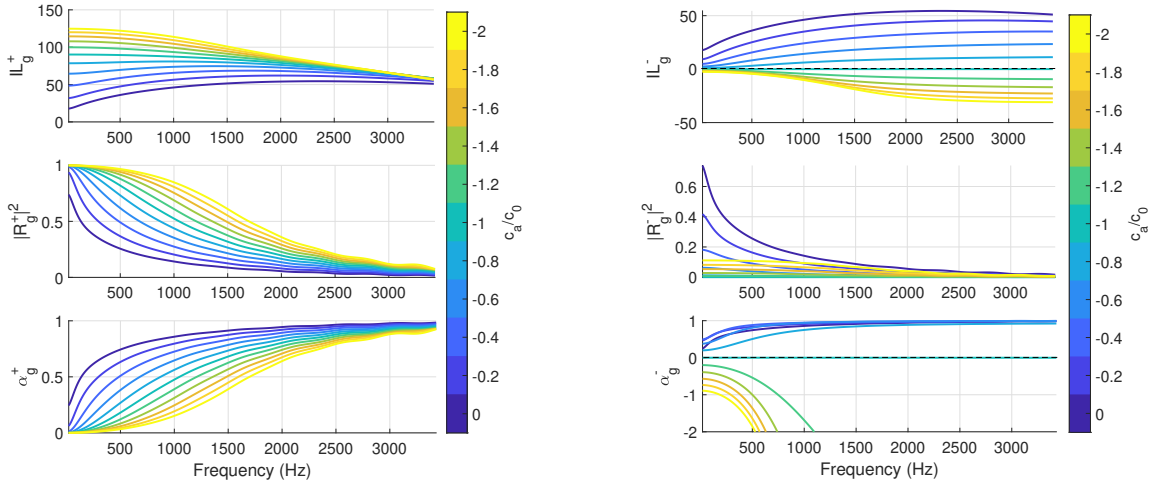

(a) (b)

Figure 3.30: Scattering performances in a 2D waveguide of cross section width $h = 0.05$ m with lined segment of length $L = 0.33$ m, lined on both sides by the boundary advection law with $\zeta_{Loc} = R_{at}/\rho_0 c_0$, and varying c_a.

In this section the boundary advection law of Eq. (3.9) is analysed in terms of the scattering performances in the plane wave regime, achieved by a lined segment of length 0.33 m in a 2D acoustic waveguide without flow, as illustrated in Figure 3.29. The lining B.C. is applied continuously on the boundary of the waveguide in the lined segment. The duct transversal dimension is $h = 0.05$ m as in the duct mode analysis of Section 3.2. Such dimensions correspond, approximately, to the experimental setup that will be presented in Section 3.5. The scattering matrix coefficients are defined in Figure 3.29 and Eq. (3.42) in the plane wave regime, which is the one treated here. The results have been obtained by FE simulations in COMSOL. The FE mesh has been built sufficiently fine to resolve frequencies up to f_{cut-on}, according to the criterion $d_{max} \approx \lambda_{cut-on}/10$, where d_{max} is the maximum element size in the mesh. The scattering problem has been outlined by defining so-called Plane Wave Radiation conditions at the inlet and outlet cross-sections of the duct, in order to reproduce anechoic terminations in the plane wave regime. Such B.C. also allows for defining incident pressure fields, without losing the anechoic character of the terminations. The scattering coefficients $T_g^{\pm}$ and $R_g^{\pm}$ have been retrieved by exciting either the left (+) or the right (−) termination. Reminding that, in the plane wave regime $p = p^+ + p^-$ and $v_x = (p^+ - p^-)/(\rho_0 c_0)$, by retrieving pressure p and velocity v_x on two cross sections, placed upstream and downstream the lined segment, sufficiently far from the treated area (in order for the evanescent waves to fully vanish), the amplitudes of sound pressure waves propagating toward $+x$ or $-x$ can be computed by the relationships:

$$p^{\pm} = \frac{p \pm \rho_0 c_0 v_x}{2}. \tag{3.43}$$

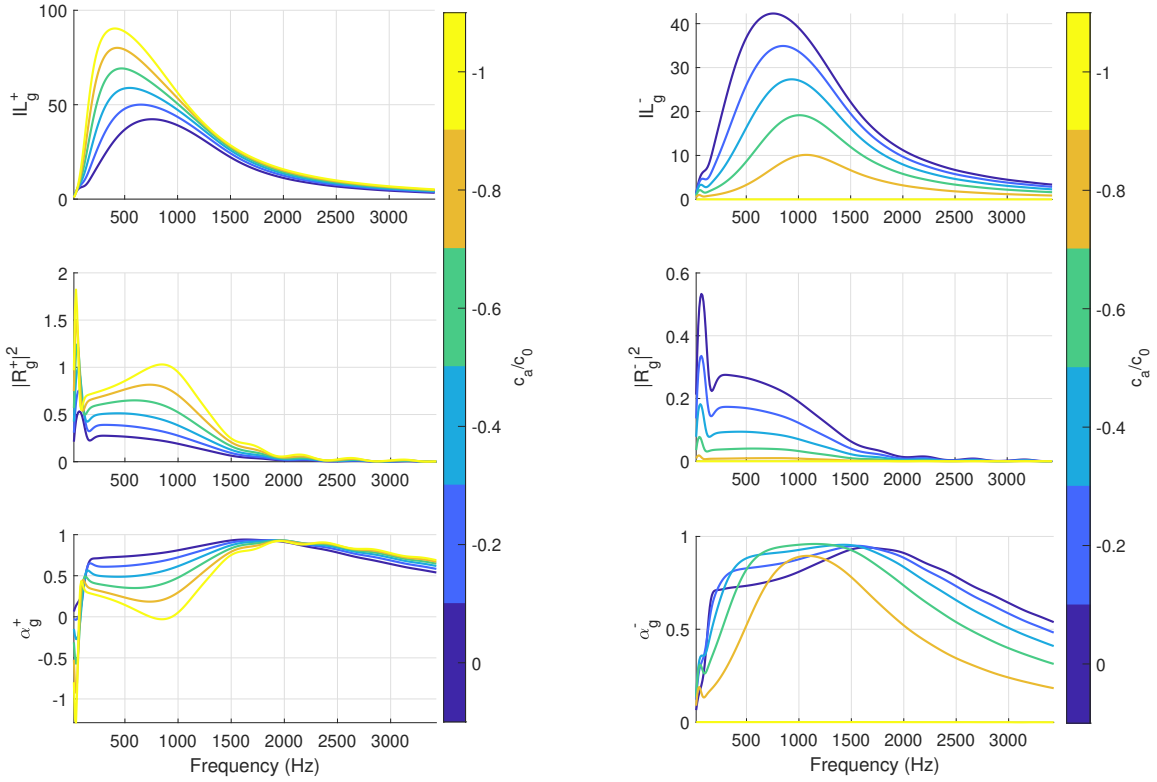

(a) (b)

Figure 3.31: Scattering coefficients in a 2D waveguide of cross section width $h = 0.05m$ with lined segment of length $L = 0.33$ m, lined on both sides by the boundary advection law with $\mu_M = \mu_K = 0.2$, $R_{at} = \rho_0 c_0$ and varying c_a.

The scattering coefficients are then obtained by exploiting the anechoic terminations assumption, thanks to which $T^{\pm} = p_2^{\pm}/p_1^{\pm}$ and $R^{\pm} = p_1^{\mp}/p_1^{\pm}$, where $p_1^{\pm}$ and $p_2^{\pm}$ are the sound pressure waves amplitudes at the upstream (superscript 1) and downstream (superscript 2) cross-sections.
As indicators of the reflective, absorptive and transmissive performances of the liner, we preferred to plot the transmission loss $TL_g^{\pm} = 10\log_{10}(1/|T^{\pm}|^2)$, the power reflection coefficient $|R_g^{\pm}|^2$ and the power absorption coefficient $\alpha_g^{\pm} = 1 - |R_g^{\pm}|^2 - |T^{\pm}|^2$ respectively, where the subscript g stays for "grazing incidence". The Insertion Loss ($IL_g^{\pm}$) gives the effect of inserting the liner with respect to the case of no boundary treatment, and is defined as the difference between the transmission losses evaluated before and after the boundary treatment, i.e. $IL_g^{\pm} = TL_g^{\pm}|_{after} - TL_g^{\pm}|_{before}$. As, in simulations, $TL_g^{\pm}|_{before} = 0$ because it corresponds to a perfectly rigid boundary, then $IL_g^{\pm} = TL_g^{\pm}|_{after}$.
The acoustical passivity in the scattering problem is assured as long as $\alpha_g^{\pm}(\omega) \geq 0$ at all frequencies.

As done in the previous sections, let us start with the case of ζ_{Loc} purely resistive. In Figure 3.30, the scattering performances are plotted with varying c_a from 0 to $-2c_0$ confirming the

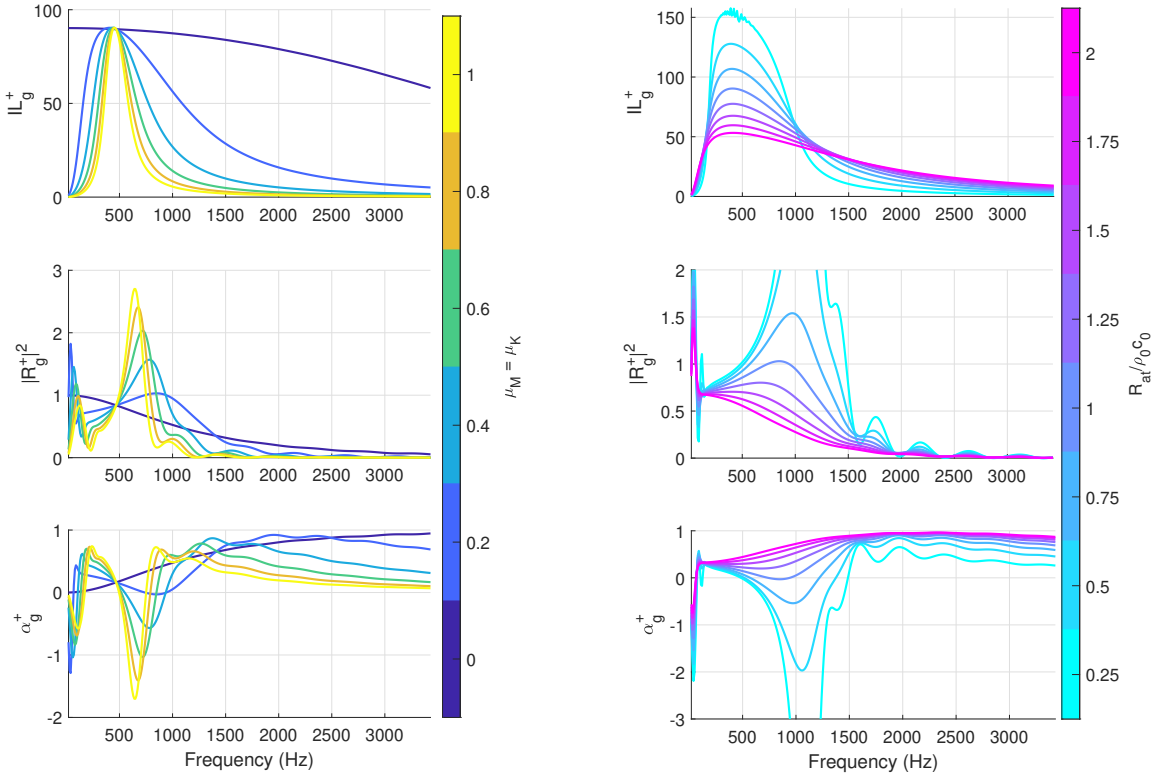

(a) (b)

Figure 3.32: Scattering coefficients in a 2D waveguide of cross section width $h = 0.05m$ with lined segment of length $L = 0.33$ m, lined on both sides by the boundary advection law with $c_a = -c_0$, **(a)** with varying $\mu_M = \mu_K$ and $R_{at} = \rho_0 c_0$, or **(b)** with $\mu_M = \mu_K = 0.2$ and varying R_{at}.

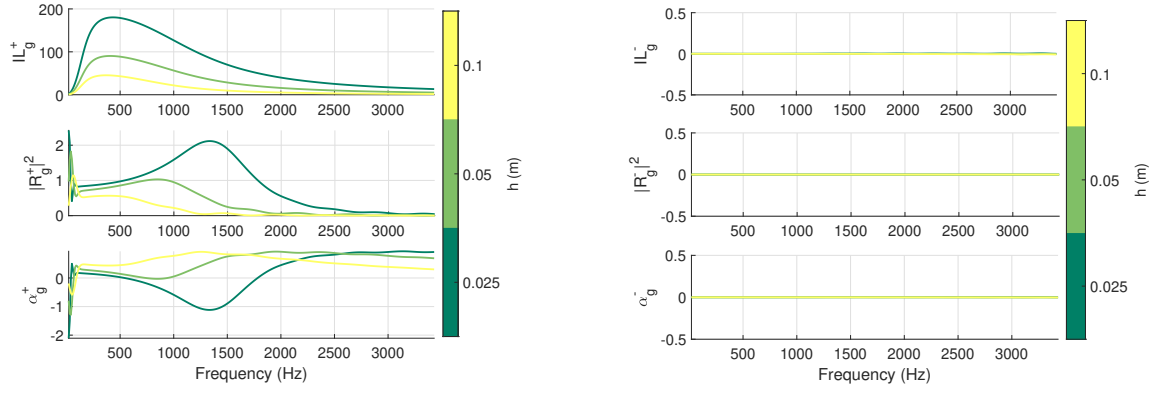

(a) (b)

Figure 3.33: Scattering coefficients in a 2D waveguide of variable cross section width h, lined segment of length $L = 0.33$ m, lined on both sides by the boundary advection law with $c_a = -c_0$, $R_{at} = \rho_0 c_0$ and $\mu_M = \mu_K = 0.2$.

results of previous sections about both passivity and non-reciprocal propagation. Looking at Figure 3.30a we remark that increasing $|c_a|$ leads to higher IL_g^+ due to a significant increase

of the reflection coefficient $|R_g^+|$, while the absorption α_g^+ is lowered. In Figure 3.30b, the "$-$" scattering confirms the perfect non-reciprocal propagation for $c_a = -c_0$, and the loss of acoustical passivity, already found in previous sections, for $|c_a| > c_0$. In Figure 3.31, same computations are carried out in case of a complex $\zeta_{Loc}(\mathrm{j}\omega)$ as in Eq. (3.41), for $\mu_M = \mu_K = 0.2$ and $R_{at} = \rho_0 c_0$. First thing catching the eye in Figure 3.31a is the negative value of α_g at very low frequencies, for values of $|c_a| \leq c_0$ and just above resonance for $c_a = c_0$. While the latter result was expected from the duct mode analysis of Section 3.2, the former was not. Indeed, we have verified in Section 3.2 that the presence of a reactive term in $\zeta_{Loc}(\mathrm{j}\omega)$ can cause unstable duct modes propagation even for $|c_a| \leq c_0$ around and beyond resonance. Nevertheless, the low-frequency non-passivity of the advection boundary law was predicted neither by the analytical formulation in semi-infinite domain (Section 3.1) nor by the duct mode analysis in an infinite duct. Hence we deduce that it might be linked to the abrupt change in the B.C. from the rigid to the advective boundary.
The advection B.C. features higher IL_g^+ due to a significant increase in backward reflection, respect to a locally-reacting boundary ($c_a = 0$). Figure 3.31b confirms the perfect non-reciprocal propagation for $c_a = -c_0$ even for complex $\zeta_{Loc}(\mathrm{j}\omega)$.
The effect of the variation of the reactive and resistive components of $\zeta_{Loc}(\mathrm{j}\omega)$ is described in Figures 3.32a and 3.32b respectively. Apart from the low-frequency unexpected loss of passivity, the impacts on acoustical passivity of both the resistive and reactive terms confirm the results of the duct mode analysis, specifically the one relative to the mode 1a (see Figure 3.28) as it is the one dominating the propagation in the lined segment for $f < f_{cut-on}$. While reducing the reactive terms leads to a larger bandwidth of efficient isolation (of high IL_g^+), reducing R_{at} increases the pick of reflection and of IL_g^+ as well, at the same time endangering the acoustical passivity around resonance.
Finally, in Figures 3.33 the duct width h is varied, confirming that a larger cross section, by reducing the impact of the lining treatment on the acoustic propagation, also dwindles the non-passive character around resonance (as was in the duct modes analysis), as well as the one at very low frequencies. The "$-$" propagation instead is not affected by cross section width and the non-reciprocal propagation is confirmed in the frequency bandwidth of efficient isolation achieved by the advection B.C., for $c_a = -c_0$.
Let us resume the main outcomes of the 2D scattering results for $f < f_{cut-on}$:

1. For a purely resistive ζ_{Loc} (for $\mu_M = \mu_K = 0$), the scattering performances are coherent with the duct modes analysis of Section 3.2.

2. *The non-reciprocal propagation is confirmed for* $|c_a| = c_0$, as perfect transmission happens in the $\mathrm{sign}(c_a)$ sense, while high isolation is achieved in the opposite sense.

3. The main effect of the advection speed c_a on isolation is a significant increase in the energy reflected backward ($|R_g^{\mathrm{sign}(c_a)}|^2$). The higher $|c_a|$ the bigger are both $|R_g^{\mathrm{sign}(c_a)}|^2$, and $IL_g^{\mathrm{sign}(c_a)}$, while $\alpha_g^{\mathrm{sign}(c_a)}$ is reduced.

4. For $|c_a| > c_0$, energy is injected in the waveguide as α_g becomes negative (loss of acoustical passivity of the advective B.C.).

5. For complex $\zeta_{Loc}(\mathrm{j}\omega)$ (for μ_M and μ_K non zero), acoustical passivity around resonance can be lost for a value of $|c_a|$ lower than c_0. This is featured by a value of $|R_g^{\mathrm{sign}(c_a)}|^2$

bigger than 1. This result is in agreement with the duct modes analyses, where mode $1^{-\text{sign}(c_a)}$ showed an unstable propagation for a value of $|c_a|$ beyond a threshold lower than c_0. Such phenomenon dwindles by reducing the quality factor of $\zeta_{Loc}(\mathrm{j}\omega)$ and/or by enlarging the duct cross-section width, in agreement with the duct mode analyses.

6. An additional unexpected loss of acoustical passivity happens at very low frequencies, which was unexpected by the duct mode analyses. Henceforth, This is probably due to the finiteness of the lined segment and the abrupt introduction of a convected boundary reaction, at the section of interface between the rigid and the advective B.C.. Such loss of acoustical passivity is related to an increase of $|R_g^{\text{sign}(c_a)}|^2$ beyond 1.

7. Even for complex $\zeta_{Loc}(\mathrm{j}\omega)$, the transmission in the $\text{sign}(c_a)$ direction is perfect in the plane wave regime for $|c_a| = c_0$, hence maintaining the strong non-reciprocal character.

Observe that also for the scattering performances, the 1D reduced model provides very satisfactory results (see Appendix G) which could be employed for fast predictions and liner design.
In the following section, a 3D waveguide is considered and the effect of B.C. discretization as well as time delay in the digital control implementation, are investigated.

3.4 Scattering simulations in 3D waveguide

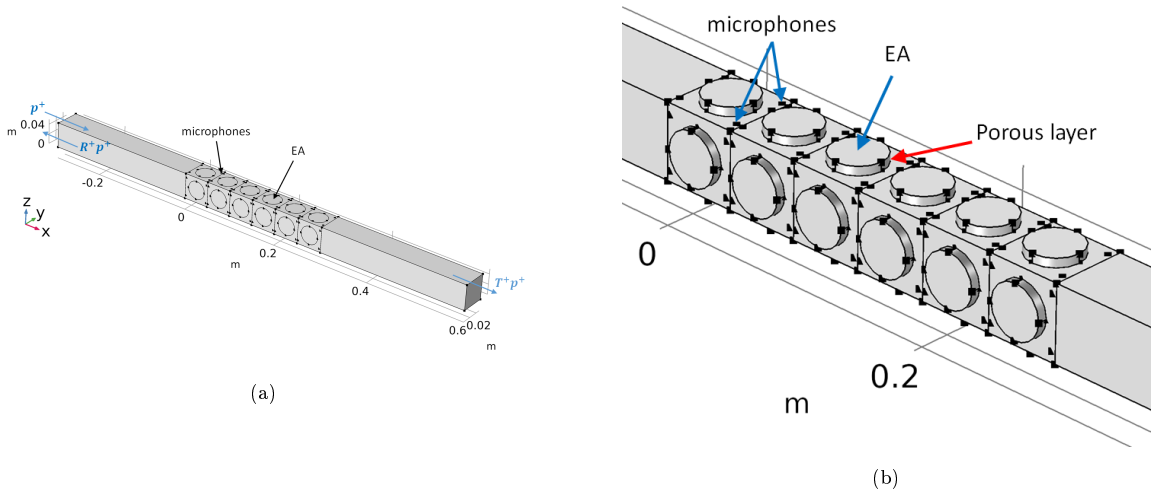

Figure 3.34: 3D geometry for scattering simulations, in case of EAs disks applied flush on the duct boundary **(a)**, and EAs disks placed behind a porous layer 6 mm **(b)**.

In this section we simulate the scattering performances in the plane wave regime of a 3D acoustic waveguide, of rectangular cross section, without flow. The boundary advection law is applied along each side of the duct for a length of 33 cm. In order to investigate the effect of implementing the B.C. by individual EAs lining the parietal walls of a rectangular cross section duct, as in the experimental test-rig of Section 3.5, the B.C. is applied on separate disks simulating the EAs (6 per each duct edge), as showed in Figure 3.34. Each speaker is

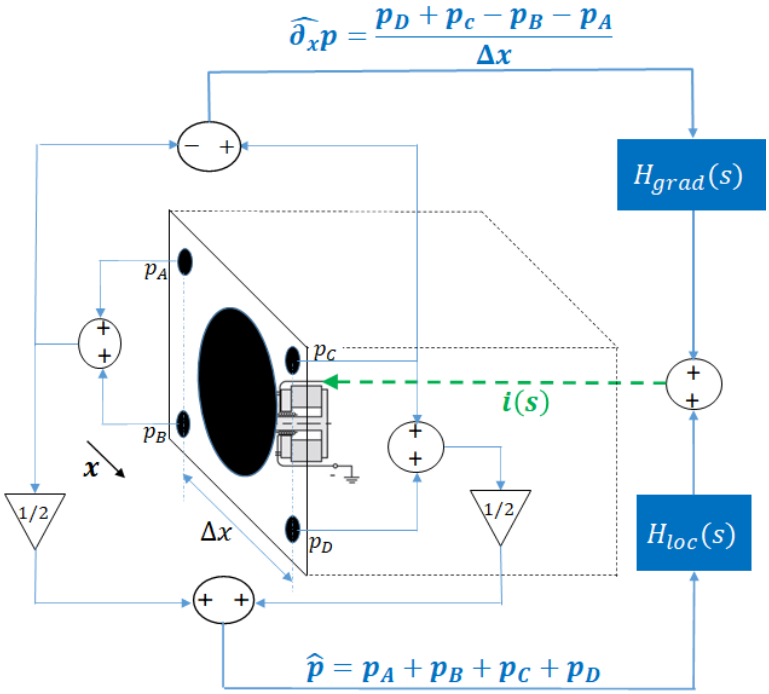

Figure 3.35: Sketch of the 4-microphones EA control, corresponding to Eq. (3.44).

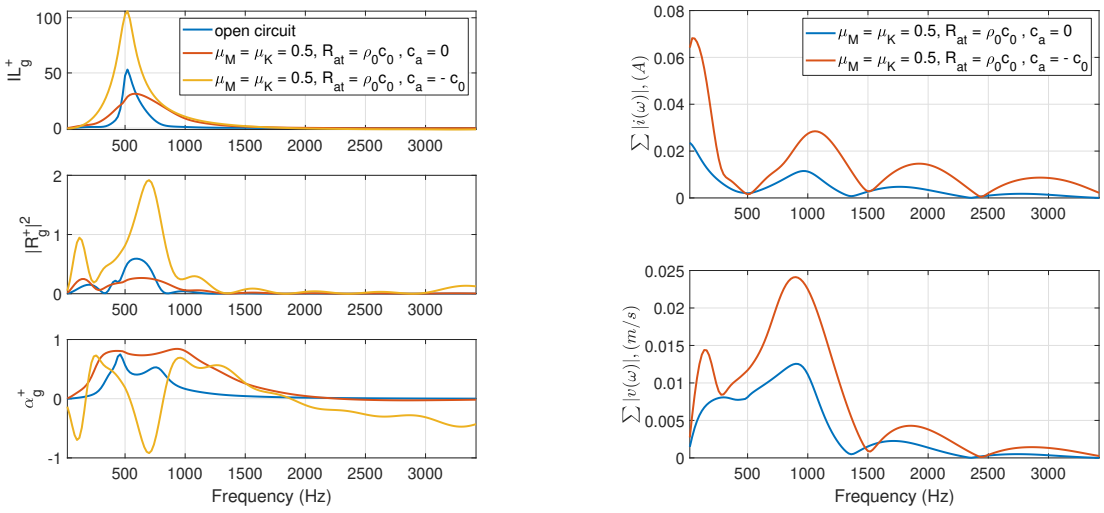

(a) (b)

Figure 3.36: **(a)**: scattering coefficients in a 3D waveguide of cross section width $h = 0.05$ m with open circuit EAs, Local ($\mu_M = \mu_K = 0.5$, $R_{at} = \rho_0 c_0$) and advective ($c_a = -c_0$) controls. **(b)**: sum of electrical current modulus spectra of all EAs $\sum |i(\omega)|$ (up), and sum of velocity modulus spectra on all EAs $\sum |v(\omega)|$ (bottom), in case of Local and Advective controls.

considered as a rigid piston, according to its SDOF model of Eq. (2.2). The advection B.C. is implemented through the electrical current $i(s)$ as in Eq. (3.44):

$$i(s) = H_{loc}(s)\hat{p}(s) + H_{grad}(s)\hat{\partial}_x p(s), \tag{3.44}$$

where $\hat{p}(s)$ and $\hat{\partial}_x p(s)$ are the local pressure and its x-derivative on each speaker diaphragm,

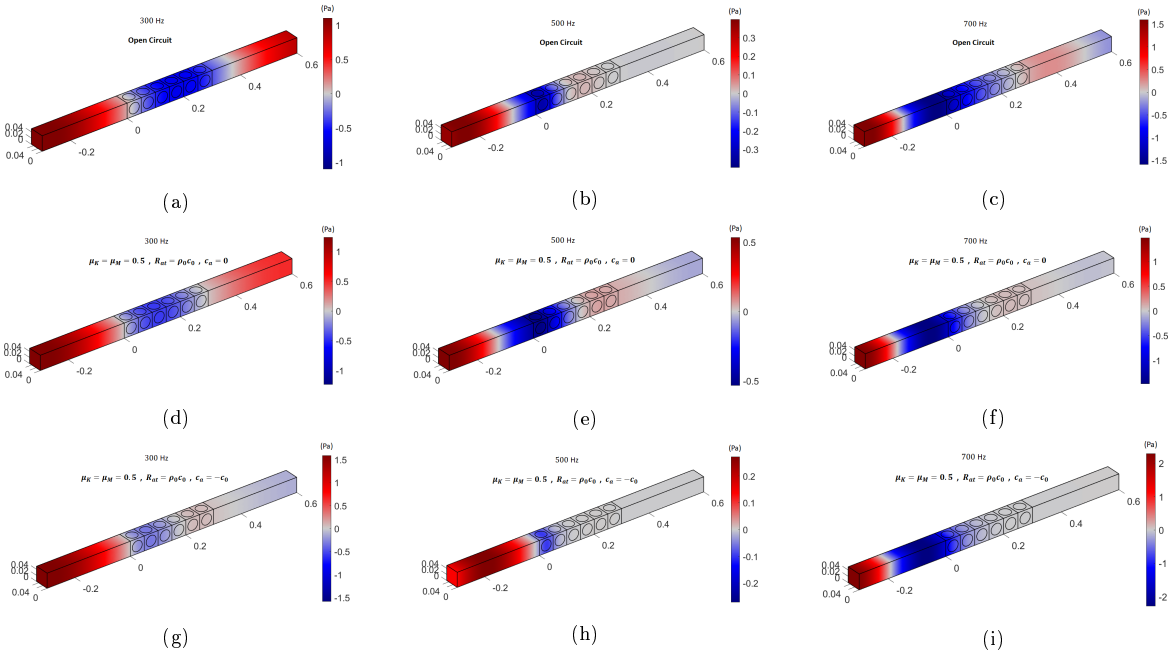

Figure 3.37: 3D surface plots.

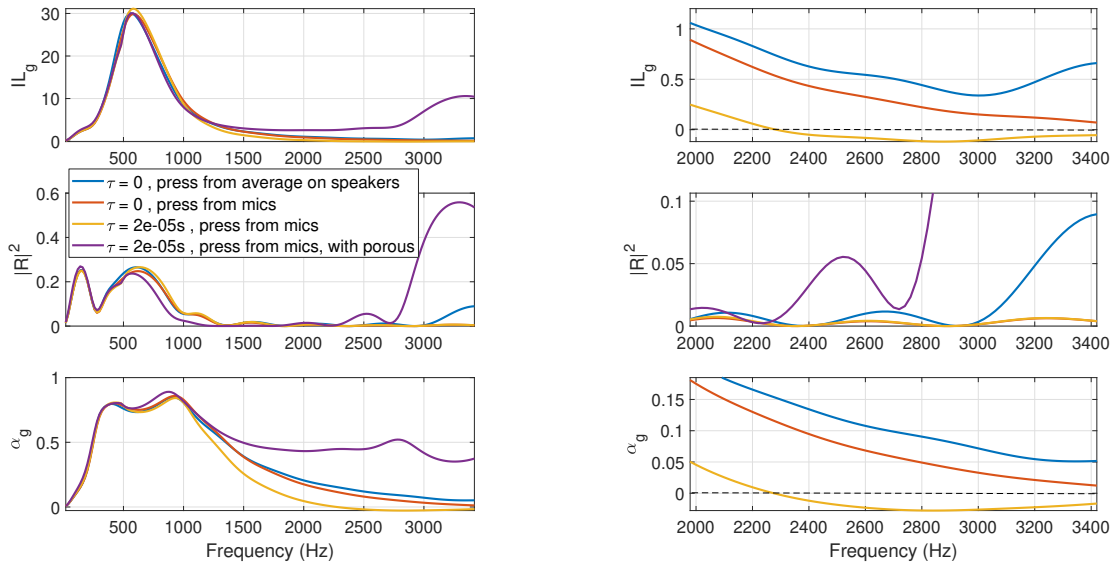

Figure 3.38: Scattering coefficients in a 3D waveguide of cross section width $h = 0.05$ m **with Local control law**, in case of pressure average evaluation on speakers and no delay (in blue), in case of pressure evaluated from corner microphone averaging and no delay (in red), in case of pressure evaluated from corner microphones and with time delay (in yellow), and in case of pressure evaluated from corner microphones, with delay and with a 6 mm thickness porous layer applied. In **(b)** a zoom at the high frequencies to highlight the effects of pressure evaluation from microphones, time-delay and porous layer application, on acoustical passivity.

in the Laplace variable s. Experimentally, on each EA, the local pressure is estimated by averaging the four microphones on the EA corners $\hat{p} = (p_A + p_B + p_C + p_D)/4$, while the

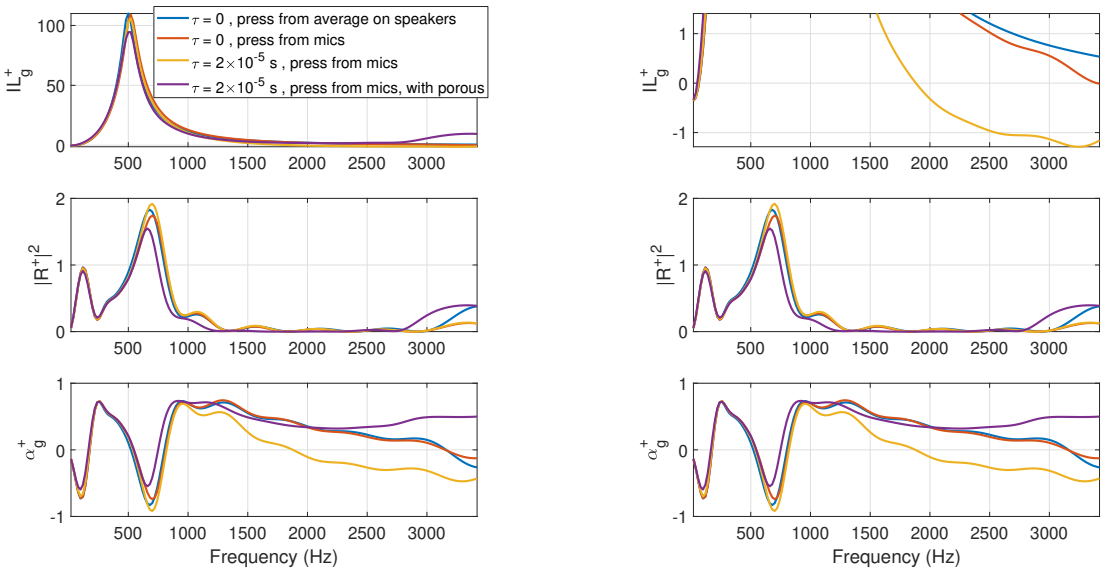

(a) (b)

Figure 3.39: Scattering coefficients "+" in a 3D waveguide of cross section width $h = 0.05$ m **with Advective control law**, in case of pressure average evaluation on speakers and no delay (in blue), in case of pressure evaluated from corner microphone averaging and no delay (in red), in case of pressure evaluated from corner microphones and with time delay (in yellow), and in case of pressure evaluated from corner microphones, with delay and with a thin (6 mm thickness) porous layer applied. In **(b)** a zoom at the high frequencies to highlight the effects of pressure evaluation from microphones, time-delay and porous layer application, on acoustical passivity.

x-derivative is estimated by a first-order finite difference $\hat{\partial}_x p = \Big((p_C + p_D) - (p_A + p_B) \Big) / \Delta x$, with $\Delta x \approx 4$ cm the distance between the microphones upstream (A,B) and downstream (C,D) each EA speaker, along the x-direction, as showed in Figure 3.35.
The transfer functions $H_{loc}(s)$ and $H_{grad}(s)$ are obtained by equating the velocity of the speaker diaphragm from its mechano-acoustical dynamics (2.2), and the velocity corresponding to the advection B.C. (3.10), and by imposing $Z_{Loc}(s) = Z_{at}(s)$. Their expressions in the Laplace space are given in Eq.s (3.45) and (3.46).

$$H_{loc}(s) = \frac{S_d}{Bl}\left(1 - \frac{Z_{a0}(s)}{Z_{at}(s)}\right), \tag{3.45}$$

$$H_{grad}(s) = \frac{S_d}{Bl}\frac{Z_{a0}(s)}{Z_{at}(s)}\frac{c_a}{s}F_{hp}(s), \tag{3.46}$$

where F_{HP} in $H_{grad}(s)$ is a high-pass filter necessary in order for $H_{grad}(\mathrm{j}\omega)$ not to become infinite for $\omega \to 0$. Equations (3.45) and (3.46) are implemented in the simulation in order to retrieve the electrical current on each EA. The mechano-acoustical dynamics equation (2.2) is then employed to retrieve the velocity assigned on each EA "disk".
The scattering performances have been simulated by FE in COMSOL. The FE mesh has been built sufficiently fine to resolve frequencies up to f_{cut-on}, according to the criterion $d_{max} \approx \lambda_{cut-on}/6$. The scattering problem has been outlined thanks to the "Port" functionality available in COMSOL for 3D geometries, which allows to define one or more incident

modes assuring the non-reflecting condition for that mode. Our problem is restricted to the plane wave mode, but such utility could be in future exploited to study the multi-modal scattering problem. By defining a port at the inlet and outlet sections of the duct, the Port functionality outputs directly the scattering coefficients between the two ports.
In Figure 3.36a, the scattering coefficients achieved by the advection law with $c_a = -c_0$, are traced along with the ones relative to open circuit ($H_{loc} = H_{grad} = 0$) and local control ($\mu_M = \mu_K = 0.5$, $R_{at} = \rho_0 c_0$ and $c_a = 0$) applied on the EAs.
As in the 2D case, the advection law demonstrates higher isolation capabilities, though being acoustically non-passive at very low frequencies, as well as after resonance.
A time delay $\tau = 2 \times 10^{-5}$ seconds is also taken into account by the exponential $e^{-\mathrm{j}\omega\tau}$ multiplying the controllers, leading to high frequency loss of acoustical passivity ($\alpha_g < 0$), which is more significant in case of $c_a \neq 0$.
In Figure 3.36b, the electrical current spectra of all the EAs are summed up to visualize how the advection law requires a much higher level of electrical current (up to 3 times) with respect to the local control. Also the sum of velocities $v(\omega)$ on the 24 EAs is reported showing once again higher levels required by the advection control law.
Figures 3.37 show the surface plots of the total acoustic pressure along the duct in case of open circuit (Figures 3.37a, 3.37b and 3.37c), local control (Figures 3.37d, 3.37e and 3.37f) and advection control law (Figures 3.37g, 3.37h and 3.37i) at 300, 500 and 700 Hz, giving a visual perception of the isolation levels achieved.

In order to assess the effect of the pressure estimation from the 4 corner microphones on each EA, in case of Local Control applied ($c_a = 0$), Figures 3.38 compare the scattering performances achieved by considering, in the controller, the acoustic pressure obtained from the 4 microphone positions, with the ones obtained by considering the average pressure on each EA disk, as well as the effect of the time delay. The zoom in Figure 3.38b shows that retrieving the acoustic pressure by averaging the values at the four microphones locations, slightly reduces the high-frequency absorption α_g, adding up to the dephasing effect introduced by the time delay. On the same figures, the effect of placing a layer of porous material on each EA (see Figure 3.34b) is also evaluated. The porous layer is modelled by the semi-empirical Miki model [83], according to which the porous behaviour is determined just by its flow resistivity (set to about 4000 Pa/(m/s)) and thickness (set to 6 mm), as in Section 3.5. Apparently, the configuration with the porous layer and the EA behind allows to satisfactorily recover the high-frequency acoustical passivity.
In Figures 3.39, the simulated scattering performances are plotted in case of advection boundary control, comparing the case where the pressure x-gradient is determined by first-order finite difference as illustrated in Figure 3.35 with the results achieved by considering the average of $\partial_x p$ on each disk, into the controller of each EA. The effect of the finite difference approximation of $\partial_x p$ further endangers the high-frequency acoustical passivity, as α_g^+ becomes negative after 3 kHz. The application of a porous layer though, can still restore the high-frequency acoustical passivity.
To sum up:

1. Discretizing the B.C. on separate disks (simulating the EAs loudspeakers) obviously reduces the liner performances as less surface area is available to treatment.

2. The advective control law is implemented by an additional transfer function $H_{grad}(s)$ multiplying the estimation of the pressure x-gradient. As $H_{loc}(s)$, also $H_{grad}(s)$ is based upon a model inversion of the EA mechano-acoustical dynamics.

3. The 3D scattering performances, with discretized boundary treatment and controller dynamics simulations, confirm the results of previous sections. Isolation is highly enhanced the advective law, though paying the price of non-passivity at very low frequencies and around resonance. Strong non-reciprocity is also confirmed.

4. Evaluating the pressure and its x-gradient through averaging and finite difference of corner microphones, introduce a high-frequency de-phasing endangering the acoustical passivity. This effect is more evident in case of advective control law, where the finite difference approximation of first order is subjected to aliasing problems at those frequencies. Such pressure-evaluation effects can induce energy injection downstream ($IL_g < 0$).

5. Time delay also jeopardize high-frequency passivity, possibly causing downstream energy injection ($IL_g < 0$).

6. Both pressure approximation and time delay also impacts the sign(c_a) scattering performances.

7. The application of a thin porous layer (even of 6 mm thickness), can restore high-frequency passivity, without significantly affecting the performances around resonance.

In the next section, the scattering performances are measured on an experimental test-bench with same EA prototypes as the one described in Section 2.1.4. The baggage of simulations showed so far will help in the interpretation of the experimental trends.

3.5 Experimental results

In this section, the advection control law is experimentally tested on an array of 24 EAs prototypes lining a squared cross-section duct of about 0.05 m side, as illustrated in the photos of Figure 3.40 and in the sketch of Figure 3.41. The EAs are placed 6 per each side of the duct, as showed in Figure 3.40. Each EA has a surface area of about $0.05 \times 0.05\ m^2$, for a total lined segment length of about 0.33 m in the duct. Both ends of the tube are filled with 45 cm of foam to reproduce quasi-anechoic conditions at the input and output of the waveguide. The external acoustic source is placed flush with the duct surface just ahead of the foam termination, sufficiently far from the lined portion of duct and from microphones M1 and M2 for plane waves to fully develop.
The control architecture is illustrated in Figure 3.42, which highlights the autonomous character of each cell (EA) driven by a current source through a numerical card specifically developed for the purpose by the FEMTO-st Institute, in the department of Applied Mechanics of the Université Bourgogne Franche-Comté. Each cell implements the control as described in Section 3.4.
The scattering performances have been estimated according to the Standard [57], based upon

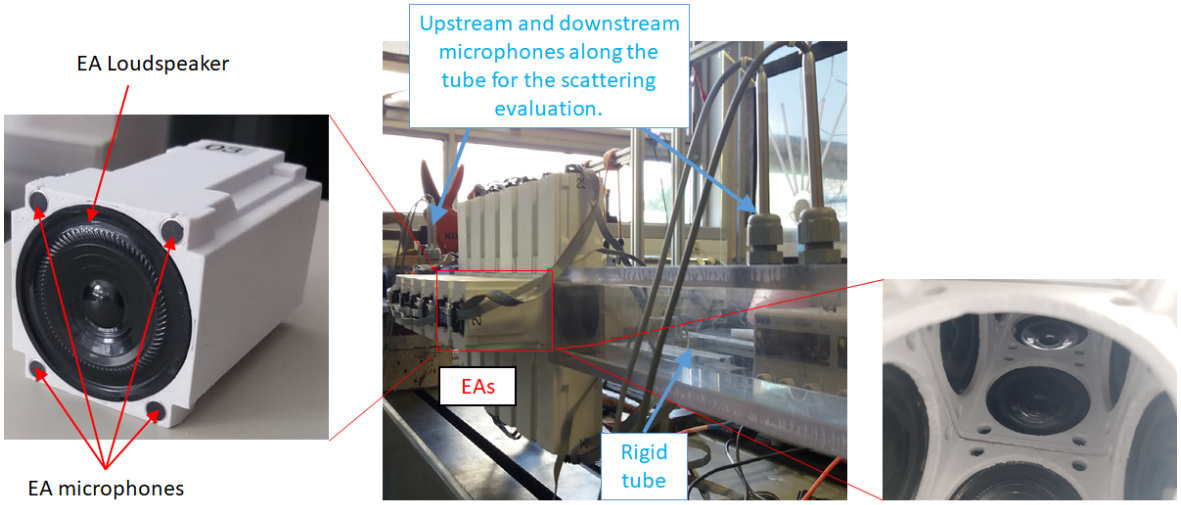

Figure 3.40: Unit EA (left); waveguide (middle) for the scattering evaluation, with internal view of the lined segment (right).

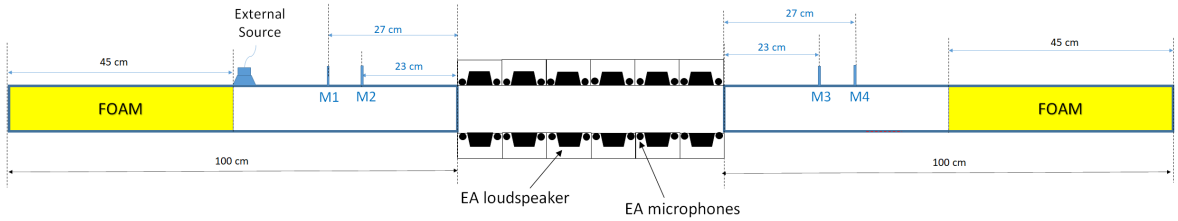

Figure 3.41: Sketch of the test-bench.

the 4-Microphones-Method (4MM). From the plane wave decomposition, the spectra of pressures evaluated at the 4 microphones positions x_1, x_2, x_3 and x_4 can be written as:

$$p_1(\omega) = A(\omega)e^{-\mathrm{j}k_0x_1} + B(\omega)e^{\mathrm{j}k_0x_1} \tag{3.47a}$$

$$p_2(\omega) = A(\omega)e^{-\mathrm{j}k_0x_2} + B(\omega)e^{\mathrm{j}k_0x_2} \tag{3.47b}$$

$$p_3(\omega) = C(\omega)e^{-\mathrm{j}k_0x_3} + D(\omega)e^{\mathrm{j}k_0x_3} \tag{3.47c}$$

$$p_4(\omega) = C(\omega)e^{-\mathrm{j}k_0x_4} + D(\omega)e^{\mathrm{j}k_0x_4} \tag{3.47d}$$

where we labelled as A, B, C and D the sound pressure wave amplitudes, upstream and downstream the lined segment, and p_1, p_2, p_3 and p_4 the total sound pressures at the four microphones locations. From Eq.s (3.47), the sound pressure wave amplitudes can be expressed in terms of the total pressures at the 4 microphones as:

$$A(\omega) = \mathrm{j}\frac{p_1(\omega)e^{-\mathrm{j}k_0x_2} - p_2(\omega)e^{\mathrm{j}k_0x_1}}{2\sin\Big(k_0(x_1 - x_2)\Big)}, \tag{3.48a}$$

$$B(\omega) = \mathrm{j}\frac{p_2(\omega)e^{-\mathrm{j}k_0x_1} - p_1(\omega)e^{-\mathrm{j}k_0x_2}}{2\sin\Big(k_0(x_1 - x_2)\Big)}, \tag{3.48b}$$

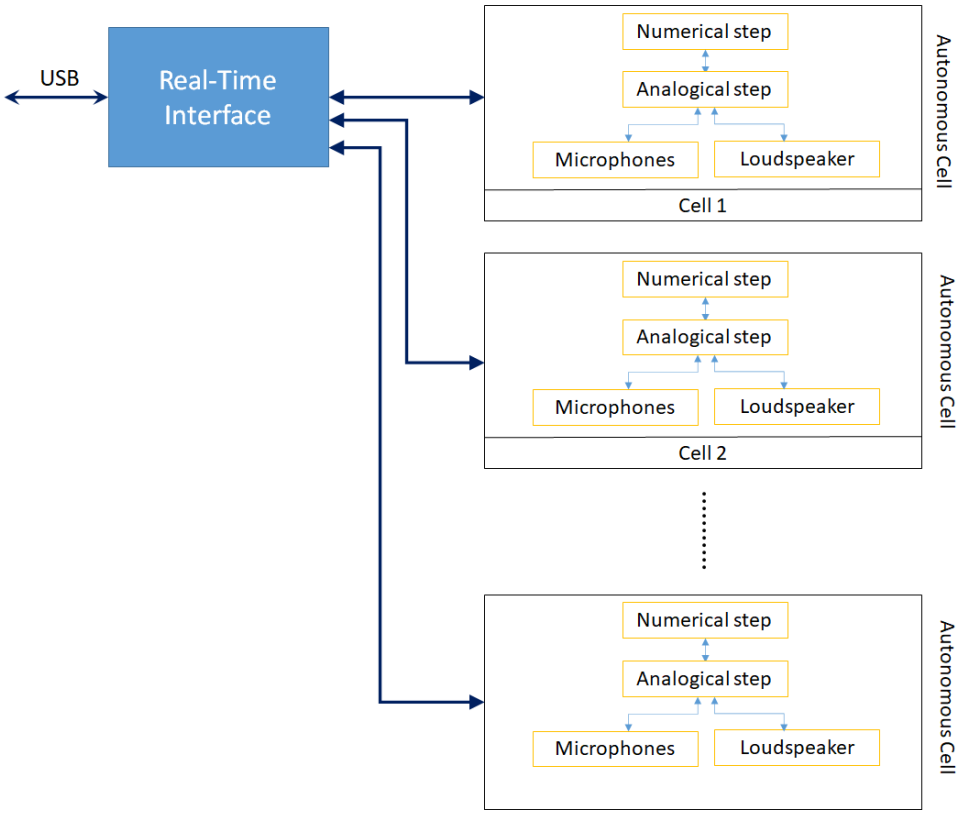

Figure 3.42: Architecture for the EAs control.

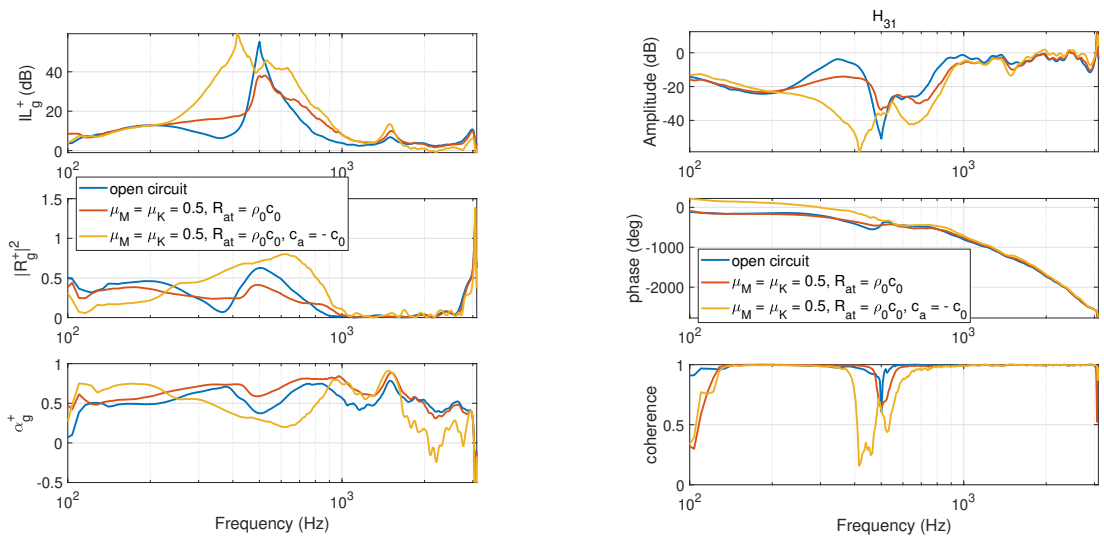

(a) (b)

Figure 3.43: Comparison among the open circuit, the local and advection control laws in terms of scattering performances **(a)** and the transfer function H_{31} **(b)**.

$$C(\omega) = \mathrm{j}\frac{p_3(\omega)e^{\mathrm{j}k_0x_4} - p_4(\omega)e^{\mathrm{j}k_0x_3}}{2\sin\Big(k_0(x_3 - x_4)\Big)}, \tag{3.48c}$$

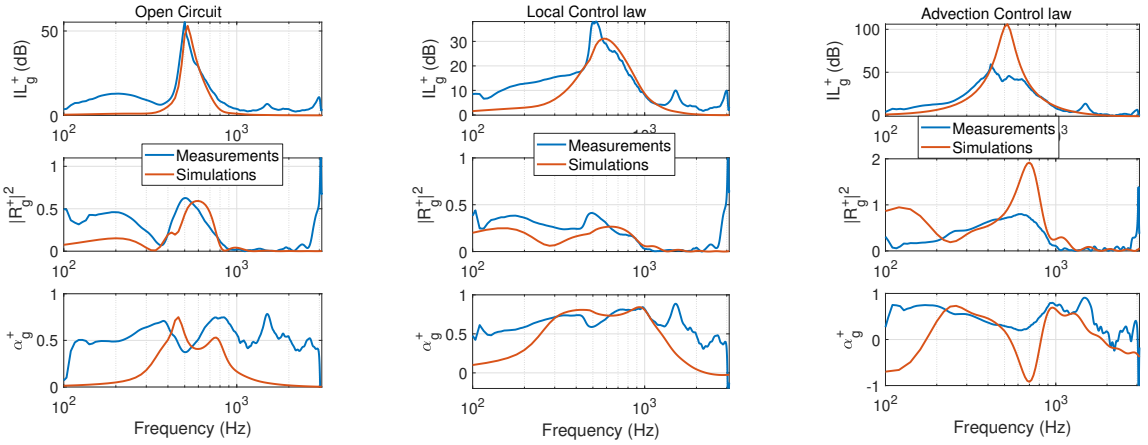

Figure 3.44: Comparison between measurements (in blue) and simulations (in red) in the cases of Open Circuit **(a)**, Local Control **(b)** (with $\mu_M = \mu_K = 0.5$, $R_{at} = \rho_0 c_0$) and Advection Control law **(c)** (with $c_a = -c_0$).

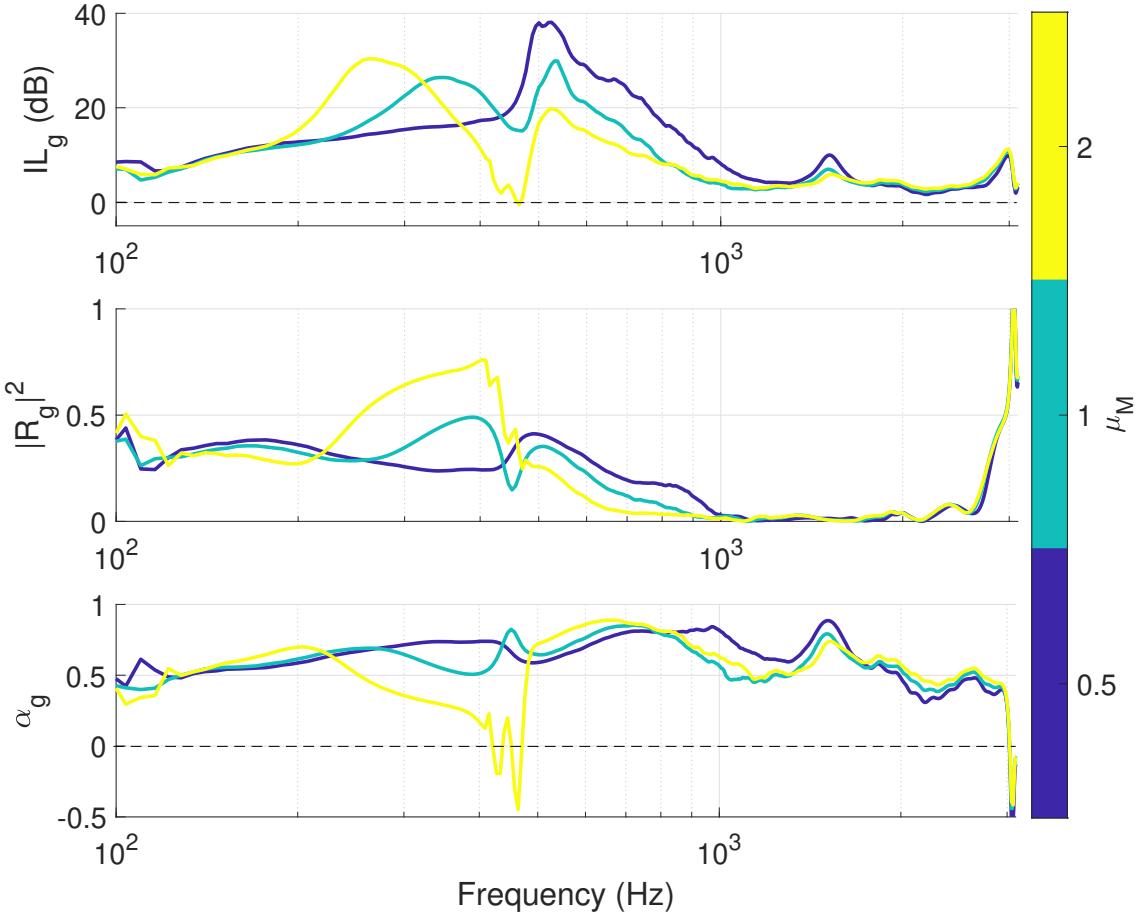

Figure 3.45: Experimental scattering performances in case of Local Control ($c_a = 0$), with varying μ_M, $\mu_K = 0.5$ and $R_{at} = \rho_0 c_0$.

$$D(\omega) = \mathrm{j}\frac{p_4(\omega)e^{-\mathrm{j}k_0 x_3} - p_3(\omega)e^{-\mathrm{j}k_0 x_4}}{2\sin\Big(k_0(x_3 - x_4)\Big)}. \tag{3.48d}$$

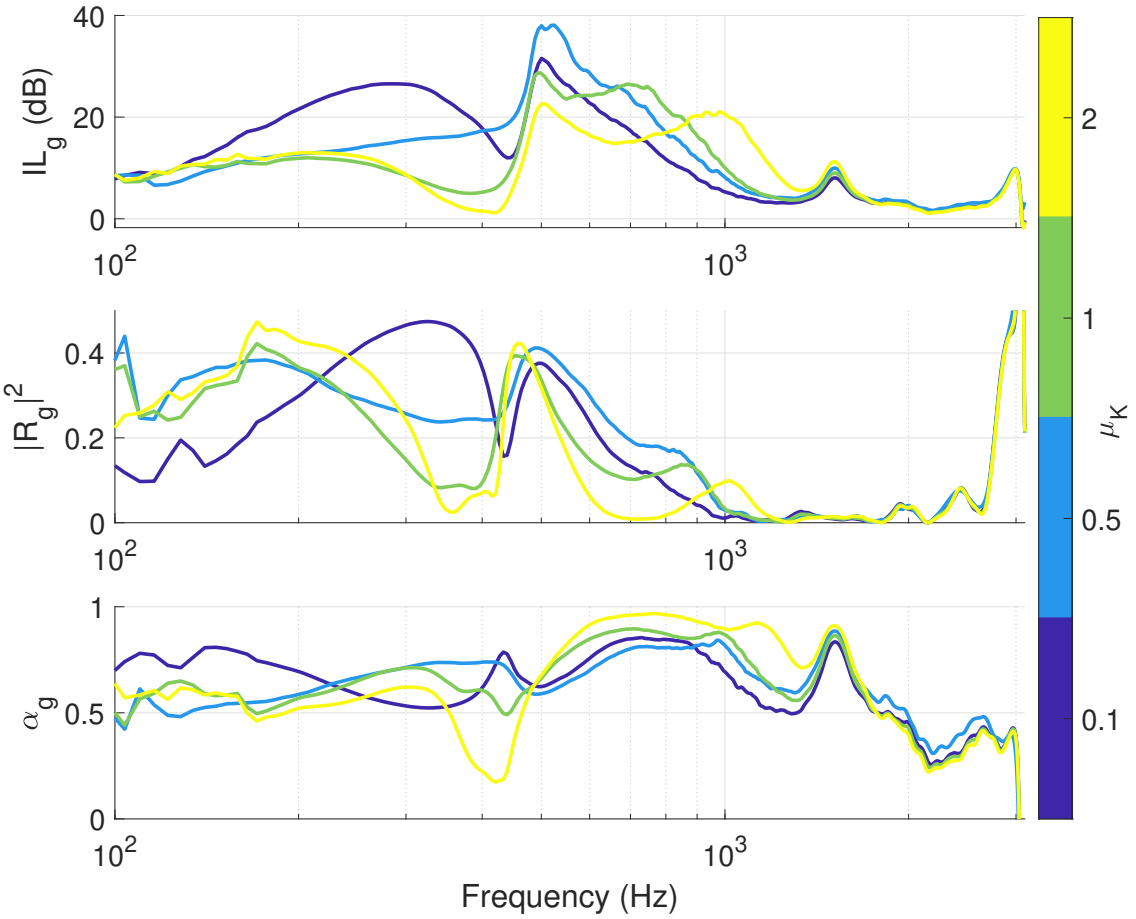

Figure 3.46: Experimental scattering performances in case of Local Control ($c_a = 0$), with $\mu_M = 0.5$, varying $\mu_K = 0.5$ and $R_{at} = \rho_0 c_0$.

Eq.s (3.48), in terms of the transfer functions spectra $H_{1n}(\omega)$ between microphone 1 (used as reference) and microphone n, gives the expressions:

$$A(\omega) = \mathrm{j}\sqrt{S_{11}}\frac{e^{-\mathrm{j}k_0x_2} - H_{21}e^{\mathrm{j}k_0x_1}}{2\sin\Big(k_0(x_1 - x_2)\Big)}, \tag{3.49a}$$

$$B(\omega) = \mathrm{j}\sqrt{S_{11}}\frac{H_{21}(\omega)e^{-\mathrm{j}k_0x_1} - e^{-\mathrm{j}k_0x_2}}{2\sin\Big(k_0(x_1 - x_2)\Big)}, \tag{3.49b}$$

$$C(\omega) = \mathrm{j}\sqrt{S_{11}}\frac{H_{31}e^{\mathrm{j}k_0x_4} - H_{41}e^{\mathrm{j}k_0x_3}}{2\sin\Big(k_0(x_3 - x_4)\Big)}, \tag{3.49c}$$

$$D(\omega) = \mathrm{j}\sqrt{S_{11}}\frac{H_{41}e^{-\mathrm{j}k_0x_3} - H_{31}e^{-\mathrm{j}k_0x_4}}{2\sin\Big(k_0(x_3 - x_4)\Big)}, \tag{3.49d}$$

where S_{11} is the autospectrum of microphone 1. In order to estimate the scattering coefficients, the amplitudes of Eq.s (3.49) must be evaluated in 2 different configurations, which

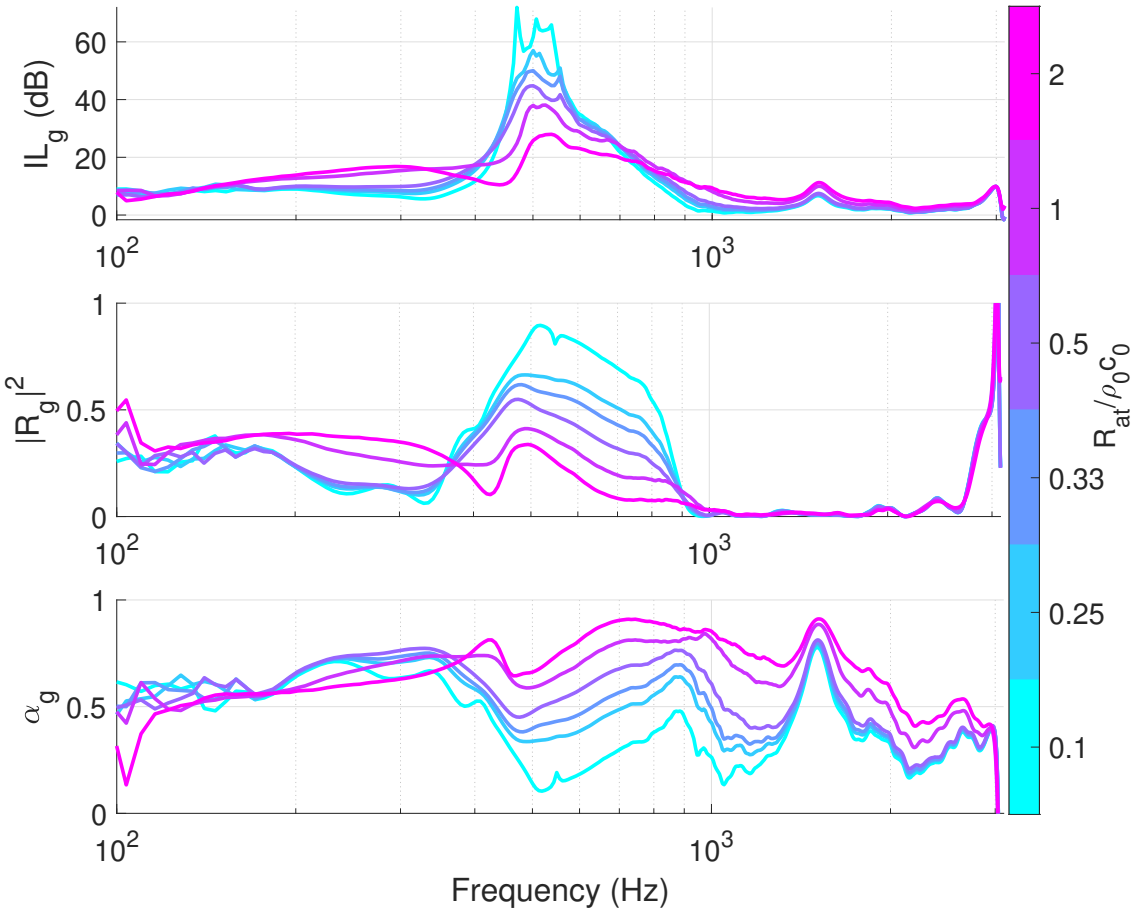

Figure 3.47: Experimental scattering performances in case of Local Control ($c_a = 0$), with $\mu_M = \mu_K = 0.5$ and varying R_{at}.

can be obtained by changing the duct termination (also called acoustic load) at the other side respect to the source. Hence, 2 set of measurements are conducted, one per each configuration. The scattering problem for both acoustic loads can be written in matrix form as:

$$\begin{bmatrix} C_a & C_b \\ B_a & B_b \end{bmatrix} = \begin{bmatrix} T^+ & R^- \\ R^+ & T^- \end{bmatrix} \begin{bmatrix} A_a & A_b \\ D_a & D_b, \end{bmatrix} \tag{3.50}$$

where the subscripts a and b correspond to the two different load configurations. By inverting the last matrix on the rhs of Eq. (3.50), the scattering coefficients can be obtained as:

$$T^+(\omega) = \frac{C_a D_b - C_b D_a}{A_a D_b - A_b D_a}, \tag{3.51a}$$

$$R^-(\omega) = \frac{-C_a A_b + C_b A_a}{A_a D_b - A_b D_a}, \tag{3.51b}$$

$$R^+(\omega) = \frac{B_a D_b - B_b D_a}{A_a D_b - A_b D_a}, \tag{3.51c}$$

$$T^-(\omega) = \frac{-B_a A_b + B_b A_a}{A_a D_b - A_b D_a}. \tag{3.51d}$$

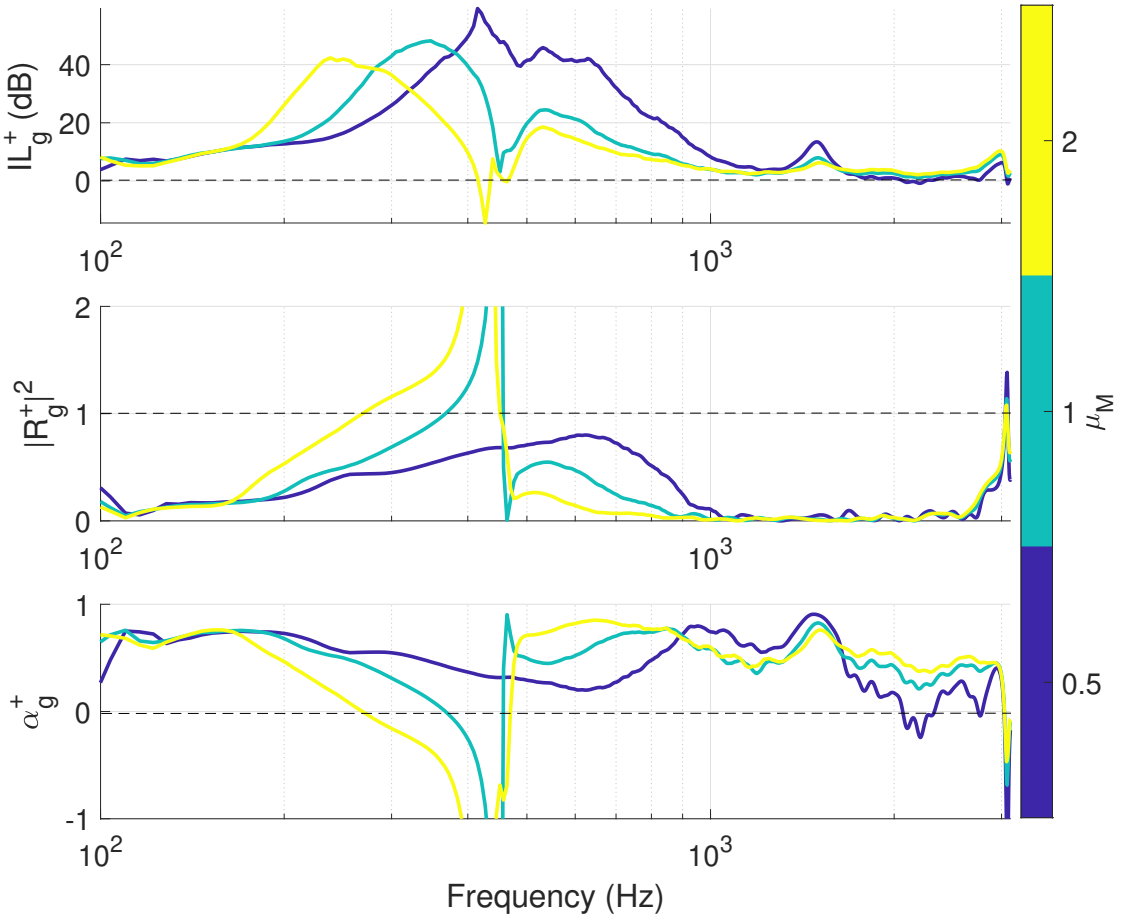

Figure 3.48: Experimental scattering performances with external incident field propagating toward $+x$, in case of Advective Control, with $c_a = -c_0$, varying μ_M, $\mu_K = 0.5$ and $R_{at} = \rho_0 c_0$.

In order to produce another load condition, additional to the quasi-anechoic one given by the 45 cm of foam, we removed the foam and get an open termination. Nevertheless, for the scattering performances R^- and T^-, it is better to invert the position of the external source for having higher coherence.

In Figures 3.43, the measurements outputs are compared among the open circuit, the local and advective control strategies. Figure 3.43a shows the scattering performances while Figure 3.43b present the transfer function H_{31}, between microphones 3 and 1, in order to visualize the coherence of the measurements. Around resonance, both the open circuit, and the controlled cases, present low coherences due to the low signal at the downstream microphones (M3 and M4). The spectra are plotted between 100 and 3100 Hz, as below 100 Hz the external source does not deliver sufficient acoustic power, and beyond 3100 Hz the higher order duct modes starts to affect the measurements.

The significant increase in isolation achieved by the advection strategy respect to the local control law is confirmed, both in bandwidth and in the maximum, as most energy is reflected backward. As TL_g^+ is really high around resonance (about 500 Hz), a low signal to noise ratio is produced, especially in case of advection control law, and the coherence of the transfer

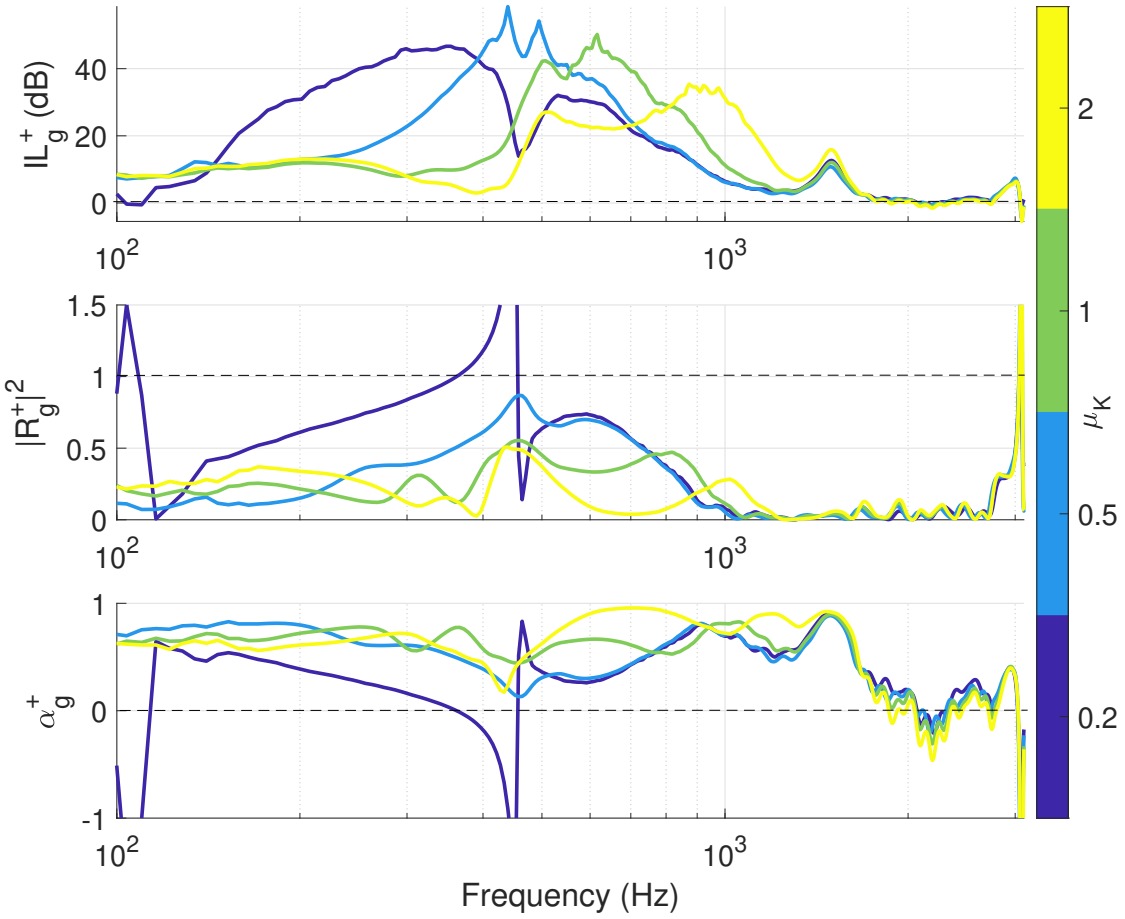

Figure 3.49: Experimental scattering performances with external incident field propagating toward $+x$, in case of Advective Control, with $c_a = -c_0$, $\mu_M = 0.5$, varying μ_K and $R_{at} = \rho_0 c_0$.

functions is very small. For this reason, the values around 500 Hz attained by the IL_g^+, R_g^+ and α_g^+ plots might not be exact.

Above 2 kHz, observe the higher deficit of acoustical passivity in the case of advection control respect to the local strategy. Such effect was predicted by the numerical simulations and mainly associated to the aliasing effect due to the first-order finite difference approximation of the x-gradient of pressure.

In Figure 3.44 the measured scattering performances are compared to the simulated ones, in the cases of Open Circuit **(a)**, Local Control **(b)** (with $\mu_M = \mu_K = 0.5$, $R_{at} = \rho_0 c_0$) and Advection Control law **(c)** (with $c_a = -c_0$). It is striking the great discrepancy between measurements and simulations especially for frequencies below and above the resonance region. The presence of another mechanical mode of the speaker around 1500 Hz (also discussed in Section 2.1.4), which is not included in the simulations, surely affects the trends above resonance. On the other hand, low frequencies are probably touched by both an additional mode of the speaker (either mechanical or, more likely acoustical due to a Helmholtz resonator effect produced by a small construction hole on the EA cell), or to a structural mode of the tube or of the skeleton holding the EAs.

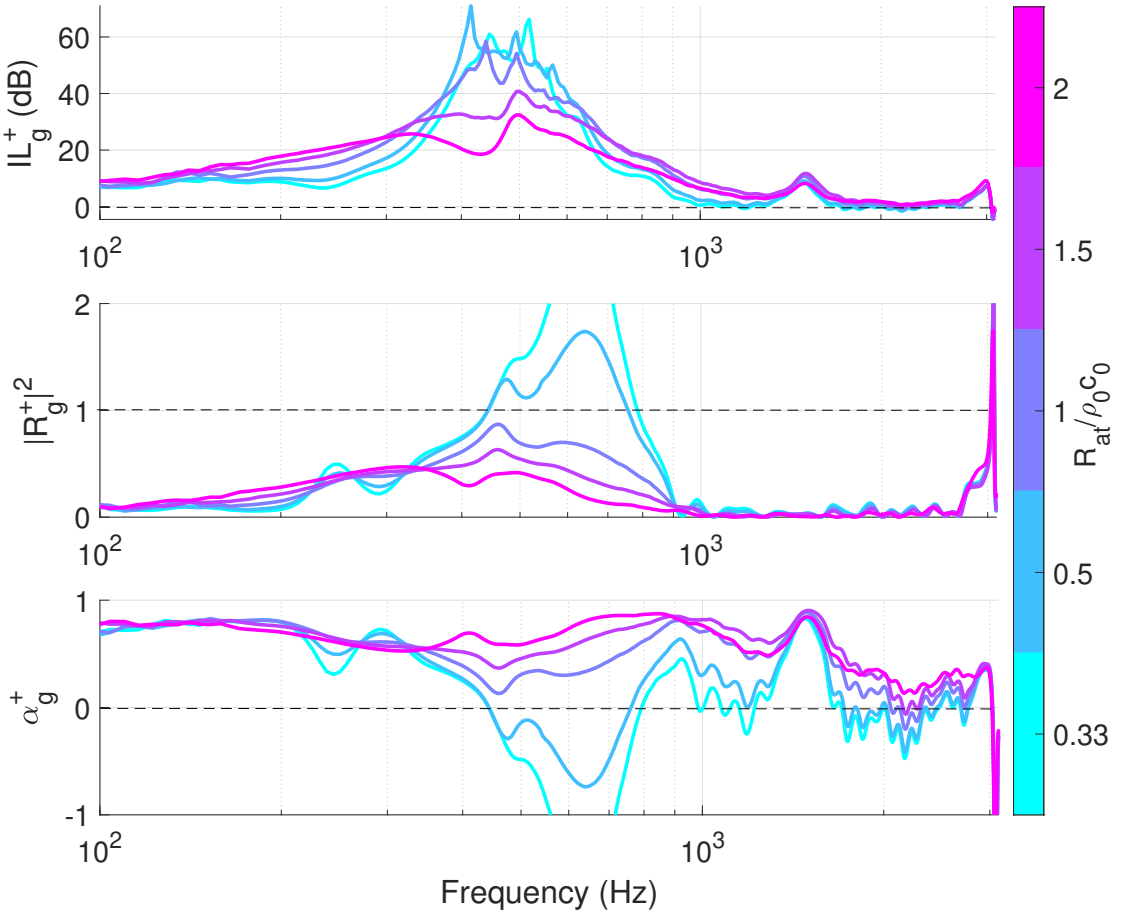

Figure 3.50: Experimental scattering performances with external incident field propagating toward $+x$, in case of Advective Control, with $c_a = -c_0$, $\mu_M = \mu_K = 0.5$ and varying R_{at}.

Then the slight shift between measurements and simulation plots around resonance, evident in the O.C. and Local Control plots, is probably due to two main reasons. A first one, is linked to the time-delay in the digital implementation of the controller, which is likely higher than the 2×10^{-5} seconds considered in simulations. A second aspect to take into account is the variability of the Thiele-Small parameters among the EAs, whereas, in simulation the Thiele-Small parameters have been defined uniquely for all the EAs (taking the average values of all the EAs prototypes).

Looking at the advection control case, we remark that measurements do not present the losses of acoustical passivity either at low frequencies or around resonance, which were expected by simulations. While for low frequencies the above mentioned discrepancy must be due to modes present either in the EA or in the test-rig structure, around resonance the low coherence (due to low signal-to-noise ratio) does not allow for detecting the exact value of IL_g^+, likely underestimating the backward reflection and, hence, overestimating α_g^+. Despite high-frequency modes of the speakers (not considered in the numerical model), the high frequency shortage of acoustical passivity in the advection control, is detectable also from measurements.

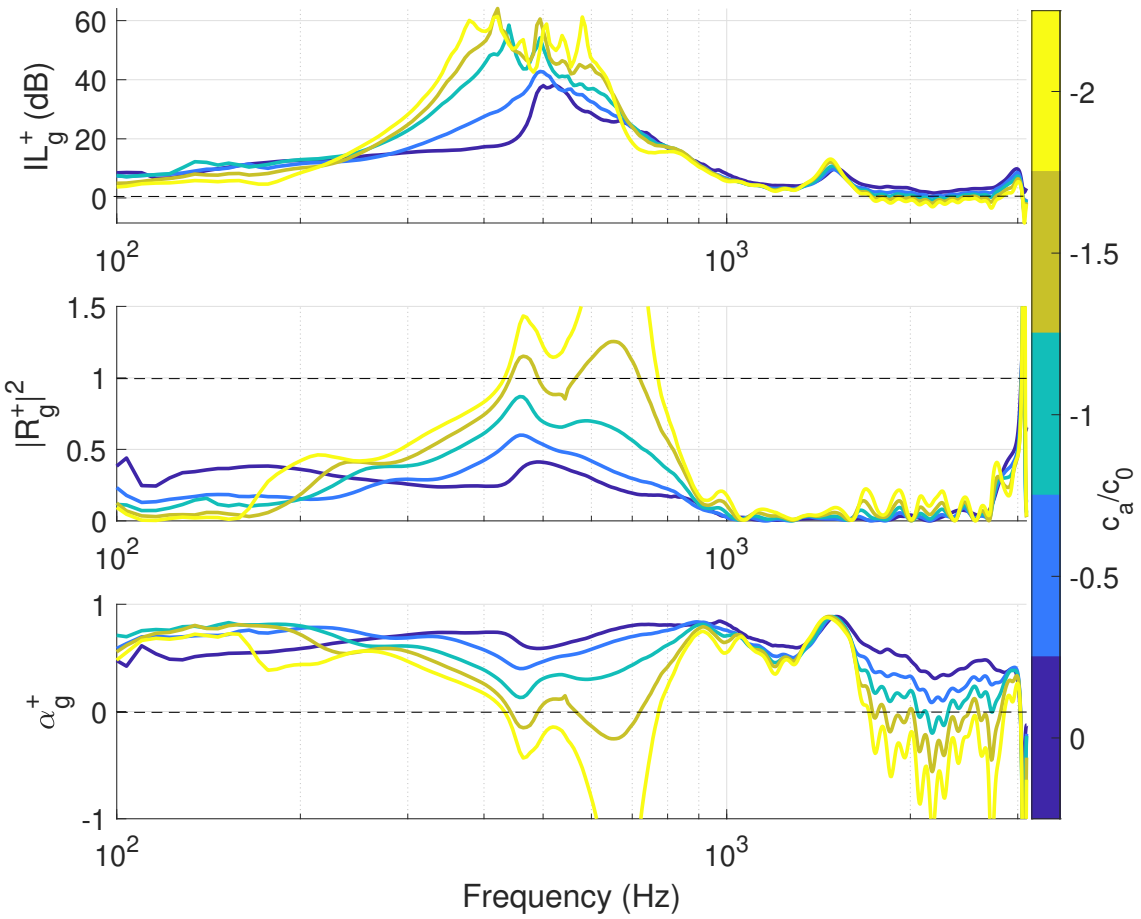

Figure 3.51: Experimental scattering performances with external incident field propagating toward $+x$, in case of Advective Control, with varying c_a, $\mu_M = \mu_K = 0.5$ and $R_{at} = \rho_0 c_0$.

An additional source of difficult predictability of experimental results are the errors in the mechanical model adopted in the control laws. These errors, either linked to parameter or dynamics uncertainties, are not considered in simulations, while affecting performances at all frequencies in the experimental control implementation.
In Figures 3.45, 3.46 and 3.47, the scattering performances of the local control law are plotted for different values of the μ_M, μ_K and R_{at} respectively. The nominal values are set to $\mu_M = \mu_K = 0.5$ and $R_{at} = \rho_0 c_0$ as in the previous plots and in the 3D simulations.
In Figure 3.45, the minimum value for μ_M is 0.5, as below it the system becames unstable for the reasons exposed in Section 2.1.2. Increasing μ_M moves the pick of IL_g and of $|R_g|^2$ towards lower frequencies, but the resonance of $Z_{a0}(\mathrm{j}\omega)$ (at f_{a0}) is not fully equalled out by the model-inversion based control law, because of both time delay (as predicted by simulations) and model uncertainties, so that there is still a residual pick at about 500 Hz. Increasing μ_M up to 2, brings a loss of acoustical passivity slightly below f_{a0}. Figure 3.46 shows how varying μ_k can move the pick of IL_g towards either lower frequencies (where the isolation performances are mainly due to an increase in the reflection coefficient), or toward higher frequencies (where the IL_g is mainly achieved thanks to higher absorption). Once again, the

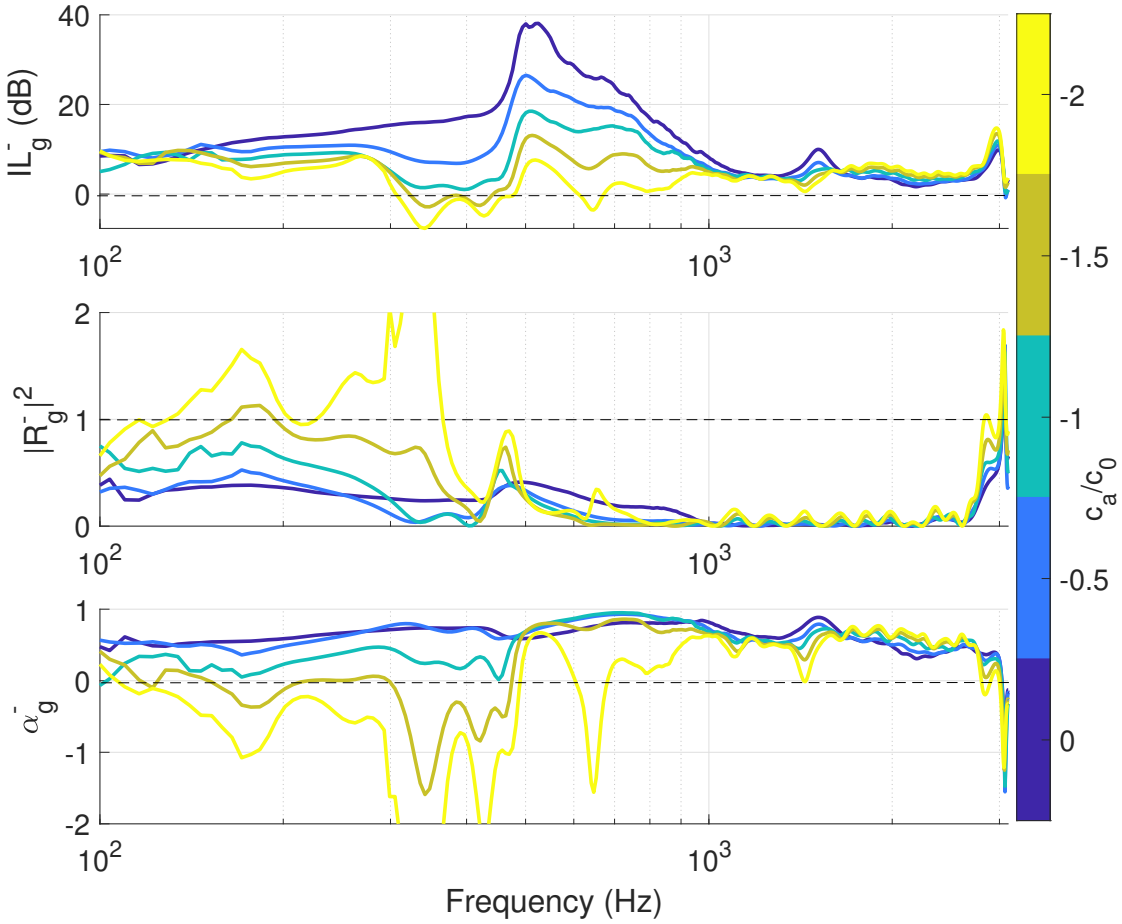

Figure 3.52: Experimental scattering performances with external incident field propagating toward $-x$, in case of Advective Control, with varying c_a, $\mu_M = \mu_K = 0.5$ and $R_{at} = \rho_0 c_0$.

residual pick at f_{a0} is not eliminated by the controller. Interestingly, the acoustical passivity just before f_{a0}, is more endangered by moving f_{at} towards higher, rather than towards lower frequencies. This is so, because moving the resonance of $Z_{at}(\mathrm{j}\omega)$ away from f_{a0} requires an increase in the corrector gain $|H_{loc}(\omega)|$ at f_{at}. Hence, if $f_{at} > f_{a0}$, then $|H_{loc}(\omega)|$ will increase at higher frequencies (see Figures 2.2), augmenting the de-phasing effect introduced by the time delay (which also increases with frequency). Nevertheless, we remark that an effective isolation $IL_g \geq 20$ dB, can be accomplished by moving f_{at} from 200 to 2000 Hz.
Figure 3.47 confirms the higher isolation performances achieved by reducing the resistive component of the EA impedance, leading to higher backward reflection.

The target impedance parameters are also varied in case of advective control law in Figures 3.48, 3.49 and 3.50. The higher isolation performances (both in terms of bandwidth and of pick) achieved by the advective B.C. are also accompanied by more severe shortage of acoustical passivity. In Figure 3.48, we can see that at $\mu_M = 1$ the system already loses passivity slightly below f_{a0}. Remind that, in case of advective B.C., numerical simulations (both duct-modes analyses of Section 3.2 and scattering simulations of Section 3.4) showed

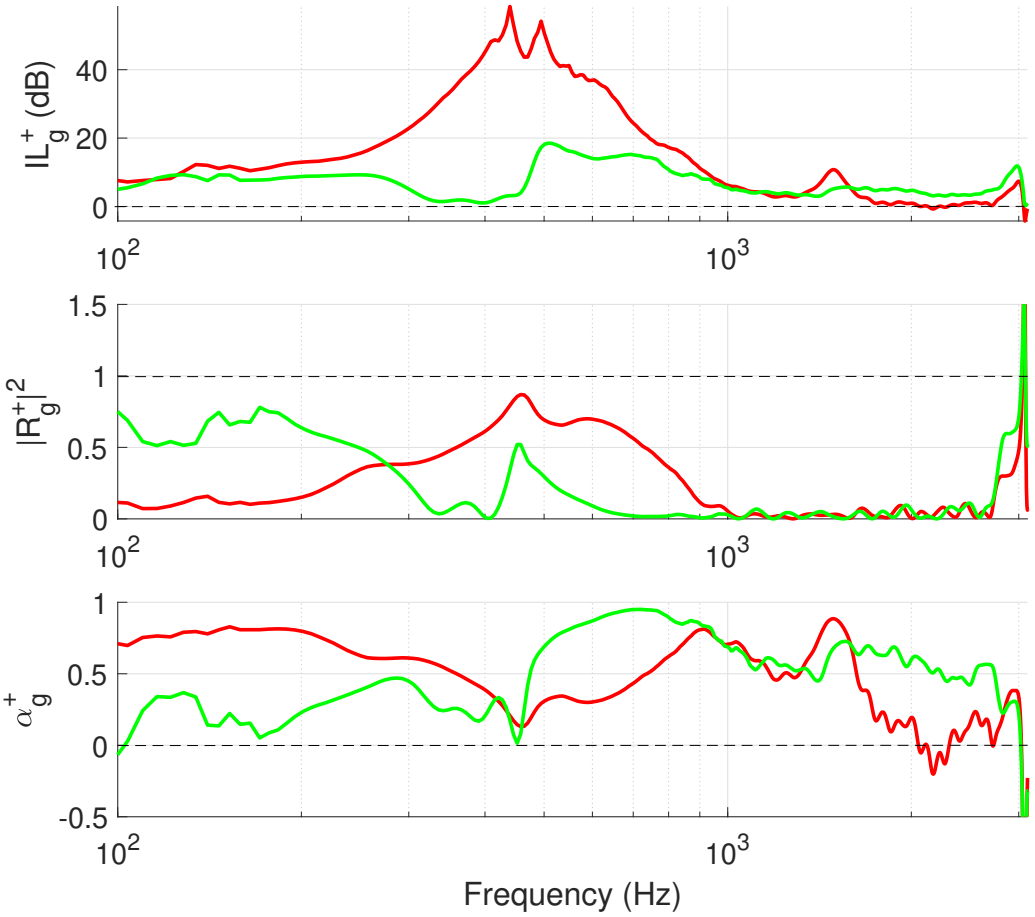

Figure 3.53: Scattering performances relative to external incident field propagating toward $+x$ ("forward", in solid green) compared to the ones relative to "backward" incident field (in solid red), in case of advective B.C. with $\mu_M = \mu_K = 0.5$, $R_{at} = \rho_0 c_0$ and $c_a = -c_0$. Also the scattering achieved by the Open Circuit configuration is plotted for comparison.

that higher quality factors of $Z_{at}(\mathrm{j}\omega)$ (i.e. increasing the reactive terms μ_M and μ_K, and/or reducing R_{at}) led to harsher loss of passivity around f_{a0}, independently of time delay. This is because the backward reflected energy becomes higher than the incident one as an outcome of the combined non-local and reactive nature of the boundary. Such phenomenon is confirmed by Figures 3.48, 3.49 and 3.50. In particular, in Figures 3.48 and 3.49, where f_{at} is varied with respect to f_{a0}, such passivity shortage is worsened by the dephasing effect of time-delay, already present in the purely local control strategy.

Figures 3.51 and 3.52 show the scattering performances by varying c_a, for positive and negative propagating incident fields respectively. Figure 3.51 confirms that higher values of $|c_a|$ produce greater isolation, but *reduce* the acoustical passivity at resonance. **A value of $|c_a|$ lower than c_0 can anyway be found such that to improve the IL_g^+ respect to the purely local control strategy, while keeping the acoustical passivity at resonance.**

The broadband non-reciprocal character of the advective B.C. is evident by look-

Figure 3.54: View of the waveguide interior. In pink, the layers of foam applied in front of the loudspeakers without interfering with the mechanical vibration of the diaphragms, and maintaining the "flush" condition of the liner.

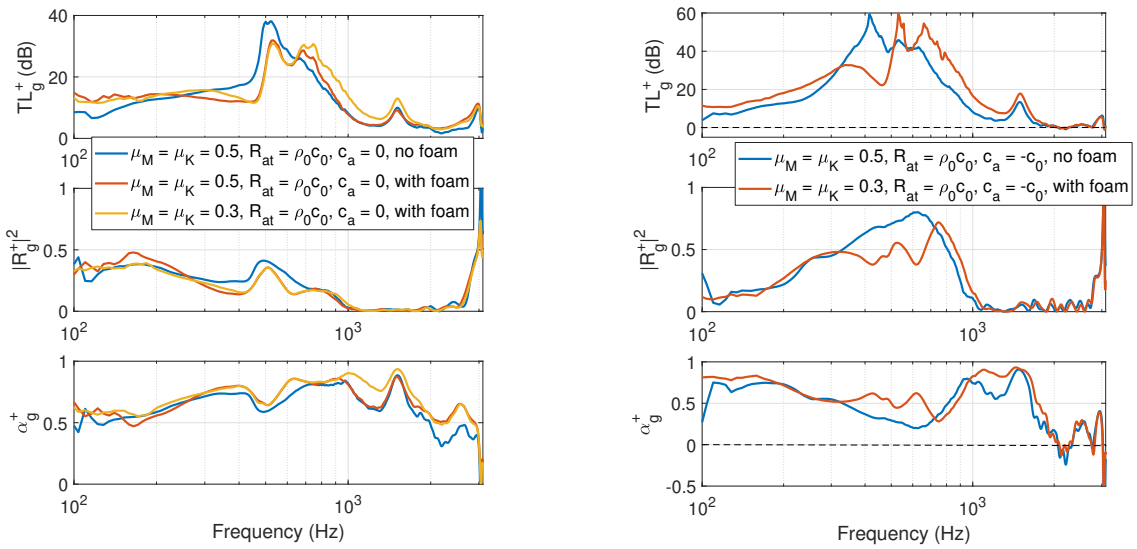

(a) (b)

Figure 3.55: Effect of the 6 mm foam layer on the scattering performances in case of Local **(a)** and advective **(b)** controls.

ing at Figure 3.52, where the external source has been placed on the other side with respect to the lined segment, and the $(-)$ scattering performances have been measured. For $|c_a| > c_0$ the system becomes non-passive as expected by both duct-modes analysis (Section 3.2) and scattering simulations (Section 3.4). Clearly, even if $c_a = -c_0$, the loudspeakers dynamics is not totally annihilated, because of time delay as well as of dynamics and model uncertainties in the control law. Therefore, the reflection and absorption coefficients are not perfectly equal to 0 (as it was in the simulations), but the insertion loss is about 30 dB lower than in the open circuit configuration at resonance, and, with respect to the other sense of propagation,

it is more than 20 dB lower from 300 to 600 Hz, and more than 40 dB lower from 400 to 500 Hz (see Figure 3.53).

In order to cope with the high-frequency shortage of acoustical passivity, as in Section 2.1.3, a 6 mm layer of foam has been applied in front of the EAs, as illustrated in Figure 3.54, without losing the flush condition of the EAs in the waveguide. The effects of the porous employment on the scattering performances are given in Figure 3.55a and 3.55a for the local and advective controls respectively. Surprisingly, the thin layer of foam shifts the pick of IL_g toward higher frequencies as in the normal absorption performance of Section 2.1.4. This was not predicted by simulations (see Figure 3.38), where the Miki model for porous materials was considered, with a flow resistivity of 4000 Pa/(m/s) extrapolated by normal absorption coefficient measurements of the foam adopted. According to such model, the porous layer is acoustically transparent below 2000 Hz. This discrepancy is likely due to the inadequacy of the model adopted for simulating the porous behaviour, which, in addition, is so thin that it can be subjected to vibrations under acoustic excitation. Nonetheless, thanks to the foam application the reactive components μ_M and μ_K could have been reduced from 0.5 (in case of no foam) to 0.3, hence slightly enlarging the bandwidth of efficient isolation, as it can be seen in Figure 3.55. Note that in the Local control case (Figure 3.55a), the high-frequency acoustical-passivity restoring effect accomplished by the foam is more evident than in the advective case (Figure 3.55b). Nevertheless, also with the advective control law, the minimum coefficients μ_M and μ_K before instability, have decreased from 0.5 to 0.3.

The main points of scattering performance measurements are reported below:

1. The experimental set-up follows the same arrangement of EA as the one in the 3D simulations of Section 3.4.

2. The measured trends around resonance follows the simulated ones, except from slight shifts probably due to an actually higher time delay than the predicted one, as well as differences in the Thiele-Small parameters among EAs. In case of advective control law, the isolation achieved is so high that low signal-to-noise ratios are obtained in the downstream microphones, henceforth the low coherence at these frequencies, and the underestimation of the reflective performances of the advective control law around resonance.

3. Below resonance there is probably an unpredicted mode: either a structural on (of the duct) or an Helmholtz resonator effect due to very little construction holes on the surface of the EA prototypes. It causes the low-frequencies discrepancy between simulation and measurements.

4. Above resonance, the trends are affected by a loudspeaker mode at 1500 Hz (not taken into account either in simulations or in the model-inversion control law).

5. The presence of time delay in the control implementation, as well as of inevitable model uncertainties, prevent to perfectly cancel out the loudspeaker own dynamics. Therefore, a residual pick around 500 Hz is always there even for $f_{at} \neq f_0$.

6. In the Local control case, shifting f_{at} toward higher frequencies increases the shortage of acoustical passivity at high-frequencies. Indeed, to impose a $f_{at} > f_0$, higher amplitude of the corrector transfer function is demanded at higher frequencies, thereby enhancing the dephasing effect of time delay at those frequencies.

7. Both in Local and Advective control cases, reducing R_{at} sharpens and augments the pick of reflection. It lowers the absorption, but increase the IL. In addition, it endangers the acoustical passivity at high frequencies, as expected.

8. The advective control law confirms to isolate better respect to the local strategy, though acoustical passivity is concerned both around resonance (especially for narrow ducts) and at high frequencies (because of aliasing effects on the pressure x-gradient estimation).

9. In order to achieve high isolation performance without too much concerning acoustical passivity, the parameters of the advective control law must be chosen according to two conflicting needs. On the one hand $|c_a|$ must be limited to the threshold assuring the passivity around resonance. Such a limit is more stringent for narrower ducts, and higher reactive components (μ_M and μ_K) in $Z_{Loc}(\mathrm{j}\omega)$. On the other hand, the lower limit of the reactive component μ_M is given by the high-frequency passivity issue related to time-delay.

10. In case of advective control law with $|c_a| = c_0$, waves propagating in the passing sense are not totally "passing", because of the non-perfect cancellation of the loudspeakers own dynamics. Though, the insertion loss is about 30 dB lower than in the open circuit configuration at resonance, and, with respect to the other sense of propagation, it is more than 20 dB lower from 300 to 600 Hz, and more than 40 dB lower from 400 to 500 Hz. **Hence the breaking of reciprocity is experimentally validated**.

11. The application of a thin (6 mm thickness) porous layer in front of the loudspeakers, allows to restore high-frequency acoustical passivity, especially in the Local Control case. Unexpectedly, the foam affects also the isolation performances around resonance. This is probably due to the uncertain behaviour of the such foam at those frequencies, both in terms of its viscous absorption and mechanical vibration.

3.6 Conclusions

In this chapter, the boundary control has been enlarged toward a non-local conception. The first order differential boundary operator first proposed in [22], also called advective B.C., has here been deeply analysed starting from its origins and physical interpretations.
From a mathematical point of view, we showed that it simulates an interface with a fictitious propagative and advective domain Ω_{fict} behind, where the phase speeds along the tangential directions (x and z) degenerate to 0, and where the advection speed c_a is along the tangential coordinate x. The phase speed along y and the advection celerity are the degree of freedom of such B.C.. The phase speed along y can be generalized to take into account complex values.

From that, the definition of the advection B.C. constituted by a first "local" term (characterized by a certain local impedance $Z_{Loc}(\mathrm{j}\omega)$ multiplying the local pressure) and an additional term which confers the advective character, given by the advection speed c_a multiplying the pressure x-gradient.
From a physical point of view, we showed that such B.C. entails the advection of the local reaction (described by the local operator $Z_{Loc}(\bullet)$ along a characteristic line on the boundary x-dimension, in the direction of $\mathrm{sign}(c_a)$.

The transport of the boundary reaction breaks the reciprocity of transmission in an acoustic waveguide. Higher isolation respect to the local boundary control is achieved for incident waves directed toward $-\mathrm{sign}(c_a)x$. Responsible of such isolation is a backward reflection which is as higher as $|c_a|$.
Instead, waves propagating toward $\mathrm{sign}(c_a)x$ are ideally perfect transmitted downstream, if $|c_a| = c_0$. *This confers the waveguide treated by the advective B.C. the feature of non-reciprocal device.*

The performances of the advective B.C. are first analysed in a semi-infinite domain. The reflection coefficient has been evaluated according to the classical ray acoustics theory, confirming the asymmetrical behaviour for incident waves coming from left or right. The reflection coefficient computation has featured a loss of acoustical passivity for $|c_a| > c_0$. This has been confirmed also by another passivity criterion which has been announced here. It is based upon the evaluation of the solution of the dispersion problem of the B.C. applied on a semi-infinite acoustic domain. The wave-number solutions of such problem have been demonstrated to give the directions of highest absorption (when the boundary behaves as passive) or highest reflection (when the boundary behaves as non-passive). Hence, by looking at those angles, it is possible to assess the acoustical passivity of any boundary operator, either locally or non-locally reacting.

The duct mode analysis in an acoustic waveguide has allowed to verify the non-reciprocal behaviour achieved: the plane wave mode propagating toward $-\mathrm{sign}(c_a)x$ testifies perfect transmission in that sense. In the opposite sense, a high $|\mathrm{Im}\{k_x\}|$ demonstrates isolation. The duct mode analysis also confirmed the passivity conclusions of the semi-infinite domain analysis. Nevertheless, another unexpected passivity shortage has resulted in case of complex $Z_{Loc}(\mathrm{j}\omega)$. Such unstable duct modes propagation can be ascribed to an increased phase shift between local pressure and velocity at the boundary, due to the reflection of sound waves on the two opposite faces of the duct, along with the convection of the boundary reaction.

Simulations in 2D and 3D waveguides confirm the break of the acoustical reciprocity principle. Also the enhanced isolation performances achieved by the advective strategy respect to the local impedance control, are featured. The duct modes unstable propagation due to the reactive components of $Z_{Loc}(\mathrm{j}\omega)$ manifests itself in a reflection coefficient higher than 1 in amplitude. A further concern has appeared at very low frequencies, where the abrupt change of boundary behaviour (from rigid to advective) probably induces an additional loss of acoustical passivity.

Despite the apparent distance between the reality of the control system and the simulations, experimental tests on a duct lined with EAs prototypes validate the numerical results in terms of isolation performances, non-reciprocal propagation, and stability concerns. In order to assure acoustical passivity in the operating frequency range, all the parameters involved in the control law must be carefully chosen. The advection speed must be limited to the threshold assuring the passivity around resonance. Such a limit is more stringent for narrower ducts, and higher reactive components (μ_M and μ_K) in $Z_{Loc}(\mathrm{j}\omega) = Z_{at}(\mathrm{j}\omega)$. On the other hand, the lower limit of the reactive component μ_M is given by the high-frequency passivity issue related to time-delay (as demonstrated in Chapter 2).
A foam applied on the EAs, as done in Chapter 2, can allow to cope with the high-frequency passivity issues, highlighting the importance of a correct porous layer design.

3.7 Next steps

The natural further development in the analysis of the advective strategy, is to investigate its multi-modal scattering performances. Moreover, it will be interesting to study the application of an advective B.C. on a convected acoustic domain (with a mean flow). This is currently under development, and the advection control law is showing to perform better isolation performances respect to the local control strategy, even in presence of mean flow.

The addition of another degree of freedom, i.e. the non-locality, in the boundary control can very much stimulate the fantasy of the interested researchers. The non-reciprocity allows also to device a focal concentration of acoustic energy (currently under testing), as well as other fanciful sound trajectory steering.

Finally, as the technological architecture employed for the advective strategy is the same as the local impedance control, the next developments proposed in Section 2.6, in terms of control optimization, are prospected here as well.

Chapter 4

Innovations achieved and next developments

This small chapter is dedicated to the main accomplishment achieved in this thesis work.

Much effort has been spent at the beginning to overcome stability issues of the boundary control strategies. This has led to an important insight on the *acoustical passivity*, and the high-frequency effect of time delay. From that, the knowledge about porous materials, has opened up to the possibility of exploiting the high-frequency absorptive qualities of foams to *passivate* the impedance controlled EA. Such "hybrid" system differs from the classical ones as here the passive absorber has the only scope to enlarge the *acoustical* passivity margin of the EA.

A great deal of study has been devoted to provide analytical tools to understand subtle aspects of the impedance control strategies. An example is the extension of the integral constraint to our electro-active impedance controlled devices. Originally, an integral constraint was obtained by Yang et al. [122] in 2017 for passive sound absorbing materials. Though, we were not aware of this result when we performed the analytical computations for the EA. The motivation for such analytical effort was given by a kind of "waterbed effect" observed when the system were "pushed" by the corrector at frequencies below or beyond resonance. The integral constraint for the EA, allows to understand both the value and the drawbacks of the electro-active impedance control with respect to purely passive absorbing materials. As the result of Yang has lead to an optimal design strategy of passive absorbers, the integral constraint here presented can drive optimal design of EAs. An interesting perspective in this sense, is to study target impedances other than the SDOF in-series one. In parallel elements (as proposed by Auregan et al. [2]) can indeed allow to efficiently target the bandwidth below resonance, and keep perfect acoustical passivity beyond it (currently under testing).

The importance of the integral constraint resides also in the better understanding of the performances of the correctors automatically synthesized by the H_∞ method. Never before, such approach has been used for the acoustical impedance control. In this work, we formulated the impedance control in the H_∞ formalism, and provided also a smart way to enforce

passivity in the specifications. Experimental tests will soon be performed to complete such study. Then, the next developments will have to take into account robustness with respect to parameter and dynamic uncertainties.

An innovative real-time implementation of the impedance control has been proposed to conceive non-linear dynamics of the EA, without the use of additional sensors. The feasibility of such Runge-Kutta based control strategy must also be validated experimentally. Though numerical simulations in both stationary and transient regimes advocate such approach.

Concerning the advection control law, its experimental implementation has been for long time a hurdle since its first appearance in 2009 [22]. A better mathematical and physical understanding was required, which have been partially achieved in this work. Moreover, the advection B.C. has been here presented for the first time as an extension of the local impedance control, realizing its advective behaviour and consequent reciprocity-breaking phenomenon.
The resulted non-reciprocal device is an unique case in non-reciprocal acoustics, as it does not rely upon internal bias fields (such as the air flow in [40]), but it is based upon a programmable boundary *reaction*.

The parametric analyses performed both numerically and experimentally, allow now to make use of such control strategies, being aware of the impacts of each parameter both on stability and performances. The filter here designed for the implementation of the advective B.C., is currently showing exceptional performances also in case of a mean flow in the duct, in the plane wave regime.
A study in case of multi-modal excitation is strongly required, as the duct mode analysis of Section 3.2 has raised important concerns on the stability of higher duct modes propagation. Nevertheless, we should not prevent ourselves from envisaging different "advective" strategies to target higher order modes isolation, as well as exploiting the *non-local* character to conceive other boundary operators allowing larger absorption performances.

List of figures

List of Tables

Bibliography

[1] Allard, J. F. and Atalla, N. (2009). *Propagation of Sound in Porous Media: Modelling Sound Absorbing Materials*. John Wiley & Sons. 17, 49, 51, 86, XXIII

[2] Aurégan, Y. and Farooqui, M. (2019). In-parallel resonators to increase the absorption of subwavelength acoustic absorbers in the mid-frequency range. *Scientific reports*, 9(1):1–6. 139

[3] Aurégan, Y., Farooqui, M., and Groby, J.-P. (2016). Low frequency sound attenuation in a flow duct using a thin slow sound material. *The Journal of the Acoustical Society of America*, 139(5):EL149—-EL153. 25, 27, 142

[4] Aurégan, Y. and Pagneux, V. (2015). Slow sound in lined flow ducts. *The Journal of the Acoustical Society of America*, 138(2):605–613. XXIV

[5] Baker, G. A., Baker Jr, G. A., BAKER JR, G. A., Graves-Morris, P., and Baker, S. S. (1996). *Padé approximants*, volume 59. Cambridge University Press, Cambridge CB2 8RY, UK. 48

[6] Bao, J., Lee, P. L., and Ydstie, B. E. (2010). Process Control: The Passive Systems Approach. *IEEE Control Systems*, 30(1):78–80. 31, 47

[7] Bardos, C., Lebeau, G., and Rauch, J. (1992). Sharp sufficient conditions for the observation, control, and stabilization of waves from the boundary. *SIAM journal on control and optimization*, 30(5):1024–1065. 18

[8] Beck, B. S., Schiller, N. H., and Jones, M. G. (2015). Impedance assessment of a dual-resonance acoustic liner. *Applied Acoustics*, 93:15–22. 24, 26, 142

[9] Bellet, R., Cochelin, B., Herzog, P., and Mattei, P.-O. (2010). Experimental study of targeted energy transfer from an acoustic system to a nonlinear membrane absorber. *Journal of Sound and Vibration*, 329(14):2768–2791. 71, 79

[10] Beranek, L. L. and Mellow, T. (2012). *Acoustics: Sound Fields and Transducers*. Academic Press, Oxford OX5 1GB, UK. 41

[11] Betgen, B. and Galland, M. A. (2011). A new hybrid active/passive sound absorber with variable surface impedance. *Mechanical Systems and Signal Processing*, 25(5):1715–1726. 30, 31, 142

[12] Boer, E. D. (1961). Theory of Motional Feedback. *IRE Trans. Audio*, AU-9(1):15–21. 31

[13] Boulandet, R. and Lissek, H. (2014). Toward broadband electroacoustic resonators through optimized feedback control strategies. *Journal of Sound and Vibration*, 333(20):4810–4825. 47, 49

[14] Boulandet, R., Lissek, H., Karkar, S., Collet, M., Matten, G., Ouisse, M., and Versaevel, M. (2018). Duct modes damping through an adjustable electroacoustic liner under grazing incidence. *Journal of Sound and Vibration*, 426:19–33. 32

[15] Boulandet, R., Rivet, E., and Lissek, H. (2016). Sensorless electroacoustic absorbers through synthesized impedance control for damping low-frequency modes in cavities. *Acta Acustica united with Acustica*, 102(4):696–704. 30, 31, 142

[16] Brambley, E. and Peake, N. (2006). Surface-waves, stability, and scattering for a lined duct with flow. In *12th AIAA/CEAS Aeroacoustics Conference (27th AIAA Aeroacoustics Conference)*, page 2688. 109

[17] Caloz, C., Alu, A., Tretyakov, S., Sounas, D., Achouri, K., and Deck-Léger, Z.-L. (2018). Electromagnetic nonreciprocity. *Physical Review Applied*, 10(4):47001. 33, 34, 142

[18] Campeau, S., Panneton, R., and Elkoun, S. (2019). Experimental Validation of an Acoustical Micro-Macro Model for Random Hollow Fibre Structures. *Acta Acustica united with Acustica*, 105(1):240–247. 26

[19] Chen, C., Du, Z., Hu, G., and Yang, J. (2017). A low-frequency sound absorbing material with subwavelength thickness. *Applied Physics Letters*, 110(22):221903. 27

[20] Clark, R. L., Frampton, K. D., and Cole, D. G. (1996). Phase compensation for feedback control of enclosed sound fields. *Journal of Sound and Vibration*, 195(5):701–718. 30

[21] Cohen-Tannoudji, C., Diu, B., and Laloe, F. (2009). Quantum mechanics. Vol. 1. 4. rev. upd. ed.; Quantenmechanik. Bd. 1. 37

[22] Collet, M., David, P., and Berthillier, M. (2009). Active acoustical impedance using distributed electrodynamical transducers. *The Journal of the Acoustical Society of America*, 125(2):882–894. 19, 20, 33, 37, 39, 86, 87, 135, 140

[23] Collet, M., Ouisse, M., and Ichchou, M. N. (2012). Structural energy flow optimization through adaptive shunted piezoelectric metacomposites. *Journal of Intelligent Material Systems and Structures*, 23(15):1661–1677. 99

[24] Cremer, L. (1953). Theory regarding the attenuation of sound transmitted by air in a rectangular duct with an absorbing wall, and the maximum attenuation constant produced during this process. *Acustica*, 3(1):249. 18, 20, 31, 43, 141

[25] Cremer, L. and Heckl, M. (2013). *Structure-borne sound: structural vibrations and sound radiation at audio frequencies*. Springer Science and Business Media. 89, 91

[26] de Bedout, J. M., Franchek, M. A., Bernhard, R. J., and Mongeau, L. (1997). Adaptive-passive noise control with self-tuning Helmholtz resonators. *Journal of Sound and Vibration*, 202(1):109–123. 28

[27] de Larminat, P. (2007). *Automatique appliquée*. Hermès Science publications/Lavoisier. 30, 54, 83

[28] D'Elia, M. E., Humbert, T., and Aurégan, Y. (2020). Effect of flow on an array of Helmholtz resonators: Is Kevlar a "magic layer"? *The Journal of the Acoustical Society of America*, 148(6):3392–3396. 17

[29] Detroux, T., Habib, G., Masset, L., and Kerschen, G. (2015). Performance, robustness and sensitivity analysis of the nonlinear tuned vibration absorber. *Mechanical Systems and Signal Processing*, 60:799–809. 71

[30] Devasia, S. (2002). Should model-based inverse inputs be used as feedforward under plant uncertainty? *IEEE Transactions on Automatic Control*, 47(11):1865–1871. 84

[31] Dullerud, G. E. and Paganini, F. (2013). *A course in robust control theory: a convex approach*, volume 36. Springer Science and Business Media. 65, 84

[32] Elliott, S. J. and Nelson, P. A. (1993). Active noise control. *IEEE signal processing magazine*, 10(4):12–35. 29, 30, 142

[33] Esfahlani, H., Karkar, S., Lissek, H., and Mosig, J. R. (2016). Acoustic carpet cloak based on an ultrathin metasurface. *Physical Review B*, 94(1):14302. 32

[34] Esteve, S. J. and Johnson, M. E. (2004). Development of an adaptive Helmholtz resonator for broadband noise control. In *ASME International Mechanical Engineering Congress and Exposition*, volume 47152, pages 47–53. 28, 142

[35] Fano, R. M. (1950). Theoretical limitations on the broadband matching of arbitrary impedances. *Journal of the Franklin Institute*, 249(1):57–83. X

[36] Filippi, P., Bergassoli, A., Habault, D., and Lefebvre, J. P. (1998). *Acoustics: basic physics, theory, and methods*. Academic press, London NW1 7DX, UK. 91, VI

[37] Fleming, A. J., Niederberger, D., Moheimani, S. O., and Morari, M. (2007). Control of resonant acoustic sound fields by electrical shunting of a loudspeaker. *IEEE Transactions on Control Systems Technology*, 15(4):689–703. 30, 31, 32, 142

[38] Fleury, R., Sounas, D., Haberman, M. R., and Alu, A. (2015a). Nonreciprocal acoustics. *Acoustics Today*, 11(ARTICLE):14–21. 33, 35, 36, 37, 142

[39] Fleury, R., Sounas, D. L., and Alù, A. (2015b). Subwavelength ultrasonic circulator based on spatiotemporal modulation. *Physical Review B*, 91(17):174306. 37, 38, 39, 143

[40] Fleury, R., Sounas, D. L., Sieck, C. F., Haberman, M. R., and Alù, A. (2014). Sound Isolation and Giant Linear Nonreciprocity in a Compact Acoustic Circulator. *Science*, 343(6170):516–519. 36, 37, 39, 140, 143

[41] Furstoss, M., Thenail, D., and Galland, M. (1997). Surface impedance control for sound absorption: direct and hybrid passive/active strategies. *Journal of Sound and Vibration*, 203(2):219–236. 30, 31, 142

[42] Gahinet, P. and Apkarian, P. (1994). A linear matrix inequality approach to H_{infty} control. *International journal of robust and nonlinear control*, 4(4):421–448. 61

[43] Galland, M.-A., Mazeaud, B., and Sellen, N. (2005). Hybrid passive/active absorbers for flow ducts. *Applied Acoustics*, 66(6):691–708. 30, 31, 51, 142

[44] Gendelman, O., Manevitch, L. I., Vakakis, A. F., and M'closkey, R. (2001). Energy pumping in nonlinear mechanical oscillators: part I—dynamics of the underlying Hamiltonian systems. *J. Appl. Mech.*, 68(1):34–41. 71

[45] Goodwin, G. C., Graebe, S. F., and Salgado, M. E. (2007). *Control System Design*, volume 27. Prentice Hall New Jersey. 43, 59, VII

[46] Gourdon, E., Alexander, N. A., Taylor, C. A., Lamarque, C.-H., and Pernot, S. (2007). Nonlinear energy pumping under transient forcing with strongly nonlinear coupling: Theoretical and experimental results. *Journal of sound and vibration*, 300(3-5):522–551. 82

[47] Groby, J.-P., Huang, W., Lardeau, A., and Aurégan, Y. (2015). The use of slow waves to design simple sound absorbing materials. *Journal of Applied Physics*, 117(12):124903. 25, 26, 142

[48] Guess, A. W. (1975). Calculation of perforated plate liner parameters from specified acoustic resistance and reactance. *Journal of Sound and Vibration*, 40(1):119–137. 24

[49] Guicking, D. and Karcher, K. (1984). Active impedance control for one-dimensional sound. 31

[50] Guicking, D. and Lorenz, E. (1984). An active sound absorber with porous plate. *Journal of Vibration and Acoustics, Transactions of the ASME*, 106(3):389–392. 30, 142

[51] Guo, X., Lissek, H., and Fleury, R. (2020). Improving Sound Absorption Through Nonlinear Active Electroacoustic Resonators. *Physical Review Applied*, 13(1):014018. 68, 71, 84

[52] Hermiller, J. M. and Maddux, M. R. (2013). Morphing Resonators for Adaptive Noise Reduction. *Acoustical Society of America Journal*, 134(5):3963. 28, 142

[53] Higdon, R. L. (1987). Numerical Absorbing Boundary Conditions for the Wave Equation. *Mathematics of Computation*, 49(179):65. 20, 32

[54] Horowitz, S. B., Nishida, T., Cattafesta III, L. N., and Sheplak, M. (2002). Characterization of a compliant-backplate Helmholtz resonator for an electromechanical acoustic liner. *International Journal of Aeroacoustics*, 1(2):183–205. 29

[55] Ingard, U. (1959). Influence of fluid motion past a plane boundary on sound reflection, absorption, and transmission. *The Journal of the Acoustical Society of America*, 31(7):1035–1036. 87, XVII

[56] Ingard, U. (2009). *Noise reduction analysis*. Jones & Bartlett Publishers. 86

[57] International, A. (2009). ASTM E2611-09 Standard Test Method for Measurement of Normal Incidence Sound Transmission of Acoustical Materials Based on the Transfer Matrix Method. ASTM. 121

[58] Johnson, M. E. and Esteve, S. (2002). Comparison of local and global adaptive strategies for the control of broadband noise in an enclosure using adaptive Helmholtz resonators. In *INTER-NOISE and NOISE-CON Congress and Conference Proceedings*, volume 2002, pages 1111–1120. Institute of Noise Control Engineering. 28

[59] Karkar, S., De Bono, E., Collet, M., Matten, G., Ouisse, M., and Rivet, E. (2019). Broadband Nonreciprocal Acoustic Propagation Using Programmable Boundary Conditions: From Analytical Modeling to Experimental Implementation. *Physical Review Applied*, 12(5):054033. 27, 33, 37, 38, 39, 143

[60] Kelkar, A. G. and Joshi, S. N. (1997). Robust control of non-passive systems via passification [for passification read passivation]. In *Proceedings of the 1997 American Control Conference (Cat. No. 97CH36041)*, volume 5, pages 2657–2661. IEEE. 49

[61] Kido, K. (1991). The technologies for active noise control. *Journal of the Acoustical Society of Japan (E)*, 12(6):245–253. 31

[62] Kinsler, L. E., Frey, A. R., Coppens, A. B., and Sanders, J. V. (1999). *Fundamentals of acoustics*. V, VI

[63] Kittel, C. (1958). Interaction of spin waves and ultrasonic waves in ferromagnetic crystals. *Physical Review*, 110(4):836. 37

[64] Kobayashi, H., Koh, M., Ozaki, S., Yokochi, M., and Sato, T. (2006). Newly-developed adaptive noise absorption control technology for high speed fan noise reduction. *JSME International Journal Series C Mechanical Systems, Machine Elements and Manufacturing*, 49(3):703–712. 28

[65] Konishi, S., Yoda, M., Hosaka, N., Sugiyama, S., and Akishita, S. (1998). Tunable acoustic absorbing system using a deep hole array. In *Proceedings MEMS 98. IEEE. Eleventh Annual International Workshop on Micro Electro Mechanical Systems. An Investigation of Micro Structures, Sensors, Actuators, Machines and Systems (Cat. No. 98CH36176*, pages 655–660. IEEE. 28

[66] Kostek, T. M. and Franchek, M. A. (2000). Hybrid noise control in ducts. *Journal of Sound and Vibration*, 237(1):81–100. 28

[67] Lagarrigue, C., Groby, J.-P., Tournat, V., Dazel, O., and Umnova, O. (2013). Absorption of sound by porous layers with embedded periodic arrays of resonant inclusions. *The Journal of the Acoustical Society of America*, 134(6):4670–4680. 25, 26, 142

[68] Lane, S. A. and Clark, R. L. (1998). Active control of a reverberant enclosure using an approximate constant volume velocity source. In *Proceedings of the American Control Conference*, volume 4, pages 2606–2610. IEEE. 30

[69] Lax, B., Button, K. J., and Hagger, H. J. (1963). Microwave ferrites and ferrimagnetics. *Physics Today*, 16(8):57. 37

[70] Leo, D. J. and Limpert, D. K. (1999). Self-sensing technique for active acoustic attenuation. In *Collection of Technical Papers - AIAA/ASME/ASCE/AHS/ASC Structures, Structural Dynamics and Materials Conference*, volume 4, pages 2603–2610, Reston, Virigina. American Institute of Aeronautics and Astronautics. 30, 31, 142

[71] Li, Y. and Assouar, B. M. (2016). Acoustic metasurface-based perfect absorber with deep subwavelength thickness. *Applied Physics Letters*, 108(6):63502. 27

[72] Liang, B., Yuan, B., and Cheng, J.-c. (2009). Acoustic Diode: Rectification of Acoustic Energy Flux in One-Dimensional Systems. *Physycal Review Letters*, 103(10):104301. 34

[73] Lin, G., Kim, C.-J., Konishi, S., and Fujita, H. (1995). Design, fabrication, and testing of a C-shape actuator. In *Proceedings of the International Solid-State Sensors and Actuators Conference-TRANSDUCERS'95*, volume 2, pages 416–419. IEEE. 28

[74] Lissek, H., Boulandet, R., and Fleury, R. (2011). Electroacoustic absorbers: Bridging a gap between active sound absorption and shunt loudspeakers. *18th Int. Congr. Sound Vib. 2011, ICSV 2011*, 1(5):141–148. 30, 31, 142

[75] Liu, F., Horowitz, S., Nishida, T., Cattafesta, L., and Sheplak, M. (2007). A multiple degree of freedom electromechanical Helmholtz resonator. *The Journal of the Acoustical Society of America*, 122(1):291–301. 29

[76] Ma, G., Yang, M., Xiao, S., Yang, Z., and Sheng, P. (2014). Acoustic metasurface with hybrid resonances. *Nature materials*, 13(9):873–878. 27

[77] Ma, X. and Su, Z. (2020). Development of acoustic liner in aero engine: a review. *Science China Technological Sciences*, pages 1–14. 21, 23, 24, 25, 28, 141

[78] Marconi, J., Riva, E., Di Ronco, M., Cazzulani, G., Braghin, F., and Ruzzene, M. (2020). Experimental observation of nonreciprocal band gaps in a space-time-modulated beam using a shunted piezoelectric array. *Physical Review Applied*, 13(3):31001. 36, 142

[79] Matsuhisa, H., Ren, B., and Sato, S. (1992). Semiactive control of duct noise by a volume-variable resonator. *JSME international journal. Ser. 3, Vibration, control engineering, engineering for industry*, 35(2):223–228. 28, 142

[80] Mcdonald, A. M., Hutchins, S. M., Stothers, I., and Crowther, P. J. (1997). Method and apparatus for attenuating acoustic vibrations in a medium. 28

[81] Mei, J., Ma, G., Yang, M., Yang, Z., Wen, W., and Sheng, P. (2012). Dark acoustic metamaterials as super absorbers for low-frequency sound. *Nature communications*, 3(1):1–7. 27

[82] Meirovitch, L. (1975). *Elements of vibration analysis*. 77

[83] Miki, Y. (1990). Acoustical properties of porous materials-Modifications of Delany-Bazley models-. *Journal of the Acoustical Society of Japan (E)*, 11(1):19–24. 49, 120

[84] Miljkovic, D. (2016). Active noise control: From analog to digital - Last 80 years. In *2016 39th International Convention on Information and Communication Technology, Electronics and Microelectronics, MIPRO 2016 - Proceedings*, pages 1151–1156. IEEE. 30

[85] Moiola, A., Hiptmair, R., and Perugia, I. (2011). Plane wave approximation of homogeneous Helmholtz solutions. *Zeitschrift fur Angewandte Mathematik und Physik*, 62(5):809–837. 17, 32

[86] Montseny, G. (1998). Diffusive representation of pseudo-differential time-operators. 86

[87] Morse, P. M. (1939). Some aspects of the theory of room acoustics. *The Journal of the Acoustical Society of America*, 11(1):56–66. 16, 17, 85

[88] Mullis, C. and Roberts, R. A. (1976). Synthesis of minimum roundoff noise fixed point digital filters. *IEEE Transactions on Circuits and Systems*, 23(9):551–562. XIII

[89] Nagaya, K., Hano, Y., and Suda, A. (2001). Silencer consisting of two-stage Helmholtz resonator with auto-tuning control. *the Journal of the Acoustical Society of America*, 110(1):289–295. 28

[90] Olson, H. F. and May, E. G. (1953). Electronic Sound Absorber. *Journal of the Acoustical Society of America*, 25(6):1130–1136. 30, 142

[91] Opiela, K. C. and Zieliński, T. G. (2020). Microstructural design, manufacturing and dual-scale modelling of an adaptable porous composite sound absorber. *Composites Part B: Engineering*, 187:107833. 26

[92] Orduna-Bustamantea, F. and Nelson, P. A. (1992). An adaptive controller for the active absorption of sound. *Journal of the Acoustical Society of America*, 91(5):2740–2747. 31

[93] Parente, C. A., Arcas, N., Walker, B. E., Hersh, A. S., and Rice, E. J. (1999). Hybrid active/passive jet engine noise suppression system. 28

[94] Parrott, T. L. and Jones, M. G. (1995). Parallel-element liner impedances for improved absorption of broadband sound in ducts. *Noise Control Engineering Journal*, 43(6):183–195. 25

[95] Pease, R. A. (2008). A Comprehensive Study of the Howland Current Pump A Comprehensive Study of the Howland Current Pump Applications for the Howland Current Pump AN-1515. *Most*, 29:12. 32

[96] Phipps, A., Liu, F., Cattafesta, L., Sheplak, M., and Nishida, T. (2009). Demonstration of a wireless, self-powered, electroacoustic liner system. *The Journal of the Acoustical Society of America*, 125(2):873–881. 29

[97] Popa, B.-I. and Cummer, S. (2014). Non-reciprocal and highly nonlinear active acoustic metamaterials. *Nature Communications*, 5. 35

[98] Pozar, D. M. (2011). *Microwave engineering*. John wiley & sons. 37

[99] Quinn, M. C. and Howe, M. S. (1984). On the production and absorption of sound by lossless liners in the presence of mean flow. *Journal of Sound and Vibration*, 97(1):1–9. 109

[100] Rienstra, S. W. (1986). Hydrodynamic instabilities and surface waves in a flow over an impedance wall. In *Aero-and Hydro-Acoustics*, pages 483–490. Springer. 109

[101] Rienstra, S. W. (2003). A classification of duct modes based on surface waves. *Wave motion*, 37(2):119–135. 109

[102] Rienstra, S. W. and Tester, B. J. (2008). An analytic Green's function for a lined circular duct containing uniform mean flow. *Journal of Sound and Vibration*, 317(3-5):994–1016. 109

[103] Rivet, E., Karkar, S., and Lissek, H. (2014). Absorbeurs électroacoustiques pour l'égalisation modale des salles: une nouvelle approche avec des haut-parleurs à double bobine (Electroacoustic Absorbers for the modal equalization in rooms: a new approach with double coil loud-speakers). In *CFA Poitiers 2014*, pages 1157–1163. 31

[104] Rivet, E., Karkar, S., and Lissek, H. (2016). Broadband low-frequency electroacoustic absorbers through hybrid sensor-/shunt-based impedance control. *IEEE Transactions on Control Systems Technology*, 25(1):63–72. 32, 39, 41, 43, 44, 47, 83

[105] Rivet, E., Karkar, S., and Lissek, H. (2017). On the optimisation of multi-degree-of-freedom acoustic impedances of low-frequency electroacoustic absorbers for room modal equalisation. *Acta Acustica United With Acustica*, 103(6):1025–1036. 32

[106] Rivet, E. T. J.-L. (2016). *Room Modal Equalisation with Electroacoustic Absorbers*. PhD thesis, EPFL. 32, 41, 43, 44, 45, 47, 54

[107] Rozanov, K. N. (2000). Ultimate thickness to bandwidth ratio of radar absorbers. *IEEE Transactions on Antennas and Propagation*, 48(8):1230–1234. X

[108] Samejima, T. (2003). A state feedback electro-acoustic transducer for active control of acoustic impedance. *The Journal of the Acoustical Society of America*, 113(3):1483–1491. 31

[109] Sasmal, A., Geib, N., Popa, B.-I., and Grosh, K. (2020). Broadband nonreciprocal linear acoustics through a non-local active metamaterial. *New Journal of Physics*, 22(6):63010. 38, 39, 143

[110] Scott, D. B., Churchill, R. V., and Brown, J. W. (1985). *Complex Variables and Applications*, volume 69. Boston: McGraw-Hill Higher Education,. VIII, IX

[111] Sounas, D. L. and Alù, A. (2017). Non-reciprocal photonics based on time modulation. *Nature Photonics*, 11(12):774–783. 36

[112] Standard, A. (2012). E1050-12,". *Stand. test method impedance Absorpt. Acoust. Mater. using a tube, two microphones, a Digit. Freq. Anal. Syst.* 53

[113] Strutt, J. W. (1871). Some general theorems relating to vibrations. *Proceedings of the London Mathematical Society*, 1(1):357–368. 33

[114] Strutt, J. W. and Rayleigh, J. W. S. B. (1877). *The theory of sound*, volume 1. Macmillan. 33

[115] Tang, Y., Ren, S., Meng, H., Xin, F., Huang, L., Chen, T., Zhang, C., and Lu, T. J. (2017). Hybrid acoustic metamaterial as super absorber for broadband low-frequency sound. *Scientific reports*, 7(1):1–11. 24, 26, 142

[116] Tester, B. (1973a). The optimization of modal sound attenuation in ducts, in the absence of mean flow. *Journal of Sound and Vibration*, 27(4):477–513. 17, 19, 20, 31

[117] Tester, B. J. (1973b). Ray models for sound propagation and attenuation in ducts, in the absence of mean flow. *Journal of Sound and Vibration*, 27(4):515–531. 19

[118] Tukuljac, H. P., Vu, T. P., Lissek, H., and Vandergheynst, P. (2018). Joint estimation of the room geometry and modes with compressed sensing. In *ICASSP, IEEE International Conference on Acoustics, Speech and Signal Processing - Proceedings*, volume 2018-April, pages 6882–6886. IEEE, IEEE. 17, 32

[119] Vakakis, A. F. and Gendelman, O. (2001). Energy pumping in nonlinear mechanical oscillators: part II—resonance capture. *J. Appl. Mech.*, 68(1):42–48. 71

[120] Wang, Y., Yousefzadeh, B., Chen, H., Nassar, H., Huang, G., and Daraio, C. (2018). Observation of nonreciprocal wave propagation in a dynamic phononic lattice. *Physical review letters*, 121(19):194301. 36, 142

[121] Xia, M., Antsaklis, P. J., and Gupta, V. (2014). Passivity indices and passivation of systems with application to systems with input/output delay. In *Proceedings of the IEEE Conference on Decision and Control*, volume 2015-Febru, pages 783–788. IEEE. 50, 51, 83

[122] Yang, M., Chen, S., Fu, C., and Sheng, P. (2017). Optimal sound-absorbing structures. *Materials Horizons*, 4(4):673–680. 26, 27, 28, 40, 57, 58, 83, 139, 142, X

[123] Yang, M. and Sheng, P. (2017). Sound absorption structures: From porous media to acoustic metamaterials. *Annual Review of Materials Research*, 47:83–114. 21, 22, 141

[124] Yang, Z., Mei, J., Yang, M., Chan, N. H., and Sheng, P. (2008). Membrane-type acoustic metamaterial with negative dynamic mass. *Physical review letters*, 101(20):204301. 27

[125] Yi, K., Ouisse, M., Sadoulet-Reboul, E., and Matten, G. (2019). Active metamaterials with broadband controllable stiffness for tunable band gaps and non-reciprocal wave propagation. *Smart Materials and Structures*, 28(6):65025. 36, 142

[126] Zames, G. (1966). On the input-output stability of time-varying nonlinear feedback systems part one: Conditions derived using concepts of loop gain, conicity, and positivity. *IEEE transactions on automatic control*, 11(2):228–238. 60

[127] Zames, G. (1981). Feedback and optimal sensitivity: Model reference transformations, multiplicative seminorms, and approximate inverses. *IEEE Transactions on automatic control*, 26(2):301–320. 60

[128] Zangeneh-Nejad, F. and Fleury, R. (2019). Active times for acoustic metamaterials. *Reviews in Physics*, 4:100031. 27

Appendix A

Loudspeaker Mechano-Acoustical Dynamics Identification

In this Appendix, we describe the methods adopted to retrieve the Thiele-Small parameters of the EA. In order to implement the model-inversion based control laws of Eq.s (3.45) and (3.46), the mechano-acoustical dynamics of the EA in open circuit is required along with the factor Bl/S_d multiplying the electrical current (the controller). In the frequency range around the piston-mode of the speaker, the mechano-acoustical dynamics of the EA in open circuit (O.C.) is described by the acoustical impedance $Z_{a0}(\mathrm{j}\omega) = M_{a0}\mathrm{j}\omega + R_{a0} + K_{a0}/\mathrm{j}\omega$. The open-circuit impedance of the EA can be estimated experimentally either with a Kundt's tube by the 2-microphone-method (2MM), or by direct measurement of pressure and velocity on the loudspeaker diaphragm. Figure 2.12 shows the Kundt's tube designed for the EA, while Figure A.1 shows the experimental setup for direct measurement of the acoustical impedance by a Laser-Doppler-Velocimeter (LDV) and a microphone. In both cases, the estimated acoustical impedance can be curve-fitted in order to retrieve M_{a0}, R_{a0} and K_{a0}. In Figure A.2 the O.C. acoustical impedances retrieved either with the Kundt's tube (left), or with the direct measurement of local pressure and velocity on the speaker diaphragm (right) are plotted, along with the corresponding curve-fitting based on the piston-mode assumption. Apparently, the use of the Kundt's tube introduces unexpected cavity modes (see the one around 1 kHz) which can affect the precision of the curve-fitting.

In order to estimate Bl/S_d, an additional measurement is required. A possibility is to exploit the current-driven control architecture to impose a proportional controller (P.C.) $i(\mathrm{j}\omega) = gp(\mathrm{j}\omega)$, with g a constant gain. By doing so, the acoustic impedance at the speaker diaphragm becomes:

$$Z_a(\mathrm{j}\omega) = \frac{Z_{a0}(\mathrm{j}\omega)}{1 - \frac{Bl}{S_d}g}. \tag{A.1}$$

As $Z_{a0}(\mathrm{j}\omega)$ has already been estimated from the O.C. measurement, another curve-fitting can be carried out to retrieve Bl/S_d, see Figure A.3.

A way to estimate Bl and S_d separately, requires the impedance measurement in an additional configuration: the short-circuit of the speaker terminals. Eq. (A.2) is the loudspeaker electrical dynamics model valid at low frequencies, with $Z_e(\mathrm{j}\omega)$ the electrical impedance at

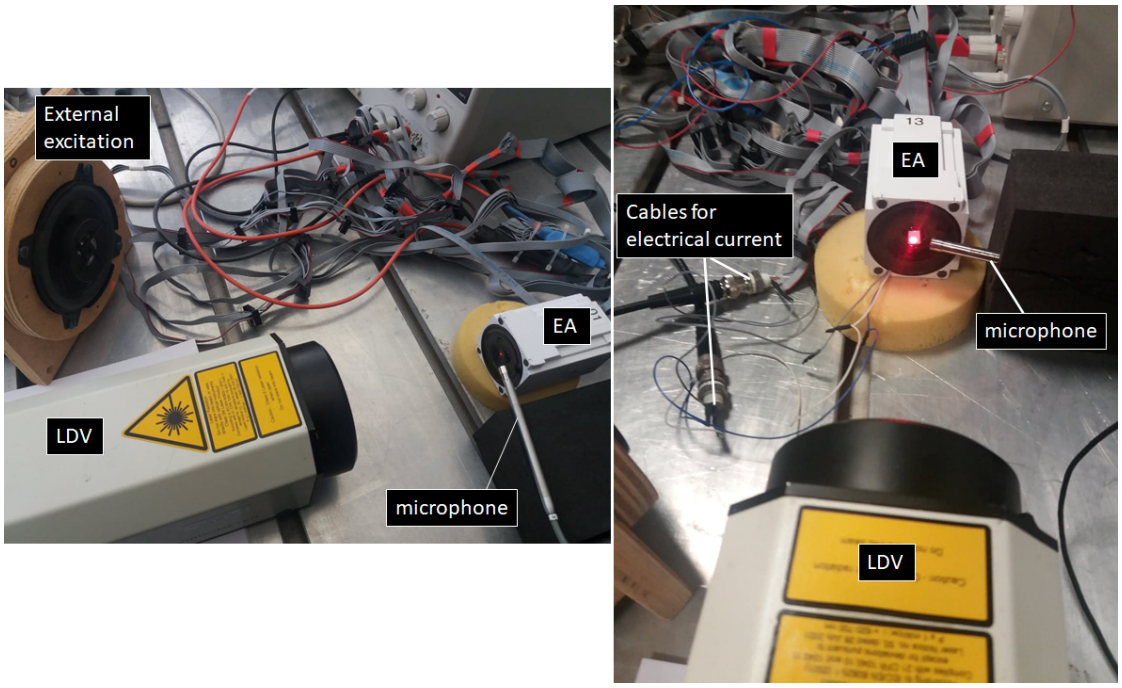

Figure A.1: Experimental setup to measure pressure and velocity on the speaker diaphragm, as well as the electrical current in the voice coil on the right.

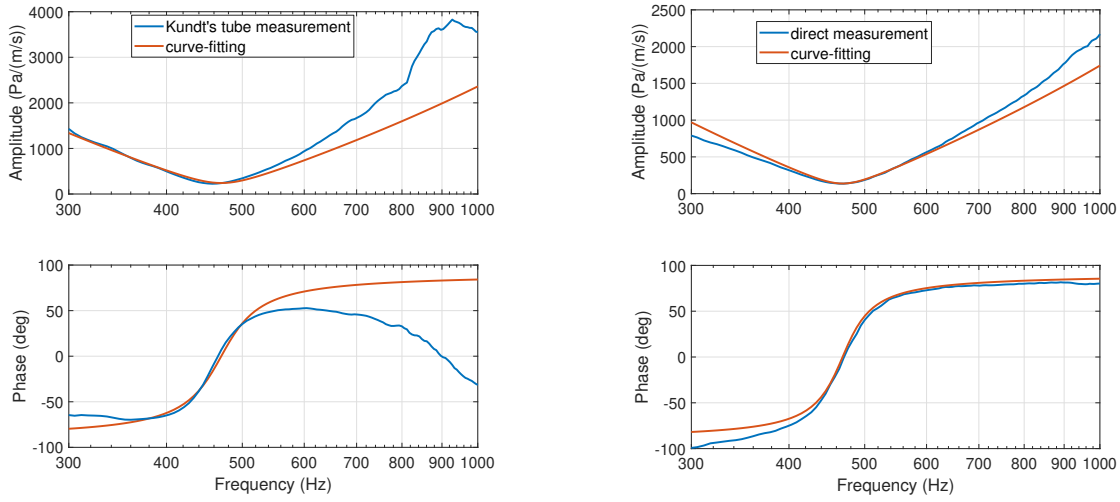

(a) (b)

Figure A.2: Acoustical impedance estimated either with the Kundt's tube (left), or with the direct measurement of local pressure and velocity on the speaker diaphragm (right), and corresponding curve-fittings, in case of O.C., around the resonance of the piston-mode.

the speaker terminals, usually approximated by $Z_e(\mathrm{j}\omega) = R_e + \mathrm{j}\omega L_e$ with R_e and L_e the electrical resistance and inductance of the voice coil respectively.

$$Z_e(\mathrm{j}\omega)i(\mathrm{j}\omega) = Blv(\mathrm{j}\omega). \tag{A.2}$$

As the inductance term is usually much lower than R_e at lower frequencies, it can be discarded to obtain $i(\mathrm{j}\omega) \approx v(\mathrm{j}\omega)Bl/R_e$. By inserting such expression in the mechano-acoustical

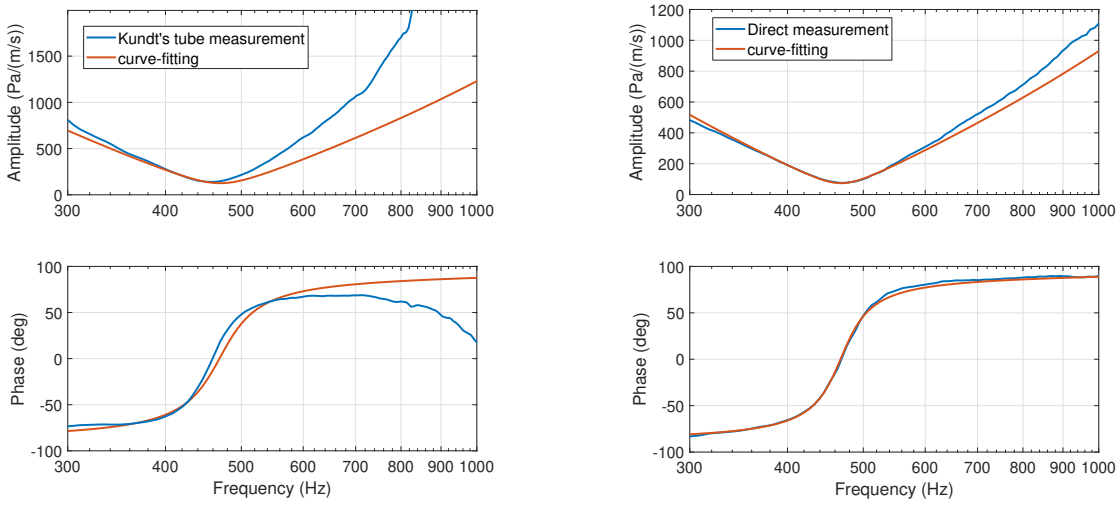

(a) (b)

Figure A.3: Acoustical impedance estimated either with the Kundt's tube (left), or with the direct measurement of local pressure and velocity on the speaker diaphragm (right), and corresponding curve-fittings, in case of P.C., around the resonance of the piston-mode.

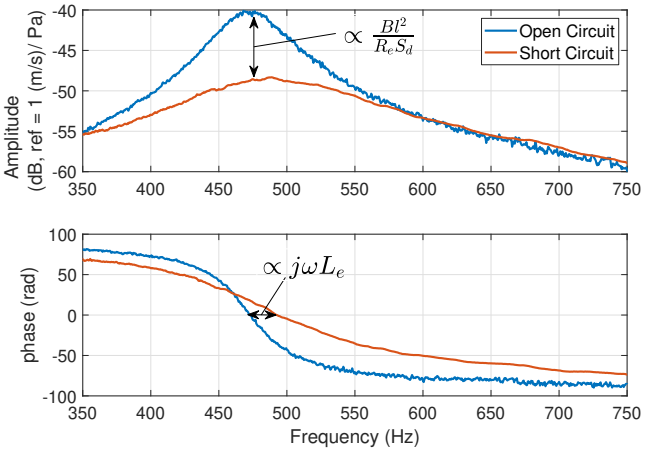

Figure A.4: Measured acoustic mobility (inverse of impedance) in case of open-circuited and short-circuited loudspeaker terminals.

dynamics, we get:

$$\left(Z_{a0}(\mathrm{j}\omega) + \frac{Bl^2}{S_d R_e}\right) v(\mathrm{j}\omega) = p(\mathrm{j}\omega). \tag{A.3}$$

Knowing R_e, by curve-fitting the measured impedance $p(\mathrm{j}\omega)/v(\mathrm{j}\omega)$ it is possible to retrieve Bl^2/S_d. As Bl/S_d can be obtained from the P.C. impedance estimation, Bl and S_d can therefore be identified separately. In Figure A.4 the O.C. mobility measurement is compared to the S.C. one, highlighting the effect of $Bl/(R_e S_d)$ and of the inductance term, on the amplitude and phase respectively.

Appendix B

Stability in a 1D acoustic cavity

Let us consider a 1D hard-walled acoustic cavity as depicted in Figure B.1 with a rigid termination on one side and a generic acoustic element, which can consist of our EA, on the other.

According to the plane wave decomposition [62] the acoustic pressure in the duct is described by $p(x,t) = p^+(x,t) + p^-(x,t)$, where $p^+(x,t)$ and $p^-(x,t)$ are the forward and backward propagating plane waves respectively. Introducing the complex frequency $\Omega = \omega + \mathrm{j}\beta$ as in [62], the solution of the lossless wave equation can be written in terms of Fourier components, as:

$$\begin{aligned} p(x,t,j\Omega) &= p_0^+(\mathrm{j}\Omega)e^{\mathrm{j}(\Omega t - Kx)} + p_0^-(\mathrm{j}\Omega)e^{\mathrm{j}(\Omega t + Kx)} \\ &= p_0^-(\mathrm{j}\Omega)\Big(R(\mathrm{j}\Omega)e^{\mathrm{j}(\Omega t - Kx)} + e^{\mathrm{j}(\Omega t + Kx)}\Big), \end{aligned} \tag{B.1}$$

where $K = \Omega/c_0$ is the complex wave number and $R(j\Omega) = p_0^+(j\Omega)/p_0^-(j\Omega)$ is the complex reflection coefficient. By imposing the boundary condition on $x = 0$:

$$v(0,t,\mathrm{j}\Omega) = -Y_a(\mathrm{j}\Omega)p(0,t,\mathrm{j}\Omega), \tag{B.2}$$

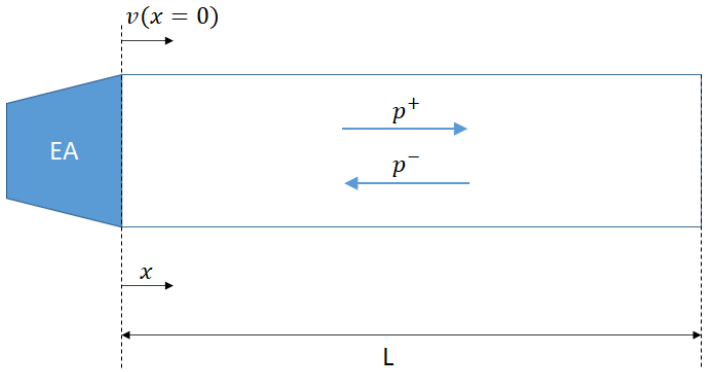

Figure B.1: 1D hard-walled acoustic cavity with an EA on the left end and a rigid termination on the right end.

where $Y_a(j\Omega)$ is the acoustic mobility at $x = 0$ (referred to the inward velocity, which explains the minus sign in Eq. (B.2)). For the Euler equation [62], the acoustic velocity is $v(x,t) = \frac{1}{\rho_0 c_0}(p^+(x,t) - p^-(x,t))$. Therefore, from Eq. (B.1) and (B.2), we retrieve the definition of the reflection coefficient [36]:

$$R(\mathrm{j}\Omega) = \frac{1 - Y_a(\mathrm{j}\Omega)\rho_0 c_0}{1 + Y_a(\mathrm{j}\Omega)\rho_0 c_0} \tag{B.3}$$

By imposing the rigid boundary condition on $x = L$:

$$v(L,t,\mathrm{j}\Omega) = p_0^-(j\Omega)\Big(R(\mathrm{j}\Omega)e^{\mathrm{j}(\Omega t - KL)} - e^{\mathrm{j}(\Omega t + KL)}\Big) = 0 \tag{B.4}$$

From Eq. (B.4), we get Eq. (B.5) and (B.6):

$$R(\mathrm{j}\Omega) = e^{2\mathrm{j}KL} = e^{2\mathrm{j}\omega/c_0 L}e^{-2\beta/c_0 L} \tag{B.5}$$

$$\ln|R(\mathrm{j}\Omega)| = -2\frac{\beta L}{c_0} \tag{B.6}$$

Therefore, a non-passive acoustical device (with $|R(j\Omega)| > 1$) in a lossless cavity, generates a negative value of β, which means instability. In Section 2.1.2 the analysis is carried out in terms of the Laplace variable s. The calculated poles s_p corresponds to $j\Omega_p$, where Ω_p are the complex natural frequencies of the system. Therefore, an $|R(s_p)| > 1$ produces a $\mathrm{Re}[s_p] = -\beta > 0$. In addition, according to Eq. (B.5), the $\mathrm{Re}[s_p]$ increases in absolute value for shorter length of the duct, i.e. the upsurge of instability is quicker in a smaller acoustic cavity, as expected.

Appendix C

The Integral Constraint on the reflection coefficient of an Impedance Controlled system

Let us consider the complex function

$$\tilde{F}(s) = \frac{1}{s^2} \ln[\tilde{R}(s)], \tag{C.1}$$

where:

$$\tilde{R}(s) = R(s) \prod_n \frac{s + s_n^*}{s - s_n}. \tag{C.2}$$

By defining:

$$F(s) = \frac{1}{s^2} \ln[R(s)], \tag{C.3}$$

and:

$$G(s) = \frac{1}{s^2} \sum_n \ln\left(\frac{s + s_n^*}{s - s_n}\right), \tag{C.4}$$

then:

$$\tilde{F}(s) = F(s) + G(s), \tag{C.5}$$

The reflection coefficient transfer function $R(s)$ is multiplied by $\prod_n \frac{s+s_n^*}{s-s_n}$ in order for $\tilde{R}(s)$ to not have "unstable zeros" (zeros with positive real part). For a stable system then, $\tilde{R}(s)$ has neither poles nor zeros in the right-half complex plane (rhp) and $\ln[\tilde{R}(s)]$ is analytic in the rhp. The use of the natural logarithm in Eq. (C.1) is convenient in order to separate numerator and denominator of a rational function (like $R_n(s)$), which is indeed a common practice in deriving the Bode integral constraints in the classical control theory (see [45] for example). The s^2 at the denominator is present in order to compensate for the unboundedness of $\ln(\tilde{R}(s))$ for large $|s|$.
Hence $\tilde{F}(s)$ is also analytic in the whole rhp except the origin, therefore for the Cauchy–Goursat Theorem [45]:

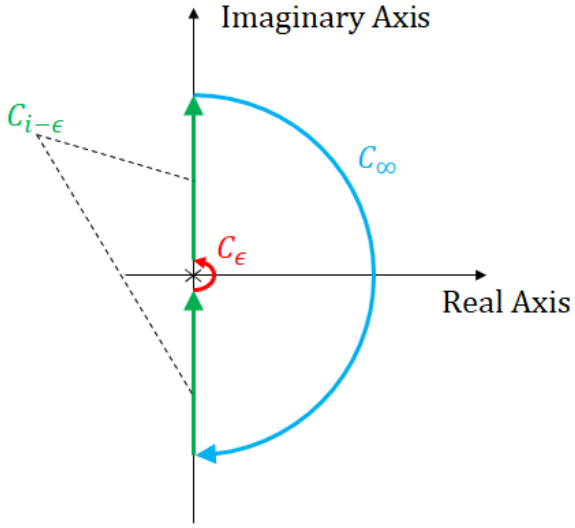

Figure C.1: Contour in the complex plane for the application of the Cauchy Integral Theorem to the function $\tilde{F}(s)$ defined in Eq. (C.1).

$$\oint_C \tilde{F}(s)ds = 0 = \int_{C_{i-\epsilon}} \tilde{F}(s)ds + \int_{C_\epsilon} \tilde{F}(s)ds + \int_{C_\infty} \tilde{F}(s)ds. \tag{C.6}$$

where C_ϵ is the closed counter-clockwise right circular indentation at the origin, of infinitesimal radius ϵ, C_∞ is the clockwise semi-circle of radius which tends to infinity, and $C_{i-\epsilon}$ is the entire imaginary axis except the origin. Let us evaluate each integral on the rhs of Eq. (C.6). From the Residue Theorem [110]:

$$\int_{C_\epsilon} \tilde{F}(s)ds = \mathrm{j}\pi \mathrm{Res}\{F(s), 0\} + \mathrm{j}\pi \mathrm{Res}\{G(s)\}. \tag{C.7}$$

The residue of $F(s)$ in zero, $\mathrm{Res}(F(s), 0)$, is calculated reminding that $F(s)$ has a double pole in zero (the s^2 at the denominator).

$$\mathrm{Res}\{F(s), 0\} = \lim_{s\to 0} \frac{d}{ds} s^2 F(s) = \lim_{s\to 0} \frac{d}{ds} \ln(R(s)) = \lim_{s\to 0} \frac{d}{ds} \Big\{ \ln[1-\eta_a(s)] - \ln[1+\eta_a(s)] \Big\}. \tag{C.8}$$

The limit appearing in Eq. (C.8) can be separated in the two following contributions:

$$\lim_{s\to 0} \frac{d}{ds} \Big\{ \ln[1-\eta_a(s)] \Big\} = \lim_{s\to 0} \frac{-\frac{d\eta_a(s)}{ds}}{1-\eta_a(s)} = -\lim_{s\to 0} \frac{d}{ds} \eta_a(s). \tag{C.9}$$

$$\lim_{s\to 0} \frac{d}{ds} \Big\{ \ln[1+\eta_a(s)] \Big\} = \lim_{s\to 0} \frac{d}{ds} \eta_a(s). \tag{C.10}$$

where $\eta_a(s)$ is the normalized acoustic mobility of the controlled EA: $\eta_a(s) = Y_a(s)\rho_0 c_0$. Reminding the expression of $Y_a(s)$ of (2.6), it appears the mechanical mobility in the Open Circuit case $Y_{m0}(s) = 1/Z_{m0}(s)$ which has a zero in zero, and the controller $H(s)$ which must be a proper and stable transfer function. Hence, also $\eta_a(s)$ must have at least a zero in zero. From the expression of $\eta_a(s)$ from Eq. (2.6), and developing the derivative, we find

$$\lim_{s\to 0}\frac{d}{ds}\eta_a(s)=\frac{\rho_0 c_0}{K_{a0}}\left(1-\frac{Bl}{S_d}\lim_{s\to 0}H(s)\right). \tag{C.11}$$

Thus, from (C.8), (C.9) and (C.10), and (C.11), we get the integral along the first term on the rhs of Eq. (C.7):

$$\mathrm{j}\pi\mathrm{Res}\{F(s),0\}=-2\mathrm{j}\pi\frac{\rho_0 c_0}{K_{a0}}\left(1-\frac{Bl}{S_d}\lim_{s\to 0}H(s)\right). \tag{C.12}$$

The residual of $G(s)$ on the rhs of Eq. (C.7) instead sums up to zero, hence:

$$\int_{C_\epsilon}\tilde{F}(s)ds=-2\mathrm{j}\pi\frac{\rho_0 c_0}{K_{a0}}\left(1-\frac{Bl}{S_d}\lim_{s\to 0}H(s)\right). \tag{C.13}$$

Also the integral along C_∞, can be written in terms of the contribution of $F(s)$ and $G(s)$. From the Jordan's Lemma [110]:

$$\int_{C_\infty}\tilde{F}(s)ds=-\mathrm{j}\pi\lim_{s\to\infty}s\tilde{F}(s)=0 \tag{C.14}$$

because

$$\lim_{s\to\infty}sF(s)=\lim_{s\to\infty}\frac{1}{s}\Big\{\ln[1-\eta_a(s)]-\ln[1+\eta_a(s)]\Big\}=-2\lim_{s\to\infty}\frac{1}{s}\eta_a(s)=0. \tag{C.15}$$

and

$$\lim_{s\to\infty}sG(s)=\lim_{s\to\infty}\frac{1}{s}\left\{\ln\left(\frac{s+s_n^*}{s-s_n}\right)\right\}=0, \tag{C.16}$$

Finally, since $F(s)$ is an even function of s according to its definition (C.3), the integral along $C_{i-\epsilon}$ becomes:

$$\int_{C_{i-\epsilon}}F(s)ds=\mathrm{j}\int_{-\infty}^{+\infty}F(\mathrm{j}\omega)d\omega=2\mathrm{j}\int_0^{+\infty}F(\mathrm{j}\omega)d\omega \tag{C.17}$$

The contribution of $G(s)$ over $C_{i-\epsilon}$ is instead:

$$\int_{C_{i-\epsilon}}G(s)ds=-2j\pi\sum_n\frac{\mathrm{Re}\{s_n\}}{|s_n|^2}, \tag{C.18}$$

so we get the last contribution of $\tilde{F}(s)$ on $C_{i-\epsilon}$:

$$\int_{C_{i-\epsilon}}\tilde{F}(s)ds=2\mathrm{j}\int_0^{+\infty}F(\mathrm{j}\omega)d\omega+2j\pi\sum_n\frac{\mathrm{Re}\{s_n\}}{|s_n|^2} \tag{C.19}$$

Therefore, inserting Eq. (C.19), (C.14) and (C.12) in (C.6), we get the integral constraint:

$$-\int_0^\infty\frac{1}{\omega^2}\ln|R(\omega)|d\omega=\frac{\pi\rho_0 c_0}{K_{a0}}\left(1-\frac{Bl}{S_d}\lim_{s\to 0}H(s)\right)-\pi\sum_n\frac{\mathrm{Re}\{s_n\}}{|s_n|^2}, \tag{C.20}$$

We highlight that Eq. (2.11) is valid for any proper transfer function $H(s)$ applied as a controller in the current-driven, pressure-based impedance control. This means that for any type of controller $H(s)$ (even different from the one defined in Eq. 2.3 and analysed in this contribution), the integral constraint (2.11) still applies. We want to emphasize that such

integral constraint, for purely passive resonators retrieves the one found by Yang in 2017 [122], which has its analogous for electro-magnetic waves in the work of Fano [35] and Rozanov [107]. The difference between our formalism (based upon the Laplace complex variable s, dearer to control engineers) and the one provided by [35], [107] and [122] (based upon the complex wave-length λ), is simply caused by the fact that Eq. (2.11) presented in this manuscript, has originally been derived without awareness of the previous works of Fano, Rozanov and Yang.

Appendix D

The digital implementation of the controller

The correctors $H_{loc}(s)$ defined in Sections 2.1 and 2.3, as well as $H_{grad}(s)$ illustrated in Section 3.5, are digitally implemented in real time by an Infinite Impulse Response (IIR) method. In Section 2.4 instead, another real time implementation is proposed in order to reproduce a non-linear mechanical behaviour of the loudspeaker, which is based upon a 4^{th} order Runge-Kutta method.
In this appendix, the IIR implementation of $H(s)$ is described, along with its balanced-realization in the state space.
The application of an analogical causal filter $H_c(s)$ in time domain corresponds to the convolution integral operator:

$$i(t) = \int_{-\infty}^{t} h_c(t-\tau)x(\tau)d\tau, \tag{D.1}$$

with $h_c(t)$ the inverse Laplace transform of $H_c(s)$. On a discrete set of time samples kT_s with sampling period T_s, the convolution product becomes:

$$i_n = \sum_{k=0}^{+\infty} h_k p_{n-k}. \tag{D.2}$$

If $H_c(s)$ is a real rational transfer function, then $h_k \neq 0 \ \forall k \in [0, +\infty)$. For this reason a convolution system of the type (D.2) is called as Infinite Impulse Response (IIR) system.
The Laplace transform $\mathcal{L}(\bullet)$ of Eq. (D.2), with the discrete functions written as distributions of Dirac δ, is:

$$i(z) = H(z)p(z), \tag{D.3}$$

with:

$$H(z) = \mathcal{L}\Big(\sum_{k=0}^{+\infty} h_k \delta_{kT_s}\Big) = \sum_{k=0}^{+\infty} h_k \mathcal{L}(\delta_{kT_s}) = \sum_{k=0}^{+\infty} h_k e^{-kT_s s} = \sum_{k=0}^{+\infty} h_k z^{-k}, \tag{D.4}$$

where the variable z comes from the change of variable $z = e^{-kT_s s}$, and gives the name of Z-transform. The functions $i(z)$, $p(z)$ are the Z-transform of the continuous signals $i(t)$, $p(t)$,

i.e. the Laplace transform of the discrete signals $i(kTs)$, $p(kT_s)$. From the definition of $z = e^{T_s s}$, then the transfer function $H(z)$ is equivalent to $H_c(s)$ as long as:

$$H(z) = H_c\Big(\frac{1}{T_s}\ln(z)\Big). \tag{D.5}$$

Nevertheless, the transfer function $H(z)$ defined in Eq. (D.5) is not a real rational transfer function in z. In order for the corrector $H(z)$ to realize a discrete transfer function which produce a recurrence equation, also $H(z)$ must be a real rational transfer function, as $H_c(s)$. Therefore, the equivalence relationship $s = \frac{1}{T_s}\ln(z)$ between the Laplace and the Z space, must be substituted by a rational expression (called transposition) which would keep as much as possible the equivalence between $H_c(s)$ and $H(z)$. Two main equivalence conditions are required: the discrete transfer function $H(z)$ must be stable if and only if also $H_c(s)$ is stable, and the frequency responses associated with the two transfer functions must coincide as much as possible. Different transpositions between s and z can be achieved based upon different integration techniques of a continuous signal from discrete values. The integral approximation by the sum of lower rectangles, leads to the transposition $s \Leftrightarrow \frac{z-1}{T_s}$, also called zero-order-holder (zoh) transform. The upper rectangles sum leads to $s \Leftrightarrow \frac{z-1}{zT_s}$. Both these transpositions do not fulfil the equivalence condition between the stability of $H(z)$ and $H_c(s)$. The trapezoidal rule for integral approximation, instead, brings the transposition $s \Leftrightarrow \frac{2}{T_s}\frac{z-1}{z+1}$ (the so-called bilinear or Tustin transform) which satisfies the equivalence condition given below:

$$\mathrm{Re}(s) < 0 \Leftrightarrow |z| < 1. \tag{D.6}$$

Therefore, the stability condition on $H(z)$ becomes $|z_d| \leq 1$, and the passivity condition $|z_n| \leq 1$, where z_d and z_n are the poles and zeros of $H(z)$ respectively.
Concerning the frequency response, the trapezoidal technique obviously leads to a better approximation respect to the rectangular sums. In particular, the level of approximation achieved by the bilinear transform in the frequency response, is given by the relationship between the angular frequency ω_c corresponding to the frequency response in s (substituting s with $j\omega_c$) and the angular frequency corresponding to the frequency response in z (substituting z with $e^{T_s j\omega}$) in the transposition $s = \frac{2}{T_s}\frac{z-1}{z+1}$. It results then:

$$\omega_c = \frac{2}{T_s}\tan(T_s\omega), \quad \Leftarrow \quad \omega = \frac{2}{T_s}\arctan(T_s\omega_c) \tag{D.7}$$

For low $T_s\omega_c$ (low sampling time or low frequencies), the two frequency responses coincide.

Thanks to the zoh or Tustin transforms, a corrector $H_c(s)$ is transposed to a rational transfer function $H(z)$ in the z-space of the type:

$$H(z) = \frac{\sum_{m=0}^{N_b} b_m z^{-m}}{\sum_{k=0}^{N_a} a_k z^{-k}}. \tag{D.8}$$

By inserting Eq. (D.8) in Eq. (D.3), we get an approximation of the discrete convolution product of Eq. (D.2).

$$i_n = \sum_{m=0}^{N_b} b_m p_{n-m} - \sum_{k=1}^{N_a} a_k i_{n-k}. \tag{D.9}$$

The recursive Eq. (D.9), differently from Eq. (D.2), requires a finite number of operations, and can be digitally implemented.

Nevertheless, the recursive algorithm (D.9) is not optimal in terms of round-off errors and required computational time. The balanced form of the state-space representation of a digital filter $H(z)$ has demonstrated [88] to provide the lowest sensitivity to round-off errors. A state-space representation of the discrete corrector $H(z)$ is:

$$\begin{aligned} i_n &= Cx_n + Dp_n \\ x_{n+1} &= Ax_n + Bp_{n-m_{del}}, \end{aligned} \tag{D.10}$$

where x is a fictitious state vector. The pressure in the state vector dynamics equation (the second in Eq. (D.10)) is evaluated at the time $t_{n-m_{del}}$ where $m_{del}T_s$ is the time delay in the control architecture. The state-space matrices A, B, C and D, corresponding to the balanced realization of $H(z)$ can be obtained by the Matlab function *balreal*.
Another important operation for the implementation of $H(z)$ is the elimination of the *uncontrollable* or *unobservable* states of the $H(z)$ state-space model. This can be achieved by evaluating the Gramian of the balanced realization as briefly described in Section 2.3. Another important tool is the Matlab function *minreal* (which stays for "minimal realization") which cancels the overlapping pole-zero pairs from the transfer function.
Both the minimal and balanced realization are very useful when we deal with high order filters, which are usually more sensitive to numerical round-off and often present several close-spaced zero-pole couples.

Appendix E

Normal incidence problem for time domain simulations

Let us consider a hard-walled waveguide as in Figure E.1 with our EA (or any other acoustic system) of inward normal displacement $w(t)$ on one side, and an anechoic termination on the other. A source is radiating a plane wave of amplitude p_s toward the EA. Since no reflection occurs at the anechoic termination, $p_s \equiv p^+$ in amplitude. In the plane wave regime, it is a 1D problem, where the incident wave $p_s(t)$ is supposed to be known at any time, and the reflected wave $p^-(t)$ is unknown. From the plane wave assumption:

$$p(x,t) = p^+(x - c_0 t) + p^-(x + c_0 t), \tag{E.1}$$

From the Euler equation at the interface $x = 0$ with the EA:

$$\ddot{w}(t) = \frac{1}{\rho_0}\Big(\partial_x p^+(x,t) + \partial_x p^-(x,t)\Big) \tag{E.2}$$

Hence, from Eq. (E.1):

$$\begin{aligned} \ddot{w}(t) &= \frac{1}{\rho_0 c_0}\Big(\partial_t p^+(t) - \partial_t p^-(t)\Big) \\ \Rightarrow \dot{w}(t) &= \frac{1}{\rho_0 c_0}\Big(p^+(t) - p^-(t)\Big), \end{aligned} \tag{E.3}$$

where we have defined as $p^+(t)$ and $p^-(t)$ the incident and reflected pressure waves at the interface with the EA. From Eq. (E.3), the reflected pressure wave at the EA interface, can be written in terms of the velocity of the EA, as $p^-(t) = p^+(t) - \rho_0 c_0 \dot{w}(t)$. In order to solve

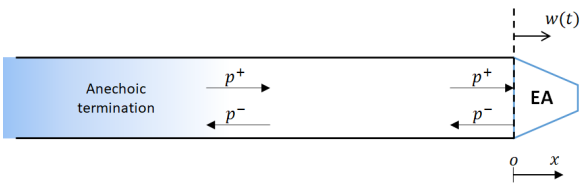

Figure E.1: Normal incidence problem, with anechoic termination on one side and EA on the other.

the normal-incidence problem, the dynamics of the EA (or any other acoustic device) must be defined as an operator $\mathcal{L}(p(t), w(t)) = 0$ relating the displacement $w(t)$ and the total sound pressure $p(t)$. For a linear locally reacting acoustic system, such operator is usually represented in the frequency domain as an acoustic impedance, so we can call it as impedance operator. For our EA, the impedance operator takes into account also the controller, that is the electrical current which is function of the measured total sound pressure. The total sound pressure to be considered in the operator $\mathcal{L}(p(t), w(t)) = 0$ is $p(t) = p^+(t) + p^-(t)$, where $p^+(t)$ is supposed to be known at any time, while $p^-(t)$ can be written in terms of the EA velocity as seen just before.
Therefore, $p(t) = 2p^+(t) - \rho_0 c_0 \dot{w}(t)$ and the impedance operator becomes a function of just $p^+(t)$ and $w(t)$ and its derivatives. As $p^+(t)$ is known, $\mathcal{L}(p(t), w(t)) = 0$ can be solved by a numerical scheme to retrieve $w(t)$.

Appendix F

Interface with the boundary advection law, in free field

In this Appendix we give the demonstration of the reflection coefficient formula reported in Eq. (3.14), for the boundary advection law (Eq. (3.10)), in the hypothesis of free plane incident field in a 2D semi-infinite domain as the one in Figure 3.2. The incident wave can be expressed as:

$$p_i(t,x,y) = p_{i0} e^{\mathrm{j}\omega t - j\frac{\omega}{c_0}\cos\theta_i x - j\frac{\omega}{c_0}\sin\theta_i y}. \tag{F.1}$$

The reflected wave field is supposed to respect the classical Snell-Descartes law of refraction, according to which the reflected plane wave propagates with a specular angle with respect to the incident one, i.e. $\theta_r = -\theta_i$. The presence of a transport at the boundary gives no reason to modify this assumption, in an analogous way to the case of air-flow different from 0 in the acoustic domain [55].
Hence, the reflected wave from a boundary advection law can be written as:

$$p_r(t,x,y) = R(\mathrm{j}\omega) p_{i0} e^{\mathrm{j}\omega t - j\frac{\omega}{c_0}\cos\theta_i x + j\frac{\omega}{c_0}\sin\theta_i y}. \tag{F.2}$$

The acoustic velocity v_y normal to the boundary is obtained by the Euler equation of acoustics $-\rho\partial_t v_y = \partial_y p$, where $p = p_o + p_r$. Substituting Eq.s (F.1) and (F.2) in the Euler equation, we find the normal velocity on the boundary $v_y(y=0)$:

$$v_y(t,x) = \frac{\sin\theta_i}{\rho_0 c_0} p_{i0}(1 - R(\mathrm{j}\omega)) e^{\mathrm{j}\omega t - j\frac{\omega}{c_0}\cos\theta_i x}. \tag{F.3}$$

Also, the boundary advection law (3.10) can be applied to the total pressure $p = p_i + p_r$ to give:

$$v_y(t,x) = \frac{1}{Z_{Loc}(\mathrm{j}\omega)}\left(1 + \frac{c_a}{c_0}\cos\theta_i\right)(1 + R(\mathrm{j}\omega)) e^{\mathrm{j}\omega t - j\frac{\omega}{c_0}\cos\theta_i x}. \tag{F.4}$$

Equating Eq. (F.3) and (F.4), we find the reflection coefficient:

$$R(\mathrm{j}\omega) = \frac{\zeta_{Loc}(\mathrm{j}\omega)\sin\theta_i - (1 - \frac{c_a}{c_0}\cos\theta_i)}{\zeta_{Loc}(\mathrm{j}\omega)\sin\theta_i + (1 - \frac{c_a}{c_0}\cos\theta_i)}, \tag{F.5}$$

where $\zeta_{Loc}(\mathrm{j}\omega) = Z_{Loc}(\mathrm{j}\omega)/\rho_0 c_0$. Observe that for $c_a = 0$ the reflection coefficient for classical locally-reacting surfaces (characterized by an impedance $Z_{Loc}(\mathrm{j}\omega)$) is retrieved.

Appendix G

1D model reduction of an acoustic waveguide

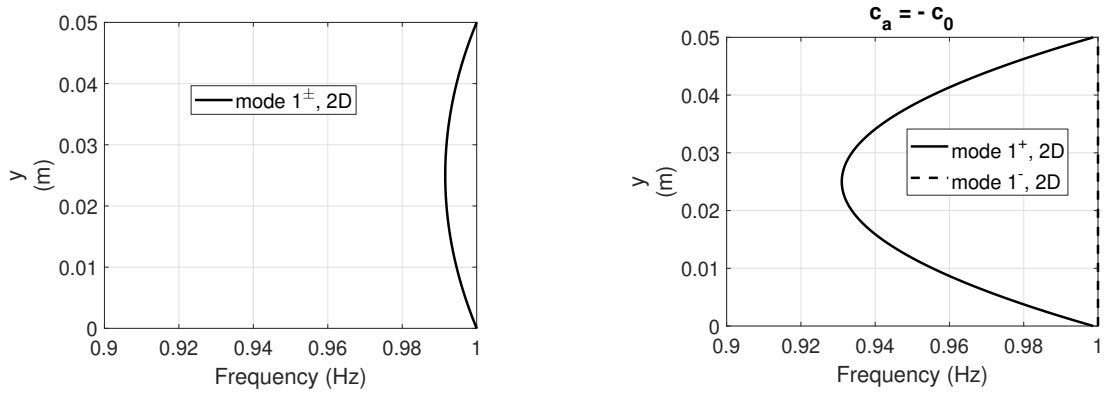

Figure G.1: First duct mode-shape propagating in both senses, in case of locally reacting liner (with $\mu_M = \mu_K = 0.2$, $R_{at} = \rho_0 c_0$ and $c_a = 0$) (**a**), and in case of advective boundary law (with $\mu_M = \mu_K = 0.2$, $R_{at} = \rho_0 c_0$ and $c_a = -c_0$) (**b**).

Let us consider the cylindrical waveguide as the one of Figure 1.3. In order to reduce the problem to 1D, let us average the equations by integrating over the cross-section:
$\forall t \in \mathbb{R}, \quad x \in \mathbb{R}$, and $(y, z) \in \Omega$,

$$\frac{1}{S} \iint_{\mathcal{A}} \Big[\frac{1}{c_0^2} \partial_{tt} p(x,y,z,t) - (\partial_{xx} + \partial_{yy} + \partial_{zz}) p(x,y,z,t) \Big] dydz = 0. \tag{G.1}$$

Denoting the mean acoustic pressure over the section $\tilde{p}(x,t) = \frac{1}{S} \iint_{\Omega} p(x,y,z,t) dydz$, and integrating by parts the second term (or, equivalently, using the divergence theorem, or Stokes' theorem), the equation now reads:
$\forall t \in \mathbb{R}, \quad x \in \mathbb{R}$,

$$\frac{1}{c_0^2} \partial_{tt} \tilde{p}(x,t) - \partial_{xx} \tilde{p}(x,t) = \frac{1}{S} \oint_{\partial \mathcal{A}} \partial_n p(x,\gamma,t) d\gamma \tag{G.2}$$

where γ is a curvilinear coordinate along $\partial \mathcal{A}$ and ∂_n is the gradient along the outward direction. In Eq. (G.3) the boundary advection law is rewritten in terms of $\partial_n p(x,s,t)$:

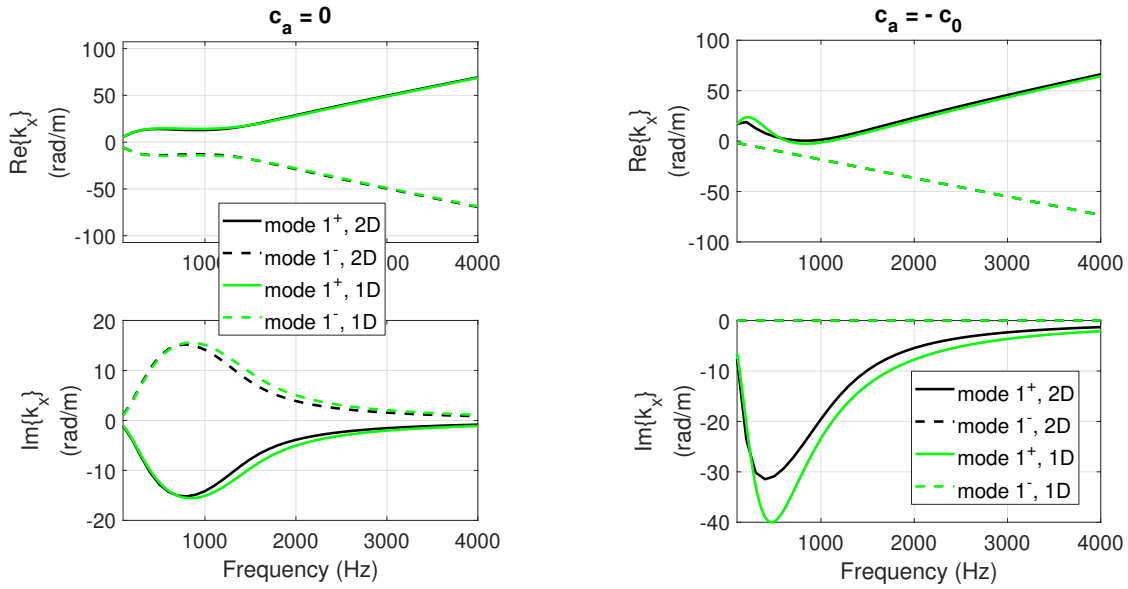

(a) (b)

Figure G.2: Comparison between 2D FE simulations and 1D analytical solutions of the dispersion plots relative to the first duct mode propagating in both senses, in case of locally-reactive liner (with $\mu_M = \mu_K = 0.2$, $R_{at} = \rho_0 c_0$ and $c_a = 0$) (**a**), and in case of advective boundary (with $\mu_M = \mu_K = 0.2$, $R_{at} = \rho_0 c_0$ and $c_a = -c_0$) (**b**).

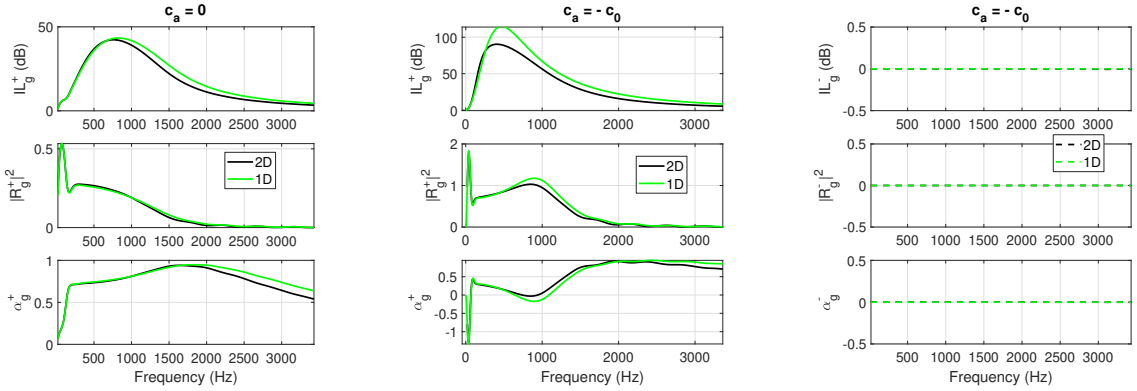

(a) (b) (c)

Figure G.3: Comparison between 2D FE simulations and 1D analytical solutions of the scattering performances in case of locally-reactive liner (with $\mu_M = \mu_K = 0.2$, $R_{at} = \rho_0 c_0$ and $c_a = 0$) (**a**), and in case of advective boundary (with $\mu_M = \mu_K = 0.2$, $R_{at} = \rho_0 c_0$ and $c_a = -c_0$) (**b**).

$$\partial_n p(x,\gamma,t) = -\eta_{Loc}\left[\frac{1}{c_0}\partial_t p + \frac{c_a}{c_0}\partial_x p\right], \tag{G.3}$$

where $\eta_{Loc}[-]$ is the time operator corresponding to the local normalized mobility $\eta_{Loc}(\mathrm{j}\omega)$ in the frequency domain. On the right-hand side of Eq. (G.2), we can now insert the boundary advection law:

$$\frac{1}{c_0^2}\partial_{tt}\tilde{p}(x,t) - \partial_{xx}\tilde{p}(x,t) = -\frac{1}{S}\oint_{\partial\mathcal{A}}\left(-\eta_{Loc}\left[\frac{1}{c_0}\partial_t p_b(x,t) + \frac{c_a}{c_0}\partial_x p_b(x,t)\right]\right)d\gamma \tag{G.4}$$

Denoting the mean acoustic pressure field along the boundary contour $p_b(x,t) = \frac{1}{L_p}\oint_{\partial\Omega} p(x,s)ds$,

where L_p is the perimeter length of the cross-section treated by a the boundary advection law (the rest is supposed as rigid), we finally get:

$$\frac{1}{c_0^2}\partial_{tt}\tilde{p}(x,t) - \partial_{xx}\tilde{p}(x,t) = -\frac{1}{S}\left(- \eta_{Loc}\left[\frac{1}{c_0}\partial_t p_b(x,t) + \frac{c_a}{c_0}\partial_x p_b(x,t)\right]\right) \tag{G.5}$$

As only the first mode can be taken into account in such 1D model reduction, the pressure at the boundary can be expressed in terms of the average pressure in the tube as:

$$p_b(x,t) = a_1\tilde{p}(x,t), \tag{G.6}$$

with a_1 a constant multiplicative factor and the average pressure $\tilde{p}(x,t)$ assimilated to the first plane mode. Observe that for non-reciprocal propagation the first modes propagating in one sense or the other, can be different from each other, hence the coefficient a_1 can be not the same. In addition, it can vary with frequency as the mode slightly changes in dispersion. In Eq. (G.7) we drop the tilde above p for simplicity.

$$\frac{1}{c_0^2}\partial_{tt}\tilde{p}(x,t) - \partial_{xx}\tilde{p}(x,t) = -\frac{L_p a_1}{S}\left(- \eta_{Loc}\left[\frac{1}{c_0}\partial_t p(x,t) + \frac{c_a}{c_0}\partial_x p(x,t)\right]\right) \tag{G.7}$$

The multiplicative factor on the rhs $\frac{L_p a_1}{S}$ is labelled as G, as it is a constant depending upon the geometry and upon the first mode. Different geometries and/or partial treatment of the waveguide boundary, would require to properly modify such parameter.
We can now pass to the frequency domain in order to find the 1D dispersion relation, allowing to determine the wave numbers of the first modes propagating toward $+x$ or $-x$. The first 1D mode has the expression:

$$p(x,t) = p_0 e^{\mathrm{j}(\omega t - k_x x)}. \tag{G.8}$$

Inserting this ansatz in the 1D reduced model of Eq. (G.7), comes:

$$k_x^2 - \mathrm{j}G\eta_{Loc}\frac{c_a}{c_0} + k_0(\mathrm{j}G\eta_{Loc} - k_0) = 0. \tag{G.9}$$

Hence the two wavenumber solutions result from the quadratic formula:

$$k_{x,1,2} = \frac{1}{2}\left(\mathrm{j}G\eta_{Loc}\frac{c_a}{c_0} \pm \sqrt{-G^2\eta_{Loc}^2\frac{c_a}{c_0} + 4k_0(k_0 - \mathrm{j}G\eta_{Loc})}\right). \tag{G.10}$$

Notice that such expression, in general, takes into account the possibility to have $k_{x,1} \neq -k_{x,2}$.

Once the modal problem has been solved for the 1D reduced system, the scattering problem can be tackled. Supposing a finite segment of the 1D acoustic waveguide lined with the boundary advection law, the scattering coefficients can be retrieved by imposing the continuity conditions at the input and output section of the lined segment, of length L. Upstream and downstream the lined segment, the 1D propagation is characterized by the wavenumber k_0 as rigid boundaries are supposed in such regions. The continuity conditions on pressure and velocity at the input and output sections of the lined segments, are reported in Eq.s (G.11) and (G.12) respectively.

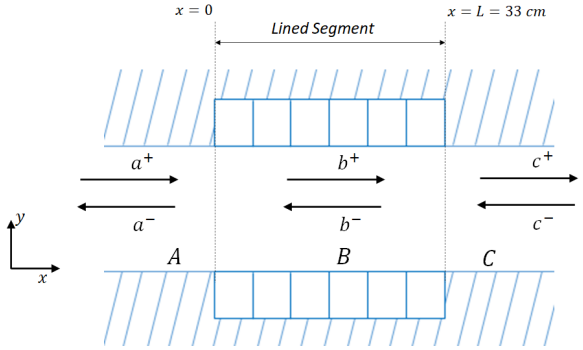

Figure G.4: Definition of the forward and backward plane modes in the waveguide: upstream (A), into (B) and downstream (C) the lined segment.

$$\begin{aligned} a^+ + a^- &= b^+ + b^- \\ a^+ - a^- &= \frac{k_b^+}{k_0} b^+ + \frac{k_b^-}{k_0} b^-, \end{aligned} \tag{G.11}$$

$$\begin{aligned} b^+ + b^- &= c^+ + c^- \\ c^+ - c^- &= \frac{k_b^+}{k_0} b^+ e^{-\mathrm{j}k_b^+ L} + \frac{k_b^-}{k_0} b^- e^{-\mathrm{j}k_b^- L}, \end{aligned} \tag{G.12}$$

where the coefficient a^+ and a^-, b^+ and b^-, c^+ and c^- correspond to the wave amplitudes of the forward and backward propagating modes, in the regions A, B and C respectively (see Figure **??**). The wavenumber in regions A and C is $k_0^{+/-} = \omega/c_0$, while in the treated segment B, it is $k_b^{+/-}$ with k_b^+ not necessarily equal to $-k_b^-$, as already mentioned above. The continuity equations can be rearranged according to the scattering matrix formulation. A convenient way to obtain the scattering coefficients without bringing along too large expressions, is to split the problem into the scattering at section $x = 0$ and at section $x = L$. The scattering at $x = 0$ is written in the matrix Eq. (G.13), while the scattering at $x = L$ is given by Eq. (G.14). The coefficients appearing in the matrices of Eq.s (G.13) and Eq. (G.14) can be labelled as "intermediate scattering coefficients".

$$\begin{bmatrix} b^+ \\ a^- \end{bmatrix} = \begin{bmatrix} T_{a\to b}^+ & R_b^- \\ R_a^+ & T_{b\to a}^- \end{bmatrix} \begin{bmatrix} a^+ \\ b^- \end{bmatrix} \tag{G.13}$$

$$\begin{bmatrix} c^+ \\ b^- \end{bmatrix} = \begin{bmatrix} T_{b\to c}^+ & R_c^- \\ R_b^+ & T_{c\to b}^- \end{bmatrix} \begin{bmatrix} b^+ \\ c^- \end{bmatrix} \tag{G.14}$$

The "intermediate scattering coefficients" are reported in Eq.s (G.15):

$$T_{a\to b}^+ = \frac{2}{1 + k_b^+/k_0} \tag{G.15a}$$

$$R_b^- = -\frac{1 + k_b^-/k_0}{1 + k_b^+/k_0} \tag{G.15b}$$

$$R_a^+ = \frac{1 - k_b^+/k_0}{1 + k_b^+/k_0} \tag{G.15c}$$

$$T^-_{b\to a} = \frac{k_b^+/k_0 - k_b^-/k_0}{1 + k_b^+/k_0} \tag{G.15d}$$

Eq.s (G.15) results to be quite intuitive. From the matrix Eq.s (G.13) and (G.14) and the expression of the intermediate scattering coefficients (G.15), the global scattering coefficients, defined in Eq. G.16, are retrieved in Eq.s G.17.

$$\begin{bmatrix} c^+ \\ a^- \end{bmatrix} \begin{bmatrix} T^+ & R^- \\ R^+ & T^- \end{bmatrix} \begin{bmatrix} a^+ \\ c^- \end{bmatrix} \tag{G.16}$$

$$T^+ = \frac{T^+_{a\to b} T^+_{b\to c}}{1 - R^-_b R^+_b} \tag{G.17a}$$

$$R^+ = \frac{R^+_a + R^+_b(-R^+_a R^-_b + T^+_{a\to b} T^-_{b\to a})}{1 - R^-_b R^+_b} \tag{G.17b}$$

$$T^- = \frac{T^-_{c\to b} T^-_{b\to a}}{1 - R^-_b R^+_b} \tag{G.17c}$$

$$R^- = \frac{R^+_c + R^-_b(-R^-_c R^+_b + T^+_{b\to c} T^-_{c\to b})}{1 - R^-_b R^+_b} \tag{G.17d}$$

We save the reader from the explicit formulas of the global scattering coefficients, nevertheless it is interesting to report their expression in case of $k_b^+ = -k_b^- = k_b$, i.e. in case of a general reciprocal boundary treatment application:

$$T^+ = T^- = 4 \frac{e^{-\mathrm{j}k_b L} \frac{k_b/k_0}{(1+k_b/k_0)^2}}{1 - e^{-2\mathrm{j}k_b L} \left(\frac{1-k_b/k_0}{1+k_b/k_0} \right)^2}. \tag{G.18}$$

$$R^+ = R^- = \left(\frac{1 - k_b/k_0}{1 + k_b/k_0} \right) \frac{-2e^{-2\mathrm{j}k_b L} \frac{k_b/k_0}{(1+k_b/k_0)^2}}{1 - e^{-2\mathrm{j}k_b L} \left(\frac{1-k_b/k_0}{1+k_b/k_0} \right)^2}. \tag{G.19}$$

Eq.s G.18 and G.19 are the formula of reflection and transmission through a 1D acoustic medium of wavenumber k_b, applying also to equivalent fluid formulations for example [1]. Indeed, the 1D model reduction has reduced the treated segment of the duct to an equivalent fluid with wavenumbers k_b^+ and k_b^- for the positive and negative propagation.

Figures G.2 show the comparison between the 2D FE and 1D analytical solutions of the wavenumbers of the first duct mode propagating in both directions, in a waveguide fully lined by either a locally reacting liner (in G.2a), with $\mu_M = \mu_K = 0.2$ and $R_{at} = \rho_0 c_0$, or by an advective boundary law (in G.2a), with $\mu_M = \mu_K = 0.2$, $R_{at} = \rho_0 c_0$ and $c_a = -c_0$. In Figures G.3, the 2D FE and 1D analytical solutions are compared in terms of the scattering performance for locally reacting (Figure G.3a) and advective B.C. (Figure G.3b and G.3c for positive and negative propagating incident field respectively). Apparently the 1D model reduction provides pretty accurate solutions, almost perfectly overlapping the 2D FE simulations both in terms of duct modes and scattering performances. The case of advective B.C. results slightly less accurately described by the 1D reduced model, even though it perfectly detects the non-reciprocity as well as the trends and levels of the scattering performances. The accuracy achieved by the 1D reduced model is mainly related to the assumption of a

single propagating mode in the 1D waveguide. The $a1$ coefficient appearing in G, will differ from 1 as much as the first mode pressure distribution differs from a plane wave. In such cases, assuming $a1 = 1$ could bring significant errors, and this factor should be correctly identified. Hence, the level of approximation of the dispersion solutions of the 1D reduced model very much depends upon the value assumed for $a1$. Moreover, the level of approximation of the scattering results obtained by the 1D reduced model depends also upon how much the first modes (propagating in both senses) differ from the plane mode, as it affects the mode-conversion at the input and output sections of the lined segment. Figures G.1a and G.1b show the first duct-mode shapes in case of locally-reacting and advective B.C.s respectively. As in case of advective B.C. the first mode-shape significantly differs from the plane mode, the $a1$ coefficient will differ from 1, and the mode-conversion at the input and output sections of the lined segment might involve higher order duct modes. These are the causes of lower accuracy in the 1D reduced model results. In order to improve the model reduction, another mode might be taken into account, as presented in [4].
The usefulness of a 1D model reduction is in providing quick low-frequency analytical results approximating both dispersion and scattering obtained by a boundary treatment in an acoustic waveguide. Such fast solutions might be exploited both for liner impedance eduction and in a first stage of boundary treatment design.